Numerical simulations of the shock wave-boundary layer interactions

Ismaïl Ben Hassan Saïdi

université PARIS-SACLAY

UNIVERSITÉ PARIS SUD
Comprendre le monde, construire l'avenir

NNT : 2019SACLS390

Numerical simulations of shock wave boundary layer interactions

Thèse de doctorat de l'Université Paris-Saclay
préparée à l'Université Paris-Sud

École doctorale n°579 Sciences mécaniques et énergétiques, matériaux et géosciences (SMEMaG)
Spécialité de doctorat : mécanique des fluides

Thèse présentée et soutenue à Orsay, le 04/11/2019, par

ISMAÏL BEN HASSAN SAÏDI

Composition du Jury :

Laurent JOLY Professeur, ISAE-SUPAERO (DAEP)	Président
Abdellah HADJADJ Professeur, INSA de Rouen (CORIA)	Rapporteur
Jean-Christophe ROBINET Professeur, Arts et Métiers (DynFluid)	Rapporteur
Guillaume LEHNASCH Maître de Conférences, ISAE-ENSMA (Institut Pprime)	Examinateur
Frédérique LAURENT-NÈGRE Chargée de Recherche, CNRS (EM2C)	Examinatrice
Christian TENAUD Directeur de recherche, CNRS (LIMSI)	Directeur de thèse
Guillaume FOURNIER Maître de Conférences, Université d'Évry (LMEE)	Co-encadrant de thèse

Thèse de doctorat

Remerciements

Je tiens tout d'abord à remercier mon directeur de thèse, monsieur Christian TENAUD, et mon co-encadrant de thèse, Monsieur Guillaume FOURNIER, avec qui j'ai beaucoup apprécié travailler durant ces trois années. Je les remercie pour leur disponibilité et pour la grande qualité de leur encadrement durant ces trois années de thèse.

Merci à Guillaume HOUZEAUX de m'avoir accueilli au Barcelona Supercomputing Center durant le mois de juin 2019.

Merci également à l'ensemble du personnel du LIMSI d'en avoir fait un lieu si agréable, dans lequel on a plaisir à travailler.

Je remercie messieurs Abdellah HADJADJ et Jean Christophe ROBINET d'avoir accepté de rapporter mes travaux de thèse.

Je remercie également monsieur Laurent JOLY d'avoir présidé mon jury de soutenance.

Je remercie madame Frédérique LAURENT-NÈGRE et monsieur Guillaume LEHNASCH d'avoir été examinateurs.

Je dédie cette thèse à mes parents, à mon frère et à ma compagne.

Synthèse en français

Le manuscrit de thèse étant rédigé en anglais, nous présentons ici une synthèse du travail effectué à l'intention des lecteurs francophones.

Les situations dans lesquelles une onde de choc interagit avec une couche limite sont nombreuses dans les industries aéronautiques et spatiales. Sous certaines conditions (nombre de Mach élevé, grand angle de choc...), ces interactions entrainent un décollement de la couche limite. Des études antérieures ont montré que la zone de recirculation et le choc réfléchi sont tous deux soumis à un mouvement d'oscillation longitudinale à basse fréquence connu sous le nom d'instabilité de l'interaction onde de choc / couche limite (IOCCL). Ce phénomène soumet les structures à des chargement oscillants à basse fréquence qui peuvent endommager les structures.

L'objectif du travail de thèse est de réaliser des simulations instationnaires de l'IOCCL afin de contribuer à une meilleure compréhension de l'instabilité de l'IOCCL et des mécanismes physiques sous-jacents.

La simulation d'écoulements compressibles turbulents présente deux difficultés majeures. D'une part, le schéma numérique doit introduire le minimum de dissipation afin de représenter les fines échelles turbulentes avec précision. Pour ce faire, l'utilisation de schémas numériques d'ordre élevé est en général privilégiée. D'autre part, les schémas d'ordre élevé sont connus pour introduire des oscillations parasites au voisinage des discontinuités pouvant apparaitre dans les écoulements compressibles (ondes de choc, surfaces de glissement). Afin du supprimer ces oscillations parasites, l'utilisation d'une capture de choc est nécessaire. Pour effectuer cette étude, une approche numérique originale est utilisée. Un schéma « One step » volume fini qui couple l'espace et le temps, reposant sur une discrétisation des flux convectifs par le schéma OSMP, est développé jusqu'à l'ordre 7 en temps et en espace. Les flux visqueux sont discrétisés en utilisant un schéma aux différences finies centré standard. Une contrainte de préservation de la monotonie (MP) est utilisée pour la capture de choc.

La validation de l'approche numérique est ensuite effectuée. Pour évaluer la capacité du schéma numérique à calculer les écoulements turbulents avec précision, le cas test du tourbillon de Taylor-Green est considéré. Un autre cas test, une interaction stationnaire 2D entre une onde de choc oblique et une couche limite laminaire se développant sur une plaque plane, est considéré pour évaluer la capture de choc. Cette validation de l'approche numérique démontre sa capacité à calculer les écoulements turbulents et la grande efficacité de la procédure MP pour capturer les ondes de choc sans dégrader la solution pour un surcoût négligeable. Il est également montré que l'ordre le plus élevé du schéma OSMP testé représente le meilleur compromis précision / temps de calcul. De plus un ordre de discrétisation des flux visqueux supérieur à 2 semble avoir une influence négligeable sur la solution pour les nombres de Reynolds relativement élevés considérés. L'ensemble des simulations présentées dans la suite du manuscrit sont donc effectuées en utilisant le schéma OSMP d'ordre 7 pour discrétiser les flux convectifs et un schéma d'ordre 2 pour discrétiser les flux visqueux.

La simulation d'un cas d'IOCCL 3D instationnaire avec une couche limite incidente laminaire est ensuite effectuée. Dans ce cas, la couche limite incidente étant laminaire, l'influence des structures turbulentes de la couche limite sur l'instabilité de l'IOCCL est supprimée. Dans ce contexte, l'unique cause d'IOCCL suspectée est liée à la dynamique de la zone de recirculation. Les résultats montrent que seul le choc de rattachement oscille aux fréquences caractéristiques de la respiration basse fréquence du bulbe de recirculation. Le point de séparation ainsi que le choc réfléchi ont une position fixe. Cela montre que dans cette configuration, l'instabilité de l'IOCCL n'a pas été reproduite.

Afin de reproduire l'instabilité de l'IOCCL, la simulation de l'interaction entre une onde de choc et une couche limite turbulente est ensuite réalisée. Une méthode de turbulence synthétique (Synthetic Eddy Method - SEM) est développée et utilisée à l'entrée du domaine de calcul pour initier une couche limite turbulente à moindre coût. L'analyse des résultats est effectuée en utilisant

notamment la méthode snapshot-POD (Proper Orthogonal Decomposition). Pour cette simulation, l'instabilité de l'IOCCL a été reproduite. Les résultats suggèrent que la dynamique du bulbe de recirculation est dominée par une respiration à moyenne fréquence. Ces cycles successifs de remplissage / vidange de la zone séparée sont irréguliers dans le temps avec une taille maximale du bulbe de recirculation variant d'un cycle à l'autre. Ce comportement du bulbe de recirculation traduit une modulation basse fréquence des amplitudes des oscillations des points de séparation et de recollement et donc une respiration basse fréquence de la zone séparée. Ces résultats suggèrent que l'instabilité de l'IOCCL est liée à cette dynamique basse fréquence du bulbe de recirculation, les oscillations du pied du choc réfléchi étant en phase avec le point de séparation.

Contents

Contents 1

List of figures 3

List of tables 9

Introduction 1
0.1 References . . . 6

1 Shock wave boundary layer interactions 9
1.1 Different shock wave boundary layer interactions in 2D flows . . . 10
1.2 Mean flow . . . 12
1.3 Strong shock wave boundary layer unsteadiness . . . 15
1.4 Conclusions and outlook of the work . . . 19
1.5 References . . . 19

2 Equations and numerical approach 23
2.1 The governing equations . . . 24
2.2 Introduction to high order numerical schemes for compressible Navier-Stokes equations . . . 26
2.3 Numerical approach applied . . . 29
2.4 Domain and boundary conditions . . . 34
2.5 Conclusions . . . 36
2.6 References . . . 36

3 Validation of the numerical approach 39
3.1 Taylor Green vortex at Re=1600 . . . 40
3.2 Shock-wave laminar boundary layer interaction. . . . 46
3.3 Conclusions . . . 52
3.4 References . . . 52

4 Shock wave laminar boundary layer 55
4.1 Physical parameters, computational domain and mesh . . . 56
4.2 Mean flow . . . 57
4.3 Flow Dynamics . . . 59
4.4 Conclusion . . . 65
4.5 References . . . 66

5 Initiating a turbulent compressible boundary layer 67
5.1 Turbulent inflow boundary conditions . . . 68
5.2 Implemented Synthetic Eddy Method . . . 71
5.3 Simulation of a turbulent compressible boundary layer over a flat plate . . . 76
5.4 Conclusion . . . 81
5.5 References . . . 81

6 Shock wave turbulent boundary layer interaction **83**
6.1 Physical parameters, computational domain and mesh 84
6.2 Mean flow organization 85
6.3 Dynamics of the flow 89
6.4 POD analysis 98
6.5 Conclusions 109
6.6 References 111

Conclusions and perspectives **113**

List of figures

1 Some typical examples of SWBLI on a hypersonic aircraft from Humble [2009]. . . . 2
2 Schlieren visualisation of a transonic airfoil from Kouchi et al. [2016]. 2
3 Supersonic air intakes from Grossman and Bruce [2018]. (a,b) Examples of the rectangular supersonic compression intakes of (a) the McDonnell Douglas F-15 Eagle and (b) the Aérospatiale–BAC Concorde. (c) Simplified schematic diagram. 3
4 Turbine cascade flow from DLR [2019] 3
5 Overexpanded nozzle from Martelli et al. [2018]. 3

1.1 Schlieren visualization of an impinging oblique-shock reflection on a flat plate from Babinsky and Harvey [2011]. 10
1.2 Schlieren visualization of a ramp induced shock wave from Babinsky and Harvey [2011]. 11
1.3 Schlieren visualization of an oblique shock wave induced by a forward-facing step from Narayan and Govardhan [2013]. 11
1.4 Schlieren visualization of a normal shock wave from Babinsky and Harvey [2011]. . 11
1.5 Schlieren visualization of an adaptation shock wave at an overexpanded nozzle exit from Babinsky and Harvey [2011]. 12
1.6 Sketch of a weak Shock Wave Boundary Layer Interaction (SWBLI) from Délery and Dussauge [2009]. 13
1.7 Pressure distribution at the wall for an inviscid shock wave regular reflection and for a viscous weak SWBLI from Délery and Dussauge [2009]. 13
1.8 Sketch of a strong SWBLI from Délery and Dussauge [2009]. 14
1.9 Pressure distribution along the wall for a strong shock wave boundary layer interaction from Délery and Dussauge [2009] 15
1.10 Dimensionless frequency (S_L) based on the mean separation length (L) of the shock wave oscillation in various configurations versus the Mach number: (■) subsonic separation from Kiya and Sasaki [1983]; (⧫) compression ramp cases; (*) IUSTI reflection cases; (+) overexpanded nozzle (restricted shock wave separation); (★) blunt fin; (•) Touber and Sandham [2008]; (∘) estimated superstructures upstream influence for the 8° IUSTI case. Figure adapted from Dussauge et al. [2006] 17

2.1 L_2 norm versus the grid spacing of the error on the the longitudinal velocity component of the Taylor Green vortex between the reference and the computed solution using either the 2^{nd}-order or the 4^{th}-order approximations of the viscous fluxes. . . 34
2.2 Computational domain of calculus and boundary conditions for the simulation of SWBLIs. 35

3.1 Initial field of the vorticity component in direction z. 40
3.2 History of the kinetic energy (on the left) and the kinetic energy dissipation (on the right) obtained using the One Step (OS)-7 scheme on several mesh sizes (32^3, 64^3, 128^3, 256^3): present solutions are compared to the reference solution Wang et al. [2013]. 42

3.3 On the left, L_2 error norms on the kinetic energy dissipation with respect to the reference Wang et al. [2013] versus the grid spacing (h). On the right, comparison on the L_∞ error norms between the 5th-order and 7th-order One-Step schemes and the DG-4 scheme Committee [2016]. . . . 43
3.4 On the left, history of the enstrophy obtained by using the OS-7 scheme on several mesh sizes (32^3, 64^3, 128^3, 256^3): present solutions are compared to the reference solution Wang et al. [2013]. On the right, L_∞ error norms on the kinetic energy dissipation with respect to the reference Wang et al. [2013] versus the grid spacing (h): comparison between the 5th-order and 7th-order One-Step schemes and the DG-4 scheme Committee [2016]. . . . 44
3.5 History of the kinetic energy dissipation obtained with and without a schock-capturing procedure on a mesh with 256^3 grid points. On the left, OS-7 and One Step Monotonicity-Preserving (OSMP)-7 solutions are compared to the reference solution Wang et al. [2013]. On the right, the OSMP-7 and OSTVD-7 solutions are compared. . . . 44
3.6 L_∞ error norms with respect to the reference Wang et al. [2013] versus the grid spacing (h), on the kinetic energy dissipation (on the left) and on the enstrophy (on the right): comparison between the unlimited (OS-7) and the (OSMP-7) 7th-order One-Step schemes. . . . 45
3.7 History of the kinetic energy dissipation obtained using the OSMP-7 on the 256^3 mesh. Comparison between results obtained with a second 2^{nd}-order and a 4^{th}-order discretization for the diffusive fluxes. Present solutions are also compared to the reference solution Wang et al. [2013]. . . . 45
3.8 L_∞ error norms with respect to the reference Wang et al. [2013] versus the grid spacing (h), on the kinetic energy dissipation (on the left) and on the enstrophy (on the right): comparison between the 2^{nd}-order and the 4^{th}-order approximations of the viscous fluxes. . . . 46
3.9 Sketch of the computational domain for the shock-wave boundary layer interaction: non-dimensional dimensions and boundary conditions. The dashed line represents the inviscid incident shock-wave location Blanchard and Renac [2016]. . . . 46
3.10 Example of mesh used for the calculation of the SWBLI with a laminar boundary layer. 47
3.11 Wall pressure (on the left) and skin friction coefficient (on the right) distributions obtained by using the OSMP-7 scheme coupled with a 2^{nd}-order centered scheme for the viscous fluxes, on several mesh sizes. . . . 49
3.12 On the left, numerical schlieren visualization obtained by using the OSMP-7 scheme coupled with a 2^{nd}-order centered scheme for the viscous fluxes, on 480×240 grid points: the red line indicates the height $y = 0.1$. On the right, pressure distribution at $y = 0.1$ obtained by using the OSMP-7 scheme coupled with a 2^{nd}-order centered scheme for the viscous fluxes, on several mesh sizes. . . . 49
3.13 Pressure distribution at $y = 0.1$ (on the left) and along the wall (on the right) for the 480×240 mesh: influence of the Monotonicity Preserving (MP) constraints. . . . 50
3.14 Skin friction coefficient distribution along the wall for the 480×240 mesh: influence of the MP contraints. . . . 50
3.15 Streamwise pressure distribution obtained either from experiments or by using several schemes: wall pression on the left, and pressure at $y = 0.1$ on the right. . . . 51
3.16 Streamwise skin friction coefficient distribution obtained either from experiments or by using several numerical approaches. . . . 51
3.17 Skin friction coefficient distribution for the 480×240 mesh obtainted by using either a 2^{nd}-order or a 4^{th}-order approximation for the diffusive fluxes. . . . 52

4.1 Sketch of the flow. . . . 57
4.2 Numerical schlieren visualization obtained by plotting the isocontours of the magnitude of the density gradient $|\nabla\rho|$ (2D slice located at the middle of the domain). . . . 57

4.3 Time mean velocity averaged in the spanwise direction in the interaction zone. The black line shows the isocontour $u = 0$. The velocities are scaled using U_∞ and the spatial coordinates are scaled using δ. The spatial coordinates are scaled using δ. Up: longitudinal velocity. Middle: vertical velocity. Bottom: transversal velocity. . . . 58
4.4 Up: time mean longitudinal velocity averaged in the spanwise direction in the separated zone. The black line shows the isocontour $u = 0$. The velocitiy is scaled using U_∞ and the spatial coordinates are scaled using δ. Bottom: Distribution along the flat plate of the time mean C_f averaged in the spanwise direction. 59
4.5 Discriminent criterion ($\frac{\Delta}{(U_\infty/\theta)^6} = 10^{-12}$) colored by the magnitude of the longitudinal component of the velocity scaled by U_∞. Shock waves are highlighted by isosurfaces of $|\nabla P|$. 60
4.6 Discriminent criterion ($\frac{\Delta}{(U_\infty/\theta)^6} = 10^{-12}$) colored by the magnitude of the longitudinal component of the velocity scaled by U_∞. 61
4.7 Time mean longitudinal velocity field averaged in the spanwise direction. The black line shows the isocontour $u = 0$. The velocitiy is scaled using U_∞ and the spatial coordinates are scaled using δ. Position of the probes. Probe 1: $x/\delta = 18.75$, $y/\delta = 0.31$, Probe 2: $x/\delta = 50$, $y/\delta = 3.84$, Probe 3: $x/\delta = 81.25$, $y/\delta = 0.93$, Probe 4: $x/\delta = 81.25$, $y/\delta = 0.31$, Probe 5: $x/\delta = 92.5$, $y/\delta = 0.31$. 61
4.8 Premultiplied power spectral density of the longitudinal velocity component. Left: probe 1. Right: probe 4. 62
4.9 Premultiplied power spectral density of the longitudinal velocity component. Left: probe 2. Right: probe 3. 62
4.10 Premultiplied power spectral density of the longitudinal velocity component at probe 5. 63
4.11 Skin friction coefficient (C_f) averaged in the spanwise direction at different times. . 63
4.12 History of the mean location in the spanwise direction of the abscissa along the flat plate of the separation point, on the left, and the reattachment point, on the right. . 64
4.13 History of the mean location in the spanwise direction of the abscissa along the flat plate of the reflected shock foot. 64
4.14 Premultiplied power spectral density of the reattachment point abscissa along the flat plate 65
4.15 Distribution of the skin friction coefficient averaged in the spanwise direction at constant time interval. 65

5.1 Sketch of the sectioning of the inlet plane into several modes from Pamiès et al. [2009]. 73
5.2 Q criterion ($\frac{\delta^2}{U_\infty^2}Q = 1$) colored by the longitudinal velocity between $x = 0$ and $x = 40\delta$. 77
5.3 Longitudinal velocity isocontours in a (x, z) plane at $y^+ \simeq 15$ above the wall. 77
5.4 Time mean skin friction coefficient (C_f) averaged in the spanwise direction along the flat plate (x/δ). 78
5.5 Left: Velocity profiles in the Van Driest transformed coordinates for $x = 20.\delta$. Right: Density-scaled Reynolds stresses for $x = 20.\delta$. 79
5.6 Left: Spanwise autocorrelations of the fluctuations at $x = 10\delta$ and $y_+ = 113$ ($y/\delta \simeq 0.28$). Right: Power spectra in the spanwise direction at $x = 10\delta$ and $y_+ = 113$ ($y/\delta \simeq 0.28$). 80
5.7 Comparison between the SEM and the results from Mullenix et al. [2013] for $Re_\theta \simeq 3500$ and $x/\delta = 62.5$. Left: Velocity profiles in the Van Driest transformed coordinates. Right: Density-scaled Reynolds stresses. 80
5.8 Comparison between the SEM and the results from Mullenix et al. [2013] for $Re_\theta \simeq 3500$. Temperature profile. 81

6.1 Sketch of the flow. 85
6.2 Numerical schlieren visualization (2D slice located at the middle of the domain). . . 85

6.3 Time mean velocity averaged in the spanwise direction in the interaction zone. Up left: longitudinal velocity (current DNS), Up right: vertical velocity (current DNS), Bottom left: longitudinal velocity (from Adler and Gaitonde [2018]), Bottom right: vertical velocity (from Adler and Gaitonde [2018]). For the results from Adler and Gaitonde [2018], the color contours correspond to a coarser mesh ($\Delta x^+ = 23.5$, $\Delta y_w^+ = 0.4$, $\Delta z^+ = 8.9$), whereas the dashed contour lines correspond to a finer mesh solution ($\Delta x^+ = 16.4$, $\Delta y_w^+ = 0.4$, $\Delta z^+ = 6.1$). 86

6.4 Mean value of u_{rms}^2/U_∞^2 averaged in the spanwise direction in the interaction zone. Up: current DNS. Bottom: Direct Numerical Simulation (DNS) from Aubard [2012] with $x^{**} = \frac{x-\overline{X}_s}{\overline{X}_r-\overline{X}_s}$ and $y^{**} = \frac{y}{\overline{X}_r-\overline{X}_s}$ ($\overline{X}_s$ is the mean separation point and $\overline{X}_r$ is the mean reattachment point). 87

6.5 Mean value of v_{rms}^2/U_∞^2 averaged in the spanwise direction in the interaction zone. Up: current DNS. Bottom: DNS from Aubard [2012] with $x^{**} = \frac{x-\overline{X}_s}{\overline{X}_r-\overline{X}_s}$ and $y^{**} = \frac{y}{\overline{X}_r-\overline{X}_s}$ ($\overline{X}_s$ is the mean separation point and $\overline{X}_r$ is the mean reattachment point). 87

6.6 Mean value of w_{rms}^2/U_∞^2 averaged in the spanwise direction in the interaction zone. Up: current DNS. Bottom: DNS from Aubard [2012] with $x^{**} = \frac{x-\overline{X}_s}{\overline{X}_r-\overline{X}_s}$ and $y^{**} = \frac{y}{\overline{X}_r-\overline{X}_s}$ ($\overline{X}_s$ is the mean separation point and $\overline{X}_r$ is the mean reattachment point). 87

6.7 Mean value of uv_{rms}/U_∞^2 averaged in the spanwise direction in the interaction zone. Up: current DNS. Bottom: DNS from Aubard [2012] with $x^{**} = \frac{x-\overline{X}_s}{\overline{X}_r-\overline{X}_s}$ and $y^{**} = \frac{y}{\overline{X}_r-\overline{X}_s}$ ($\overline{X}_s$ is the mean separation point and $\overline{X}_r$ is the mean reattachment point). 88

6.8 Time mean C_f averaged in the spanwise direction with respect to x/δ. $\overline{L}$ denotes the mean separation length, $\overline{X}_s$ denotes the mean separation point and $\overline{X}_r$ denotes the mean reattachment point. 88

6.9 Time mean pressure averaged in the spanwise direction with respect to $(x-\overline{x}_r)/(\overline{x}_r-\overline{x}_s)$. 89

6.10 Time mean C_f averaged in the spanwise direction with respect to $(x-\overline{x}_r)/(\overline{x}_r-\overline{x}_s)$. 89

6.11 2D slices visualization of $|\nabla P|$ at time intervals of $1.92.L/U_\infty$ (from left to right and top to bottom). The position of the time mean separation and reattachment points positions averaged in the spanwise direction are respectively denoted by $\overline{X}_s$ and $\overline{X}_r$. 91

6.12 Time mean longitudinal velocity field averaged in the spanwise direction. Locations of the probes. Probe 1: $x/\delta = 34.3$, $y^+ = 0$, Probe 2: $x/\delta = 36.2$, $y^+ = 150$ ($y/\delta \simeq 0.37$), Probe 3: $x/\delta = 37.5$, $y^+ = 150$ ($y/\delta \simeq 0.37$), Probe 4: $x/\delta = 41$, $y^+ = 150$ ($y/\delta \simeq 0.37$), Probe 5: $x/\delta = 46$, $y^+ = 150$ ($y/\delta \simeq 0.37$), Probe 6: $x/\delta = 56.6$, $y^+ = 150$ ($y/\delta \simeq 0.37$). . 91

6.13 Power spectral density of the longitudinal velocity signal for several probes located in the shear layer and the downstream boundary layer (see figure 6.12) with respect to the Strouhal number based on the separation length: Up left: probe 2. Up right: probe 3. Middle left: probe 4. Middle right: probe 5. Bottom: probe 6. 92

6.14 Time history of the spanwise averaged locations of the separation point $x_s(t)$ and the reattachment point $x_r(t)$ 93

6.15 Power spectral density of the time history of the spanwise averaged location of the separation point $x_s(t)$ (red) and the time history of the spanwise averaged location of the reattachment point $x_r(t)$ (blue). 93

6.16 Cross power spectral density between the histories of the spanwise averaged location of separation point $x_s(t)$ and reattachment point $x_r(t)$. 94

6.17 Distribution of the covariance coefficient between the spanwise averaged separation and reattachment point positions as a function of the non dimensionalized time lag $\tau U_\infty/L$ 94

6.18 Probability density function of $Cf = 0$ averaged in the spanwise direction 95

6.19 History of the skin friction averaged in the spanwise direction at 4 abscissa in the interaction region. The 4 abscissa are highlighted by vertical lines in figure 6.18. Up left: $x/\delta = 34.25$ (mean separation point). Up right: $x/\delta = 40.9$ (mean reattachment point). Bottom left: $x/\delta = 34.0$. Bottom right: $x/\delta = 42.75$. 96
6.20 Time history of the length of the separation bubble $L(t) = x_r(t) - x_s(t)$ 97
6.21 Power spectral density of the time history of the length of the separation bubble $L(t) = x_r(t) - x_s(t)$. 97
6.22 Power spectral density of the wall pressure signal at the reflected shock foot (probe 1) with respect to the Strouhal number based on the separation length. 97
6.23 Time history of the spanwise averaged location of the separation point $x_s(t)$ and the reflected shock foot $X_{shock}(t)$. 98
6.24 Covariance between $x_s(t)$ and $X_{shock}(t)$. 98
6.25 Proper Orthogonal Decomposition (POD) spectrum on the velocity field. The first mode is not shown because it is too large, representing the time-average of the field. 99
6.26 Power spectral density of the temporal amplitudes α^m for the POD on the velocity field; only values bigger than 0.01 are plotted. 100
6.27 Left: average of the power spectral density of α^m over two distinct sets of modes for the POD on the velocity field. Right: spectral density of POD energy for two distinct sets of modes for the POD on the velocity field. 101
6.28 POD spectrum on the pressure field. The first mode is not shown because it is too large ($\lambda^1 = 236432$). 101
6.29 Power spectral density of the temporal amplitudes α^m for the POD on the pressure field; only values bigger than 0.01 are plotted. 102
6.30 Left: average of the power spectral density of α^m over two distinct sets of modes for the POD on the pressure field . Right: spectral density of POD energy for two distinct sets of modes for the POD on the pressure field. 102
6.31 Reconstructed fields using the first 30 POD modes. Top: longitudinal reconstructed velocity. Middle: magnitude of the spanwise vorticity reconstructed with the velocity field. Bottom: reconstructed pressure. 103
6.32 Power spectral density of the longitudinal velocity signal for several probes (see figure 6.12) with respect to the Strouhal number based on the separation length: Up left: probe 2. Up right: probe 3. Bottom: probe 4. 104
6.33 Left: pressure signal at the reflected shock foot (same coordinates than probe 1, see figure 6.12). Right: power spectral density of the wall pressure signal at the reflected shock foot with respect to the Strouhal number based on the separation length. . . . 105
6.34 Left: sequence of visualizations of the reconstructed longitudinal velocity averaged in the spanwise direction at time intervals of $1.92L/U_\infty$. Right: sequence of visualizations of the reconstructed pressure field averaged in the spanwise direction at the same times. 106
6.35 Power spectral density of the longitudinal velocity signal for a probe located at ($x/\delta = 41$, $y/\delta = 0.1$ corresponding to $y^+ \simeq 30$) in the zone of large shedding of fluid from the recirculation bubble (see figure 6.34). 107
6.36 Visualization of the reconstructed longitudinal velocity field at different times. . . . 108
6.37 Left: Isocontours of the longitudinal component of the 7^{th} spatial modes of the POD of the velocity field. Right: Isocontours of the longitudinal component of the 8^{th} spatial modes of the POD of the velocity field. 109
6.38 Left: power spectral density of α^7. Right: power spectral density of α^8. 109

List of tables

5.1 Analytical expression of the shape functions. ϵ_1, ϵ_2 and ϵ_3 are random signs (i.e. ± 1). 75
5.2 Low and up limits, length scales and convection velocity of turbulent structures associated with each mode, expressed in wall units. 75
5.3 Flow conditions. 76

6.1 Flow conditions. 84

Introduction

The development of supersonic and hypersonic vehicles represents an active research and development field as well as a major issue for aeronautical and spatial industries. Moreover, it encompases a large variety of applications. The following non exhaustive list highlights the current and future importance of these applications:

— Civil aviation:
Two supersonic aircrafts designed to transport passengers have been developed and exploited in the history. The Tupolev Tu-144 flew between 1968 and 1997. The Concorde flew between 1969 and 2003. Since the retirement of Concorde, the desire for a second-generation supersonic aircraft has remained within some elements of the aviation industry. Several projects are currently under study to develop such vehicles (Malik [2018]). For instance, Boeing unveiled a new hypersonic passenger plane concept at the AIAA Aviation Forum 2018 (Atlanta on June 26) that could travel at Mach 5. First commercial flights are scheduled for the late 2030s. An other example of the current interest for such vehicles is the current project of the NASA that is developing a demonstrator of supersonic passenger plane (X-59 QueSST) that would enable affordable supersonic transportation without the loud sonic booms that come with it. First flight tests are scheduled for 2022.

— Military aviation:
The development of supersonic weapons (fighter aircrafts, balistic missile, ...) remains a major issue for the military industry.

— Space exploration:
The design of launch vehicles has been and remains a major issue for the spatial industry. For instance, the European Space Agency is currently developing the rocket Ariane 6. Moreover, the design of vehicles allowing autonomous controlled reentry for return missions from low Earth orbit is an objective of the European Space Agency. In particular the agency is currently carrying out the Intermediate eXperimental Vehicule (IXV) research project on this specific issue (Dussy et al. [2011]).

SWBLI occur when a shock wave impiges upon a boundary layer developing on a solid body. Supersonic and hypersonic vehicles are emblematic examples in which SWBLIs occur. Figure 1 shematically illustrates some typical examples of SWBLI which may occur on a supersonic/hypersonic aircraft. The aircraft flying at supersonic speed, changes in the slope of the surface of the vehicle are likely to create shock waves that interact with the boundary layer developing on the surface of the aircraft (Compression surface, leading edge interaction, corner flow).

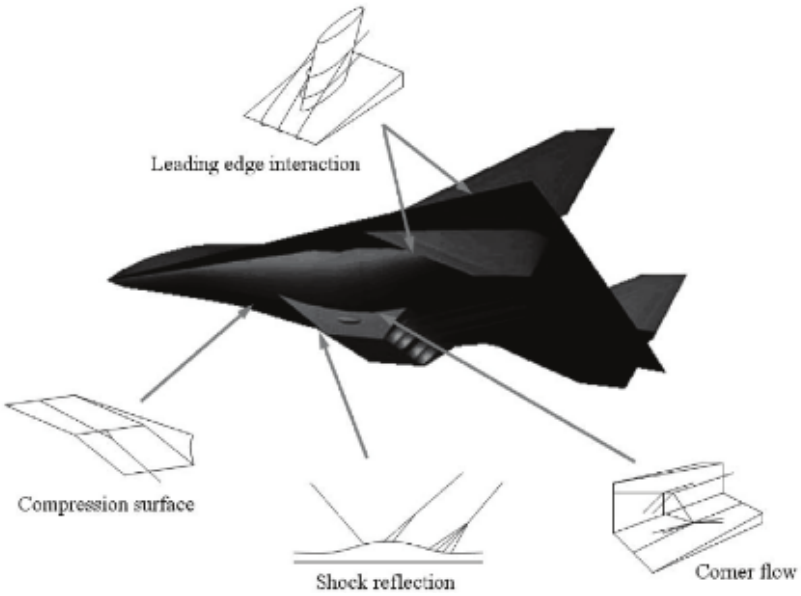

FIGURE 1 – Some typical examples of SWBLI on a hypersonic aircraft from Humble [2009].

An other example of SWBLI developing around vehicles flying at high speed is given by the transonic airfoil. Normal shock waves are known to be created above the upper surface of such airfoils, interacting with the boundary layer developing on the airfoil wall. A schlieren visualization of such interaction is shown in figure 2.

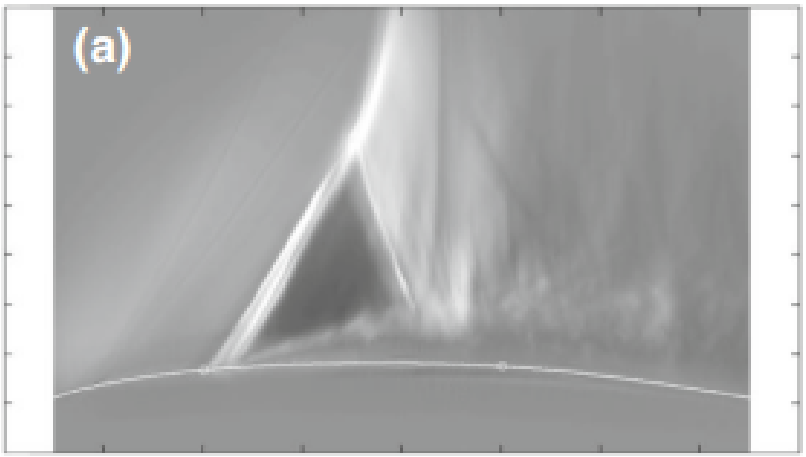

FIGURE 2 – Schlieren visualisation of a transonic airfoil from Kouchi et al. [2016].

The propulsion system of supersonic aircrafts can also be the sit of SWBLIs. Figure 3 shows examples of supersonic air intakes that equip the propulsion system of supersonic aircrafts. The supersonic incoming flow is rendered subsonic by crossing shock waves created by geometrical discontinuities of the walls. The shock waves created impinge the opposite walls, thus interacting with boundary layers.

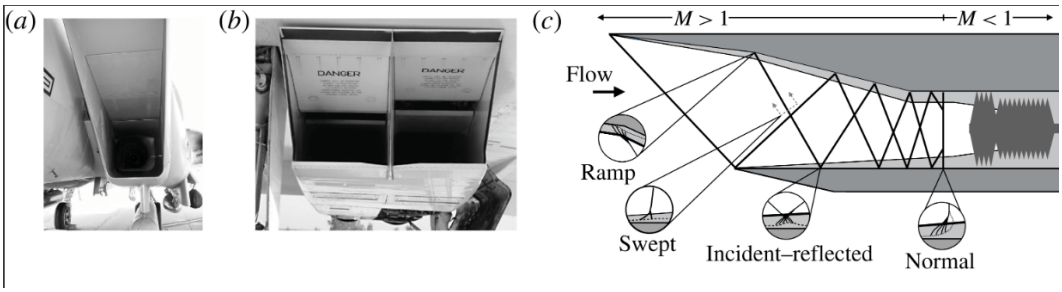

FIGURE 3 – Supersonic air intakes from Grossman and Bruce [2018]. (a,b) Examples of the rectangular supersonic compression intakes of (a) the McDonnell Douglas F-15 Eagle and (b) the Aérospatiale–BAC Concorde. (c) Simplified schematic diagram.

SWBLIs are also likely to occur inside turbojets. For instance, (figure 4) shows a turbine cascade flow where normal shock waves, created between turbine blades, interact with the boundary layers developing on the blades surfaces.

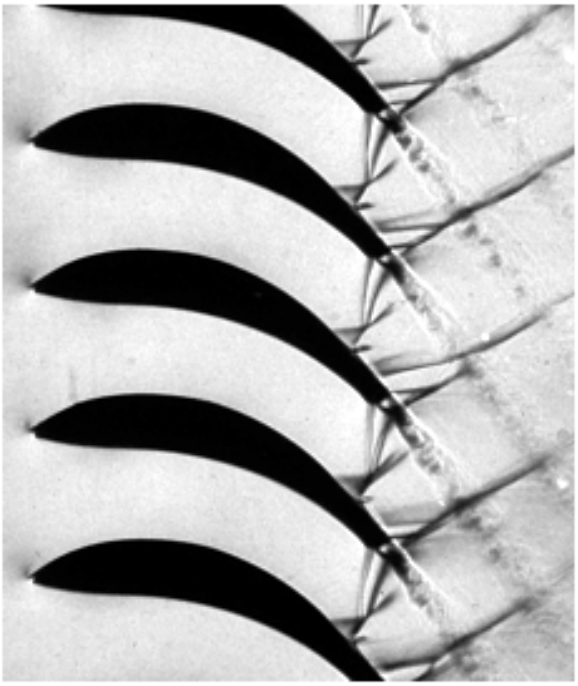

FIGURE 4 – Turbine cascade flow from DLR [2019]

The last example presented here is the case of the overexpanded nozzle shown in figure 5. These nozzles being designed to be adapted at high altitude, they are over expanded at launch and low altitudes. A shock wave is then created that enables the flow in the nozzle to adapt to the higher external pressure. This shock wave interacts with the boundary ayer developing on the nozzle surface.

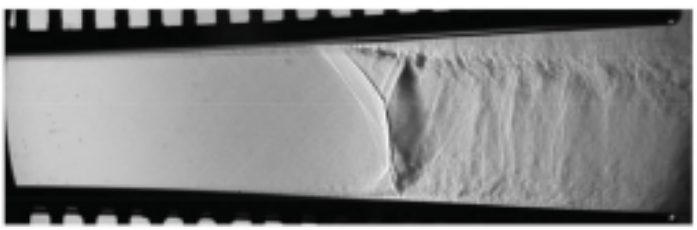

FIGURE 5 – Overexpanded nozzle from Martelli et al. [2018].

The SWBLI is therefore a reccurent physical phenomenon present in aeronautical and space systems. This phenomenon concerns both external and internal aerodynamics aplications.
In a SWBLI, if the shock wave is strong enough, the subsequently adverse pressure gradient can lead to a separation of the boundary layer. A separation bubble is then created surrounded by a complex system of shock waves. The highly three-dimensional separation bubble leads to a steep increase of the drag force, the heat fluxes and the pressure fluctuations at the wall. Previous studies have additionally shown that the recirculation bubble as well as the reflected shock wave are subjected to a low frequency streamwise motion called «the unsteadiness» of the SWBLI.
These properties, and particularly the SWBLI unsteadiness, imply major negative effects of the SWBLI on the systems in which they occur. Indeed, the SWBLI unsteadiness subjects structures to oscillating loads that can be dangerous for the structure integrity.
In the case of transonic airfoil, this pheomenon is called transonic buffet and can lead to structure fatigue and flight accidents, thus significantly constraining the flight envelope of the aircrafts (Yun et al. [2017]).
When occuring in turbine or compressors, the SWBLI unsteadiness also impose fluctuating loads that could damage the blades integrity (Szwaba et al. [2017]).
The SWBLI unsteadiness has also major consequencies on the behavior of supersonic mixed-compression air intakes. For these intakes, such as the one that equiped the Condorde, supersonic compression takes place inside the intake duct, the flow crossing shock waves that interact with boundary layers developing oblique the surface of the duct (figure 3-(c)). The SWBLI unsteadiness can cause large structural loads. It can also be the cause of the inlet unstart. As stated in Tabanli and Yuceil [2017]: "during unstart, the original inlet shock system can eventually take the form of a detached bow shock that resides upstream of the inlet entrance. The unstart process can be severe with high transient pressure loads and it can lead to a loss of engine thrust". Due to these flow features, the design of the Concordes air intakes has been identified as one of the most difficult part of the aircraft development and needed the use of active flow control devices. It is also identified as one of the most difficult part of the development of the new generation of supersonic transport aircrafts (Chassaing et al. [2002]).
The SWBLI unsteadiness due to the presence of the adaptation shock wave in over expanded nozzles at low altitudes, leads to an unsteady asymmetry of the separation line in the divergent part of the nozzle that creates strong unsteady side loads. These side loads require a robust conception of the structure that yields to an increase of the launcher weight (Alziary de Roquefort [2002]).

These examples justify the importance of a careful study of SWBLIs and particularly its low frequency unsteadiness. Even if this phenomenon is well known, the mechanism leading to the SWBLI unsteadiness is still not well understood. As it will be introduced in chapter 1, mainly two kind of mechanisms have been refered to in order to explain the existence of the SWBLI unsteadiness (Délery and Dussauge [2009]). The first one constists in an excitation of the SWBLI by the large scales of the incoming turbulent boundary layer. The second one consists in the imposition of the dynamics of the recirculation zone to the whole SWBLI system. Despite arguments in favour of each mechanism, no definitive explanation have been yet provided.

Reynolds-averaged Navier–Stokes equations (RANS) approaches have shown their inability to predict both mean and unsteady properties of the SWBLI (Dolling [2001]). Time resolved simulations appears necessary to efficiently simulate SWBLIs. Time resolved numerical simulation of high Reynolds number compressible flows involving shock waves is a challenging task. It requires the use of a high-order numerical scheme able to precisely compute turbulent scales and robustly capture shock waves without spoiling the accuracy in the vicinity of the discontinuity.

The aim of the present work is to perform well resolved DNS of SWBLIs and analyse results in order to contribute to a better understanding of the SWBLI unsteadiness and the physical mechanism causing these low frequency oscillations. To this end, the canonical configuration of an

oblique shock wave impinging a boundary layer developing on a flat plate is considered.

The work presented in this document is divided in three parts.
A first part concerns the presentation and the validation of the numerical approach used to perform the simulations. This numerical strategy relies on an original numerical scheme (OSMP) (Daru and Tenaud [2004]) implemented in the in house parallel (Message Passing Interface (MPI)) Finite Volume (FV) based DNS solver (code CHORUS) that has been developed at LIMSI-CNRS. The validation relies on evaluating separately the ability of the numerical schemes to compute turbulent flows with accuracy and to capture shock waves with robustness. To this end, two canonical test-cases that have been considered in the International Workshop on High-Order CDF Method (HiOCFD workshop) to compare the Computational Fluid Dynamics (CFD) software performances (**?**) are simulated: namely, the three dimensional Taylor-Green vortex and the steady two dimensional shock wave laminar boundary layer interaction. Moreover, the influence of the order of the diffusive flux discretization on the results is studied.
A second part of the work is devoted to the DNS and analyses of a 3D unsteady Shock Wave Laminar Boundary Layer Interaction (SWLBLI). Indeed, in order to better understand the mechanisms leading to the SWBLI unsteadiness, we first chose to perform a SWBLI simulation suppressing one of the two suspected mechanisms leading to the unsteadiness. By simulating the interaction between a laminar boundary layer and a incident shock wave, we suppress the suspected influence of the large turbulent structures of the boundary layer on the SWBLI unsteadiness. The only remaining suspected cause of unsteadiness would be the dynamics of the separation bubble.
A third part is devoted to the simulation and analysis of the interaction between a turbulent boundary layer and a incident shock wave. In this context, the accurate simulation of a turbulent compressible incoming boudary layer is of great importance. A Synthetic Eddy Method (SEM) (Jarrin et al. [2006]) that we adapted to compressible flows, has been developed to achieve this objective without prohibitive additional computational costs. This implemented SEM is used at the inlet of the simulation domain for the simulation of the interaction between a turbulent boundary layer and a incident shock wave.

Organization of the document

Chapter 1 is devoted to the physical introduction of the SWBLI with a particular emphasis on the description of the dynamics of the flow. A review of the previous works available in the litterature with regard to the study of the SWBLI unsteadiness is also presented.

The mathematical modelling of the problem, namely the system of equations to be solved and the boundary conditions, is introduced in chapter 2 together with the numerical approach used to solve it.

Chapter 3 concerns the validation of the numerical strategy on a 3D Taylor Green vortex and a steady 2D SWLBLI.

A DNS of a 3D unsteady SWLBLI is presented in chapter 4. A special attention is paid to the analysis of the low frequency dynamics of the flow. In particular, the dynamics of the recirculation bubble and the foot of the reclected shock wave are analysed to verify wether the SWBLI unsteadiness is obtained.

The implement SEM is presented in chapter 5. Numerical results obtained using this turbulent inflow condition for the simulation of a turbulent compressible boundary layer on a flat plate are presented and compared to reference results.

The implemented SEM is used for performing a DNS of a Shock Wave Turbulent Boundary Layer Interaction (SWTBLI) presented in chapter 6. Different techniques are used in order to ana-

lyse the dynamics of the flow. Statistical and spectral analysis of the DNS results are performed together with a POD analysis of the interaction zone in order to characterize the SWTBLI unsteadiness.

The document ends with concluding remarks and perspectives.

0.1 References

Tariq Malik. Boeing's hypersonic vision: A sleek passenger plane that can hit mach 5. 2018. doi: https://www.space.com/41042-boeing-hypersonic-passenger-plane-concept.html. 1

Stephane Dussy, Jean-Philippe Preaud, Giovanni Malucchi, V Marco, Elio Zaccagnino, and A Drocco. Intermediate experimental vehicle (ixv), the esa re-entry demonstrator. In *AIAA Guidance, Navigation, and Control Conference*, page 6340, 2011. 1

Raymond Humble. *Unsteady flow organization of a Shock wave-boundary-layer interaction*. Eburon Academic Publisher, 2009. 3, 2

Toshinori Kouchi, Shingo Yamaguchi, Shunske Koike, Tsutomu Nakajima, Mamoru Sato, Hiroshi Kanda, and Shinichiro Yanase. Wavelet analysis of transonic buffet on a two-dimensional airfoil with vortex generators. *Experiments in Fluids*, 57(11):166, 2016. 3, 2

Ilan J Grossman and Paul JK Bruce. Confinement effects on regular–irregular transition in shock-wave–boundary-layer interactions. *Journal of Fluid Mechanics*, 853:171–204, 2018. 3

DLR. Dlr web page. 2019. doi: https://www.dlr.de/at/en/desktopdefault.aspx/tabid-1565/2433_read-3790/. 3

E Martelli, PP Ciottoli, L Saccoccio, F Nasuti, M Valorani, and M Bernardini. Characterization of unsteadiness in an overexpanded planar nozzle. *AIAA Journal*, 57(1):239–251, 2018. 3

TIAN Yun, GAO Shiqi, LIU Peiqing, and WANG Jinjun. Transonic buffet control research with two types of shock control bump based on rae2822 airfoil. *Chinese Journal of Aeronautics*, 30(5): 1681–1696, 2017. 4

Ryszard Szwaba, Piotr Doerffer, and Piotr Kaczynski. Transition effect on shock wave boundary layer interaction on compressor blade. In *International Conference on RailNewcastle Talks*, pages 31–44. Springer, 2017. 4

Hasan Tabanli and K Bulent Yuceil. Introduction to shock wave-boundary layer interaction and unstart in supersonic inlets. In *Advanced Study Institute on NATO ASI on Quantum Nano-Photonics*, pages 385–386. Springer, 2017. 4

J.C. Chassaing, F. Filaire, G. Gérolymos, E. Sauret, I. Vallet, C. Tenaud, Y. Fraigneau, Ph. Duveau, P. d'Espiney, B. Michel, C. Corre, and A. Lerat. Outils numériques avancés pour la conception aérodynamique des prises d'air avec systmes de contrôle, 2002. 4

T Alziary de Roquefort. Unsteadiness and side loads in over-expanded supersonic nozzles. In *Fourth Symposium on Aerothermodynamics for Space Vehicles*, volume 487, page 93, 2002. 4

Jean Délery and Jean-Paul Dussauge. Some physical aspects of shock wave/boundary layer interactions. *Shock waves*, 19(6):453, 2009. 4

David S Dolling. Fifty years of shock-wave/boundary-layer interaction research: what next? *AIAA journal*, 39(8):1517–1531, 2001. 4

V. Daru and C. Tenaud. High order one-step monotonicity-preserving schemes for unsteady compressible flow calculations. *Journal of Computational Physics*, **193**(2):563 – 594, 2004. ISSN 0021-9991. doi: https://doi.org/10.1016/j.jcp.2003.08.023. 5

N. Jarrin, S. Benhamadouche, D. Laurence, and R. Prosser. A synthetic-eddy-method for generating inflow conditions for large-eddy simulation. *International Journal of Heat and Fluid Flow*, 27:585–593, 08 2006. doi: 10.1016/j.ijheatfluidflow.2006.02.006. 5

Chapter 1

Shock wave boundary layer interactions: Physical aspects and state of the art

Contents

1.1 Different shock wave boundary layer interactions in 2D flows 10
1.2 Mean flow 12
1.2.1 Weak interactions 12
1.2.2 Strong interactions 13
1.3 Strong shock wave boundary layer unsteadiness 15
1.3.1 Dynamics of the shock wave boundary layer interaction 15
1.3.2 Recent works and mechanisms proposed in the literature 17
1.4 Conclusions and outlook of the work 19
1.5 References 19

We present an overview of the knowledge available in the literature about the SWBLI. For the sake of brevity, we reduce our presentation to 2D flows. Details about 3D SWBLI can be found in the fifth chapter of the book Babinsky and Harvey [2011]. In a first section, we introduce the different basic 2D flows involving SWBLIs. We then describe, in a second section, the mean flow organization for the particular cases of an impinging oblique shock wave reflection and a ramp flow. In the next section, we describe the dynamic features of such interactions. A last section is devoted to the SWBLI unsteadiness.

1.1 Different shock wave boundary layer interactions in 2D flows

In supersonic flows, the solutions of the Navier-Stokes equations can be discontinuous. These discontinuities can be contact discontinuities or shock waves. Moreover, at solid body walls, viscous flows satisfy the non slip condition. The effects of the viscosity are significant in a thin boundary layer in the vicinity of the solid wall, where the velocity of the fluid varies from the null velocity at the wall to the free stream velocity. SWBLI occurs when a shock wave interacts with a boundary layer. During the past decades, the fundamental physics of SWBLI have been extensively studied in 2D canonical situations. Five canonical flows are described in Babinsky and Harvey [2011]: Each canonical interaction corresponds to a supersonic viscous flow in which a shock wave provoked by a geometrical modification interacts with a boundary layer:

1. impinging oblique-shock wave reflection (figure 1.1):

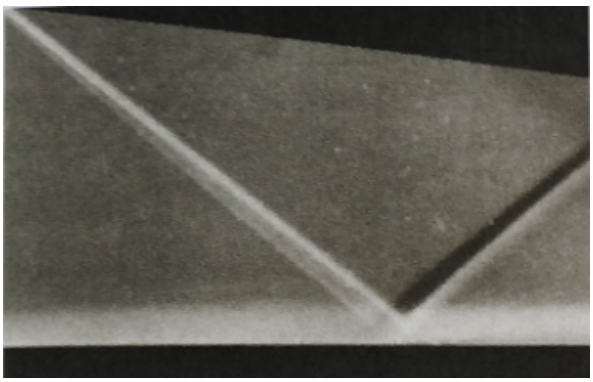

FIGURE 1.1 – Schlieren visualization of an impinging oblique-shock reflection on a flat plate from Babinsky and Harvey [2011].

   This interaction occurs when a supersonic boundary layer developing on a solid wall is impinged by an oblique shock wave that is reflected at the wall.

2. ramp flow (figure 1.2):

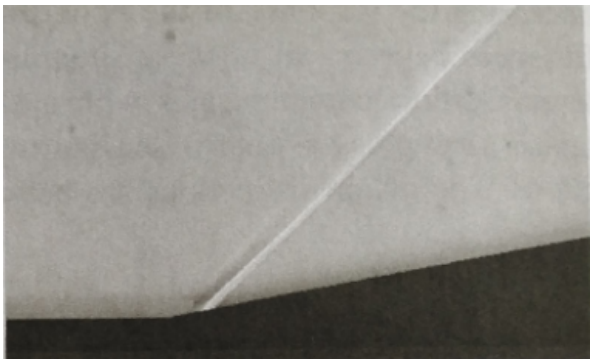

FIGURE 1.2 – Schlieren visualization of a ramp induced shock wave from Babinsky and Harvey [2011].

When a supersonic boundary layer develops on a solid wall that presents a sudden deviation with a positive slope, a shock wave is created at the wall due to the deflection of the flow.

3. oblique shock wave induced by a forward-facing step (figure 1.3)

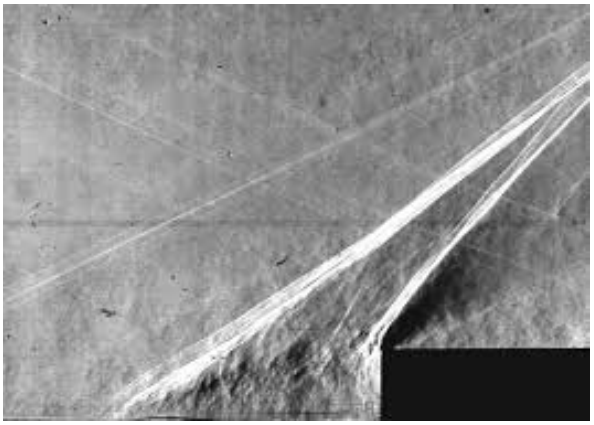

FIGURE 1.3 – Schlieren visualization of an oblique shock wave induced by a forward-facing step from Narayan and Govardhan [2013].

When a boundary layer developing on a solid wall encounters an obstacle (for example, a forward-facing step), the boundary layers separates upstream of the obstacle and a recirculation zone is created. When the boundary layer is supersonic, a shock wave is created at the separation point.

4. normal shock wave (figure 1.4)

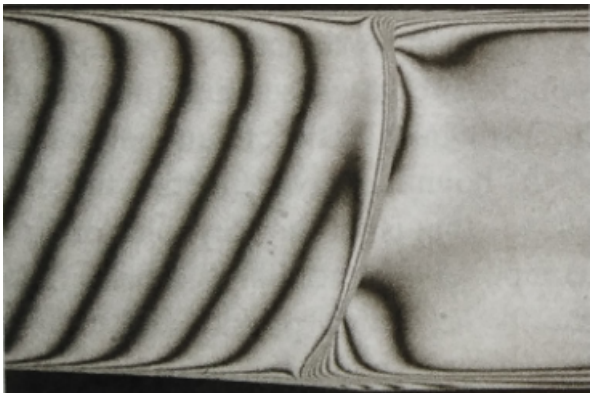

FIGURE 1.4 – Schlieren visualization of a normal shock wave from Babinsky and Harvey [2011].

A normal shock wave can be produced in a supersonic flows such as supersonic chanel flows or transonic airfoils. The supersonic flow becomes subsonic by passing through the shock wave. A SWBLI occurs at the shock foot where a boundary layer develops either on the chanel boundaries or around a transonic airfoil.

5. imposed pressure jump (figure 1.5)

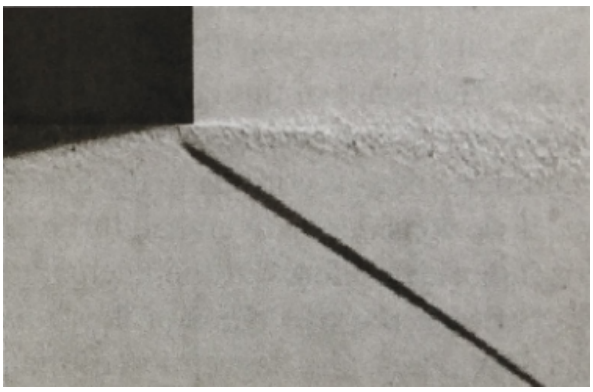

FIGURE 1.5 – Schlieren visualization of an adaptation shock wave at an overexpanded nozzle exit from Babinsky and Harvey [2011].

When an internal supersonic flow ends up at an atmosphere at higher pressure (for example at the end of an over expanded nozzle), an oblique adaptation shock wave is created whose foot is located at the extremity of the nozzle.

For each canonical flow introduce above, the boundary layer can be either laminar (SWLBLI) or turbulent (SWTBLI). SWBLIs have important repercutions on the flows that will be introduced in the following sections tackling the mean properties and the dynamics features of the SWBLI.

1.2 Mean flow

We introduce the mean flow organisation of a SWBLI. As in Délery and Dussauge [2009], for conciseness we concentrate our attention on the first canonical interaction, namely the interaction induced by the impact of an oblique shock wave on a boundary layer developing on a surface. Indeed, this flow corresponds to the direct numerical simulations of the SWBLI performed in this thesis. Moreover, as claimed in Délery and Dussauge [2009], most of the conclusions could be applied *mutatis mutandis* to other kinds of interactions.
SWBLIs can be splitted into two categories: weak SWBLIs for which the boundary layer does not separates and strong SWBLIs for which separation occurs.

1.2.1 Weak interactions

A sketch of a weak interaction between an oblique shock wave and a laminar boundary layer is shown in figure 1.6 coming from Délery and Dussauge [2009]. By weak interaction we mean that no separation of the boundary layer occurs. The free stream flow undergoes a deviation of angle $\Delta\varphi_1$ through the incident shock wave **C1**. The flow undergoes a deviation of angle $\Delta\varphi_2 = -\Delta\varphi_1$ through the reflected shock wave **C2** so that the downstream flow is parallel to the wall. In an inviscid flow where no boundary layer would exist, the regular reflection would be located at a point on the wall (inviscid shock wave reflection on a solid surface). The viscous character of the fluid implies the existence of a boundary layer in the vicinity of the wall which modifies the organization of the flow. Indeed, when the incident shock wave **C1** penetrates into the boundary layer, it progressively bends because of the local Mach number decrease. Moreover, the strength of the shock wave decreases until it vanishes when it reaches the sonic line within the boundary layer. The adverse pressure gradient felt by the boundary layer due to the incident shock wave **C1**

implies a thickening of the boundary layer and consequently a deviation of the streamlines near the wall. The subsonic layer is then also thickened and the pressure rise due to the shock wave **C1** is transmitted upstream through this subsonic region. The deviation of the flow implies the creation of compression waves (η) that coalesce and form the reflected shock wave **C2**. The consequence of the presence of the boundary layer is then to spread the interaction zone that would be reduced to a point in an inviscid shock wave reflection.

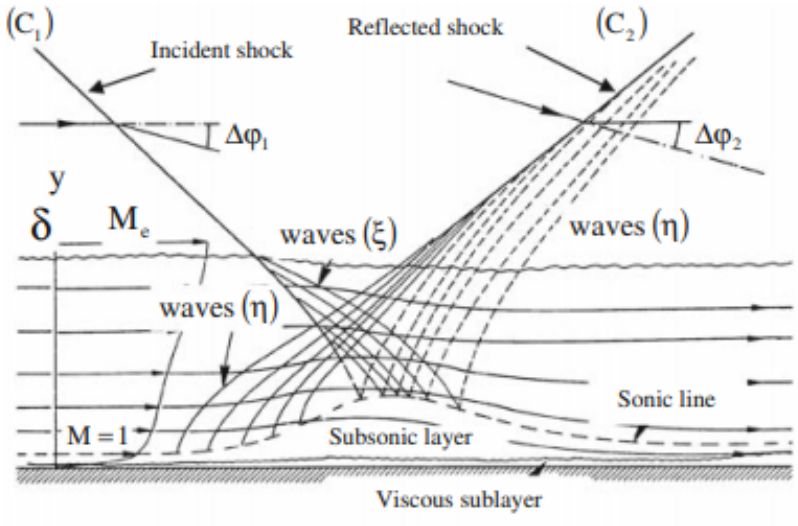

FIGURE 1.6 – Sketch of a weak SWBLI from Délery and Dussauge [2009].

The effect of the viscosity on the solution is highlighted by considering the pressure distribution at the wall for a viscous weak SWBLI compared with an inviscid shock wave regular reflection as shown in figure 1.7.

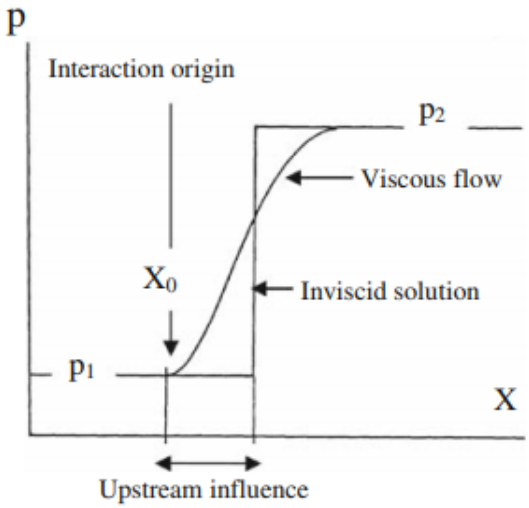

FIGURE 1.7 – Pressure distribution at the wall for an inviscid shock wave regular reflection and for a viscous weak SWBLI from Délery and Dussauge [2009].

1.2.2 Strong interactions

The weak interaction differs from the strong interaction where the boundary layer separates in the sense that accounting for the viscous effects is a mere correction to the inviscid solution that is already close to the reality. When the incident shock wave is strong enough, the adverse pressure gradient felt by the boundary layer is likely to provoke its separation so that a separation

bubble is created. Depending on the strength of the shock wave, the separation can be incipient or well developed. The incipient case corresponds to interactions where isolated and intermittent spots exist containing fluid with negative velocity but producing no average separation. The well developed separations correspond to flows where an entire specific zone experience reverse velocity during periods long enough to produce an average separated bubble. In the following, we focus on SWBLI with well developed separations. Indeed the low frequency unsteadiness of the SWBLI that is the subject of interest in this work (see section 1.3) occures only for this kind of interaction. A strong SWBLI with well developed separation is sketched in figure 1.8 (coming from Délery and Dussauge [2009]) where the separation point is noted **S** and the reattachement point is noted **R**. A shear layer develops, that bounds the upper part of the separation bubble. The flow being subsonic under the sonic line (S), the pressure rise due to the incident shock wave **(C1)** is sensed upstream of the location where the incident shock wave would impact the wall because of slow acoustic waves, explaining the location of the separation point upstream of the impact location. The presence of the recirculation bubble induces compression waves that converge to form the reflected shock wave **(C2)**. The incident shock wave **(C1)** is transmitted as **(C4)** through the separation shock wave **(C2)** and is reflected as expansion waves. At the reattachement point **R**, the deviation of the supersonic flow due to the presence of the wall leads to compression waves that also coalesce to form the so called reattachment shock wave. In such a strong SWBLI, the viscosity at play in the boundary layer leads to a complete restructuring of the flow even in the outer region where a different system of shock waves is created, with respect to the inviscid Mach shock wave reflexions on a wall.

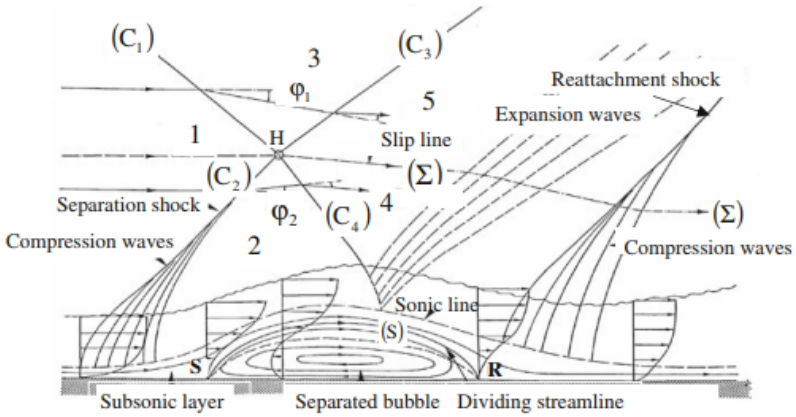

FIGURE 1.8 – Sketch of a strong SWBLI from Délery and Dussauge [2009].

Such a strong interaction is characterized by a typical wall pressure distribution as shown in figure 1.9 where the wall pressure distribution for a strong shock wave boundary layer interaction is compared with the distribution for an inviscid Mach shock wave regular reflection. The first part of the interaction consists in a steep rise of the pressure associated with the separation followed by a plateau like of pressure characteristic of separated flows. The second part of the interaction consists in a second wall pressure rise associated with the reattachment process, leading to the same pressure downstream the reattachment as in the inviscid case. The wall pressure distribution is then an important quantity to assess the accuracy of the simulations.

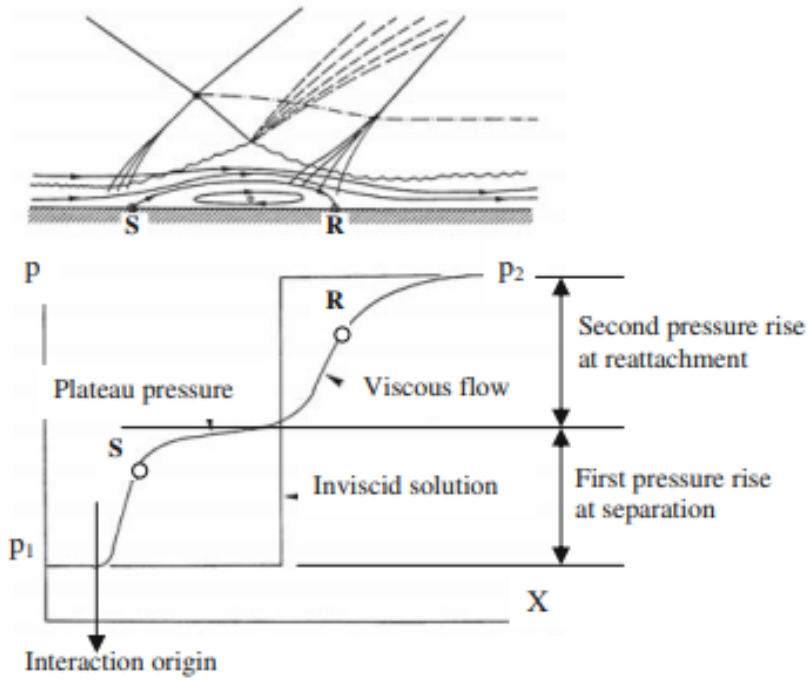

FIGURE 1.9 – Pressure distribution along the wall for a strong shock wave boundary layer interaction from Délery and Dussauge [2009]

The extent of the recirculation bubble is driven by the intensity of the incident shock wave, let say the pressure ratio from each side of the shock wave, and by the incoming boundary layer velocity profile. Indeed, the stronger the shock wave, the stronger the adverse pressure gradient leading to the separation of the boundary layer. Furthermore, the larger the normal to the wall velocity gradient within the boundary layer, the better the boundary layer is able to resist to the separation caused by the adverse pressure gradient. For instance, a laminar boundary layer is more prone to separation than a turbulent one when subjected to a steep adverse pressure gradient. The separation bubble extent then characterizes the interaction studied. It is largely bigger when the incoming boundary layer is laminar (Sansica et al. [2014]).

1.3 Strong shock wave boundary layer unsteadiness

For strong SWBLIs, it is well established that the separation bubble and the system of shock waves (included the reflected shock wave whose foot is located upstream from the separation point of the boundary layer) are subjected to low frequency longitudinal oscillations called “the unsteadiness” of the SWBLI. This oscillatory motion can spread over a large extent with respect to the boundary layer thickeness. Even if this phenomenon is well known and have been studied both experimentally and numerically for decades, the related mechanisms are still not well understood.

1.3.1 Dynamics of the shock wave boundary layer interaction

We here describe the dynamic features of strong SWBLIs that are characterized by several unsteady phenomena whose characteristic scales spread over a large broadband spectrum range.

High frequency features

For SWTBLI, the incoming boundary layer is turbulent with the most energetic fluctuations at high frequencies characterized by a Strouhal number $S_\delta = \frac{f\delta}{U_e} \sim 1$ (where f, δ and U_e are respectively the characteristic frequency of the fluctuations, the boundary layer thickeness before the

interaction and the free stream velocity).
Low amplitude oscillations of the reflected shock wave have been observed in several numerical simulations of strong SWBLIs (for example Touber and Sandham [2008]) at the same frequency scale than the most energetic fluctuations of the incoming boundary layer (i.e. at high frequency). As explained in Babinsky and Harvey [2011], these small unsteady ripples of the reflected shock waves were also observed in simulations of weak interactions. These high frequency oscillations of the reflected shock waves are then linked to the incoming turbulence whose most energetic scales excite the reflected shock wave.

Medium frequency features

The dynamics of subsonic separated and reattaching flows have been extensively studied and characteristic frequency scales have been characterized (Cherry et al. [1984] Kiya and Sasaki [1985]). In particular these study highlighted that the shear layer bounding the upper part of the separation bubble, is subjected to two instabilities of medium characteristic frequencies.
The shear layer is submitted to a convective instability (Kelvin-Helmholtz waves). The non linear evolution of the Kelvin-Helmholtz waves leads to a vortex shedding at a Strouhal number around $S_L = \frac{fL}{U_e} \simeq 0.6 - 0.8$ based on the length (L) of the recirculation bubble .
The shear layer is also submitted to an absolute instability called "flapping" of the shear layer that has the characteristic frequency $S_L = \frac{fL}{U_e} \simeq 0.12 - 0.15$. This flapping consists in successive enlargment and shrinkage of the recirculation bubble. The shrinkage is associated to a vortex shedding downstream of the recirculation bubble.

Low frequency features

For supersonic flows, a low frequency flapping mode of the shear layer have also been observed in addition to the medium frequency flapping at a Strouhal number of $S_L = \frac{fL}{U_e} \simeq 0.03 - 0.04$ (Dupont et al. [2007] Piponniau et al. [2009]). This low frequency flapping mode is also called the "breathing" of the separation bubble.
A low frequency oscillation of the whole SWBLI system (the recirculation bubble in phase with the system of shock waves) is also observed in simulations and experiments (Délery and Dussauge [2009]). This instability, called the "unsteadiness" of the SWBLI, consists in an oscillation of the recirculation bubble coupled to the shock wave system. This low frequency phenomenon has the same characteristic Strouhal number as the breathing of the separation bubble, namely $S_L = \frac{fL}{U_e} \simeq 0.03 - 0.04$. It is shown in figure 1.10 from Dussauge et al. [2006] where the dominant Strouhal mumber S_L is plotted against the Mach number (ranging from 0 to 5) for several data for separated flows available in the literature. The SWBLI unsteadiness is further discussed in the followings.

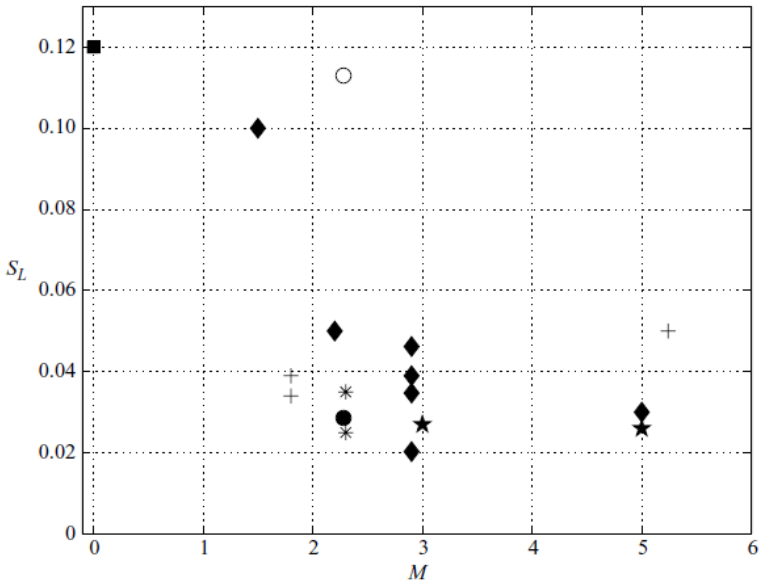

FIGURE 1.10 – Dimensionless frequency (S_L) based on the mean separation length (L) of the shock wave oscillation in various configurations versus the Mach number: (■) subsonic separation from Kiya and Sasaki [1983]; (♦) compression ramp cases; (*) IUSTI reflection cases; (+) overexpanded nozzle (restricted shock wave separation); (★) blunt fin; (•) Touber and Sandham [2008]; (○) estimated superstructures upstream influence for the 8° IUSTI case. Figure adapted from Dussauge et al. [2006]

1.3.2 Recent works and mechanisms proposed in the literature

Until the 2000's, researches about SWBLI unsteadiness have essentially been experimental. These works allowed to characterize the mean properties of the flow as well as to detect the low frequency oscillations of the SWBLI. Nevertheless, the prediction of unsteady pressure loads, the precise characterization of the unsteadiness and the causal explanation of this low frequency behavior of the interaction remained open research fields. A overview of the knowledge available in the literature about SWBLIs in 2001 can be found in Dolling [2001]. After this date, a significant improvement in the comprehension of the SWBLI unsteadiness have been obtained using experimental means and modern simulation techniques. In particular, successive increases of computer capabilities allowed high fidelity simulations over times long enough to capture and characterize the low frequency unsteadiness. These works mainly focused on impinging oblique-shock wave reflections as well as ramp flows, that are configurations that share the same dynamic features. These research efforts leaded to new explanations of physical mechanisms responsible for the SWBLI unsteadiness. These mechanisms can be coarsly classified in two main categories (Délery and Dussauge [2009]).

The first mechanism consists in a perturbation of the SWBLI by the large scales within the incoming turbulent boundary layer. Indeed, an experimental study (Ganapathisubramani et al. [2006]) of a separated compression ramp interaction at M = 2 has evidenced very long ($\simeq 30\delta$) coherent structures in the incoming turbulent boundary layer convected at a speed of $0.75U_\infty$. The resulting frequency is therefore $S_L = 0.025\frac{L}{\delta}$ expressed in terms of a Strouhal number based on the length of the separated zone L (δ being the boundary layer thickness). If L is of the order of the boundary layer thickness ($L \sim \delta$), the resulting frequency is of the order of the characteristic frequency of the SWBLI unsteadiness ($S_L \simeq 0.03-0.04$). Consequently, the excitation of the reflected shock wave by these long structures were suspected to trigger the SWBLI unsteadiness. Strong links between upstream large scales and unsteadiness in the interaction in the case of a Mach 2 compression ramp flow have been evidenced by same authors (Ganapathisubramani et al. [2007a] Ganapathisubramani et al. [2007b]). Nevertheless, the proposed mechanism was challenged by other experimental and numerical results. For instance, an experimental study (Dupont et al. [2005]) of the interac-

tion between an oblique shock wave and a turbulent boundary layer developing on a flat plate at M = 2.3 presented ratios $L/\delta \simeq 5-7$ for the recirculation bubble and a SWBLI unsteadiness at $S_L \simeq 0.03-0.04$. The authors claimed that links between upstream large scales and unsteadiness in the interaction were not significant in their experimental flow. Moreover, the SWBLI unsteadiness have been observed in a large eddy simulation (LES) (Touber and Sandham [2009]) in which no elongated coherent structure was identified in the incoming turbulent boundary layer.
A second kind of mechanism has also been introduced in the literature, for which the dynamics of the recirculation bubble must be related to the unsteadiness of the whole SWBLI system and and in particular to the reflected shock wave oscillations. In addition to the work of Dupont et al. [2005], several numerical works advocate for this second mechanism. The DNS of Pirozzoli and Grasso [2006] and the LES of Aubard et al. [2013] that studied the interaction between an incident oblique shock wave and a turbulent boundary layer on a flat plate at M = 2.25 proposed two slightly distinct mechanisms to explain the oscillations of the reflected shock wave based on the coupling between this shock wave and the dynamics of the boundary layer recirculation. In Aubard et al. [2013], the reflected shock wave have been suspected to behave as a low pass filter. The foot of the shock wave being excited by the recirculation dynamics, the characteristic frequency of the oscillatory movement is suspected to be prescribed by the low frequency breathing of the separation zone. The separation point was then observed to oscillate with the foot of the reflected shock wave. In Pirozzoli and Grasso [2006], authors claim that the interaction between the vortical structures of the shear layer and the incident shock wave generates feedback pressure waves that excite the separation point region at the frequency of the SWBLI unsteadiness, producing self-sustained oscillations. In Piponniau et al. [2009], a simple model was proposed from experimental observations, based on the entrainment characteristics of the shear layer. The Dynamic Mode Decomposition (DMD) analysis performed by Priebe et al. [2016] on a previously DNS of a Mach 2.9, 24° compression ramp SWBLI (Priebe and Martín [2012]) allowed authors to infere that the SWBLI unsteadiness would be related to the presence of Görtler-like vortices in the downstream separated flow due to an underliying centrifugal instability.
Despite arguments in favor of each mechanism, no definitive explanation have yet been provided. Some authors argue that both mechanisms are at play in the onset of the SWBLI unsteadiness but the influence of the first mechanism decreases as far as the strength of the interaction decreases (Souverein et al. [2009] Clemens and Narayanaswamy [2014]).
In additions to these two main families of mechanims, a third kind of model have been introduced in the literature. It accounts for the incoming turbulence without requiring the existence of superstructures. Touber and Sandham [2011] proposed a quantitative model involving the incoming boundary layer disturbrances in which the shock wave / separation bubble system is seen as a black-box filter/amplifier converting incoherent background disturbances into the observed spectra. In mathematical terms the model is a first order ordinary differential equation with stochastic forcing. This was first proposed empirically by J. Plotkin [1975]. This model only requires very low amplitude background disturbances in the flow and these do not need to be in the form of coherent structures. Nevertheless, this model have the major drawback of not explaining the causes of the SWBLI unsteadiness. The relevance of this model have been strengthened by Sansica et al. [2014] who reproduced numerically the SWBLI unsteadiness (in particular the low frequency oscillations of the separation point) by forcing a 2D SWLBLI with white noise. This white noise perturbation of the SWLBLI (involving no incoming turbulent fluctuations), mimicking the broadband background distrurbances due to a turbulent incoming boundary layer, were found sufficient to produce the low frequency unsteadiness wherease simulations of a non forced 2D SWLBLI did not exhibit these low frequency oscillations of the separation point and the reflected shock wave (Fournier et al. [2015]).
In a recent work (Adler and Gaitonde [2018]) the authors performed a statistically stationary linear response analysis of the SWTBLI using the synchronized large-eddy simulation method. Their results demonstrated that the SWTBLI fosters a global absolute linear instability corresponding to a time-mean linear tendency of the reflected shock for restoration to more moderate displacements

when experiencing an extrem (upstream or downstream) displacement. They interpreted the low frequency unsteadiness of the SWTBLI as a non linear forcing of the reflected shock wave by the medium frequency flapping of the separation bubble. The competition between the linear restoring tendency of the reflected shock wave and the non linear flapping of the separation bubble have been said responsible for the low frequency oscillations of the bubble. This mecanism gathers some aspects of several mecanisms cited hereinabove. Indeed, this model confirms the linear restoring tendency of the reflected shock wave which is the premise of the model proposed by J. Plotkin [1975]. Moreover, this linear behavior of the reflected shock wave is coupled with a non linear mass-depletion mechanism wich corresponds to the mechanism proposed by Piponniau et al. [2009].

1.4 Conclusions and outlook of the work

In this chapter, an overview of the knowledge available in the literature about the SWBLI has been presented. In particular we focused on the the low frequency SWBLI unsteadiness phenomenon. As pointed out in section 1.3.2, non consensus has been reached in the explanation of the physical mechanism leading to these low frequency oscillations of the whole SWBLI system. Some explanations link the SWBLI unsteadiness to the large coherent structures from the incoming turbulent boundary layer whereas other proposed mechanisms link the SWBLI unsteadiness to the low frequency dynamics of the recirculations bubble.
In order to better understand the mechanisms leading to the unsteadiness of the SWBLI, we have first chosen to perform a SWBLI simulation suppressing one of the two suspected mechanisms leading to the unsteadiness. By simulating the interaction between a laminar boundary layer and a incident shock wave, we have suppressed the suspected influence of the large scale turbulent structures within the boundary layer on the SWBLI unsteadiness. The only remaining suspected cause of unsteadiness would be the dynamics of the separation bubble. The results are shown in chapter 4. The numerical approach used shows its ability to capture the dynamics of the recirculation zone. Mainly, the detachment of the boundary layer recovers a steady location while the reattachment location is sensitive to the instabilities of the recirculation bubble, namely the low frequency breathing, the flapping and the Kelvin-Helmholtz frequencies. The unsteadiness of the whole SWBLI system have however not been recovered for this interaction with a laminar boundary layer. Nevertheless, the oscillatory motion of the reattachment shock wave have been recorded obviously in phase with the motion of the reattachment point. These results point out that the dynamics of the recirculation bubble is not the only phenomenon responsible to the SWBLI unsteadiness and the turbulent structures of the incoming boundary layer might play an important role in triggering the whole unsteadiness.
The rest of this manuscript is then devoted to the simulation and analysis of the SWTBLI.

1.5 References

Holger Babinsky and John K Harvey. *Shock wave-boundary-layer interactions*, volume 32. Cambridge University Press, 2011. 3, 10, 11, 12, 16

M Jayaprakash Narayan and Raghuraman N Govardhan. Experimental study of supersonic flow over a forward facing step. In *International Symposium on Shock Waves*, pages 1211–1216. Springer, 2013. 3, 11

Jean Délery and Jean-Paul Dussauge. Some physical aspects of shock wave/boundary layer interactions. *Shock waves*, 19(6):453, 2009. 3, 12, 13, 14, 15, 16, 17

A Sansica, ND Sandham, and Z Hu. Forced response of a laminar shock-induced separation bubble. *Physics of fluids*, 26(9):093601, 2014. 15, 18

Emile Touber and Neil Sandham. Oblique shock impinging on a turbulent boundary layer: Low-frequency mechanisms. 06 2008. ISBN 978-1-60086-989-1. doi: 10.2514/6.2008-4170. 3, 16, 17

N.J. Cherry, R. Hillier, and M. E. M. P. Latour. Unsteady measurements in a separated and reattaching flow. *Journal of Fluid Mechanics*, 144, 1984. 16

M. Kiya and K. Sasaki. Structure of large scale vortices and unsteady reverse flow in the reattaching zone of a turbulent separation bubble. *Journal of Fluid Mechanics*, 154, 1985. 16

Pierre Dupont, Sébastien Piponniau, Andreï Sidorenko, and Jean François Debiève. Investigation of an oblique shock reflection with separation by piv measurements. In *45th AIAA Aerospace Sciences Meeting and Exhibit*, page 119, 2007. 16

S. Piponniau, J. P. Dussauge, J. F. Debiève, and P. Dupont. A simple model for low-frequency unsteadiness in shock-induced separation. *Journal of Fluid Mechanics*, 629:87–108, 2009. 16, 18, 19

Jean-Paul Dussauge, Pierre Dupont, and Jean-Francois Debiève. Unsteadiness in shock wave boundary layer interactions with separation. *Aerospace Science and Technology*, 10(2):85–91, 2006. 3, 16, 17

Masaru Kiya and Kyuro Sasaki. Structure of a turbulent separation bubble. *Journal of Fluid Mechanics*, 137:83–113, 1983. 3, 17

David S Dolling. Fifty years of shock-wave/boundary-layer interaction research: what next? *AIAA journal*, 39(8):1517–1531, 2001. 17

B. Ganapathisubramani, N. T. Clemens, and D. S. Dolling. Planar imaging measurements to study the effect of spanwse structure of upstream turbulent boundary layer on shock-induced separation. *AIAA paper*, page 324, 2006. 17

Bharathram Ganapathisubramani, NT Clemens, and DS Dolling. Effects of upstream boundary layer on the unsteadiness of shock-induced separation. *Journal of fluid Mechanics*, 585:369–394, 2007a. 17

Bharathram Ganapathisubramani, Noel Clemens, and David Dolling. Effects of upstream coherent structures on low-frequency motion of shock-induced turbulent separation. In *45th AIAA Aerospace Sciences Meeting and Exhibit*, page 1141, 2007b. 17

P. Dupont, C. Haddad, J. P. Ardissone, and J.F. Debiève. Space and time organisation of a shock wave/turbulent boundary layer interaction. *Aerospace Science and Technology*, 9:561–572, 2005. 17, 18

E. Touber and N. D. Sandham. Large-eddy simulation of low-frequency unsteadiness in a turbulent shock-induced separation bubble. *Theoretical and computational fluid dynamics*, 23:79–107, 2009. 18

S. Pirozzoli and F. Grasso. Direct numerical simulation of impinging shock wave/turbulent boundary layer interaction at m=2.25. *Physics of Fluids*, 18(6):065113, 2006. doi: 10.1063/1.2216989. 18

G. Aubard, X. Gloerfelt, and J.-C. Robinet. Large-Eddy Simulation of Broadband Unsteadiness in a Shock/Boundary-Layer Interaction. *AIAA Journal*, 51:2395–2409, 2013. 18

Stephan Priebe, Jonathan H Tu, Clarence W Rowley, and M Pino Martín. Low-frequency dynamics in a shock-induced separated flow. *Journal of Fluid Mechanics*, 807:441–477, 2016. 18

Stephan Priebe and M Pino Martín. Low-frequency unsteadiness in shock wave–turbulent boundary layer interaction. *Journal of Fluid Mechanics*, 699:1–49, 2012. 18

L. Souverein, P. Dupont, J. F. Debiève, J.-F. Dussauge, B. van Oudheusden, and F. Scarano. Effect of Interaction Strength on the Unsteady Behavior of Shock Wave Boundary Layer Interactions. *AIAA paper*, page 3715, 2009. 18

N. T. Clemens and V. Narayanaswamy. Low-Frequency Unsteadiness of Shock Wave/Turbulent Boundary Layer Interactions. *Annual Review of Fluid Mechanics*, 46:469–492, 2014. 18

E. Touber and N. D. Sandham. Low-order stochastic modelling of low-frequency motions in reflected shock-wave/boundary-layer interactions. *Journal of Fluid Mechanics*, 671:417–465, 2011. doi: 10.1017/S0022112010005811. 18

K. J. Plotkin. Shock wave oscillation driven by turbulent boundary-layer fluctuations. *AIAA Journal*, 13:1036–1040, 07 1975. doi: 10.2514/3.60501. 18, 19

Guillaume Fournier, A Chpoun, Yann Fraigneau, and Christian Tenaud. Direct numerical simulations of the shock-induced separation of a laminar boundary layer. In *Direct and Large-Eddy Simulation 10, Limasol ,Cyprus*, 2015. 18

M. C. Adler and D. V. Gaitonde. Dynamic linear response of a shock/turbulent-boundary-layer interaction using constrained perturbations. *Journal of Fluid Mechanics*, 840:291–341, 2018. 18

Chapter 2

Equations and numerical approach

Contents

2.1 The governing equations . . . 24
2.1.1 Compressible Navier-Stokes equations . . . 24
2.1.2 Non-dimensionalized compressible Navier–Stokes equations . . . 25
2.2 Introduction to high order numerical schemes for compressible Navier-Stokes equations . . . 26
2.2.1 Method of lines . . . 26
2.2.2 One step approaches . . . 27
2.2.3 Shock capturing procedures . . . 27
2.2.4 Approaches used for high fidelity SWBLI simulations . . . 29
2.3 Numerical approach applied . . . 29
2.3.1 The One-Step Monotonicity-Preserving (OSMP) scheme. . . . 29
2.3.2 Approximation of the viscous fluxes. . . . 32
2.4 Domain and boundary conditions . . . 34
2.4.1 Adiabatic wall boundary conditions . . . 35
2.4.2 Inflow and outflow conditions . . . 36
2.5 Conclusions . . . 36
2.6 References . . . 36

The DNS of high Reynolds number compressible flows involving shock waves, such as the SWBLI introduced in chapter 1, is a challenging task since one must use a numerical scheme that can both represent small scale turbulent structures with the minimum of numerical dissipation, and capture discontinuities with the robustness that is common to Godunov-type methods without spoiling the accuracy in the vicinity of the discontinuity.
In this chapter, we first present the compressible Navier-Stokes equations that have to be solved in order to perform SWBLI simulations. The domain of the simulation, as well as the boundary conditions are then described. In section 2.2, an overview of the numerical methods classically used to solve this problem is given. The numerical methodology used in this work is then presented. We finally give details about the implementations of the boundary conditions.

2.1 The governing equations

2.1.1 Compressible Navier-Stokes equations

We consider here the compressible Navier-Stokes equations expressed in a cartesian coordinate system:

$$\frac{\partial \mathbf{U}}{\partial t} + \nabla \cdot \mathbf{F}(\mathbf{U}) - \nabla \cdot \mathbf{F_v}(\mathbf{U}, \nabla(\mathbf{U})) = 0, \tag{2.1}$$

where $\mathbf{U}$ is the vector of conservative variables, $\mathbf{F}(\mathbf{U})$ the convective fluxes, and $\mathbf{F_v}(\mathbf{U}, \nabla(\mathbf{U}))$ the diffusive fluxes that write respectively:

$$\mathbf{U} = \begin{bmatrix} \rho \\ \rho\mathbf{u} \\ \rho E \end{bmatrix}, \quad \mathbf{F} = \begin{bmatrix} \rho\mathbf{u} \\ \rho\mathbf{u}\otimes\mathbf{u} + P\mathbf{I} \\ (\rho E + P)\mathbf{u} \end{bmatrix}, \quad \text{and} \quad \mathbf{F_v} = \begin{bmatrix} 0 \\ \sigma \\ \mathbf{u}.\sigma + \lambda\nabla T \end{bmatrix}. \tag{2.2}$$

with ρ is the density, $\mathbf{u}$ is the velocity vector, E is the total energy per unit of mass. P is the thermodynamic pressure related to the conservative variables by the following relationship: $P = \rho(\gamma - 1)\left(E - \frac{1}{2}\mathbf{u}\cdot\mathbf{u}\right)$, and T is the static temperature. γ is the ratio of heat capacities and λ is the thermal conductivity.
The viscous stress tensor is expressed as:

$$\sigma = \mu(\nabla\mathbf{u} + \nabla^T\mathbf{u}) - \frac{2}{3}\mu\nabla\cdot\mathbf{u}.$$

μ is the dynamic viscosity, related to the static temperature using the Sutherland's law:

$$\mu = \mu_0\left(\frac{T}{T_0}\right)^{(3/2)}\frac{T_0 + S}{T + S}, \tag{2.3}$$

where μ_0 is a reference viscosity, T_0 is a reference temperature and S is the Sutherland constant. For air at moderate temperatures and pressures, $\mu_0 = 1.789410^{-5}$ kg/(m.s), $T_0 = 273.11$ K and $S = 110.56$ K.
The Prandtl number Pr and the heat capacity at constant pressure C_p are assumed to be constant, so that the ratio between λ and μ is constant. It allows to relate λ to the static pressure T:

$$\lambda = \frac{\mu C_p}{Pr} \tag{2.4}$$

To close the system of equations, the ideal gaz assumption is used and the dimensionless equation of state writes:

$$\frac{P}{\rho} = rT. \tag{2.5}$$

where r is the specific gas constant.

2.1.2 Non-dimensionalized compressible Navier–Stokes equations

Dimensionless quantities

In order to define dimensionless quantities, we introduce the reference quantities that are chosen to represent the flow characteristics:

— the reference length L_0 (m)
— the reference speed U_0 $(m.s^{-1})$
— the reference density: ρ_0 $(kg.m^{-3})$
— the reference temperature T_0 (K)
— the reference speed of sound $c_0 = \sqrt{\gamma r \mathrm{T}_0}$
— the reference dynamic viscosity $\mu_0 = \mu(\mathrm{T}_0)$ $(kg.m^{-1}.s^{-1})$
— the reference thermal conductivity: $\lambda_0 = \lambda(\mathrm{T}_0)$ $(\mathrm{W}.m^{-1}.\mathrm{K}^{-1})$

Values assigned to these reference quantities depend on the problem under consideration. For example, different specific values are assigned to the reference variables for the Taylor-Green vortex and for the steady SWLBLI simulations presented in chapter 3.
The dimensionless quantities are then defined as follows:

— the dimensionless coordinate $\mathbf{x}^* = \frac{\mathbf{x}}{\mathrm{L}_0}$
— the dimensionless velocities $\mathbf{u}^* = \frac{\mathbf{u}}{\mathrm{U}_0}$
— the dimensionless time $t^* = \frac{\mathrm{L}_0}{\mathrm{U}_0} t$
— the dimensionless density $\rho^* = \frac{\rho}{\rho_0}$
— the dimensionless temperature $\mathrm{T}^* = \frac{\mathrm{T}}{\mathrm{T}_0}$
— the dimensionless total energy $\rho^* \mathrm{E}^* = \frac{\rho \mathrm{E}}{\rho_0 \mathrm{U}_0^2}$
— the dimensionless pressure $\mathrm{P}^* = \frac{p}{\rho_0 \mathrm{U}_0^2}$
— the dimensionless dynamic viscosity $\mu^* = \frac{\mu}{\mu_0}$
— the dimensionless thermal conductivity $\lambda^* = \frac{\lambda}{\lambda_0}$

The dimensionless compressible Navier-Stokes equations then writes:

$$\frac{\partial \mathbf{U}^*}{\partial t^*} + \nabla^* \cdot \mathbf{F}^*(\mathbf{U}^*) - \nabla^* \cdot \mathbf{F}_\mathbf{v}^*(\mathbf{U}^*, \nabla^* \mathbf{U}^*) = 0, \tag{2.6}$$

where $\nabla^* = (\frac{\partial}{\partial x^*}, \frac{\partial}{\partial y^*}, \frac{\partial}{\partial z^*})^\mathrm{T}$ is the dimentionless nabla symbol, $\mathbf{U}^*$ is the dimensionless vector of conservative variables, $\mathbf{F}^*(\mathbf{U}^*)$ the dimensionless convective fluxes, and $\mathbf{F}_\mathbf{v}^*(\mathbf{U}^*, \nabla^*(\mathbf{U}^*))$ the dimensionless diffusive fluxes that write respectively:

$$\mathbf{U}^* = \begin{bmatrix} \rho^* \\ \rho^* \mathbf{u}^* \\ \rho^* \mathrm{E}^* \end{bmatrix}, \quad \mathbf{F}^* = \begin{bmatrix} \rho^* \mathbf{u}^* \\ \rho^* \mathbf{u}^* \otimes \mathbf{u}^* + \mathrm{P}^* \mathbf{I} \\ (\rho^* \mathrm{E}^* + \mathrm{P}^*) \mathbf{u}^* \end{bmatrix},$$
$$\text{and} \qquad \mathbf{F}_\mathbf{v}^* = \begin{bmatrix} 0 \\ \frac{1}{\mathrm{Re}_0} \sigma^* \\ \frac{1}{\mathrm{Re}_0} \mathbf{u}^* . \sigma^* + \frac{\mu^*}{(\gamma - 1) \mathrm{Re}_0 \mathrm{P}r_0 \mathrm{M}_0^2} \nabla^* \mathrm{T}^* \end{bmatrix}. \tag{2.7}$$

$\mathrm{Re}_0 = \frac{\rho_0 \mathrm{U}_0 \mathrm{L}_0}{\mu_0}$ is the Reynolds number, $\mathrm{M}_0^2 = \frac{\mathrm{U}_0^2}{c_0^2}$ is the Mach number, and $\mathrm{P}r_0 = \frac{\mu_0 \mathrm{C}p}{\lambda_0}$ the Prandtl number. $\mathrm{C}p$ is the heat capacity at constant pressure.
The viscous stress tensor is expressed as:

$$\sigma^* = \mu^* (\nabla^* \mathbf{u}^* + \nabla^* \mathbf{u}^*) - \frac{2}{3} \mu^* \nabla^* \cdot \mathbf{u}^*. \tag{2.8}$$

To close the system of equations, the ideal gaz assumption is used and the dimensionless equation of state writes:

$$\frac{P^*}{\rho^*} = \frac{1}{\gamma M_0^2} T^*. \tag{2.9}$$

Finally, for a given fluid, *i.e.* for a given value of heat capacity ratio γ, the problem is completely defined by 3 dimensionless numbers, namely, the Reynolds number (Re_0), the Mach number (M_0) and the Prandtl number (Pr_0).

2.2 Introduction to high order numerical schemes for compressible Navier-Stokes equations

In this work, the targeted DNS is the simulation of a SWBLI. Such high Reynolds number flows are often turbulent and therefore one must use a numerical scheme that represents small scale turbulent structures with the minimum of numerical dissipation. For this purpose, high order scheme are often used, because of "their potential in delivering higher accuracy with lower cost than low order methods" (Wang et al. [2013]). Nevertheless, SWBLIs involve shock waves and the use of high order schemes is known to produce spurious oscillations in the viscinity of discontinuities. One must use a shock capturing procedure in order to avoid these spurious oscillations without degrading the precision of the scheme near extrema in smooth parts of the flow.

2.2.1 Method of lines

One classical approach to develop high order schemes is the method of lines. In this approach, time and space are considered separately. Time discretization is generally handled by a multistage time integration such as the Runge-Kutta time discretization. A high order discretization scheme equipped with a shock capturing technique, ensuring non-oscillatory and conservation properties, is applied in each stage of the time integration. Using this approach, one does not control the total truncation error of the scheme. The support of the high order spatial discretization being relatively large, applying it in each stage of the time integration leads to large stencils and hence to high computational costs. Besides, the shock capturing procedure is applied only on the spatial discretization scheme. Consequently, it is not possible to reach very high order of accuracy in time without introducing spurious oscillations (Daru and Tenaud [2004]). For instance, using a Runge–Kutta method, the Total Variation Diminishing (TVD) property cannot be recovered for an accuracy greater than fifth order without solving adjoint problems that considerably increases the computational cost.
Different high order schemes can be used following the method of lines approach.
The family of Finite Difference (FD) schemes is frequently used, especially in the academic community for DNS and Large Eddy Simulation (LES) of compressible turbulent flows. A review about numerical methods for high speed flows can be found in Pirozzoli [2011] where the author focuses on FD methods. Due to their non-dissipative properties, central schemes are often privilegied. Nevertheless, these schemes are known to produce numerical instabilities. Different methods have been developed to stabilize these schemes. Some methods relie on the filtering of the solution, other methods consist in imposing the energy or entropy conservation in a discrete sence. Details and relevant references can be found about these methods in Pirozzoli [2011].
Other numerical methods can be used for the spatial discretization. The high order FD methods leads to relatively large stencils. A way to reach high order discretization on unstructured grids avoiding large stencils, is to increase the number of degrees of freedom inside each mesh cells. Following this philosophy, different class of methods have been designed: the Discontinuous Galerkin (DG) technique (Reed and Hill [1973]) is based on the Finite Element (FE) framework; the Spectral Volume (SV) (Wang [2002]) technique is based on the FV framework; the Spectral Difference (SD) (Liu et al. [2006]) technique follows the FD approach. The main advantage of these

methods is that their are particularly well adapted to complex geometries as their are suited to unstructured meshes. Nevertheless, they share the drawbacks inherent to the method of lines approach.

2.2.2 One step approaches

The FV framework can be used to develop OS schemes using the Lax-Wendroff approach. In this work, we use this approach and more details can be found in section 2.3. One step schemes have two major advantages. As the time integration requires only one step, the stencil is small with respect to stencils used in the method of lines approaches for the same order of accuracy. Moreover, one step schemes allow to control the total truncation error involving both the error due to time integration and the error due to spatial discretization. Nevertheless, one step scheme derived using the Lax-Wendroff approach are restricted to structured meshes.

2.2.3 Shock capturing procedures

Whatever the approach used, the high order numerical scheme needs a shock capturing procedure to avoid the spurious oscillations arising from the high order discretization of discontinuities. Different shock capturing procedures have been introduced in the litterature. These methods introduce numerical diffusion near discontinuisties in a more or less implicit way.

Total Variation Diminishing constraint

The TVD constraint has been introduced for the hyperbolic scalar conservation law in the form:

$$\frac{\partial u}{\partial t} + \frac{\partial f(u)}{\partial x} = 0. \tag{2.10}$$

The exact solution of equation 2.10 satisfies the TVD constraint as stated in Harten [1983]:

$$\mathrm{TV}(u(.,t2)) \leq \mathrm{TV}(u(.,t1)), \quad \forall\, t_2 \geq t_1, \tag{2.11}$$

where $\mathrm{TV}(u(.,t))$ is the Total Variation (TV) of u, the solution of equation 2.10 at time t.
The TV is defined as follows:

$$\mathrm{TV}(u(.,t)) = \sup \sum_{j=1}^{\mathrm{N}} \mid u(\xi_j, t) - u(\xi_{j-1}, t) \mid, \tag{2.12}$$

where the sup is token on all the possible subdivisions of the line $-\infty < \xi_0 < \xi_1 < ... < \xi_{\mathrm{N}} = \infty$.
In Harten [1983], the author introduced a discrete version of the TVD constraint for the discrete approximation u_j^n of u at time n:

$$\mathrm{TV}(u_j^{n+1}) \leq \mathrm{TV}(u_j^n), \tag{2.13}$$

where j is the number of the mesh cell.
The discrete TV property has been defined as follows:

$$\mathrm{TV}(u^n) = \sum_j \mid u_{j+1}^n - u_j^n \mid, \tag{2.14}$$

and a methodology has been developed in order to build numerical schemes that verify the discrete TVD constraint. The scheme is written in the conservative form:

$$u_j^{n+1} = u_j^n - \frac{\delta t}{\delta x}(\mathrm{F}_{j+1/2} - \mathrm{F}_{j-1/2}), \tag{2.15}$$

where δt is the time step, δx is the spatial step, and F is the flux at cell interfaces that is approximated in the following form:

$$\mathrm{F}_{j+1/2} = \mathrm{F}^1_{j+1/2} + \Phi(\mathrm{F}^p_{j+1/2} - \mathrm{F}^1_{j+1/2}). \tag{2.16}$$

F^1 is a first order flux approximation, F^p is a p^{th} order flux approximation and Φ is a flux limiter function that verifies the so called TVD constraints (Harten [1983]) so that it is close to zero near discontinuities and close to one far from discontinuities. The numerical scheme is then expected to be p^{th} order far from discontinuities and first order (diffusive) at discontinuities ensuring the avoidance of spurious oscillations.
This shock capturing procedure can be extendent to hyperbolic systems by applying the scheme "scalarly to each of the characteristic variables" (Harten [1983]).
TVD schemes are efficient in computing shock waves. Nevertheless, they are known to affect the accuracy of the scheme also in smooth regions of the flow. Indeed, due to the TVD constraints, the order of the scheme is reduced to one at extrema and not only at discontinuities. This is known as the "clipping" of extrema by TVD schemes Daru and Tenaud [2004].

MP constraint

The solution of equation 2.10 satisfies the monotony preservation property stated by Godunov [1959]: "initially monotone data remain monotone for all time". A way of circumventing the drawback of TVD scheme, that is the clipping of extrema in smooth regions, has been introduced by Suresh and Huynh [1997] who enforced the MP constraint at the discret level. This method has been further adapted by Daru and Tenaud [2004]. By doing so, the TVD constraints are enlarged at extrema and the high order flux reconstruction is preserved in smooth regions of the flow while TVD constraints acts near discontinuities to avoid spurious oscillations.
As the TVD constraint, the MP constraint can be applied "scalarly to each of the characteristic variables" in order to be used to solve hyperbolic systems such as Euler equations (inviscid limit of Navier-Stokes equations).

Essentially Non-Oscillatory (ENO) and Weighted Essentially Non-Oscillatory (WENO) schemes

An other family of classical shock capturing procedure includes the ENO and WENO schemes. The ENO method was introduced in Harten et al. [1987]. The basic idea of this method is the use of an adaptative support and the selection of the smoothest stencil allowing the high order reconstruction of the numerical flux at cells interfaces. The reconstruction is said ENO in the sense that the spurious oscillation that may arise from the descritization of discontinuities are of the order of the trucation error. This approach were found efficient in avoiding the spurious oscillations near discontinuisites while maintaining high order discretization in smooth regions of the flow. Nevertheless, this approach is costly since the flux reconstruction at cell interface must be computed for the different competing stencils.
An other drawback of the ENO approach is the use of an adaptative stencil that can be the source numerical artefacts in the results Daru and Tenaud [2005]. WENO schemes have been developed in order to overcome this drawback. Unlike in the ENO procedure, where the best support candidate is selected for the flux reconstruction, the reconstruction is obtained as a convex linear combination of all candidate stencils in the WENO approach (Liu et al. [1994]). The coefficients of the linear combination are chosen in order to obtain the maximal formal order of accuracy in smooth regions whereas quasi null coefficients are assigned to the stencils introducing spurious oscilations.

Artificial viscosity methods

An other possible shock capturing procedure relies on the use of an artificial viscosity. In this class of methods, artificial diffusive terms are added in the Navier-Stokes equations. These adjustable terms are designed so that the amount of diffusivity needed to avoid spurious oscillations is added at discontinuities whereas vanishing far from discontinuities. An example of this kind of shock capturing procedure has been introduced in Jameson et al. [1981]. Shock sensor are needed to detect the presence of shock waves. One of the most used shock sensor has been introduced by Ducros et al. [1999].

2.2.4 Approaches used for high fidelity SWBLI simulations

Most of the high fidelity simulations of the SWBLI available in the literature have been performed using the method of lines approach with a Runge-Kutta time integration and finite differences for the spatial discretization. We here summarize the numerical approaches used in studies already cited in chapter 1 (section 1.3.2) that are representative from the classical numerical approaches used in the last decade to perform high fidelity simulations of the SWBLI.

— In Pirozzoli and Grasso [2006], the authors use a 4^{th} order Runge-Kutta time integration scheme. A 7^{th} order WENO reconstruction of the characteristic inviscid fluxes that uses a local Lax–Friedrichs flux difference approach is used. A 4^{th} order compact FD scheme (Lele [1992]) is used for the the viscous fluxes approximation.

— In Touber and Sandham [2009] the time integration is performed using a 3^{rd} order Runge-Kutta scheme. The spatial discretization is performed by a 4^{th} order central FD scheme both for the convective and the viscous fluxes. The so called "entropy splitting" method imposes the entropy conservation in order to stabilize the discretization of the convective fluxes. In order to enhance the stability of the viscous fluxes approximation, the laplacian form is used. The shock capturing procedure relies on a variant of the TVD constraint coupled with the Ducros sensor (Ducros et al. [1999]).

— In Aubard et al. [2013] a 6 steps 4^{th} order Runge-Kutta scheme is used for the time integration. The convective fluxes are discretized by mean of a 4^{th} order low dissipative and low dispertive FD scheme. An artificial viscosity method is used as a shock capturing procedure.

— In Priebe et al. [2016] the time integration is performed using a 3^{rd} Runge-Kutta scheme. A 4^{th} order WENO FD scheme is used for the approximation of the convective fluxes whereas a 4^{th} order standard FD scheme is used for the viscous fluxes.

2.3 Numerical approach applied

The Navier-Stokes equations (2.6, 2.7, 2.9) are solved using a high order finite volume approach on cartesian meshes. We denote by $\mathbf{U}^n_{i,j,k}$ the discrete quantity $\mathbf{U}(\mathbf{x},t)$ estimated at a grid point $x_{i,j,k} = (i\,\delta x, j\,\delta y, k\,\delta z)^{\mathrm{T}}$ and at a time $t^{(n)} = n\,\delta t$ (δt, δx, δy and δz are respectively the time step and the space steps in each direction).

The Euler part is discretized by means of a high-order one-step Monotonicity Preserving scheme, namely the OSMPp scheme Daru and Tenaud [2004], based on a Lax-Wendroff approach, which ensures a p^{th}-order accuracy in both time and space in the regular regions. Besides, the discretization of the diffusive fluxes is obtained by means of a classical centered (2^{nd}-order or 4^{th}-order) scheme.

2.3.1 The One-Step Monotonicity-Preserving (OSMP) scheme.

The unlimited OS scheme.

We first present the unlimited scheme on the one dimensional Euler equation:

$$\frac{\partial \mathbf{U}}{\partial t} + \frac{\partial \mathbf{F}(\mathbf{U})}{\partial x} = \mathbf{0}. \tag{2.17}$$

This equation is discretized using the following conservative approximation:

$$\mathbf{U}_i^{n+1} = \mathbf{U}_i^n - \frac{\delta t}{\delta x}(\mathbf{F}_{i+1/2} - \mathbf{F}_{i-1/2}). \tag{2.18}$$

The numerical flux $\mathbf{F}_{i+1/2}$ is approximated by a p^{th}-order One-Step scheme (OSp) developed in Daru and Tenaud [2004]:

$$\mathbf{F}_{i+1/2} = \mathbf{F}^{Roe}_{i+1/2} + \frac{1}{2}\sum_k \left(\Phi^p_k(1-|\nu_k|)\right)\delta\alpha_k\,|\lambda_k|\,.\mathbf{r}_k)_{i+1/2}, \tag{2.19}$$

where $\mathbf{F}^{Roe}_{i+1/2}$ is the Roe flux at the cell interface:

$$\mathbf{F}^{Roe}_{i+1/2} = \frac{1}{2}\left(\mathbf{F}(\mathbf{U}^n_i) + \mathbf{F}(\mathbf{U}^n_{i+1})\right) - \frac{1}{2}\sum_k \left(|\lambda_k|\,\delta\alpha_k.\mathbf{r}_k\right)_{i+1/2}. \tag{2.20}$$

$\delta\alpha_{ki+1/2} = \mathbf{l}_{ki+1/2}\cdot\left(\mathbf{U}^n_{i+1} - \mathbf{U}^n_i\right)$ is the k^{th} Riemann invariant. $\lambda_{ki+1/2}$, $\mathbf{l}_{ki+1/2}$, and $\mathbf{r}_{ki+1/2}$ are respectively the k^{th} eigenvalue, and the corresponding left and right eigenvectors of the Jacobian matrix of the Euler flux ($\nabla_{\mathbf{U}}\mathbf{F}(\mathbf{U})$), expressed at the cell interface. $\nu_{ki+1/2} = \frac{\delta t}{\delta x}\lambda_{ki+1/2}$ is the local CFL number.

As far as, in the One Step procedure, the even derivatives are expressed using centered approximations while the odd ones use upwind approximations, the p^{th}-order accuracy functions ($\Phi_k{}^p_{i+1/2}$) are splitted into even and odd contributions following:

$$\Phi_k{}^p_{i+1/2} = \sum_{n=1}^{m} \Psi_k{}^{2n}_{i+1/2} - js\sum_{n=1}^{m_1} \Psi_k{}^{2n+1}_{i+1/2-js/2}, \tag{2.21}$$

where $m = \lfloor p/2 \rfloor$, $m_1 = \lfloor \frac{(p-1)}{2} \rfloor$ ($\lfloor\ \rfloor$ is the integer division symbol), and $js = sign(\lambda_{ki+1/2})$. The even and odd functions $\Psi_k{}^{2n}_{i+1/2}$ and $\Psi_k{}^{2n+1}_{i+1/2-js/2}$ are given by the recurrence formulae (for $n \geq 1$):

$$\Psi_k{}^{2n}_{i+1/2} = \sum_{l=0}^{2n-2} (-1)^l \mathrm{C}^l_{2n-2}.(c_k{}^{(2n)}\delta\alpha_k)_{i+1/2+n-1-l}, \tag{2.22}$$

$$\Psi_k{}^{2n+1}_{i+1/2} = \sum_{l=0}^{2n-1} (-1)^l \mathrm{C}^l_{2n-1}.(c_k{}^{(2n+1)}\delta\alpha_k)_{i+1/2+(n-1-l).js}; \tag{2.23}$$

where $\mathrm{C}^l_r = \frac{r!}{(r-s)!s!}$.

The coefficients $c_k{}^{(q)}$ depend on the local CFL number ($\nu_{ki+1/2}$), and are given by:

$$(c_k{}^{(q+1)})_{i+1/2} = \frac{|\nu_k|_{j+1/2} + (-1)^q \lfloor \frac{(q+1)}{2} \rfloor}{q+1}.(c_k{}^{(q)})_{i+1/2}, \quad q > 2. \tag{2.24}$$

with

$$c_k{}^2_{i+1/2} = |\lambda_k|_{i+1/2}\left(1 - |\nu_k|_{i+1/2}\right) \tag{2.25}$$

Using the accuracy function Φ^p (2.21), the scheme is p^{th}-order accurate in both space and time. This scheme has been derived up to the 11^{th}-order and more detailed information can be found in Daru and Tenaud [2004] and Daru and Gloerfelt [2007].

The limited OSMP scheme.

In the classic way for high order approximations, spurious oscillations could occur in the vicinity of discontinuities. Total Variation Diminishing (TVD) constraints Harten [1983] are commonly employed to cure this problem. The TVD constrain are written for each characteristic field:

$$\Phi_k{}^{p-\mathrm{TVD}}_{i+1/2} = max(0, min(\frac{2r_{ki+1/2}}{|\nu_k|_{i+1/2}}\frac{1-|\nu_k|_{i-js/2}}{1-|\nu_k|_{i+1/2}}, \Phi_k{}^p_{i+1/2}, \frac{2}{1-|\nu_k|_{i+1/2}})), \tag{2.26}$$

where $r_{ki+1/2} = \frac{\delta\alpha_{ki+1/2-js}}{\delta\alpha_{ki+1/2}}$.

Nevertheless, as it is well known, the TVD constraints clip the extrema although the solution is smooth Daru and Tenaud [2004]. To overcome this drawback, we employ Monotonicity-Preserving (MP) constraints that locally relaxe the TVD constraints near extrema. These constraints, first developed by Suresh and Huynh [1997] and further extended by Daru and Tenaud [2004], are applied

on the accuracy function ($\Phi^{p-\mathrm{MP}}$) to recover a scheme that is p^{th}-order in time and space everywhere except near discontinuities where the scheme is Monotonicity-Preserving (Daru and Tenaud [2004]). The constrained accuracy function writes:

$$\Phi_{k\,i+1/2}^{p-\mathrm{MP}} = max(\Phi_{k\,i+1/2}^{min}, min(\Phi_{k\,i+1/2}^{p}, \Phi_{k\,i+1/2}^{max})), \tag{2.27}$$

where

$$\Phi_{k\,i+1/2}^{min} = max(min(0, \Phi_{k\,i+1/2}^{md}), min(0, \frac{2r_{k\,i+1/2}}{\mid \nu_k \mid_{i+1/2}}, \Phi_{k\,i+1/2}^{lc})), \tag{2.28}$$

and

$$\Phi_{k\,i+1/2}^{max} = min(max(\frac{2}{1-\mid \nu_k \mid_{i+1/2}}, \Phi_{k\,i+1/2}^{md}), max(0, \frac{2r_{k\,i+1/2}}{\mid \nu_k \mid_{i+1/2}}, \Phi_{k\,i+1/2}^{lc})). \tag{2.29}$$

The mid-data accuracy function ($\Phi_{k\,i+1/2}^{md}$) and the large curvature accuracy function ($\Phi_{k\,i+1/2}^{lc}$) are defined as follows:

$$\Phi_{k\,i+1/2}^{md} = \frac{2}{1-\mid \nu_k \mid_{i+1/2}} \frac{\delta \mathrm{F}_{k\,i+1/2}^{md}}{\mid \lambda_k \mid_{i+1/2} \delta\alpha_{k\,i+1/2}}, \tag{2.30}$$

$$\Phi_{k\,i+1/2}^{lc} = \frac{2r_{k\,i+1/2}}{\mid \nu_k \mid_{i+1/2}} \frac{1-\mid \nu_k \mid_{i+1/2-js}}{1-\mid \nu_k \mid_{i+1/2}} \frac{\delta \mathrm{F}_{k\,i+1/2}^{lc}}{\delta \mathrm{F}_{k\,i+1/2}^{ul}}. \tag{2.31}$$

Finally, the upper-limit, mid-data and large curvature flux differences are defined as follows:

$$\delta \mathrm{F}_{k\,i+1/2}^{ul} = \frac{r_{k\,i+1/2}}{\mid \nu_k \mid_{i+1/2}} (1-\mid \nu_k \mid_{i-js/2}) \mid \lambda_k \mid_{i+1/2} \delta\alpha_{k\,i+1/2}, \tag{2.32}$$

$$\delta \mathrm{F}_{k\,i+1/2}^{md} = \frac{1}{2} \mid \lambda_k \mid_{i+1/2} \delta\alpha_{k\,i+1/2} - \frac{1}{2} d_{k\,i+1/2}, \tag{2.33}$$

and

$$\delta \mathrm{F}_{k\,i+1/2}^{lc} = \frac{1}{2} \delta \mathrm{F}_{k\,i+1/2}^{ul} + \frac{1}{2} \frac{1-\mid \nu_k \mid_{i+1/2-js}}{\mid \nu_k \mid_{i+1/2}} d_{k\,i+1/2-js}, \tag{2.34}$$

with $d_{k\,i+1/2} = minmod(d_{k\,i}, d_{k\,i+1})$, where $d_{k\,i} = \lambda_{k\,i+1/2} \delta\alpha_{k\,i+1/2} - \lambda_{k\,i+1/2} \delta\alpha_{k\,i-1/2}$ is a local curvature term.

Extension to 3D systems of equations.

The extension in the multidimensional case is delicate as far as a coupled time and space approach is used. In fact, we need to consider cross derivative terms that appear in the second and higher order terms, which are left uncontrolled if one applies a direction by direction MP correction to a Lax-Wendroff unsplit scheme. We also need to guarantee that the resulting scheme is non-oscillatory. The simplest way to avoid problems with cross derivatives and to recover good properties of the one-dimensional scheme is to use a Strang directional splitting strategy LeVeque [1992]; Strang [1968] which is unfortunately only second order accurate when directional operators do not commute. While the order of accuracy is lowered compared to the tensorial multistage approach, the OSMP scheme with the Strang algorithm provides results with very small error level at low cost Daru and Tenaud [2004, 2009].

In three dimensions, the splitting of the system of equations can be constructed to give symmetric accurate solution every six time steps:

$$\begin{aligned} \mathbf{U}_{i,j,k}^{n+6} = \; & \big(\mathrm{L}_{\delta x}(\delta t) \cdot \mathrm{L}_{\delta y}(\delta t) \cdot \mathrm{L}_{\delta z}(\delta t)\big)\big(\mathrm{L}_{\delta x}(\delta t) \cdot \mathrm{L}_{\delta z}(\delta t) \cdot \mathrm{L}_{\delta y}(\delta t)\big) \\ & \big(\mathrm{L}_{\delta y}(\delta t) \cdot \mathrm{L}_{\delta z}(\delta t) \cdot \mathrm{L}_{\delta x}(\delta t)\big)\big(\mathrm{L}_{\delta y}(\delta t) \cdot \mathrm{L}_{\delta x}(\delta t) \cdot \mathrm{L}_{\delta z}(\delta t)\big) \\ & \big(\mathrm{L}_{\delta z}(\delta t) \cdot \mathrm{L}_{\delta y}(\delta t) \cdot \mathrm{L}_{\delta x}(\delta t)\big)\big(\mathrm{L}_{\delta z}(\delta t) \cdot \mathrm{L}_{\delta x}(\delta t) \cdot \mathrm{L}_{\delta y}(\delta t)\big) \cdot \mathbf{U}_{i,j,k}^{n}. \end{aligned} \tag{2.35}$$

Here $L_{\delta x}$, $L_{\delta y}$ and $L_{\delta z}$ are discrete approximations of the Euler operators in each space direction. For instance, $L_{\delta x}$ denotes the Euler operator of the following problem:

$$L_{\delta x}(\delta t)\cdot \mathbf{U}^n_{i,j,k} = \mathbf{U}^n_{i,j,k} - \frac{\delta t}{\delta x}\left(\mathbf{F}^n_{i+1/2} - \mathbf{F}^n_{i-1/2}\right)_{j,k}. \tag{2.36}$$

When directional operators do not commute, the second order accuracy is recovered every six time steps.

2.3.2 Approximation of the viscous fluxes.

Until now, only the resolution of the Euler system has been adressed. In order to extend the numerical approach to the resolution of the Navier Stokes system, the approximation of the viscous fluxes is added in each sub step of the Strang directional splitting. The operators $L_{\delta x}$, $L_{\delta y}$ and $L_{\delta z}$ therefore become discrete approximations of the Navier Stokes operator in each space direction. For instance $L_{\delta x}$ now denotes the Navier Stokes operator of the following problem:

$$L_{\delta x}(\delta t)\cdot \mathbf{U}^n_{i,j,k} = \mathbf{U}^n_{i,j,k} - \frac{\delta t}{\delta x}\left(\mathbf{F}^n_{i+1/2} - \mathbf{F}^n_{i-1/2}\right)_{j,k} + \frac{\delta t}{\delta x}\left(\mathbf{F_v}^n_{i+1/2} - \mathbf{F_v}^n_{i-1/2}\right)_{j,k}. \tag{2.37}$$

A classical 2^{nd}-order central finite difference scheme is applied to approximate the divergence of the viscous fluxes. To study the influence of the order of accuracy of the viscous fluxes especially in case of wall bounded flows, a 4^{th}-order central scheme has been implemented in the CHORUS code. The two spatial approximations have been tested and results are show in chapter 3.

The 2^{nd} and 4^{th}-order approximations of the viscous fluxes are presented hereafter.

2^{nd}-order approximation:

Considering the direction (ξ) normal to the cell interface, we look for a numerical approximation of the viscous flux $\mathbf{F}^{\xi}_{\mathbf{v}}(\mathbf{U},\nabla\mathbf{U})$ at the cell interface $(i+1/2)$ that satisfies the relationship:

$$\frac{\partial \mathbf{F}^{\xi}_{\mathbf{v}}}{\partial \xi}\Big|_{i,j,k} = \frac{1}{\delta\xi}\left(\mathbf{F_v}_{i+1/2} - \mathbf{F_v}_{i-1/2}\right)_{j,k} + O(\delta\xi^2). \tag{2.38}$$

This is fulfilled once the velocity and temperature gradients involved in the numerical viscous fluxes satisfy the following relationships:

— in the normal to the cell interface (ξ), considering the cell centered variable ϕ, the gradient at the cell interface is:

$$\frac{\partial \phi}{\partial \xi}\Big|_{i+1/2,j,k} = \frac{1}{\delta\xi}\left(\phi_{i+1,j,k} - \phi_{i,j,k}\right) + O(\delta\xi^2); \tag{2.39}$$

— in the tangential directions (represented by η), lying in the plane of the cell interface, the gradient is expressed as:

$$\frac{\partial \phi}{\partial \eta}\Big|_{i+1/2,j,k} = \frac{1}{4.\delta\eta}\left(\phi_{i+1,j+1,k} + \phi_{i,j+1,k} - \phi_{i+1,j-1,k} - \phi_{i,j-1,k}\right) + O(\delta\eta^2). \tag{2.40}$$

4^{th}-order approximation:

Considering the direction (ξ) normal to the cell interface, we look for a numerical approximation of the viscous flux $\mathbf{F}^{\xi}_{\mathbf{v}}(\mathbf{U},\nabla\mathbf{U})$ at the cell interface $(i+1/2)$ that satisfies the relationship:

$$\frac{\partial \mathbf{F}^{\xi}_{\mathbf{v}}}{\partial \xi}\Big|_{i,j,k} = \frac{1}{\delta\xi}\left(\mathbf{F_v}_{i+1/2} - \mathbf{F_v}_{i-1/2}\right)_{j,k} + O(\delta\xi^4). \tag{2.41}$$

This is fulfilled once the velocity and temperature gradients involved in the numerical viscous fluxes satisfy the following relationships:

— in the normal to the cell interface (ξ), considering the cell centered variable ϕ, the gradient at the cell interface is:

$$\frac{\partial \phi}{\partial \xi}\Big|_{i+1/2,j,k} = \frac{1}{12.\delta\xi}\left(\phi_{i-1,j,k} - 15.\phi_{i,j,k} + 15.\phi_{i+1,j,k} - \phi_{i+2,j,k}\right) + O(\delta\xi^4); \tag{2.42}$$

— in the tangential directions (represented by η), lying in the plane of the cell interface, the gradient is expressed as:

$$\frac{\partial \phi}{\partial \eta}\Big|_{i+1/2,j,k} = \frac{1}{12.\delta\eta}\left(\widehat{\phi}_{i+1/2,j-2,k} - 8.\widehat{\phi}_{i+1/2,j-1,k} + 8.\widehat{\phi}_{i+1/2,j+1,k} - \widehat{\phi}_{i+1/2,j+2,k}\right) + O(\delta\eta^4), \tag{2.43}$$

with

$$\widehat{\phi}_{i+1/2,j,k} = \frac{1}{12.}\left(-\phi_{i-1,j,k} + 7.\phi_{i,j,k} + 7.\phi_{i+1,j,k} - \phi_{i+1,j,k}\right). \tag{2.44}$$

Check of the order of accuracy on a manufactured solution.

The approximation of the viscous fluxes introduced above has been validated using a manufactured solution corresponding to the initial flow field of the well known three-dimensional Taylor-Green vortex test case (see the chapter 3 for the initial state). The following 3-D diffusive problem has been solved with an initial flow field at rest:

$$\frac{\partial \mathbf{U}}{\partial t} - \nabla \cdot \mathbf{F_v}(\mathbf{U}, \nabla\mathbf{U}) = \mathbf{S}(\mathbf{U}, \nabla\mathbf{U}), \tag{2.45}$$

where $\mathbf{S}(\mathbf{U}, \nabla\mathbf{U})$ is the source term equal to the viscous flux computed analytically from the reference flow field of the Taylor-Green vortex test case. The solution of equation (2.45) converges towards the initial flow field of the Taylor-Green vortex test case with a zero machine residual. Figure 2.1 shows the L_2 norm of the error on the longitudinal velocity component between the reference Taylor-Green vortex solution (*i.e.* the initial state) and the steady solution obtained with the 2^{nd}- or the 4^{th}-order approximations of the viscous fluxes. These errors are plotted versus the grid spacing $h = \frac{1}{N}$ (N being the number of equally spaced grid points in each direction). We clearly observe that the 2^{nd}-order approximation of the viscous fluxes implemented leads to an approximation slightly better than 2^{nd}-order accuracy. Besides, the 4^{th}-order approximation leads to an approximation slightly better than the 4^{th}-order of accuracy. These results clearly validate the implementation of the 2^{nd}- and 4^{th}-order approximations of the viscous fluxes.

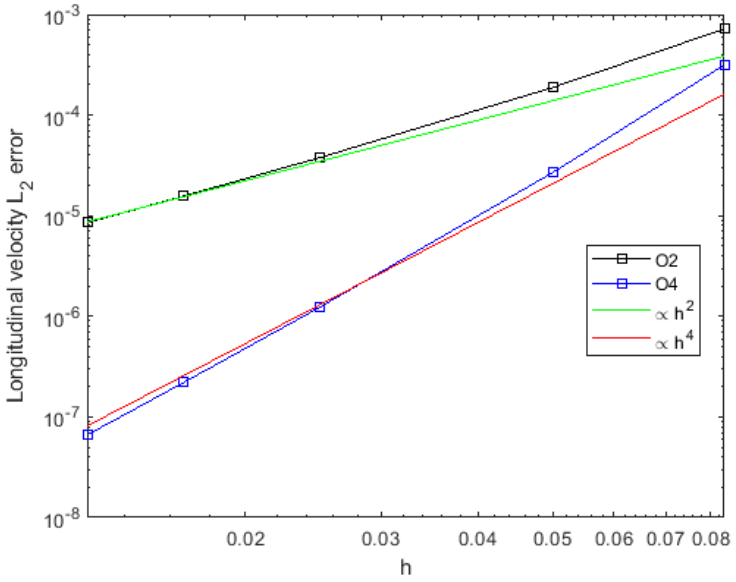

FIGURE 2.1 – L_2 norm versus the grid spacing of the error on the the longitudinal velocity component of the Taylor Green vortex between the reference and the computed solution using either the 2^{nd}-order or the 4^{th}-order approximations of the viscous fluxes.

Equivalent results have also been obtained for the other components of the velocity.

2.4 Domain and boundary conditions

A sketch of the spatial domain and boundary conditions considered in this work for SWBLI simulations is presented in figure 2.2. Both the SWLBLI and the SWTBLI simulations presented in chapters 4 and 6 are pseudo 2D simulations in the sense that periodic boundary conditions are imposed in the transversal direction. The inflow conditions are laminar or turbulent boundary layer profiles depending on wether a SWLBLI or a SWTBLI is simulated. More details are available in chapter 4 for the laminar boundary layer profile. For the turbulent boundary layer, unsteady inflow boundary conditions are imposed using the SEM that is presented in chapter 5. On the flat plate, on which the boundary layer develops, adiabatic wall boundary conditions (zero heat flux) are prescribed. Moreover, we impose the non-slip condition at the wall. On the top boundary, the Rankine-Hugoniot relationships are imposed in order to propagate the shock wave in the domain. Finally, we impose non reflecting boundary conditions for the downstream boundary.

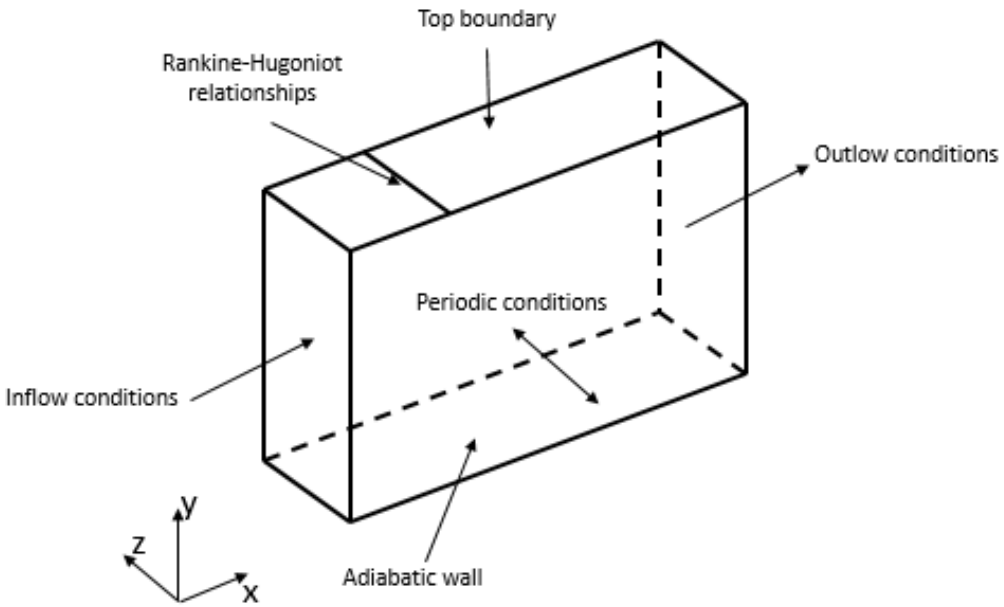

FIGURE 2.2 – Computational domain of calculus and boundary conditions for the simulation of SWBLIs.

2.4.1 Adiabatic wall boundary conditions

We give hereafter details about the adiabatic wall boundary conditions used at the wall.

As already written below, the non slip condition as well as the adiabatic wall conditions are imposed at the wall. These conditions write:

$$u\,|_{y=0}^{n+1} = 0, \tag{2.46}$$

$$v\,|_{y=0}^{n+1} = 0, \tag{2.47}$$

$$w\,|_{y=0}^{n+1} = 0, \tag{2.48}$$

$$\left(\frac{\partial \mathrm{T}}{\partial y}\right)|_{y=0}^{n+1} = 0. \tag{2.49}$$

The temperature at the wall is prescribed by expressing the first order wall normal derivative (equation 2.49) through a 4^{th} order forward FD approximation. The wall temperature at time $(n+1)\delta t$ is then expressed as a linear relationship of the temperature above the wall at time $(n+1)\delta t$:

$$\mathrm{T}_{j=1}^{n+1} = \frac{48\mathrm{T}_{j=2}^{n+1} - 36\mathrm{T}_{j=3}^{n+1} + 16\mathrm{T}_{j=4}^{n+1} - 3\mathrm{T}_{j=5}^{n+1}}{25} \tag{2.50}$$

using a 4^{th} order forward FD discretization of equation 2.49.
The density is then prescribed at the wall by solving the continuity equation wich reduces to the following equation due to the non-slip condition ($u\,|_{y=0} = v\,|_{y=0} = w\,|_{y=0} = 0$):

$$\frac{\partial \rho}{\partial t} = -\frac{\partial \rho v}{\partial y}\,|_{y=0} \tag{2.51}$$

where the wall normal derivative is also approximated by a 4^{th} order forward FD formulation leading to :

$$\rho_{j=1}^{n+1} = \rho_{j=1}^{n} - \frac{\delta t}{\delta y}(4\rho_{j=2}^{n+1} v_{j=2}^{n+1} - 3\rho_{j=3}^{n+1} v_{j=3}^{n+1} + \frac{4}{3}\rho_{j=4}^{n+1} v_{j=4}^{n+1} - \frac{1}{4}\rho_{j=5}^{n+1} v_{j=5}^{n+1}) \tag{2.52}$$

2.4.2 Inflow and outflow conditions

We give hereafter details about the inflow and outflow boundary conditions.

As the Strang directional splitting is used in the present numerical approach, the Navier-Stokes equations are solved successively in each direction, that is, a succession of 1D equation is solved. The inflow and outflow conditions are prescribed as time dependent boundary conditions for 1D hyperbolic systems as introduced by Thompson [1987]. For example, we consider the x direction. The 1D system of equations is written in the characteristic base as a set of wave equations:

$$\frac{\partial V_i}{\partial t} + \lambda_i \frac{\partial V_i}{\partial x} = 0 \tag{2.53}$$

where V_i is the i^{th} Riemann invariant associated with the characteristic velocity λ_i. λ_i is known to be the eigen value of the Jacobian matrix of the Euler flux in this direction.
Depending on the sign of λ_i, the characteristic wave is entering or exiting from the domain.
The value imposed at the boundary depends wether it is an inflow or outflow boundary:

- Inflow boundary:
  - Entering characteristic wave ($\lambda_i \geqslant 0$): the value of the characteristic fields is prescribed.
  - Exiting characteristic wave ($\lambda_i < 0$): the value of the characteristic field is obtained at the boundary using a second order upwind scheme to approximate the gradient of the Riemann invariant in the considered direction.
- Outflow boundary:
  - Entering characteristic wave ($\lambda_i < 0$): the value of the characteristic field is obtained by prescribing a non reflecting condition. This is obtained by canceling the velocity of the characteristic wave. The equation to be solved is therefore:

$$\frac{\partial V_i}{\partial t} = 0. \tag{2.54}$$

  - Exiting characteristic wave ($\lambda_i \geqslant 0$): the value of the characteristic field is obtained at the boundary using a second order upwind scheme to express the derivative of V_i in the considered direction.

2.5 Conclusions

In this chapter, the numerical approach used to perform SWBLI simulations has been presented. The convective fluxes are discretized using an original high order one-Step scheme based on the Lax-Wendroff approach. A MP constraint is employed as a shock capturing procedure. The viscous fluxes are approximated using a standard centred FD scheme. The Strang directional splitting is used. The validation of this approach is presented in chapter 3.

2.6 References

Z.J. Wang, Krzysztof Fidkowski, Rémi Abgrall, Francesco Bassi, Doru Caraeni, Andrew Cary, Herman Deconinck, Ralf Hartmann, Koen Hillewaert, H.T. Huynh, Norbert Kroll, Georg May, Per-Olof Persson, Bram van Leer, and Miguel Visbal. High-order cfd methods: current status and perspective. *International Journal for Numerical Methods in Fluids*, **72**(8):811–845, 2013. doi: 10.1002/fld.3767. 26

V. Daru and C. Tenaud. High order one-step monotonicity-preserving schemes for unsteady compressible flow calculations. *Journal of Computational Physics*, **193**(2):563 – 594, 2004. ISSN 0021-9991. doi: https://doi.org/10.1016/j.jcp.2003.08.023. 26, 28, 29, 30, 31

S. Pirozzoli. Numerical methods for high-speed flows. *Annual Review of Fluid Mechanics*, 43(1): 163–194, 2011. doi: 10.1146/annurev-fluid-122109-160718. URL https://doi.org/10.1146/annurev-fluid-122109-160718. 26

William H Reed and TR Hill. Triangular mesh methods for the neutron transport equation. Technical report, Los Alamos Scientific Lab., N. Mex.(USA), 1973. 26

Zhi Jian Wang. Spectral (finite) volume method for conservation laws on unstructured grids. basic formulation: Basic formulation. *Journal of computational physics*, 178(1):210–251, 2002. 26

Y. Liu, M. Vinokur, and Z. J. Wang. Spectral difference method for unstructured grids i: basic formulation. *Journal of Computational Physics*, 216(2):780–801, 2006. 26

A. Harten. High resolution schemes for hyperbolic conservation laws. *Journal of Computational Physics*, 49(3):357 – 393, 1983. ISSN 0021-9991. doi: https://doi.org/10.1016/0021-9991(83)90136-5. URL http://www.sciencedirect.com/science/article/pii/0021999183901365. 27, 28, 30

Sergei Konstantinovich Godunov. A difference method for numerical calculation of discontinuous solutions of the equations of hydrodynamics. *Matematicheskii Sbornik*, 89(3):271–306, 1959. 28

A. Suresh and H.T. Huynh. Accurate monotonicity-preserving scheme with Runge-Kutta time stepping. *Journal of Computational Physics*, 136(**1**):83–99, 1997. 28, 30

A. Harten, B. Engquist, S. Osher, and S. R. Chakravarthy. Uniformly high order accurate essentially non-oscillatory schemes, iii. In *Upwind and high-resolution schemes*, pages 218–290. Springer, 1987. 28

V. Daru and C. Tenaud. Approximations d'ordre élevé pour les écoulements compressibles avec discontinuités, 2005. 28

X.-D. Liu, S. Osher, and T. Chan. Weighted essentially non-oscillatory schemes. *Journal of computational physics*, 115(1):200–212, 1994. 28

A. Jameson, W. Schmidt, and E. Turkel. Numerical solution of the euler equations by finite volume methods using runge kutta time stepping schemes. In *14th fluid and plasma dynamics conference*, page 1259, 1981. 28

F. Ducros, V. Ferrand, F. Nicoud, C. Weber, D. Darracq, C. Gacherieu, and T. Poinsot. Large-eddy simulation of the shock/turbulence interaction. *Journal of Computational Physics*, 152(2):517–549, 1999. 28, 29

S. Pirozzoli and F. Grasso. Direct numerical simulation of impinging shock wave/turbulent boundary layer interaction at m=2.25. *Physics of Fluids*, 18(6):065113, 2006. doi: 10.1063/1.2216989. 29

S. K. Lele. Compact finite difference schemes with spectral-like resolution. *Journal of Computational Physics*, **103**(**1**):16–42, 1992. 29

E. Touber and N. D. Sandham. Large-eddy simulation of low-frequency unsteadiness in a turbulent shock-induced separation bubble. *Theoretical and computational fluid dynamics*, 23:79–107, 2009. 29

G. Aubard, X. Gloerfelt, and J.-C. Robinet. Large-Eddy Simulation of Broadband Unsteadiness in a Shock/Boundary-Layer Interaction. *AIAA Journal*, 51:2395–2409, 2013. 29

Stephan Priebe, Jonathan H Tu, Clarence W Rowley, and M Pino Martín. Low-frequency dynamics in a shock-induced separated flow. *Journal of Fluid Mechanics*, 807:441–477, 2016. 29

V. Daru and X. Gloerfelt. Aeroacoustic computations using a high-order shock-capturing scheme. *AIAA Journal*, **45**(10):2474–2486, 2007. 30

R. J. LeVeque. *Numerical Methods for Conservation Laws*. Birkhäuser, 2nd edition, 1992. 31

G. Strang. On the construction and comparison of difference schemes. *SIAM J. Numer. Anal.*, **5**: 506–517, 1968. 31

V. Daru and C. Tenaud. Numerical simulation of the viscous shock tube problem by using a high resolution monotonicity-preserving scheme. *Computers & Fluids*, **38**:664–676, 2009. 31

K.W. Thompson. Time Dependent Boundary Conditions for Hyperbolic Systems. *Journal of computational physics*, **68**(1):1–24, 1987. 36

Chapter 3

Validation of the numerical approach

Contents

3.1 Taylor Green vortex at Re=1600 40
3.2 Shock-wave laminar boundary layer interaction. 46
3.3 Conclusions 52
3.4 References 52

In this chapter, the numerical approach presented in chapter 2 is validated. As explained in chapter 2, two main difficulties in the simulation of high Reynolds number compressible flows are the accurate computation of small turbulent scales and the capture of discontinuities without spoiling the accuracy of the numerical scheme. In order to study specificly the performances of the numerical approach with respect to each one of these two specific issues, we evaluate separately the ability of the numerical schemes to compute turbulent flows with accuracy and to capture shock waves with robustness. Capabilities of the numerical method are evaluated on two canonical test-cases that have been considered in the International Workshop on High-Order CFD Method (HiOCFD workshop) Committee [2016] to compare the CFD software performances Wang et al. [2013]: namely, the three dimensional Taylor-Green vortex and the steady two dimensional shock wave laminar boundary layer interaction.

3.1 Taylor Green vortex at Re=1600

First, the well documented 3-D Taylor-Green vortex is considered at a Reynolds number of Re = 1600 Wang et al. [2013]; Brachet et al. [2006]. The Taylor-Green vortex is a simple configuration allowing to simulate a turbulent energy cascade in the framework of Isotropic Homogeneous Turbulence (IHT). This problem allows us to evaluate the ability of the numerical procedure to compute transitional solutions in decaying IHT.

A 3D periodic domain (Ω) of 2π non-dimensional side length is considered, in which a non dimensional initial flow field, which is an analytic solution of the Navier-Stokes equations, is prescribed. This initial flow field, consisting in eight planar vortices, writes:

$$\begin{aligned}
&u = sin(x)cos(y)cos(z),\\
&v = -cos(x)sin(y)cos(z),\\
&w = 0,\\
&\mathrm{P} = \frac{1}{\gamma \mathrm{M}_0} + \frac{1}{16}(cos(2x)+cos(2y))(cos(2z)+2),\\
&\mathrm{T} = 1,\\
&\rho = \frac{\gamma \mathrm{P} \mathrm{M}_0^2}{\mathrm{T}},\\
&\mathrm{E} = \frac{1}{(\gamma-1)\gamma \mathrm{M}_0^2}\mathrm{T} + \frac{1}{2}(u^2+v^2+w^2).
\end{aligned} \tag{3.1}$$

The initial field of the vorticity component in direction z is shown in figure:

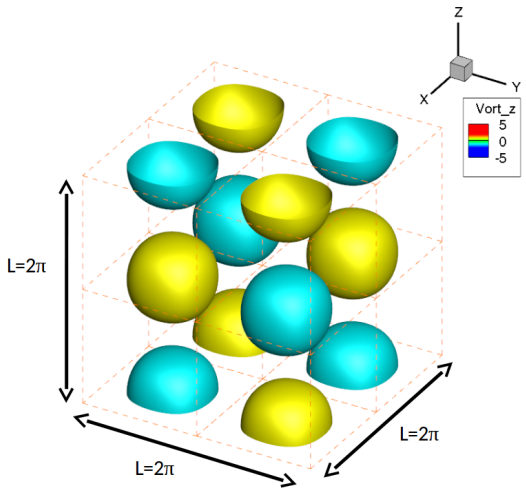

FIGURE 3.1 – Initial field of the vorticity component in direction z.

Nonlinear interactions between these initial vortices create smaller and smaller vortices until kinetic energy dissipation into heat occurs following the so called Kolmogorov energy cascade.

The flow is completely characterized by the following set of non dimensional values:

$$\begin{aligned} \mathrm{M}_0 &= \frac{\mathrm{U}_0}{c_0} = 0.1, \\ \gamma &= 1.4, \\ \mathrm{R}e_0 &= \frac{\rho_0 \mathrm{U}_0 \mathrm{L}_0}{\mu_0} = 1600, \\ \mathrm{P}r_0 &= \frac{\mu_0 \mathrm{C}p_0}{\lambda_0} = 0.71, \end{aligned} \tag{3.2}$$

where the reference variables (index 0) refer to the flow at the initial state. U_0 is the greatest value of the flow speed in the domain. c_0 is the speed of sound, given by the uniform initial temperature T_0. $\mathrm{L}_0 = 2\pi$ is the characteristic size of the domain. μ_0 and λ_0 are respectively the initial dynamic viscosity and thermal conductivity of the fluid, given by the uniform temperature T_0. As the flow is considered almost incompressible ($\mathrm{M}_0 = 0.1$), μ and λ are considered as constant, equal to unity.

Several uniform grids have been used to study grid convergence (namely, 32^3, 64^3, 128^3 and 256^3). To judge of the quality and accuracy of the solution, several integral quantities have been computed to be compared to the literature:

— The integral kinetic energy on the domain (Ω) is calculated at every time step during the simulation as follows:

$$\mathrm{E}_k = \frac{1}{|\Omega|}\int_\Omega \rho \frac{\mathbf{u}\cdot\mathbf{u}}{2} d\Omega, \tag{3.3}$$

where $|\Omega|$ is the volume of the computational domain (Ω).

— The kinetic energy dissipation at every time step is defined as:

$$\epsilon = -\frac{d\mathrm{E}_k}{dt}. \tag{3.4}$$

The kinetic energy dissipation is computed using equation (3.4) by first order derivatives of the kinetic energy. For a compressible flow and using the Stokes hypothesis, the kinetic energy dissipation can also be written as:

$$\epsilon = \frac{2\mu}{|\Omega|}\int_\Omega \mathbf{S}^d : \mathbf{S}^d d\Omega - \frac{1}{|\Omega|}\int_\Omega \mathrm{P}\nabla\cdot\mathbf{u} d\Omega, \tag{3.5}$$

where $\mathbf{S}^d$ is the deviatoric part of the strain rate tensor $\mathbf{S}$:

$$\mathbf{S} = \frac{1}{2}\left(\nabla\mathbf{u} + \nabla^{\mathrm{T}}\mathbf{u}\right). \tag{3.6}$$

— The enstrophy integral on the domain Ω is given by:

$$\varepsilon = \frac{1}{|\Omega|}\int_\Omega \rho \frac{\boldsymbol{\omega}\cdot\boldsymbol{\omega}}{2} d\Omega, \tag{3.7}$$

where $\boldsymbol{\omega} = \nabla\times\mathbf{u}$ is the vorticity vector. The vorticity components are calculated from the velocity derivatives approximated by using a 4^{th}-order Pade scheme Lele [1992].

For compressible flows, the following approximate equality relating the kinetic energy dissipation and the enstropy stands:

$$\epsilon \approx 2\frac{\mu}{\rho_0}\varepsilon. \tag{3.8}$$

The time evolution of the kinetic energy, its dissipation and the enstrophy production in the domain are pivotal quantities representative of both the energy cascade between turbulent scales and the turbulent vorticity production.

In the following, we first evaluate the ability of the unlimited OS scheme to compute acurately the turbulent cascade. We then evaluate the effect of the MP constraint on the results. Finally, the influence of the accuracy order of the diffusive fluxes is checked.

Results using the unlimited OS scheme and the 2^{nd}-order viscous fluxes approximation.

Simulations are first performed using the unlimited OSMP-7 scheme and a 2^{nd}-order spatial discretization for the diffusive terms. A constant CFL number value of 0.5 is used. The enstrophy, is computed by equation (3.7).

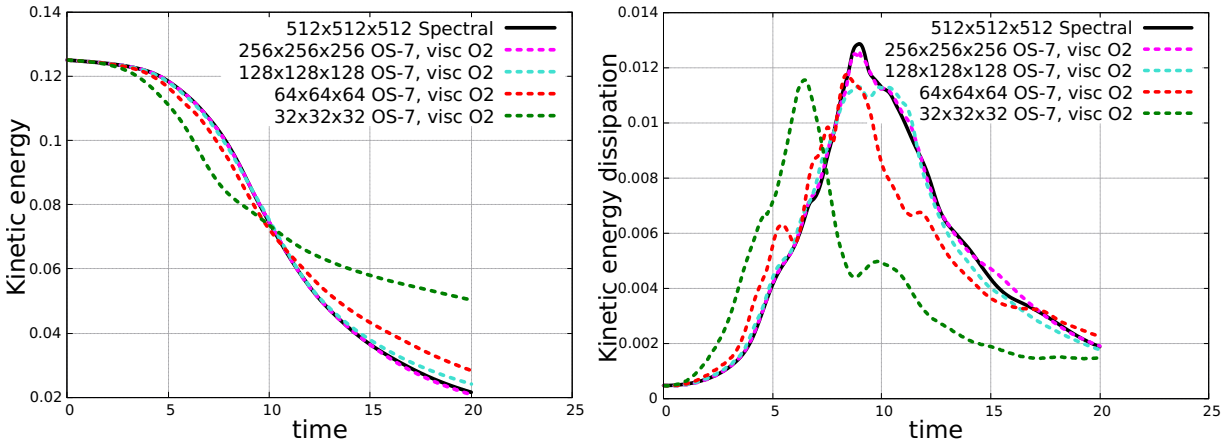

FIGURE 3.2 – History of the kinetic energy (on the left) and the kinetic energy dissipation (on the right) obtained using the OS-7 scheme on several mesh sizes (32^3, 64^3, 128^3, 256^3): present solutions are compared to the reference solution Wang et al. [2013].

Figure 3.2 shows respectively the evolution versus time of the kinetic energy (on the left) and its dissipation (on the right) for several mesh sizes (32^3, 64^3, 128^3, 256^3). Results are compared to a reference solution obtained by a de-aliazed pseudo-spectral spatial discretization coupled with a three-step Runge-Kutta scheme for the time integration, on a 512^3 grid Wang et al. [2013]. We observe the convergence of the solution toward the reference solution when the mesh is refined. The decrease of the kinetic energy in the domain can be splitted into two separate zones. In the first zone between times 0 and 9, the kinetic energy dissipation increases until it reaches a maximum value of almost 0.013 around time 9. This growth of kinetic energy dissipation is related to the transition towards turbulence creating smaller and smaller structures through the Kolmogorov energy cascade until the energy dissipation into internal energy occurs. The maximum of kinetic energy dissipation corresponds to an inflection point in the history of the kinetic energy. As far as no energy has been injected into the domain (Ω) from the initial time, this maximum dissipation is followed by a second period where the dissipation decreases as the flow relaxes.

On the one hand, It is clearly visible in figure 3.2 that simulations on meshes 32^3 and 64^3 completely fail to recover the right behavior since the histories of kinetic energy and kinetic energy dissipation computed on these two meshes largely differ from the reference solution. As meshes are not fine enough to capture small scales, the maximum of the kinetic energy dissipation, acting at small scales, occurs too early.

Simulations on meshes 128^3 and 256^3 exhibit rather good agreement with the reference solution for both the kinetic energy and the dissipation, as shown in figure 3.2. Results obtained on 256^3 grid points are almost superposed with the reference solution. Mainly, the values of the maximum of the kinetic energy dissipation and its time location obtained on 256^3 grid points are clearly in accordance with the reference and largely better computed than using 128^3 points. This highlights the importance of the mesh refinement on the accuracy of the solution.

The same simulations have secondly been performed using the 5^{th}-order One Step scheme (OS-5). In order to quantify the grid convergence, we define the L_∞ and L_2-norm errors of a quantity s with respect to the reference solution s^{ref} as:

$$Error_{L_\infty(t^k\in[0;10])} = max_{(t^k\in[0;10])} \mid s_k - s_k^{ref} \mid, \tag{3.9}$$

$$Error_{L_2(t^k\in[0;20])} = \sqrt{\frac{1}{20}\sum_k \mid s_k - s_k^{ref} \mid^2 dt}, \tag{3.10}$$

where s_k is the value of s at time $t^k = k.\delta t$ (with δt the time step and $k \in \mathbb{N}$), and s_k^{ref} is the reference value (pseudo-spectral spatial discretization on a 512^3 grid Wang et al. [2013]) of s at time t^k. The L_∞ norm is computed considering only the first half of the simulation time as it was defined in the International Workshop on High-Order CFD Method Committee [2016], while the L_2 norm is computed considering the whole simulation time. Linear interpolation is used to evaluate the value of s at the same discrete times t^k as the reference solution s^{ref}. The L_2 and L_∞ error norms on the kinetic energy dissipation are plotted in figure 3.3 versus the grid spacing $h = \frac{1}{N}$ (N is the number of grid points in each direction). Since errors are calculated with respect to an approximated solution (de-aliased pseudo-spectral solution on 512^3 grid), slopes do not correctly reflect on the order of accuracy.

On the L_2 error norms (figure 3.3-left), the higher the order of accuracy of the One-Step scheme, the lower the error level with respect to the reference solution for the same mesh size. It is then possible to obtain the same error level with a lower order of accuracy if a finer grid is used. For instance, to recover the same error level on the L_2 norm as the one obtained with the 7th-oder One-Step scheme using 32^3 grid points, we need 42^3 grid points with the 5th-order OS scheme. To know if it is relevant to use a higher order scheme, we computed the CPU time of the simulation for each case. The OS-7 scheme on 32^3 grid points needs only 90 % of the CPU time used by the OS-5 scheme on 42^3 grid points. We conclude and claim that the use of the highest order tested of the OS scheme is relevant in term of simulation time and accuracy compromise.

To compare with, the best results obtained in the HIOCFD workshop Committee [2016] using the DG-4 scheme are also plotted on the right part of figure 3.3, regarding the L_∞ error norms. Results obtained using the OS-5 and OS-7 schemes compare very favorably with one of the best results obtained by the HIOCFD workshop participants Committee [2016]; Wang et al. [2013] since L_∞ error norms of the OS schemes are more than one order of magnitude smaller than the one obtained using the DG-4 scheme. To recover the same error levels, the DG-4 scheme therefore needs far more points than the OS-7 scheme.

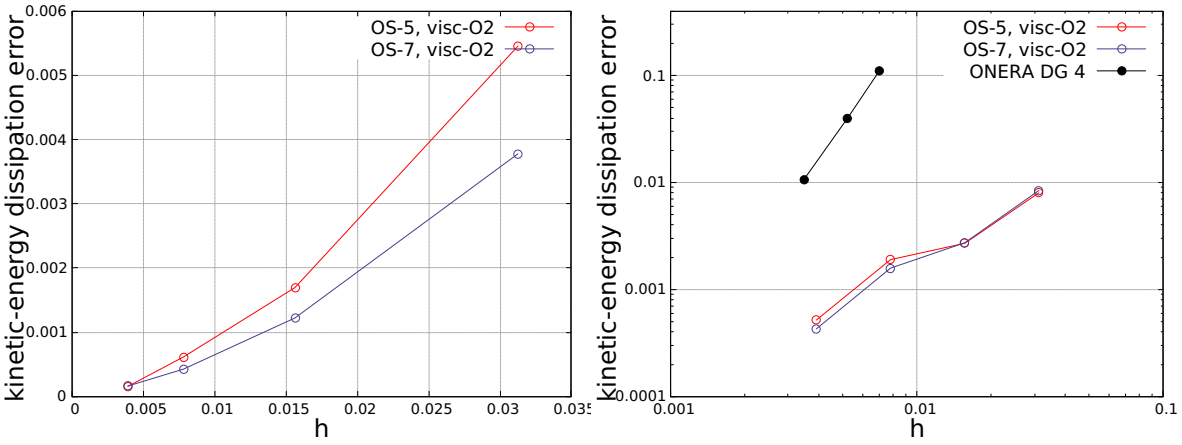

FIGURE 3.3 – On the left, L_2 error norms on the kinetic energy dissipation with respect to the reference Wang et al. [2013] versus the grid spacing (h). On the right, comparison on the L_∞ error norms between the 5th-order and 7th-order One-Step schemes and the DG-4 scheme Committee [2016].

The history of the enstrophy production is plotted in figure 3.4 on the left. As for the kinetic energy dissipation, it is splitted in two different areas. The first region corresponds to the transition towards turbulence; the enstrophy increases until it reaches a maximum value of 10.25 around time equal 9. Then, in the second region, the enstrophy decreases as the flow relaxes. Again, the finer the mesh, the closer to the reference the estimation of the enstrophy production. The time when maximum enstrophy occurs and its maximum value are not well predicted when using the 32^3 and 64^3 meshes. The prediction of the time of maximum enstrophy is correct when 256^3 grid points are used, but its value is slightly underestimated. Nevertheless, results obtained with the One-Step approach on the enstrophy production compare well with results of the HIOCFD work-

shop Committee [2016] Wang et al. [2013] as shown in figure 3.4-right, where the L_∞ entrophy dissipation error with respect to the reference solution is plotted versus the mesh size. The grid convergence is clearly visible in figure 3.4-right. We see that the higher the order of the OS scheme, the lower the error. The discrepancies between the error obtained with the DG-4 scheme and the OS scheme is not as large as for the kinetic energy dissipation error. The DG-4 scheme still needs however far more points than the OS schemes to recover the same error level on enstrophy dissipation.

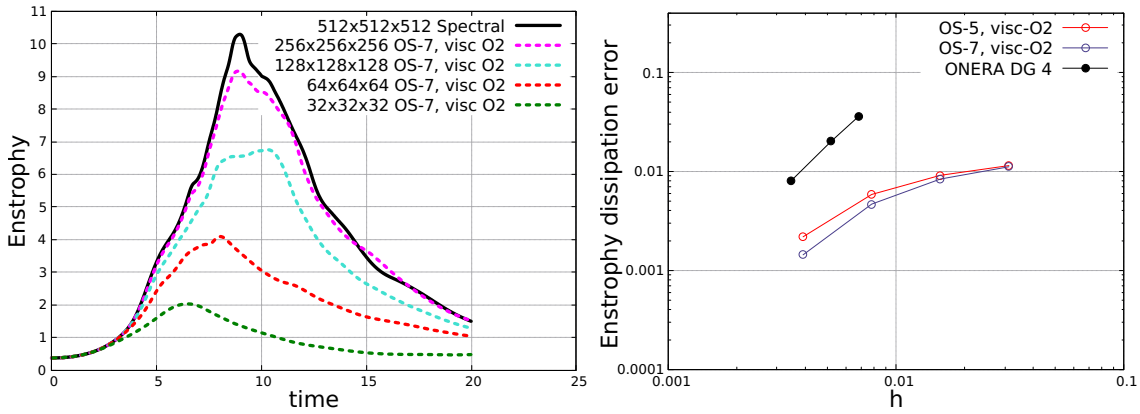

FIGURE 3.4 – On the left, history of the enstrophy obtained by using the OS-7 scheme on several mesh sizes (32^3, 64^3, 128^3, 256^3): present solutions are compared to the reference solution Wang et al. [2013]. On the right, L_∞ error norms on the kinetic energy dissipation with respect to the reference Wang et al. [2013] versus the grid spacing (h): comparison between the 5th-order and 7th-order One-Step schemes and the DG-4 scheme Committee [2016].

Effect of the MP constraint on the results.

The previous simulations have also been performed using the shock capturing procedure to check the influence of the Monotonicity-Preserving constraints on a smooth solution since this procedure, inherently diffusive, could spoil the solution obtained through an accurate scheme.

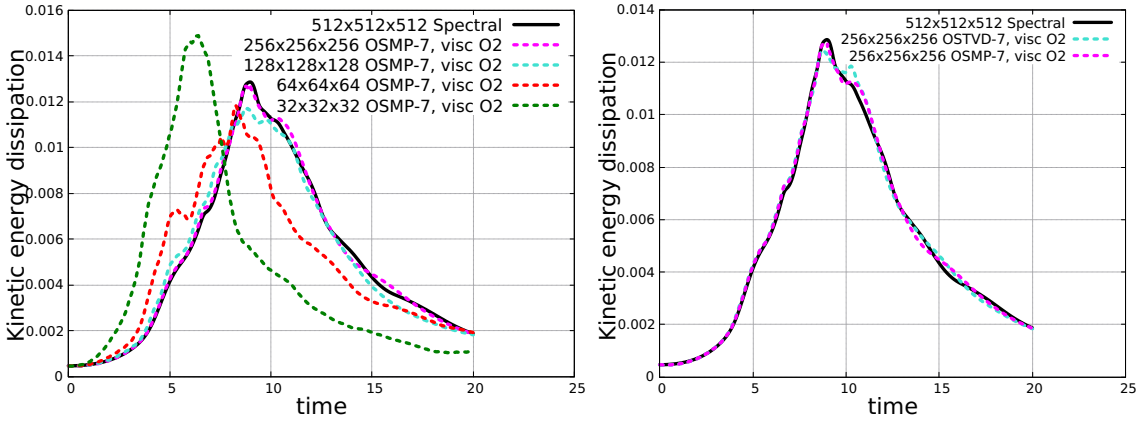

FIGURE 3.5 – History of the kinetic energy dissipation obtained with and without a schock-capturing procedure on a mesh with 256^3 grid points. On the left, OS-7 and OSMP-7 solutions are compared to the reference solution Wang et al. [2013]. On the right, the OSMP-7 and OSTVD-7 solutions are compared.

The comparison between the time evolution of the kinetic energy dissipation computed with and without the MP procedure on the 256^3 mesh is plotted in figure 3.5. Results are almost the same with very small discrepancies, demonstrating that the MP constraints have a very little influence on a smooth solution on the opposite of the TVD constraint that spoils the smooth solution (clipping of extrema of the solution Daru and Tenaud [2004, 2009]) as shown in figure 3.5-right.

The L_∞ error norms with respect to the reference, obtained with and without the MP procedure are plotted in figure 3.6 for the kinetic energy dissipation (on the left) and for the enstrophy (on the right). Similar level of errors are recovered in both cases (with and without the MP constraint). The use of the shock capturing procedure has a very weak influence on the computation of the kinetic energy dissipation and on the enstrophy in the domain. These results show that the MP constraint can efficiently be used to simulate continuous flows.

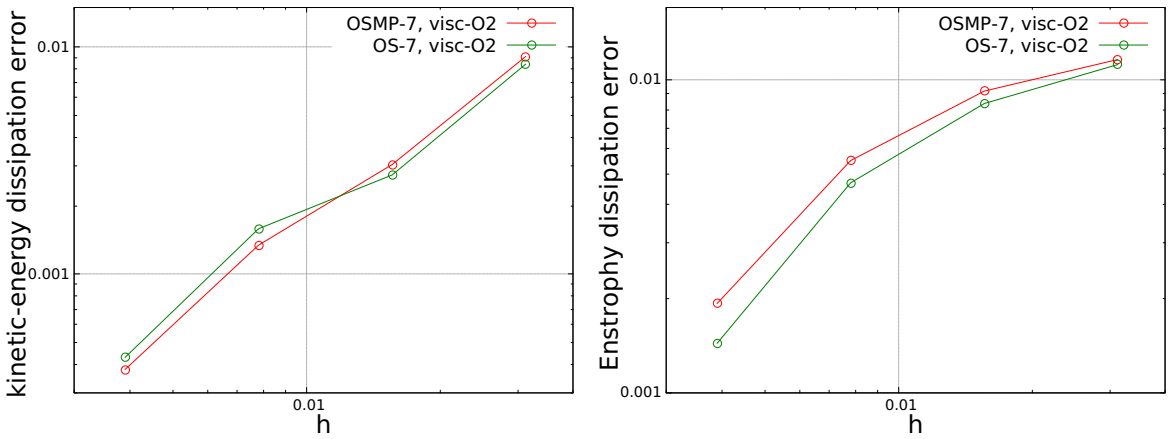

FIGURE 3.6 – L_∞ error norms with respect to the reference Wang et al. [2013] versus the grid spacing (h), on the kinetic energy dissipation (on the left) and on the enstrophy (on the right): comparison between the unlimited (OS-7) and the (OSMP-7) 7th-order One-Step schemes.

Influence of the accuracy order approximation of the diffusive fluxes.

Simulations have also been performed using a 4^{th} order centered finite difference approximation for the diffusive fluxes as far as the high order approximation might have an influence on the dissipation process occurring at small scales. This scheme is coupled with a OSMP-7 scheme for the advection approximation.

The history of the kinetic energy dissipation obtained with a 4^{th}-order centered viscous fluxes is compared with the results obtained using a 2^{nd}-order centered finite difference approximation for the diffusive fluxes in figure 3.7. The use of an order higher than second order for the diffusive fluxes have a negligeable influence on the results for such a converged simulation at relatively high Reynolds number. Very small discrepancies are only visible in the second part of the distribution where dissipation plays a key role in the turbulence relaxation, but are not relevant to justify the use of high-order viscous discretization.

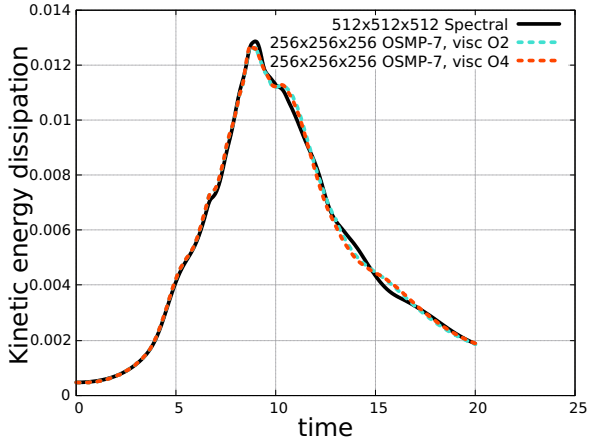

FIGURE 3.7 – History of the kinetic energy dissipation obtained using the OSMP-7 on the 256^3 mesh. Comparison between results obtained with a second 2^{nd}-order and a 4^{th}-order discretization for the diffusive fluxes. Present solutions are also compared to the reference solution Wang et al. [2013].

The L_∞ error norms on dissipation and enstrophy with respect to the reference obtained using the 2^{nd} and 4^{th}-order discretizations of the diffusive fluxes are plotted versus the mesh size in figures 3.8. The L_∞ errors are nearly the same in both cases since the errors are only computed on the first part of the distribution $t \in [0, 10]$. The use of the 4^{th}-order discretization of the viscous fluxes leads to a drastic increase of the computational time of 65 % with respect to the one of a 2^{nd}-order approximation of the viscous fluxes. These results demonstrate that using of approximations of order higher than the 2^{nd}-order for the diffusive fluxes is not relevant for such unbounded high Reynolds number configurations.

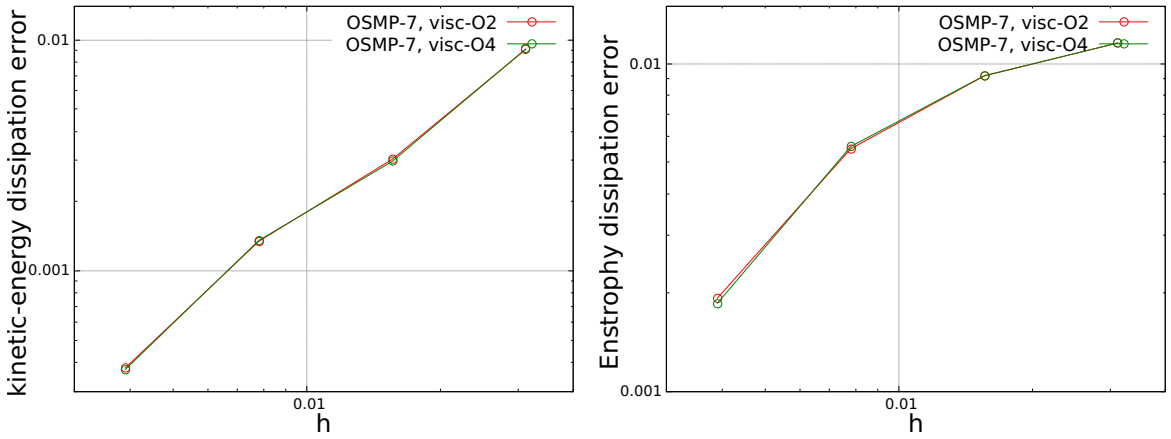

FIGURE 3.8 – L_∞ error norms with respect to the reference Wang et al. [2013] versus the grid spacing (h), on the kinetic energy dissipation (on the left) and on the enstrophy (on the right): comparison between the 2^{nd}-order and the 4^{th}-order approximations of the viscous fluxes.

3.2 Shock-wave laminar boundary layer interaction.

Secondly, the ability of the present numerical procedure to compute discontinuous solutions have been reviewed. We consider the interaction between an incident oblique shock wave impinging a laminar boundary layer developing over a flat plate. The interaction produces a separation of the flow and a subsequent recirculation bubble. This flow which here is steady has been experimentally and numerically studied in Degrez et al. [1987].

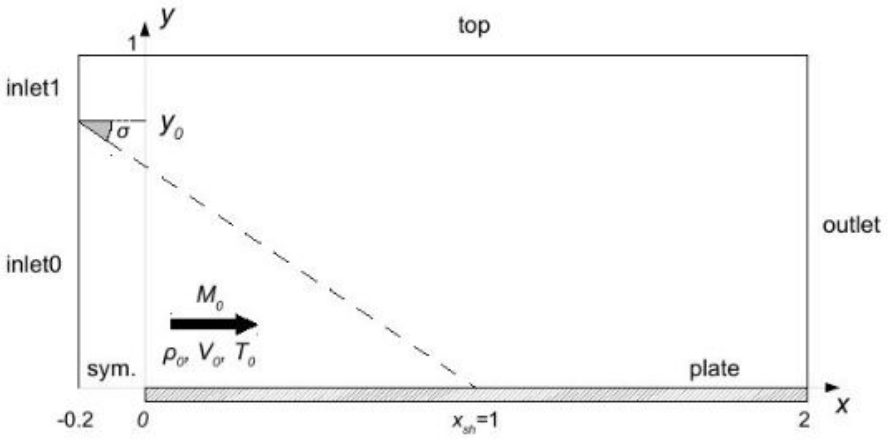

FIGURE 3.9 – Sketch of the computational domain for the shock-wave boundary layer interaction: non-dimensional dimensions and boundary conditions. The dashed line represents the inviscid incident shock-wave location Blanchard and Renac [2016].

The flow consists in a supersonic uniform flow over a flat plate leading to the development of a laminar boundary layer. Sketch of the computational domain is given in figure 3.9. A supersonic uniform flow is imposed at the inlet. At a height (y_0), the Rankine-Hugoniot relationships are prescribed, so that a shock-wave at an angle $\sigma = 30.8°$ is created in the domain that impinges the wall at $x_{sh} = 1$ when considering the non viscous solution. No-slip and adiabatic wall conditions are prescribed for $y = 0$ and $x \geqslant 0$ whereas a symmetry boundary condition is imposed in front of the leading edge of the flat plate ($x < 0$). Outlet time dependent non-reflecting boundary conditions are imposed at the top and at the outlet boundaries regions Thompson [1987].

The flow in the region *inlet 0* ($y < y_0$) is prescribed by using the similitude numbers that completely characterize the flow:

$$\begin{aligned} M_0 &= \frac{U_0}{c_0} = 2.15, \\ Re_0 &= \frac{\rho_0 U_0 x_{sh}}{\mu_0(T_0)} = 10^5, \\ Pr_0 &= \frac{\mu_0 C p_0}{\lambda_0(T_0)} = 0.71, \\ \gamma &= 1.4, \end{aligned} \tag{3.11}$$

where subscript 0 denotes values prescribed at the inlet boundary region *inlet 0*. The evolution of the dynamic viscosity μ and the thermal conductivity λ with the temperature is given by the Sutherland's law (equation 2.3).

The domain is discretized using a cartesian mesh with non uniform spacing in both x and y directions. In the longitudinal direction, the mesh is refined in the vicinity of the flat plate leading edge and in the vicinity of the shock wave impact abscissa x_{sh}. In the vertical direction, the mesh is tightened close to the wall using a hyperbolic tangent law to obtain a minimum grid spacing over the plate of $\Delta y_{min} = 10^{-4}$. An example of mesh employed for the simulation is given in figure 3.10.

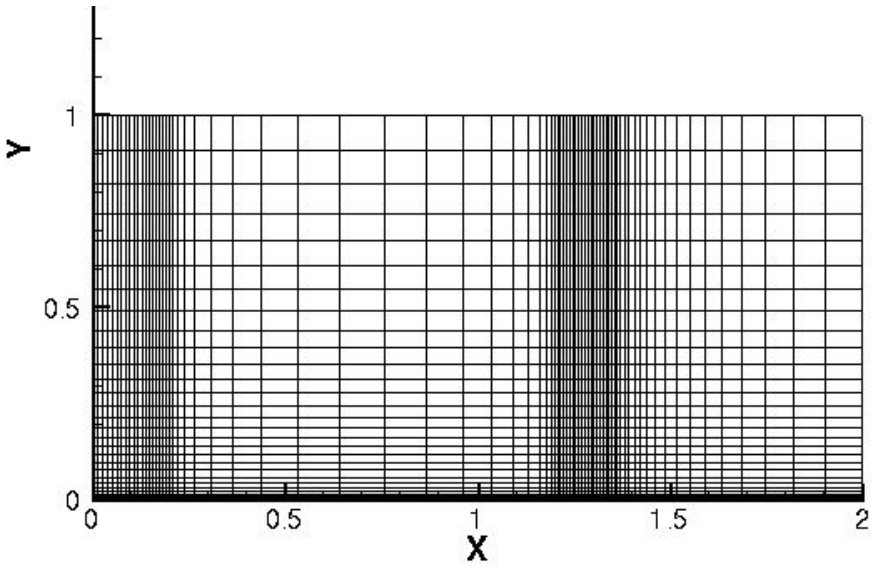

FIGURE 3.10 – Example of mesh used for the calculation of the SWBLI with a laminar boundary layer.

The organization of this steady SWLBLI corresponds to the description of the mean flow for a strong SWBLI as described in section 1.2.2 of chapter 1. As already stated in chapter 1 the separation bubble extent characterizes the interaction studied. The skin friction coefficient C_f is then an important quantity as it allows us to determine locations of the separation (where C_f becomes negative) and reattachment points (where C_f becomes positive again). The skin friction coefficient is defined as follows:

$$C_f = 2.\frac{\tau_w}{\rho_0 U_0^2}, \tag{3.12}$$

where $\tau_w = \mu_w \left.\frac{\partial u}{\partial y}\right|_{y=0}$ is the shear stress at the wall.

As previously described, due to the strong shock wave boundary layer interaction studied here, a complex system of shock waves, compression and expansion waves is formed in the supersonic part of the flow. The accuracy of the calculation in this part of the flow depends greatly on the ability of the numerical scheme to capture the discontinuities (shock waves) without spoiling the accuracy of the solution in the vicinity of the discontinuity. In the following, we evaluate the efficiency of the present shock capturing procedure to predict the pressure distribution in the supersonic part of the flow.

Grid convergence study.

Figures 3.11 and 3.12 show respectively the wall pressure and the skin friction coefficient distributions, and the pressure distribution at an altitude $y = 0.1$ for different mesh sizes obtained by using the OSMP-7 scheme coupled with a 2^{nd}-order centered scheme for the viscous fluxes. The different mesh sizes considered are 80×40, 200×100, 280×140, 360×180, and 480×240. The use of the limited version of the scheme OSMP-7 is first favored as far as a shocked flow is considered here.

For each mesh, a steady solution is obtained at the machine precision except in the viscinity of the leading edge of the flat plate.

The 80×40 mesh fails to recover the right behavior previously described since the mesh is not fine enough to capture the interaction. Regarding other meshes, the wall pressure distribution estimated by the numerical scheme is in good agreement with the theoretical considerations previously reminded: two steep rises of the wall pressure separated by a plateau like pressure. The wall pressure values before and after the interaction are the same for each mesh size used and corresponds to the non-viscous values. Discrepancies between several meshes on the wall pressure distribution are noticeable inside the region of interaction. The finer the mesh, the earlier the first pressure rise, and the later the second pressure rise. A grid convergence is however observed towards a unique solution as the mesh is refined. The value and the extent of the plateau of pressure is nearly the same for every meshes.

We also observe a grid convergence towards a unique steady solution for the skin friction coefficient distribution shown in figure 3.11-right. The same observations as for the pressure distribution hold for the locations of the separation and the reattachment points in accordance with the mesh refinements.

The pressure distribution at $y = 0.1$ is shown in figure 3.12 for different meshes. The Mach line created at the leading edge of the flat plate is clearly visible in the numerical Schlieren visualization os the flow. This Mach line is responsible for the peak of pressure observed around $x = 0.2$ in the pressure distribution at $y = 0.1$. At $y = 0.1$, which is in the non viscous region away from the separation, the pressure distribution clearly exhibits the locations of compression and expansion waves: a sharp compression corresponding to the incident shock **(C1)** followed by a continuous compression corresponding to the reflected compression waves **(C2)**. This continuous compression is followed by a sharp decrease of the pressure corresponding to the expansion waves coming from the top of the detachment bubble. This is followed by a continuous compression due to the compression waves relative to the reattachment of the boundary layer. Meshes of 80×40 and 200×100 grid points are not fine enough to correctly capture the rapid pressure evolutions, namely the shock wave and the expansion waves. For finer meshes, results converge towards a unique steady solution.

For the three quantities described (figures 3.11 and 3.12), very weak discrepancies can be exhibited between results on the 360×180 mesh and the 480×240 mesh. Therefore, we believe that the solution on the 480×240 mesh is the converged solution of this steady problem and the following analyses consider this configuration.

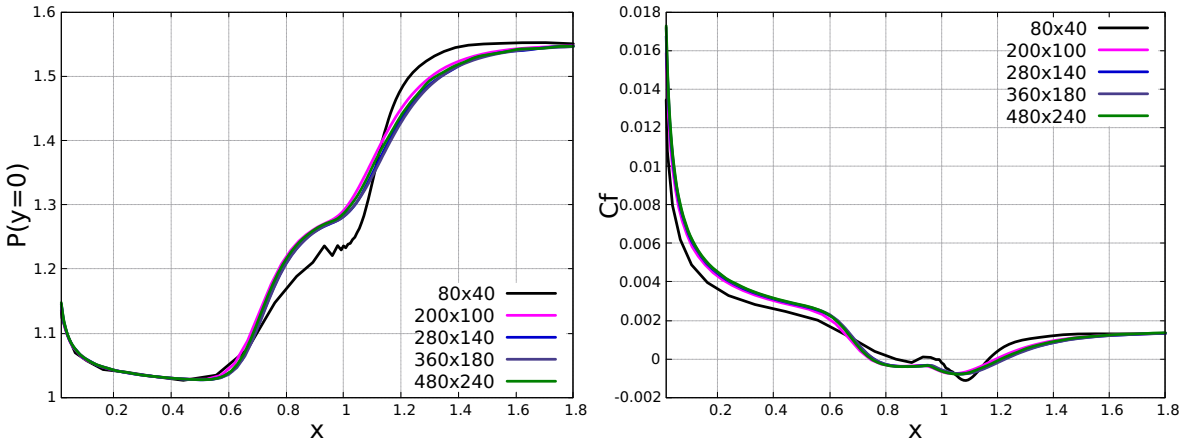

FIGURE 3.11 – Wall pressure (on the left) and skin friction coefficient (on the right) distributions obtained by using the OSMP-7 scheme coupled with a 2^{nd}-order centered scheme for the viscous fluxes, on several mesh sizes.

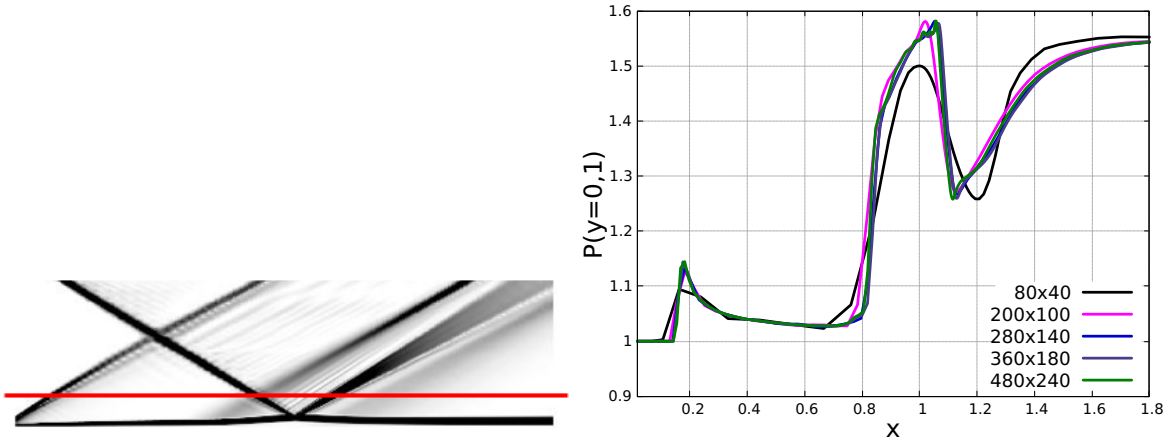

FIGURE 3.12 – On the left, numerical schlieren visualization obtained by using the OSMP-7 scheme coupled with a 2^{nd}-order centered scheme for the viscous fluxes, on 480×240 grid points: the red line indicates the height $y = 0.1$. On the right, pressure distribution at $y = 0.1$ obtained by using the OSMP-7 scheme coupled with a 2^{nd}-order centered scheme for the viscous fluxes, on several mesh sizes.

Effect of the MP constraints on the results.

The effect of using the OSMP-7 instead of the unlimited OS-7 scheme is highlighted in figures 3.13 and 3.14 in which the pressure distribution at the wall and at an altitude $y = 0.1$, obtained using the OS-7 and OSMP-7 are plotted for the 480×240 mesh. As expected, the pressure distribution at $y = 0.1$ (figure 3.13-left) highlights that the use of the OS-7 scheme leads to spurious oscillations in the vicinity of the discontinuities. These oscillations are almost cancelled when the shock capturing procedure (MP constraints) is activated, namely when the OSMP-7 scheme is used. No noticeable differences are observed for the wall pressure distribution between the results obtained using the OS-7 and the OSMP-7 schemes. Thus, the spurious pressure oscillations produced around the shock wave does not influence the wall pressure distribution. On the contrary, the skin friction calculated with the OS-7 scheme differs slightly from the skin friction coefficient calculated using the OSMP-7 scheme in the recirculation zone (figure 3.14), where oscillations are observed for the result using the unlimited scheme. It shows that the spurious oscillations created in the vicinity of the discontinuities influence the solution in the entire domain.

These results show that the MP constraints are efficient to recover a good quality of the solution without an extra cost since the simulation time when the MP constraints are used is only 2,7 % greater than for the unlimited OS scheme. This additional cost is almost negligible.

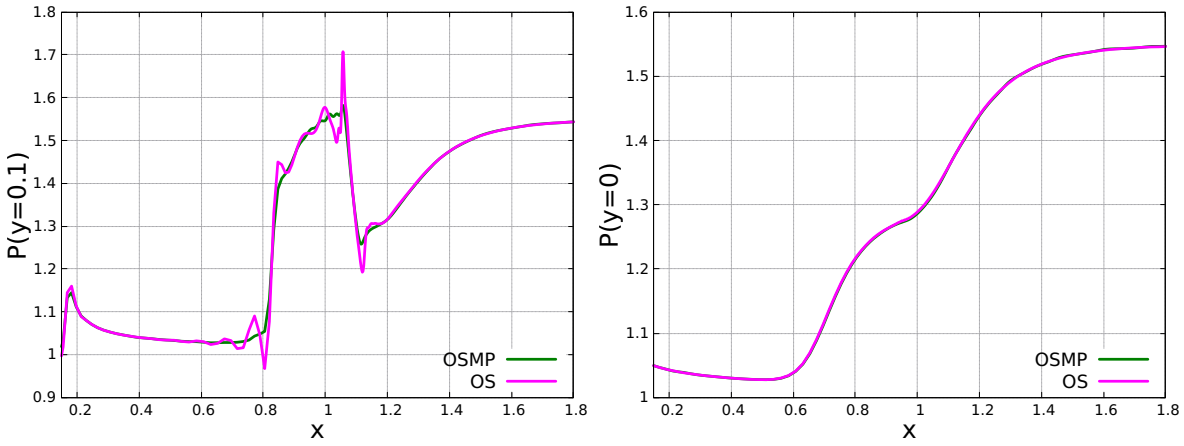

FIGURE 3.13 – Pressure distribution at $y = 0.1$ (on the left) and along the wall (on the right) for the 480×240 mesh: influence of the MP constraints.

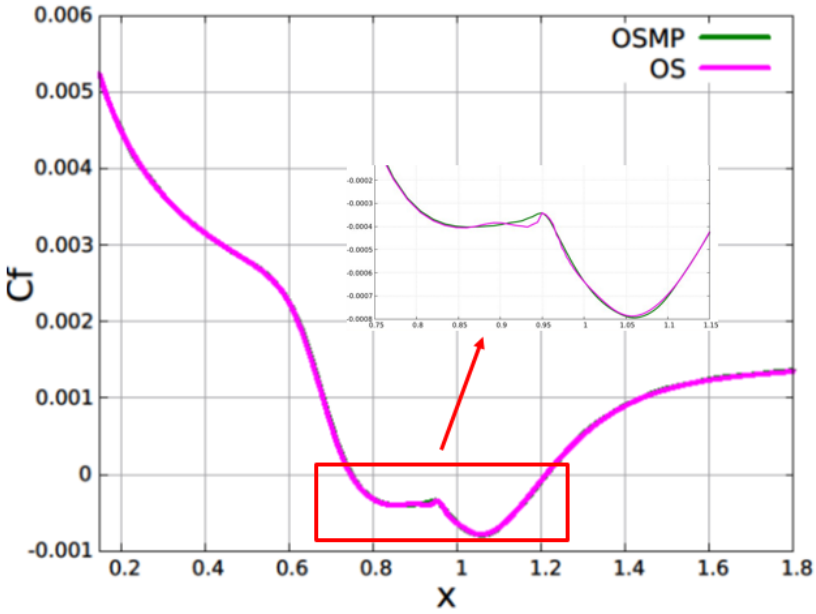

FIGURE 3.14 – Skin friction coefficient distribution along the wall for the 480×240 mesh: influence of the MP contraints.

Comparison of the present results with numerical and experimental results from the literature.

Previous results are compared with either experimental or numerical results from the literature. Experimental results come from Degrez *et al.* Degrez et al. [1987] who designed the present test case. Degrez *et al.* also provided numerical results Degrez et al. [1987]. Other high-order numerical results have also been selected to compare with as they have been obtained with two numerical scheme commonly used to simulate compressible flows: the DNS of Gross and Fasel using a 9^{th} accurate WENO method based on the Van Leer (VL) flux vector splitting Gross and Fasel, and the DNS of Blanchard and Renac performed in the framework of the HIOCFD workshop using a 6^{th} order Discontinuous Galerkin (DG) scheme Blanchard and Renac [2016].

The comparison of the wall pressure distributions is plotted in figure 3.15-left. It is noteworthy that the pressure levels before and after the interaction are the same for every results. The results using the OSMP-7 scheme match perfectly the results obtained by Blanchard and Renac Blanchard and Renac [2016], even in the interaction zone. Gross and Fasel Gross and Fasel obtained results that seem more in agreement with the experimental results. The difference must be attributed to

the inlet boundary condition that are based on a laminar boundary layer similarity solution on the opposite of uniform flow conditions prescribed for Blanchard and Renac and the present results that consider the full boundary layer development from the leading edge of the flat plate. Besides, the pressure distribution at $y = 0.1$ obtained with OSMP-7 scheme is compared with the distribution provided by Blanchard and Renac Blanchard and Renac [2016] in figure 3.15-right. No shock capturing technique is used in the DNS of Blanchard and Renac explaining the spurious oscillations in the vicinity of the discontinuities. The slopes of the pressure variations and the locations of the shock wave, the expansion waves and the reattachment recompression agree very well in both simulations.

Streamwise distributions of the skin friction coefficient are compared in figure 3.16. Experiments of Degrez *et al.* Degrez et al. [1987] only provided the measured locations of the separation and reattachment points. Results obtained using the OSMP-7 scheme is one more time in good agreement with results of Blanchard and Renac Blanchard and Renac [2016]. Results provided by Gross and Fasel Gross and Fasel agree well with the experiments. The fact that the inlet conditions used by Gross and Fasel are different from ours influence the development of the boundary layer and then the distribution of the shear stress along the plate.

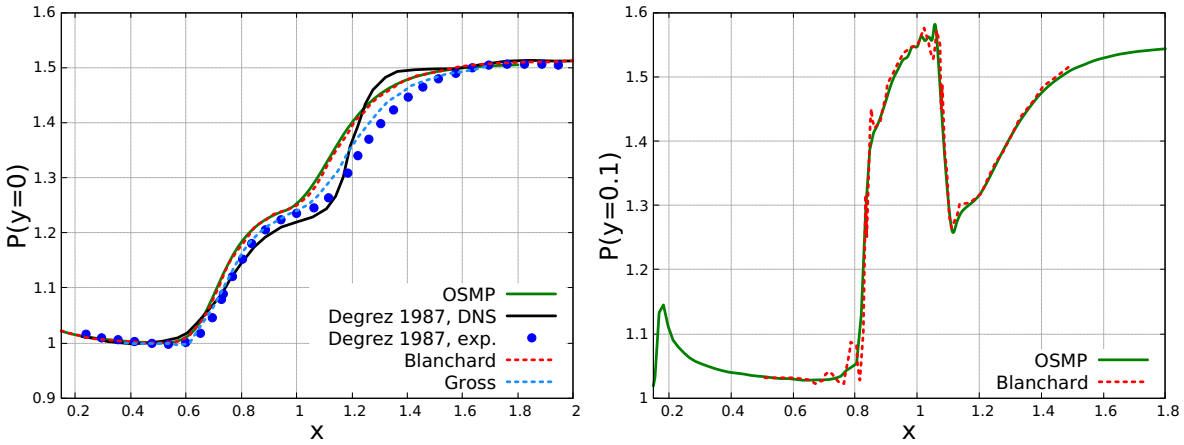

FIGURE 3.15 – Streamwise pressure distribution obtained either from experiments or by using several schemes: wall pression on the left, and pressure at $y = 0.1$ on the right.

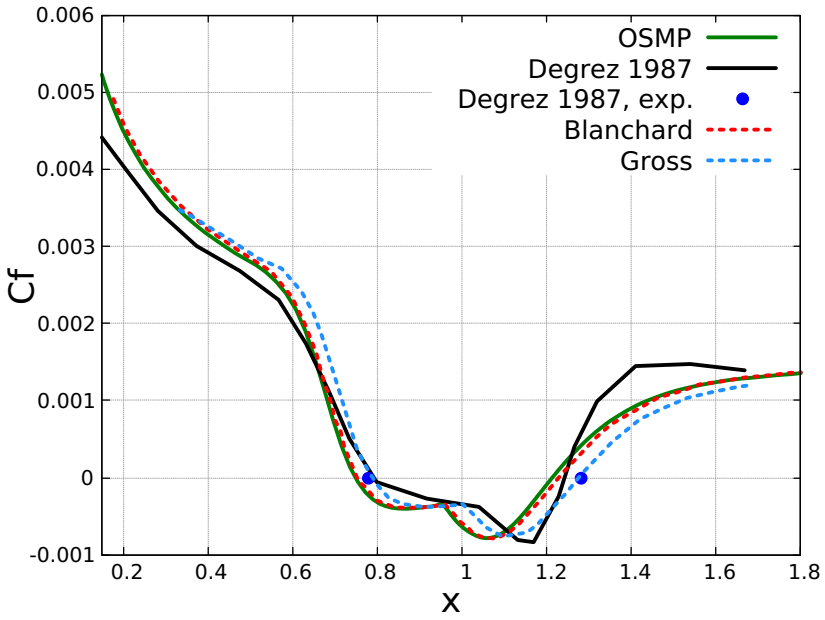

FIGURE 3.16 – Streamwise skin friction coefficient distribution obtained either from experiments or by using several numerical approaches.

Influence of the order of accuracy of the diffusive fluxes

The comparison of the results obtained using the OSMP-7 scheme coupled with a 4^{th}-order centered finite difference approximation for the diffusive fluxes are compared with those using a 2^{nd}-order centered finite difference approximation. The comparison is only performed on the skin friction coefficient distribution that is more sensitive than the pressure to the order of accuracy of the viscous fluxes discretization. No difference is noticeable between these results, even for quantities calculated close to the wall where viscosity plays a dominant role. It shows that, using this mesh, a 2^{nd}-order centered finite difference approximation for the diffusive fluxes is sufficient to accurately simulate the present flow at such high Reynolds number.

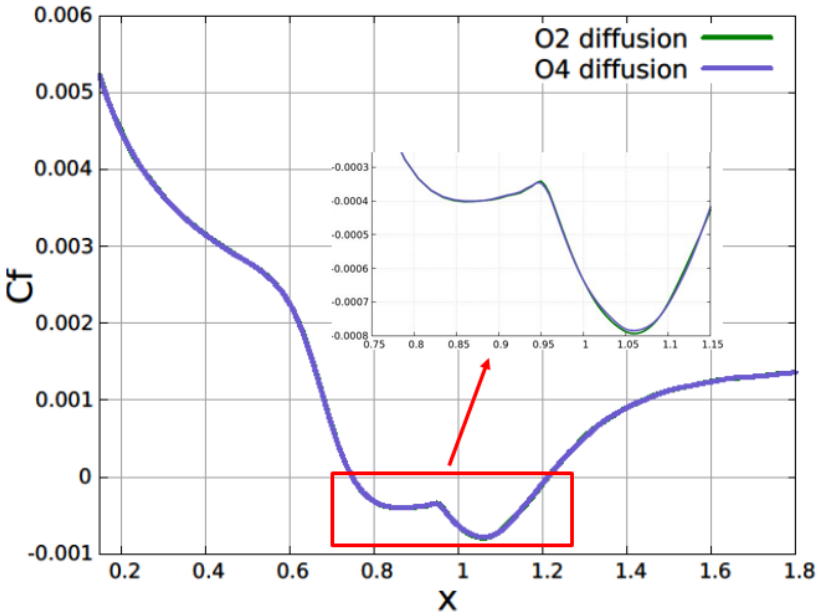

FIGURE 3.17 – Skin friction coefficient distribution for the 480 × 240 mesh obtainted by using either a 2^{nd}-order or a 4^{th}-order approximation for the diffusive fluxes.

3.3 Conclusions

The ability of the OSMP scheme to accurately compute high Reynolds compressible flows has been assessed for two well documented test-cases coming from the HiOCFD workshop: the Taylor-Green vortex problem and the laminar shock-wave boundary layer interaction. Results demonstrate the correct accuracy of the OSMP scheme to predict turbulent features and the great efficiency of the MP procedure to capture discontinuity without spoiling the solutions. Moreover, an order of accuracy higher than 2^{nd}-order for approximating the diffusive fluxes seems to have a negligible influence on the solution for such relatively high Reynolds numbers.

3.4 References

HiOCFD4 Committee. HiOCFD4 web site. [https://how4.cenaero.be], 2016. 4, 40, 43, 44

Z.J. Wang, Krzysztof Fidkowski, Rémi Abgrall, Francesco Bassi, Doru Caraeni, Andrew Cary, Herman Deconinck, Ralf Hartmann, Koen Hillewaert, H.T. Huynh, Norbert Kroll, Georg May, Per-Olof Persson, Bram van Leer, and Miguel Visbal. High-order cfd methods: current status and perspective. *International Journal for Numerical Methods in Fluids*, **72**(8):811–845, 2013. doi: 10.1002/fld.3767. 3, 4, 40, 42, 43, 44, 45, 46

M. Brachet, D I. Meiron, S. A. Orszag, B. G. Nickel, R. H. Morgf, and u. Frish. Small-scale structure of the Taylor-Green vortex. *Journal of fluid mechanics*, **130**(23):411–452, 2006. 40

S. K. Lele. Compact finite difference schemes with spectral-like resolution. *Journal of Computational Physics*, **103**(**1**):16–42, 1992. 41

V. Daru and C. Tenaud. High order one-step monotonicity-preserving schemes for unsteady compressible flow calculations. *Journal of Computational Physics*, **193**(2):563 – 594, 2004. ISSN 0021-9991. doi: https://doi.org/10.1016/j.jcp.2003.08.023. 44

V. Daru and C. Tenaud. Numerical simulation of the viscous shock tube problem by using a high resolution monotonicity-preserving scheme. *Computers & Fluids*, **38**:664–676, 2009. 44

G. Degrez, C. H. Boccadoro, and J. F. Wendt. The interaction of an oblique shock wave with a laminar boundary layer revisited. An experimental and numerical study. *Journal of fluid mechanics*, **177**(13):247–263, 1987. 46, 50, 51

R. Blanchard and F. Renac. Baseline test case summaries. Case BL2: Shock Wave / Laminar Boundary Layer Interaction. [https://how4.cenaero.be], 2016. 4, 46, 50, 51

K.W. Thompson. Time Dependent Boundary Conditions for Hyperbolic Systems. *Journal of computational physics*, **68**(1):1–24, 1987. 47

A. Gross and H. F. Fasel. *Numerical Investigation of Shock Boundary-Layer Interactions*. doi: 10.2514/6.2016-0347. URL https://arc.aiaa.org/doi/abs/10.2514/6.2016-0347. 50, 51

Chapter 4

Shock wave laminar boundary layer

Contents

4.1 Physical parameters, computational domain and mesh 56
4.2 Mean flow 57
4.3 Flow Dynamics 59
4.4 Conclusion 65
4.5 References 66

In order to better understand the mechanisms leading to the unsteadiness of the SWBLI, it has been chosen to perform a SWBLI simulation suppressing one of the two suspected mechanisms leading to the unsteadiness. By simulating the interaction between a laminar boundary layer and an incident shock wave, the suspected influence of the large scale turbulent structures within the incoming boundary layer on the SWBLI unsteadiness has been suppressed. The only remaining suspected cause of the unsteadiness would be the dynamics of the separation bubble.
In this chapter, we present a DNS of the interaction between an oblique shock wave and a laminar boundary layer. We first present the physical parameters of the flow and the mesh used for this simulation. The mean properties of the flow are then analysed. A third section focuces on the dynamics of the flow. A special attention is paid to the analysis of the low frequency dynamics of the SWLBLI.

4.1 Physical parameters, computational domain and mesh

We consider the interaction between a laminar boundary layer and an incident oblique shock wave. A sketch of the flow is shown in figure 4.1. The flow is characterized by the same non-dimensionalized numbers as the steady interaction designed by Degrez *et al.* Degrez et al. [1987] (C.f. chapter 3):

$$\begin{aligned} \mathrm{M}_\infty &= \frac{\mathrm{U}_\infty}{c_\infty} = 2.15, \\ \mathrm{Re}_\infty &= \frac{\rho_\infty \mathrm{U}_\infty x_{sh}}{\mu_\infty(\mathrm{T}_\infty)} = 10^5, \\ \mathrm{Pr}_\infty &= \frac{\mu_\infty \mathrm{C}p_\infty}{\lambda_\infty(\mathrm{T}_\infty)} = 0.71, \\ \gamma &= 1.4, \end{aligned} \tag{4.1}$$

where subscript ∞ denotes values prescribed at the inlet of the simulation domain outside of the bounday layer and x_{sh} denotes the abscissae at which the incident shock wave impinges the flat plate. The evolution of the dynamic viscosity μ and the thermal conductivity λ with the temperature is given by the Sutherland's law.
The unsteadiness of the interaction is triggered by increasing the shock wave angle until unsteadiness appears in the separation bubble. We impose a shock angle $\sigma = 33.8°$ larger than the shock angle prescribed in the experiment designed by Degrez. According to Robinet [2007], the recirculation bubble at this shock wave angle exhibits an unsteady behavior with presence of three dimensional patterns.
As for the computations of the steady 2D SWLBLI presented in the previous chapter, the OSMP 7^{th} order scheme is here employed as far as shock waves are present in the flow. Following results obtained in chapter 3, 2^{nd}-order discretization is also used for the viscous fluxes. The boundary conditions imposed are the same as for the 2D simulation of the steady SWBLI (§ 3.2) for the outlet, the top and the wall boundaries. At the inlet of the domain, the incoming laminar boundary layer is realistically approximated using a 4^{th} order polynomial approximation of the Blasius profile defined by $\frac{u(y)}{\mathrm{U}_\infty} = \frac{y}{\delta}(2 - 2(\frac{y}{\delta})^2 + (\frac{y}{\delta})^3)$ where δ is the boundary layer thickeness at the inlet of the domain. This function has the advantage to verify the boundary conditions both for the velocity at the wall and outside the boundary layer, and for the first-order derivative at $z = \delta$ and $z \longrightarrow \infty$. Periodic boundaries are imposed in the spanwise direction (z). The mesh used is refined near the wall in the y direction normal to the wall with a minimum grid spacing $\Delta y = 0.0125\delta$ (whith δ the boundary layer thickeness at the inlet of the domain). A uniform mesh is used in the longitudinal and spanwise directions (respectively x and z). The mesh size employs $400\times102\times200$ cells in ($\mathbf{x}\times\mathbf{y}\times\mathbf{z}$) and the computational domain has an extent of 4 m$\times$1 m$\times$2 m (corresponding to 250 δ $\times$ 62.5 δ $\times$ 125 δ) in these directions.

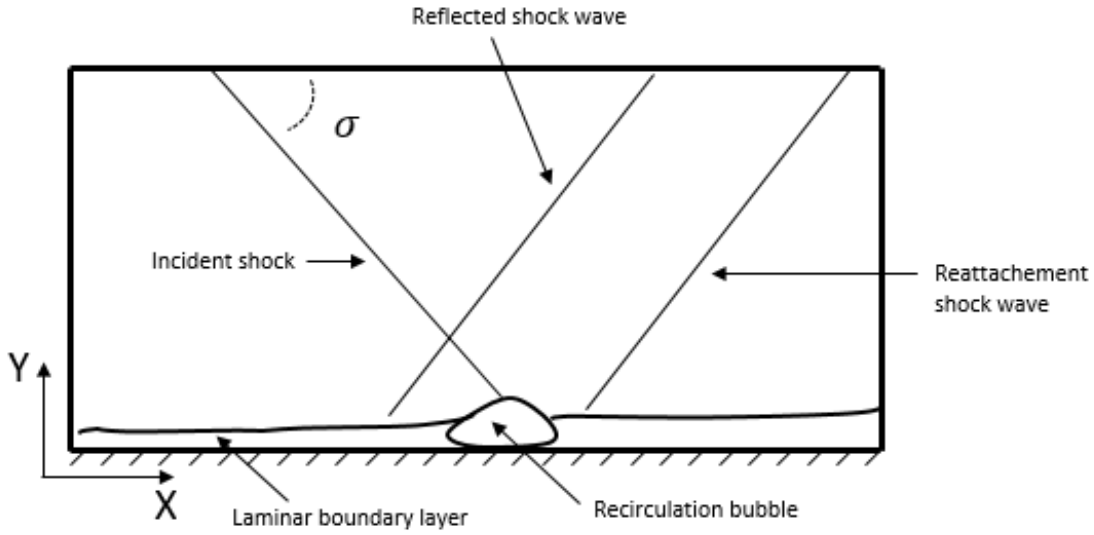

FIGURE 4.1 – Sketch of the flow.

4.2 Mean flow

A numerical schlieren visualization (2D slice located at the middle of the domain) is shown in figure 4.2. This representation is obtained by plotting the isocontours of the magnitude of the density gradient $|\nabla\rho|$. The overall organization of a SWLBLI described in chapter 1 is recovered. The strong adverse pressure gradient imposed by the incident shock wave creates a large recirculation bubble. The reflected shock wave, the reflection of the incident shock wave as expansion waves and the compression waves at the reattachement of the boundary layer are clearly visible. Moreover, a Mach line is created at the leading edge of the flat plate. The numerical Shlieren also highlights the transition to turbulence of the boundary layer downstream of the interaction.

FIGURE 4.2 – Numerical schlieren visualization obtained by plotting the isocontours of the magnitude of the density gradient $|\nabla\rho|$ (2D slice located at the middle of the domain).

The time mean velocity components averaged in the spanwise direction in the interaction zone are plotted in figure 4.3. The velocity components are scaled by the infinite velocity. The black line shows the isocontour $u = 0$. It allows to clearly identify the recicrulation bubble in which the mean longitudinal velocity is negative. The velocity magnitude in the transversal direction is very low with respect to the other velocity components. Beside, spots of positive and negative values are visible in the mean transversal velocity field within the separation bubble. It shows the 3D nature of the separated flow.

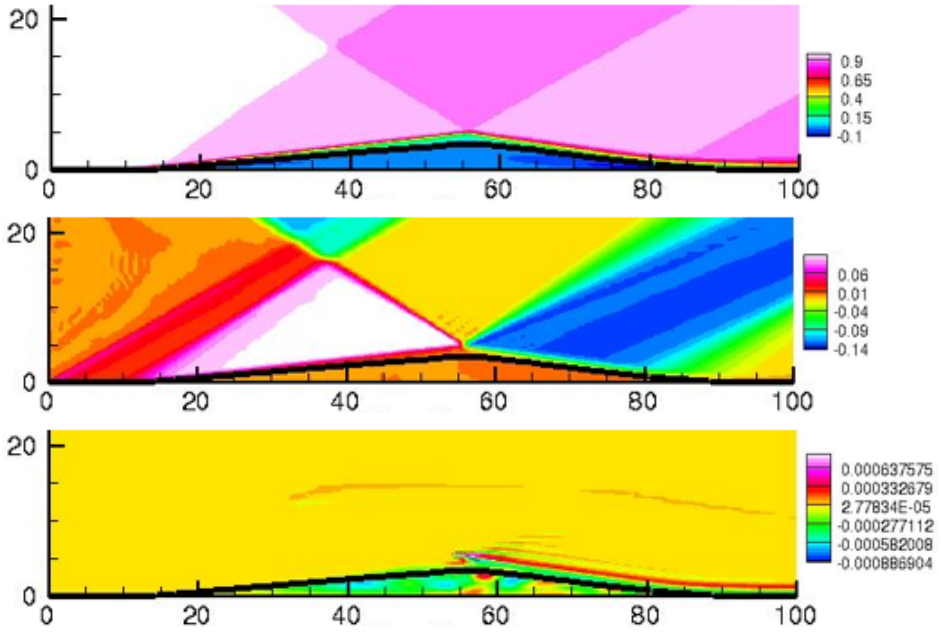

FIGURE 4.3 – Time mean velocity averaged in the spanwise direction in the interaction zone. The black line shows the isocontour $u = 0$. The velocities are scaled using U_∞ and the spatial coordinates are scaled using δ. The spatial coordinates are scaled using δ. Up: longitudinal velocity. Middle: vertical velocity. Bottom: transversal velocity.

The time mean value of the skin friction coefficient (C_f) averaged in the spanwise direction is shown in figure 4.4-bottom. The recirculation bubble corresponds to the region in which the mean skin friction coefficient is negative. The mean abscissa of the separation point $\overline{X}_s = 13.76\delta$, the mean abscissa of the reattachement point $\overline{X}_r = 89.27\delta$ and the mean separation length $\overline{L} = 75.56\delta$ are evaluated from the mean distribution of C_f.
The distribution of C_f within the recirculation bubble contains two local minima respectively located in the early part and in the latter part of the separation zone. These two minimum values of the skin friction coefficient are separated by a plateau whose maximum value is close to zero. The separation zone is almost composed of two distinct recirculation bubbles. Moreover, the absolute value of the second local minimum of the skin friction coefficient is bigger than the first one, indicating a stronger reverse flow in the latter part than in the early part of the separation zone. This is visible in figure 4.4-up where the detail of the mean longitudinal velocity in the separation zone is shown. The reverse mean longitudinal velocity is larger in the latter part of the separation than in its early part.

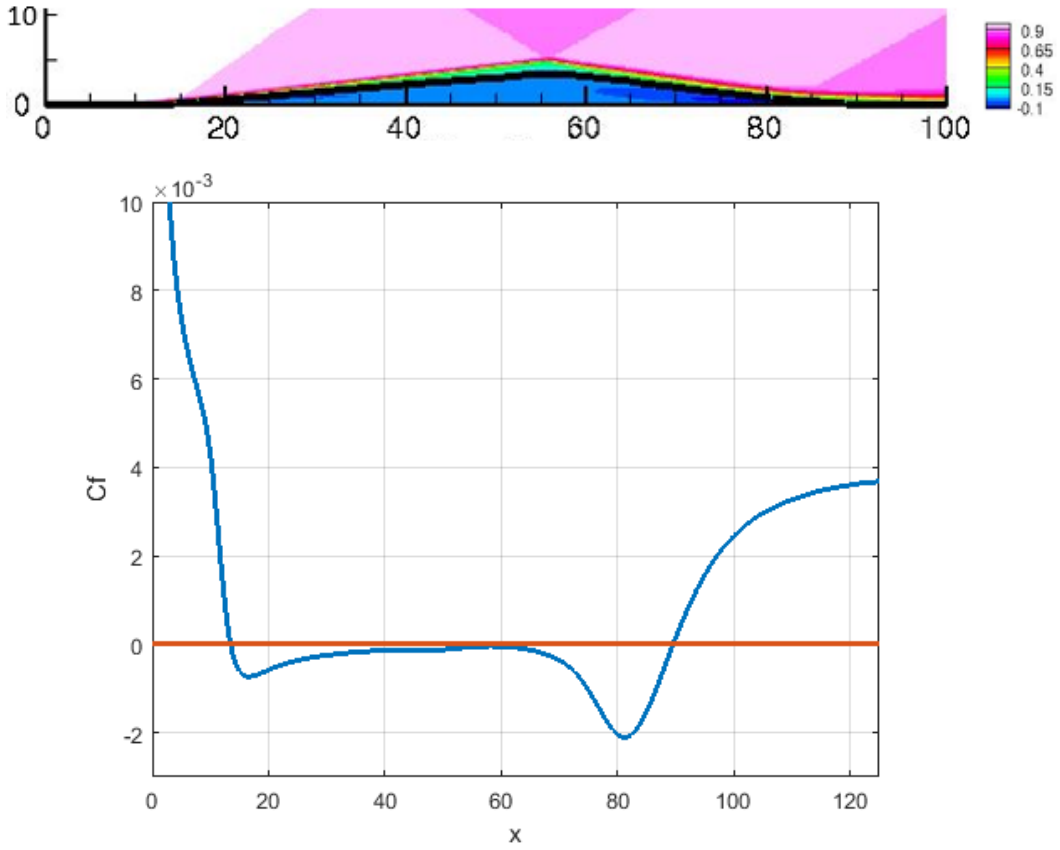

FIGURE 4.4 – Up: time mean longitudinal velocity averaged in the spanwise direction in the separated zone. The black line shows the isocontour $u = 0$. The velocitiy is scaled using U_∞ and the spatial coordinates are scaled using δ. Bottom: Distribution along the flat plate of the time mean C_f averaged in the spanwise direction.

4.3 Flow Dynamics

A snapshot of the flow is shown in figure 4.5. The discriminant criterion, introduced in Chong et al. [1998] already used by Pirozzoli and Grasso [2006] in the context of SWTBLI simulations, is used to identify the vortex structures present in the flow. The discriminant is defined as follows:

$$\Delta = \frac{27}{4}I_3^2 + (I_1^3 - \frac{9}{2}I_1I_2)I_3 + (I_2^3 - \frac{1}{4}I_1^2I_2^2) \tag{4.2}$$

where I_1, I_2 and I_3 are respectively the first, second and third invariant of $\nabla\mathbf{U}$ defined as follows:

$$\begin{aligned} I_1 &= \mathrm{tr}(\nabla\mathbf{U}) \\ I_2 &= \mathrm{tr}(\mathrm{com}(\nabla\mathbf{U})) \\ I_3 &= \det(\nabla\mathbf{U}) \end{aligned} \tag{4.3}$$

with "tr" denoting the "trace", "com" denoting the comatrix and det denoting the determinant. Vortices are identified as regions in which the local topology of the streamlines is focal as defined in Chong et al. [1998]. The discriminant is positive in these regions. In figure 4.5, the vortical structures are highlighted by plotting the isosurfaces:

$$\frac{\Delta}{(U_\infty/\theta)^6} = 10^{-12} \tag{4.4}$$

where θ is the momentum thickness of the incoming boundary layer at the inlet of the simulation domain. These isosurfaces are colored by the magnitude of the longitudinal velocity. The shock

waves are highlighted by isosurfaces of | ∇P | colored in grey.

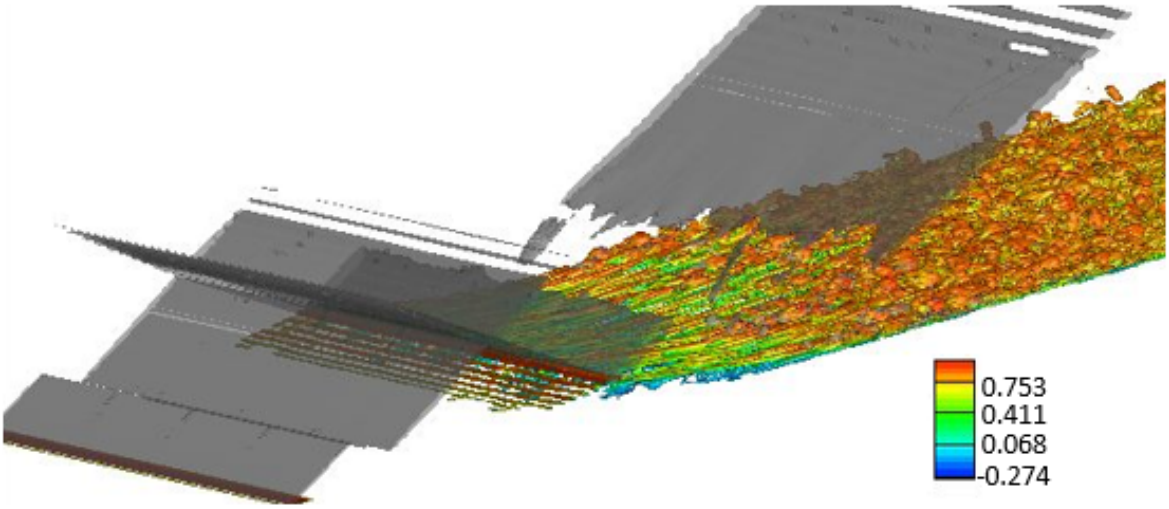

FIGURE 4.5 – Discriminent criterion ($\frac{\Delta}{(U_\infty/\theta)^6} = 10^{-12}$) colored by the magnitude of the longitudinal component of the velocity scaled by U_∞. Shock waves are highlighted by isosurfaces of | ∇P |.

A zoom around the separation bubble is shown in figure 4.6 where the isosurfaces of the discriminant criterion are reproduced. Large spanwise vortices, corresponding to the Kelvin-Helmholtz rolls that progressively develop, are clearly visible in the shear layer edging the recirculation bubble between the reflected and the incident shocks. After the incident shock impingement, the shear layer is populated by elongated structures in the streamwise direction that form hairpin like vortices characteristic of a turbulent boundary layer downstream of the reattachment. In the recirculation bubble, 3D structures are visible in the downstream part of the separation zone. Nevertheless, no coherent structures are visible in the early part of the interaction. The dynamical activity inside the recirculation bubble seems to be mainly concentrated in the second part of the separation.

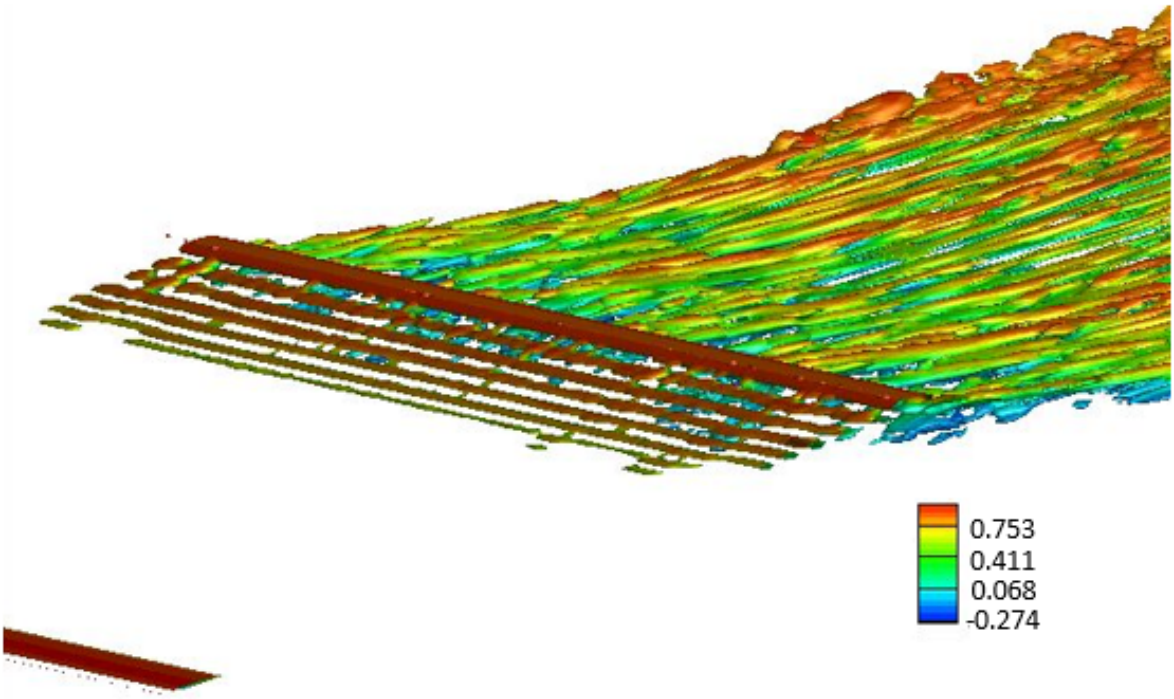

FIGURE 4.6 – Discriminent criterion ($\frac{\Delta}{(U_\infty/\theta)^6} = 10^{-12}$) colored by the magnitude of the longitudinal component of the velocity scaled by U_∞.

Several probes have been located in the flow along lines in the spanwise direction. The locations of these probes in the plane $(\mathbf{x},\mathbf{y})$ are shown in figure 4.7. Probes 1 ($x/\delta = 18.75$, $y/\delta = 0.31$) and 4 ($x/\delta = 81.25$, $y/\delta = 0.31$) are located in the recirculation bubble, respectively in the early part (first minimum of C_f, see figure 4.4-bottom) and latter part of the separation (second minimum of C_f, see figure 4.4-bottom). Probes 2 and 3 are located in the shear layer bounding the recirculation bubble. Probe 2 is located upstream of the incident shock wave impingement ($x/\delta = 50$, $y/\delta = 3.84$) whereas probe 3 is located downstream of the incident shock wave impingement ($x/\delta = 81.25$, $y/\delta = 0.93$). Finally, probe 5 have been located close to the wall just downstream of the reattachment of the boundary layer ($x/\delta = 92.5$, $y/\delta = 0.31$). For each probe location in the plane $(\mathbf{x},\mathbf{y})$, the signal of any quantity corresponds to it spanwise averaged value.

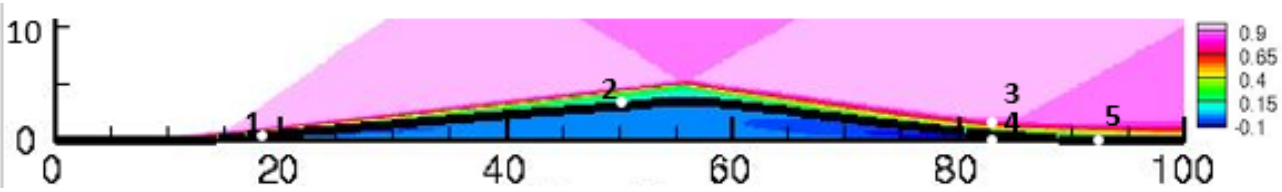

FIGURE 4.7 – Time mean longitudinal velocity field averaged in the spanwise direction. The black line shows the isocontour $u = 0$. The velocitiy is scaled using U_∞ and the spatial coordinates are scaled using δ. Position of the probes. Probe 1: $x/\delta = 18.75$, $y/\delta = 0.31$, Probe 2: $x/\delta = 50$, $y/\delta = 3.84$, Probe 3: $x/\delta = 81.25$, $y/\delta = 0.93$, Probe 4: $x/\delta = 81.25$, $y/\delta = 0.31$, Probe 5: $x/\delta = 92.5$, $y/\delta = 0.31$.

The power spectral density of the longitudinal velocity signals for the probes 1 and 4 are shown in figure 4.8 with respect to the Strouhal number based on the separation lengh $S_L = \frac{f U_\infty}{L}$. The amplitude of the spectrum at probe 1 is about 50 times smaller than for probe 4. It confirms the observation made in figure 4.6 that the dynamical activity inside the recirculation bubble is mainly concentrated in the second part of the separation. The characteristic frequencies characterizing the dynamics inside the recirculation bubble are in agreement with the characteristic frequencies of the recirculation bubble and its shear layer introduced in chapter 1. At probe 1, the spectrum is dominated by low frequencies in the range $S_L \simeq 0.01 - 0.05$ characteristic of the breathing of

the recirculation bubble. A second frequency packet at $S_L \simeq 0.11 - 0.15$ corresponds to the medium frequency flapping of the shear layer. The spectrum at probe 4 is also characterized by low ($S_L \simeq 0.01 - 0.05$) and medium frequencies $S_L \simeq 0.15$. Moreover, higher frequencies $S_L \simeq 0.5 - 0.6$, characteristic of the vortex shedding from the shear layer are present in the spectrum at probe 4.

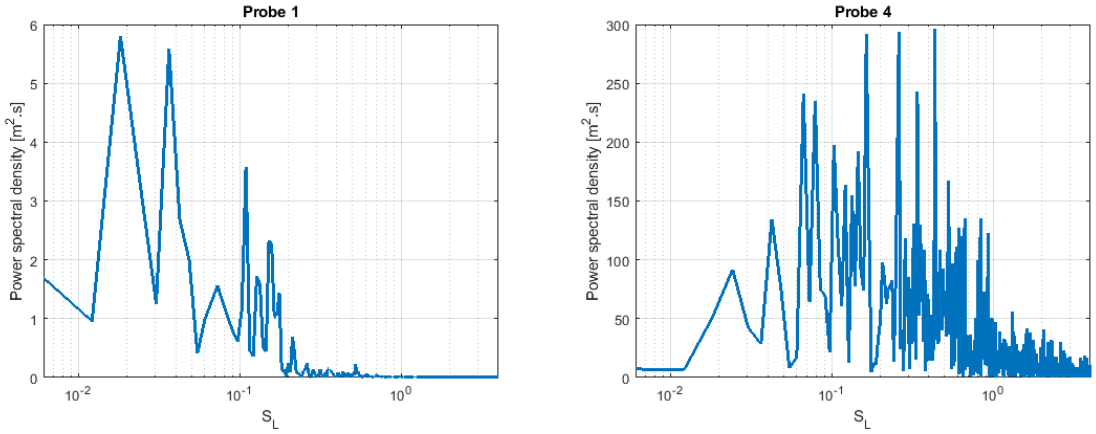

FIGURE 4.8 – Premultiplied power spectral density of the longitudinal velocity component. Left: probe 1. Right: probe 4.

The power spectral density of the longitudinal velocity signals for the probes 2 and 3 are shown in figure 4.9 with respect to the Strouhal number based on the separation lengh $S_L = \frac{f U_\infty}{\bar{L}}$. It allows to compare the characteristic frequencies of the shear layer before and after the incident shock wave impingement. The spectrum at probe 2 (before the incident shock wave) shows an activity of the shear layer at low frequencies ($S_L \simeq 0.01 - 0.03$) characteristic of the breathing of the separation bubble and medium frequencies ($S_L \simeq 0.15$) characteristic of the medium frequency flapping. The frequencies characterizing the vortex shedding from the shear layer ($S_L \simeq 0.5 - 0.6$) seems to be present in the spectrum but at a much lower amplitude. At probe 3, the amplitude of the spectrum are much larger than at probe 2. It shows that the dynamics of the shear layer is much more intense in the latter part of the separation zone. The characteristic frequencies of the low and medium frequency flapping of the shear layer are present in the spectrum. Moreover, higher frequencies around $St_L \simeq 3$ characterizing the vortex shedding are present in the spectrum with high amplitude. The same characteristic frequency ($St \simeq 3$) has also been recorded for the Kelvin-Helmholtz instabilities in a large separation at a blunt flat plate leading edge Debesse et al. [2016].

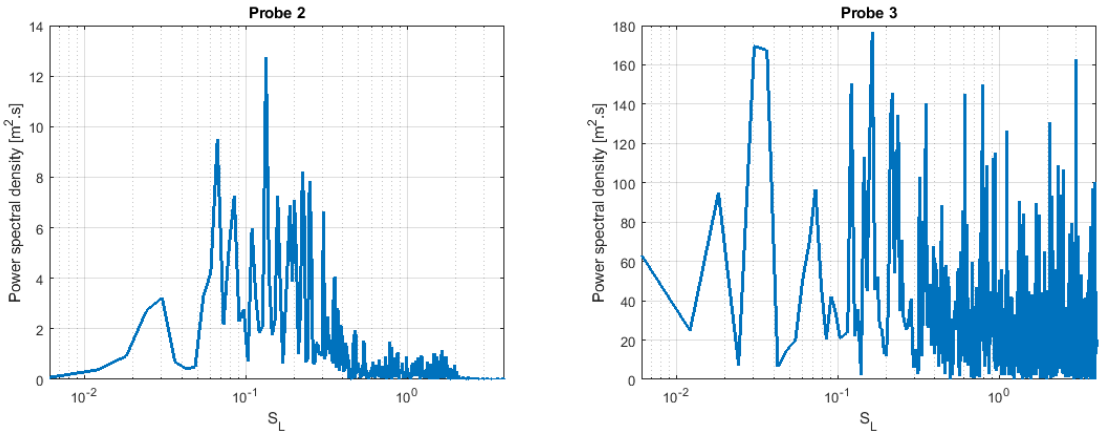

FIGURE 4.9 – Premultiplied power spectral density of the longitudinal velocity component. Left: probe 2. Right: probe 3.

The power spectral density of the longitudinal velocity signal for probe 5 is shown in figure

4.10 with respect to the Strouhal number based on the separation lengh $S_L = \frac{f U_\infty}{\bar{L}}$. The dynamics is characterized by almost the sames frequency ranges than at probe 3 with an increased intensity.

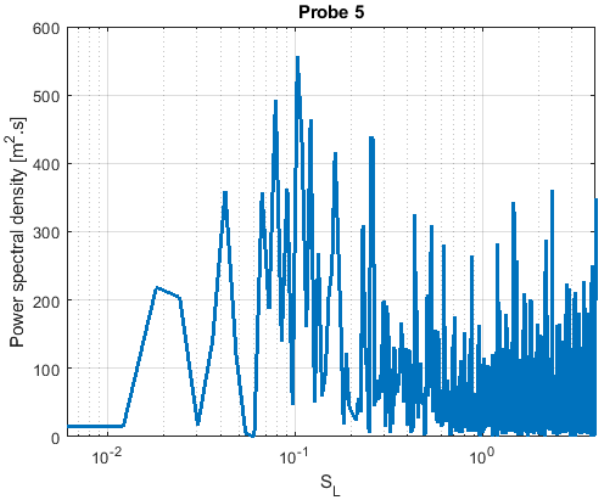

FIGURE 4.10 – Premultiplied power spectral density of the longitudinal velocity component at probe 5.

The study of the spectra of the longitudinal velocity at probes located in the interaction zone shows that the low frequency range characteristic of the SWBLI unsteadiness ($S_L \simeq 0.03 - 0.04$) is present in all the interaction zone. Moreover, the velocity fluctuations in the shear layer are characteristic from the flapping. Besides, the dynamics is much more intense in the latter part of the separation zone with the apparition of higher frequencies characteristic of the vortex shedding.
The distribution of the skin friction coefficient averaged in the spanwise direction at constant time interval ($\Delta t \simeq 10 \frac{L}{U_\infty}$) is plotted in figure 4.10. The value of C_f recovers a steady distribution in the first part of the separation zone in contrast with the second part of the separation zone where significant fluctuations of C_f are evidenced. It confirms that most of the dynamic activity of the recirculation bubble is located in its latter part. The recirculation zone seems to be divided in two distinct recirculation bubble, the first being almost stationnary and the second being submitted to fluctuations of its size.

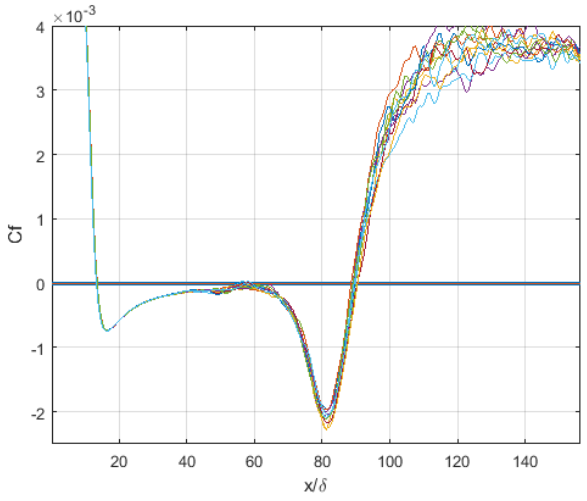

FIGURE 4.11 – Skin friction coefficient (C_f) averaged in the spanwise direction at different times.

Regarding the separation and the reattachment points, we show the history of the mean value in the spanwise direction of the abscissa along the plate in figure 4.12. These abscissa are computed regarding the skin friction value (null or changing sign for two consecutive mesh points in

the streamwise direction). We clearly see that, after a transient period where the location moves rapidly upstream, the separation point remains at a fixed position along the flat plate (figure 4.12-left). The history of the location along the flat plate of the foot of the reflected shock wave is plotted in figure 4.13. The foot of the shock wave is identified at each time of acquisition as the abscissa where the wall pressure becomes 20% bigger than P_∞. The reflected shock wave location along the flat plate remains constant versus time. Consequently, the SWBLI unsteadiness, characterized among other by the oscillations of the reflected shock wave and the separation point is not observed in our DNS of a SWLBLI. Nevertheless, as already shown in figure 4.11, we see that the reattachment point is submitted to an oscillatory motion (figure 4.12-right).

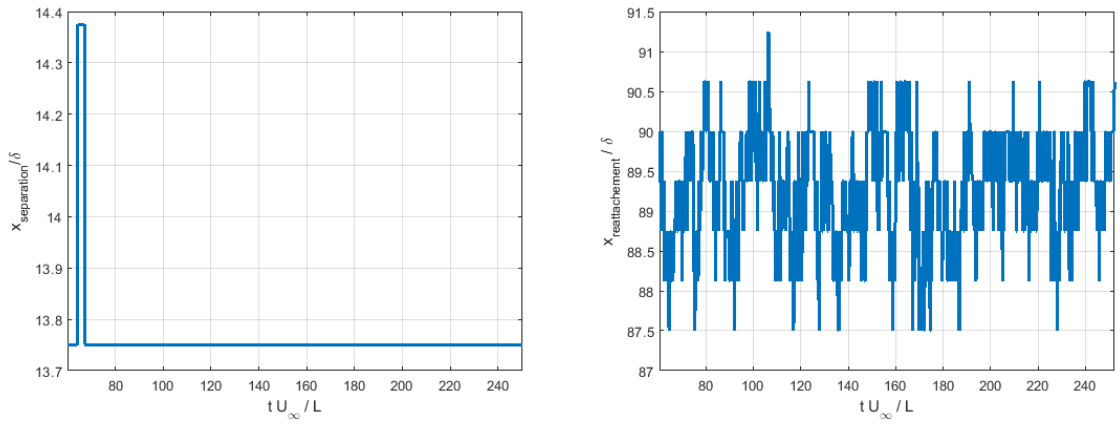

FIGURE 4.12 – History of the mean location in the spanwise direction of the abscissa along the flat plate of the separation point, on the left, and the reattachment point, on the right.

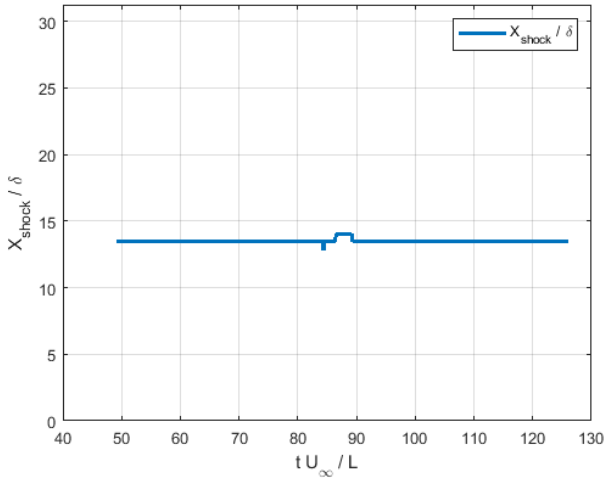

FIGURE 4.13 – History of the mean location in the spanwise direction of the abscissa along the flat plate of the reflected shock foot.

To find out the characteristic frequencies at which the reattachment point moves, we computed its power spectral density shown in figure 4.14. A first low frequency peak is visible at a Strouhal number $S_L = \frac{f_1 L}{U_e} \simeq 0.04$ characteristic of the breathing of the separation bubble. We observe a second peak at a Strouhal of $S_L = \frac{f_2 L}{U_e} \simeq 0.145$ characteristic of the flapping of the shear layer. Further peaks around $S_L = \frac{f_3 L}{U_e} \simeq 0.6$ appear, that can be related to the shedding mode of this shear layer. The power spectrum of the location of the reattachment point clearly exhibits the generally admitted values of a separated boundary layer dynamics. Even if the dynamics of the separation bubble is well recovered, no unsteadiness of the whole SWBLI system is recorded and only the motion of

the reattachment shock is observed. Obviously, this shock motion is linked to the reattachment movement.

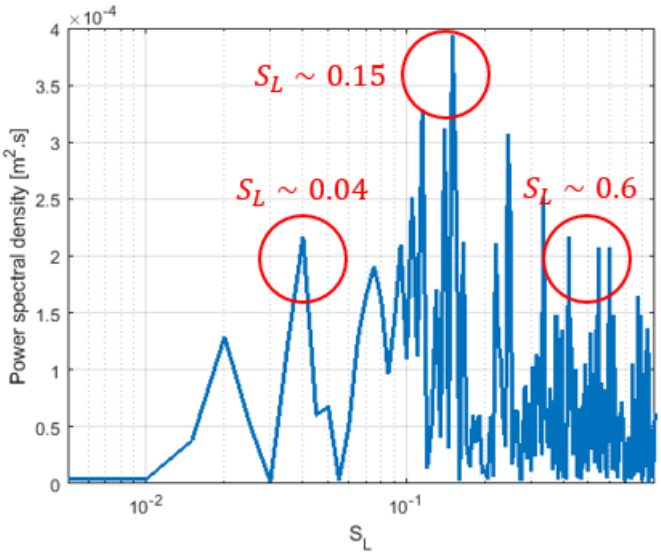

FIGURE 4.14 – Premultiplied power spectral density of the reattachment point abscissa along the flat plate

The extent of the separation bubble L (calculated as the difference between the reattachment point abscissa and the separation point abscissa) with respect to time is shown in figure 4.15. The separation zone is submitted to successive enlargments and shrinkages. The standard deviation of L is 0.0093L. As we will see in chapter 6, this standard deviation is very low compared to the one obained for the interaction with a turbulent incoming boundary layer.

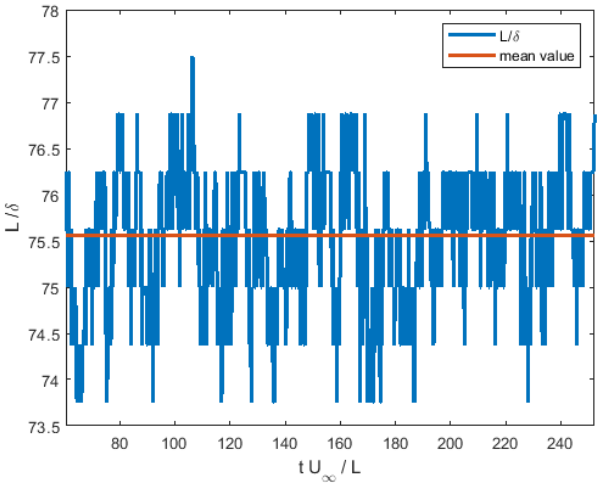

FIGURE 4.15 – Distribution of the skin friction coefficient averaged in the spanwise direction at constant time interval.

4.4 Conclusion

The three-dimensional simulation of an unsteady interaction between a laminar boundary layer and an oblique incident shock wave have here been performed. The time mean value of the skin friction coefficient averaged in the spanwise direction allowed us to identify two zones of intense reverse fow, respectively in the early part and in the latter part of the separation, separated by a plateau of almost null skin friction. The analysis of the dynamics in the recirculation bubble

and in the shear layer has shown that the dynamical activity in the second part of the separation is much more intense than in the early part. Moreover, characteristic frequencies of the instabilities of the recirculation bubble have been observed. The first part of the separation is mainly submitted to the frequencies characterizing the low frequency breathing of the recirculation bubble and the medium frequency flapping of the shear layer. The second part, submitted to fluctuations of higher intensity, is also submitted to the low frequency breathing of the recirculation bubble and the medium frequency flapping of the shear layer in addition to higher frequencies characteristic of the vortex shedding from the shear layer.
The analyses of the locations of the foot of the reflected shock wave, the separation point and the reattachement point with respect to time have shown that the reflected shock wave and the detachment of the boundary layer recover a steady location while the reattachment location is sensitive to the instabilities of the recirculation bubble. Consequently, the unsteadiness of the whole SWBLI system have not been recovered for this interaction with a laminar boundary layer though the characteristic frequencies of the separation bubble have been recorded. This points out the importance of the turbulent structures in the incoming boundary layer to trigger the unsteadiness of the separation location and subsequently, the unsteadiness of the whole SWBLI system.

4.5 References

G. Degrez, C. H. Boccadoro, and J. F. Wendt. The interaction of an oblique shock wave with a laminar boundary layer revisited. An experimental and numerical study. *Journal of fluid mechanics*, **177**(13):247–263, 1987. 56

J.-C. Robinet. Bifurcations in shock-wave/laminar-boundarylayer interaction: global instability approach. *Journal of Fluid Mechanics*, **579**:85–112, 2007. 56

Min S Chong, Julio Soria, AE Perry, J Chacin, BJ Cantwell, and Y Na. Turbulence structures of wall-bounded shear flows found using dns data. *Journal of Fluid Mechanics*, 357:225–247, 1998. 59

S. Pirozzoli and F. Grasso. Direct numerical simulation of impinging shock wave/turbulent boundary layer interaction at m=2.25. *Physics of Fluids*, 18(6):065113, 2006. doi: 10.1063/1.2216989. 59

Ph. Debesse, L. Pastur, F. Lusseyran, Y. Fraigneau, C. Tenaud, C. Bonamy, A. V. G. Gavalieri, and P. Jordan. A comparison of data reduction techniques for the aeroacoustics analysis of flow over a blunt flat plate. *Theoretical and Computational Fluid Dynamics*, **30**:253–274, 2016. 62

Chapter 5

Initiating a turbulent compressible boundary layer

Contents

5.1 Turbulent inflow boundary conditions 68
5.2 Implemented Synthetic Eddy Method 71
5.2.1 Prescription of the velocity at the inlet of the domain 71
5.2.2 Prescription of the temperature and the density fields at the inlet of the domain 75
5.3 Simulation of a turbulent compressible boundary layer over a flat plate 76
5.3.1 Numerical results 76
5.4 Conclusion 81
5.5 References 81

In this work, a high order scheme (presented in chapter 2 and validated in chapter 3) is used to accurately compute turbulent compressible flows. In order to perform a realistic SWTBLI simulation, this high fidelity numerical method must be coupled to realistic boundary conditions. In particular, the inlet turbulent boundary condition is of critical importance as it affects the realism of the turbulent boundary layer and consequently the realism of the SWTBLI being simulated. The simulation of the SWTBLI requires an accurate simulation of the compressible turbulent boundary layer. A naive approach could be the use of a sufficiently long simulation domain in the streamwise direction that would allow the natural transition of a laminar boundary layer until it reaches a fully-developed turbulent regime. The domain should be long enough so that the different stages of the boundary layer natural transition could be simulated inside the domain. In the DNS of a zero-pressure gradient boundary layer developing on a flat plate, these stages include [Cousteix [1989]]:

— the receptivity stage in which the environmental disturbances are transformed into small perturbations within the boundary layer. In the case of a DNS, these environmental disturbances reduce to numerical disturbance at the machine precision.

— the primary mode growth in which the initial disturbances grow (or decay) in a manner described by linear stability theory leading to the presence of the so called two dimensional Tollmien and Schlichting waves [Schlichting and Gersten [2016]] in the flow.

— the secondary destabilization of the primary mode leads to the three dimentionalization of the Tollmien and Schlichting waves untill hairpinlike vortices appears in the boundary layer.

— the apparition of turbulent spots in the boundary layer due to the strong perturbations induced in the flow by the hairpinlike vortices. These turbulent spots then groth and finally contaminate the rest of the boundary layer that becomes fully turbulent.

Therefore, the simulation of the natural transition to turbulence would be of prohibitive cost as it implies the use of very long domain of simulation to reach a fully-developed turbulent boundary layer. For example, in Comte et al. [1996], the LES of the transition to turbulence of an incompressible boundary layer has been undertaken. 600 boundary layer thickenesses were necessary to reach a of fully turbulent state.
In order to lower the numerical cost associated to the simulation of turbulent boundary layers, turbulent inlet boundary conditions have been developed. Some methods consist in accelerating the destabilization of a laminar boundary layer imposed at the inlet of the domain. Other methods consist in feeding the inlet of the domain with instationnary boundary conditions representative of the turbulent boundary layers. Reviews on this subject can be found in Dhamankar et al. [2015]; Tabor and Baba-Ahmadi [2010]; Sagaut et al. [2006].
In this chapter, we first present different turbulent inlet boundary conditions available in the litterature, emphasizing on they advantages and drawbacks with respect to the context of SWTBLI simulation. As a lot of different methods are available in the litterature, this presentation is not exhaustive highlighting the major approaches. We then present the SEM that have been implemented in the code CHORUS. Finally, we present the numerical results obtained for the simulation of a turbulent compressible boundary layer.

5.1 Turbulent inflow boundary conditions

Some methods impose a laminar boundary layer at the inlet of the simulation domain and force the transition to turbulence. This kind of method have been use for the simulation of compressible turbulent boundary layers. for example in Mullenix et al. [2013], a steady counterflow actuator with properties based on a dielectric Dielectric Barrier Discharge (DBD) is employed to trip an incoming laminar boundary layer. About 45δ (where δ is the boundary layer thickeness at the inlet of the domain) are necessary to recover satisfactory values of the skin friction coefficient. Other technics rely on adding perturbations in the flow. For example, in Aubard et al. [2013], a laminar boundary-layer velocity profile, deformed near the wall to exhibit an inflection point,

was submitted to perturbations so that inflectional Kelvin–Helmholtz-type instabilities trigger the transition to turbulence. A long adaptation distance of 100δ was necessary to recover a flow independant from the inlet conditions.
Other methods consist in feeding the inlet of the domain with instationnary boundary conditions representative of the turbulent boundary layers. These methods are expected to need a shorter adaptation distance. Such methods are refered to as turbulent inflow boundary conditions. In Dhamankar et al. [2015], 7 criteria have been quoted that would be satified by an ideal turbulent inflow boundary condition. The quality of a turbulent inflow condition can be evaluated with respect to these criteria recalled here after:

1. The method should be able to impose all the known information about the turbulent field for the problem under consideration. It includes first, second and third order statistical momentum, the spectral distribution of turbulent kinetic energy and the orientation of resolved length scales. In practice, no method available in the litterature reconstructs all the known information about the turbulent field. Each method imposes a sufficient amount of information at the inlet so that a realistic turbulent state is obtained in the domain after an as short as possible adaptation distance.
2. The information imposed at the inlet of the domain should be realistic enough so that no adaptation distance is needed after the inlet domain to recover a fully developed turbulent flow. As stated in the previous criterion, no method available in the litterature allows to impose a fully developed turbulent state directly at the inlet of the simulation domain. Therefore, an adaptation distance is necessary after the inlet to recover a developed turbulent field. The more the efficiency of the turbulent inflow, the shorter the adaptation distance.
3. No non physical information, such as non physical acoustic waves or non physical periodicity should be injected in the flow due to the turbulent inflow condition.
4. In order to avoid additive costs due to the storing and reading of the turbulent information imposed at the domain inlet, this information should be generated on the fly by the method.
5. In order to be easily protable, the method should not be limited to any kind of numerical scheme nor to any kind of mesh.
6. The implementation of the turbulent inflow condition should not require unreasonnable effort.
7. In order to be used in parallel computations, the turbulent inflow condition should be parallelizable.

None of the methods available in the litterature satisfies all of these criteria, that would be satisfied by an ideal method. Nevertheless, each method has advantages and drawbacks. In this context, the selection of the method to be used must be done with respect to the criteria of high importance for the specific problem to be solved.
The problem of interest in this work is the DNS of the SWTBLI in order to characterize the low frequency dynamics of the flow. In this context, the criterion 3 is of fundamental importance. Indeed, the introduction of any spurious frequencies at the inlet of the domain could influence the dynamics of the interaction zone and consequently degrade dramatically the quality of the simulation. As SWTBLIs involve low frequency phenomena, the physical time of the simulation must be large enough to capture a sufficiently high number of low frequency cycles. Consequently, any method involving the storage of the information to be injected at the inlet of the domain should be avoided. Indeed, their use in the context of SWTBLI simulation would require the storing and reading of a particularly large amout of information. The criterion 4 is then crutial and a method generating the inflow on the fly must be chosen in our case. The selected method is expected to be used to perform parallelized numerical simulation of the SWTBLI. The criterion 7 therefore imperatively been satisfied.
The library-based methods consits in a family of turbulent inflow conditions for which the unsteady field imposed at the inlet is taken from a library that is not generated by the main simulation Dhamankar et al. [2015]. This library can be preexistent, taken from a precursor simula-

tion/experiment. This approach does not satisfy the 4^{th} criterion that is crutial in our case. The library can also be generated on the fly by a concurrent simulation specificly run to sample planes that are directly imposed in the inlet plane of the main simulation. This second alternative allows to reduce the quantity of information to be stored. Neverthless the synchronisation of the two simulations adds to the complexity of the simulation program. Moreover a turbulent inflow condition must be used for generating the turbulent boundary layer in the concurrent simulation. Therefore, it appears easier to use it directly in the main simulation Dhamankar et al. [2015].
A second family of methods is the so called recycling-rescaling-based methods. This approach has first been introduced by Lund et al. [1998] for the simulation of spatially-developing boundary layers on flat plates. It consists in sampling and rescaling the velocity field from a downstream plane in order to impose the obtained field at the inlet of the main simulation. Historically, this approach was first used in a concurrent simulation to generate the inflow velocity field for a main simulation. It has then been successfully used directly in the main simulation. The main difficulty of the method is the starting of the simulation. Indeed, a judiciously perturbed flow field must be imposed at the initial time between the inlet and the downstream station in order to avoid relaminarization of the flow. The method is known to introduce a low frequency component in the flow based on the length between the inlet plane and the downstream recycling plane that is a major drawback for its use in the context of the study of the low frequency dynamics of SWBLIs. Moreover, the parallelization of the method is not straightforward because of the communications between the inlet plane and the downstream recycling plane.
Alternativelly to the library based and recycling-rescaling-based methods, the so called synthetic turbulence methods consist in feeding the inlet of the domain with structures that mimic realistic turbulent structures. A possibility is to impose a white noise as fluctuations superimposed to a mean profile. Nevertheless, this approach fails and a relaminarization of the flow is often observed due to the lack of spatial an temporal statistical coherence. The synthetic turbulence methods aims at introducing as much as possible of the realistic turbulence statistical coherence.
Among the synthetic turbulence methods, the Fourier transform-based approach aims at constructing turbulent velocity fields with a prescibed turbulent energy spectrum. This approach has been introduced by Kraichnan [1970] to generate isotropic turbulent velocity fields. It has then been modified by Smirnov et al. [2001], who designed the so called Random Flow Generation (RFG) method consisting in a superposition of harmonic functions with random amplitudes and phases to generate a velocity field with prescribed length, time scales and energy spectrum. The prescription of the targeted Reynolds stress tensor is then performed by subjecting the velocity field obtained to a tensor-scaling operation and to an orthogonal transformation. These modifications allow the use of the method for problems with anisotropic turbulence such as wall bounded flows.
An other way of imposing synthetic turbulence at the inlet of the simulaton domain is the digital-filter based approach. This approach was first proposed by Klein et al. [2003] and consists in the use of a digital filter to impose a prescribed two points correlation function to a random signal prescribed at the inlet of the domain. The obtained signal can be further transormed in order to impose a prescribed Reynolds stress tensor. In Klein et al. [2003], this last operation is performed using a transformation introduced in Lund et al. [1998] based on the Cholesky decomposition of the Reynolds stress tensor. This transformation is described in paragraph 5.2.1. In the original formulation by Klein et al. [2003], the length scale was uniform in the domain inlet. In Veloudis et al. [2007], the authors proposed a modified version of the method in which the inlet plane is split into several zones in which different length scales are prescribed. This improvement of the method is important for its use for the simulation of wall bounded flows in which the turbulent length scale reduces to zero towards the wall. This method have been used for the simulation of the SWTBLI by Touber and Sandham [2009] and an adaptation length of about 20δ were found necessary to recover a reasonably good skin friction coefficient.
The SEM have first been introduced by Jarrin et al. [2006]. It consists in the superimposition of a normalized stochastic velocity signal to a mean velocity profile. The stochastic signal is formed by a superimposition of Gaussian structures with prescribed length, time scale and shape. These

Gaussian structures have random time and location of appearance in the inlet plane. The Reynolds stress tensor is prescribed using the transformation introduced by Lund et al. [1998] described in paragraph 5.2.1. The method have then been improved by Pamiès et al. [2009] for its use in the context of wall bounded flows. Pamiès et al. [2009] used the information available in the literature to designe shape function describing structures of varying shapes and length scales in the wall normal direction. These structures, mimicing the coherent structures present in a boundary layer, were used to build the stochastic signal superimposed to the mean velocity profile. This method has been used for performing the simulation of an incompressible boundary layer and an adaptation distance of 5δ has been necessary to recover a reasonably good skin friction coefficient and 7δ to recover satisfactory Reynolds stress profiles.
The Fourier filter-based approach, the digital filter-based approach and the SEM appears to be well suited to the simulation of SWTBLI. Indeed, these methods allow the generation of turbulent fields on the fly (satisfying criterion 3) without introducing spurious low frequencies in the flow (satisfying criterion 4). The SEM appears particularly promising as it requires a particulaly short adaptation distance (Pamiès et al. [2009]). Moreover, the SEM is straightforward to parallelize (satisfying criterion 7). The SEM method has then been selected and implemented in the CHORUS code for the purpose of its use for SWTBLI simulations.

5.2 Implemented Synthetic Eddy Method

The SEM has been developed for incompressible flows Jarrin et al. [2006]. We here present the SEM adapted for compressible that has been implemented in the CHORUS code.
In the following, the variables are decomposed using a Reynolds decomposition $f = \overline{f} + f'$ where $\overline{f}$ denotes the ensemble average of f and f' is the fluctuation of f centered on $\overline{f}$.

5.2.1 Prescription of the velocity at the inlet of the domain

The SEM uses the Cholesky decomposition $A_{ij}(y)$ of a prescribed Reynolds stress tensor $R_{ij}(y)$ to assign second order moments to a normalized stochastic signal $\widetilde{u}_j(y,z,t)$ surimposed to a mean velocity profile $\overline{u}_i(y)$ at the inlet of the domain,

$$u_i(y,z,t) = \overline{u}_i(y) + \sum_j A_{ij}(y)\widetilde{u}_j(y,z,t), \quad i = 1,2,3. \tag{5.1}$$

This operation proposed in Lund et al. [1998] allows to prescribe both first and second order moments at the inlet of the domain if $\widetilde{u}_j(y,z,t)$ is a centered random sequence with unit variance and zero covariance: $\overline{\widetilde{u}_i \widetilde{u}_j} \mid = \delta_{ij}$.

$$\mathbf{A} = \begin{bmatrix} \sqrt{(R_{11})} & 0 & 0 \\ R_{21}/A_{11} & \sqrt{(R_{22} - A_{21}^2)} & 0 \\ R_{31}/A_{11} & \dfrac{R_{32} - A_{21}A_{31}}{A_{22}} & \sqrt{R_{33} - A_{31}^2 - A_{32}^2} \end{bmatrix}, \tag{5.2}$$

where $R_{ij} = \overline{u_i' u_j'}$ denotes the componants of the Reynolds stress tensor. As seen in equation 5.1, the SEM needs three inputs: the mean velocity profile, the Reynolds stress tensor at the inlet of the domain and a random signal $\widetilde{u}_j(y,z,t)$. In the following, we will introduce these three inputs of the SEM as they have been implemented in the CHORUS code.

Prescribed mean velocity profile at the inlet of the domain

We first recall the definitions of some characteristic quantities of the boundary layer:

— the boundary layer momentum thickness $\theta = \int_0^\infty \dfrac{\rho \overline{u}_1}{\rho_\infty U_\infty}\left(1 - \dfrac{\overline{u}_1}{U_\infty}\right) dy$

— the displacement thickness $\delta^* = \int_0^\infty 1 - \frac{\rho \overline{u}_1}{\rho_\infty U_\infty} dy$

— the shape factor $H = \frac{\delta^*}{\theta}$

— the friction velocity $u_\tau = \sqrt{\frac{\tau_w}{\rho_w}}$, where τ is the shear stress and the subscript w refers to the value of the variable at the wall

The mean velocity profile of the boundary layer at the inlet of the domain is prescribed using the analytical approximation introduced in L. Whitfield [1977]. Only the longitudinal component $\overline{u}_1$ is not null. It is build from prescibed values of the free stream velocity U_∞, the skin friction coefficient C_f, the boundary layer momentum thickness θ and the shape factor H:

$$\overline{u}_1(y) = u_\tau \frac{1}{0.09} \text{atan}(0.09 y^+) + (|\frac{C_f}{2}|^{-1/2} - \frac{\pi}{0.18})(\tanh(a(\frac{y}{\theta})^b))^{1/2}, \tag{5.3}$$

where $y^+ = \frac{u_\tau y}{\nu_w}$ is the vertical coordinate in wall units characterizing the viscous sublayer and:

$$\begin{aligned}
u_\tau &= U_\infty |\frac{C_f}{2}|^{1/2} \\
a &= (\text{arctanh}(g^2(2)))/2^b \\
b &= (\ln(\frac{\text{arctanh}(g^2(2))}{\text{arctanh}(g^2(5))}))/\ln(\frac{2}{5}), \\
g(2) &= (\frac{U}{U_\infty}(2) - \frac{1}{0.09}(\frac{|C_f|}{2})^{1/2}\text{atan}(0.18 Re_\theta(\frac{|C_f|}{2})^{1/2}))/(1 - \frac{\pi}{0.18}(\frac{|C_f|}{2})^{1/2}), \\
g(5) &= (\frac{U}{U_\infty}(5) - \frac{1}{0.09}(\frac{|C_f|}{2})^{1/2}\text{atan}(0.45 Re_\theta(\frac{|C_f|}{2})^{1/2}))/(1 - \frac{\pi}{0.18}(\frac{|C_f|}{2})^{1/2}), \\
\frac{\overline{u}_1}{U_\infty}(2) &= (\text{arctanh}(\frac{8.5 - H}{7.5}) - 0.364)/1.95, \\
\frac{\overline{u}_1}{U_\infty}(5) &= 0.155 + 0.795\cosh(0.51(H - 1.95)),
\end{aligned} \tag{5.4}$$

Even if the formulation $u_\tau = U_\infty |\frac{C_f}{2}|^{1/2}$ holds only for an incompressible boundary layer, we use this formulation to prescribe the mean velocity profile at the inlet of the simulation domain without knowing ρ_w.

Prescribed Reynolds stress tensor at the inlet of the domain

The determination of the Reynolds stress tensor at the inlet of the domain requires knowing the fluctuating velocity field. As this information is not available, we impose approximate Reynolds stress components derived from the mean velocity profile using the Bousinesq hypothesis:

$$-\overline{u'v'} = \nu_t(\frac{\partial \overline{u}_1}{\partial y}), \tag{5.5}$$

where ν_t is the turbulent viscosity.
The mixing length model is used in order to evaluate the turbulent viscosity:

$$\nu_t = l^2 D^2 \frac{\partial \overline{u}_1}{\partial y}, \tag{5.6}$$

where l is the mixing length and D is the damping function. These functions are evaluated as follows:

$$l = 0.085\delta\tanh(\frac{\chi}{0.085}\frac{y}{\delta}) \quad \text{with} \quad \chi = 0.41, \tag{5.7}$$

$$\mathrm{D} = 1 - e^{(y^+/26)}, \tag{5.8}$$

where δ is the boundary layer thickness at the inlet of the domain. δ is defined as the distance from the wall at which the velocity reaches $0.99\mathrm{U}_\infty$.

The value of the turbulent kinetic energy profile $k = \frac{1}{2}\sum_{i=1}^{3}\overline{u_i'^2}$ is then derived using the assumption of Bradshaw et al. [1967] and Townsend [1980] that the ration between k and $\overline{u'v'}$ is a constant:

$$k = \frac{-\overline{u'v'}}{\sqrt{\mathrm{C}_\mu}}, \tag{5.9}$$

where the structure parameter C_μ has a generally admitted value $\mathrm{C}_\mu = 0.09$.
We then use the Wilcox's hyptothesis Wilcox et al. [1998] to evaluate the value of the diagonal components of the Reynods stress tensor.

$$\overline{u'^2} = \tfrac{4}{9}2k, \quad \overline{v'^2} = \tfrac{2}{9}2k, \quad \overline{w'^2} = \tfrac{1}{3}2k. \tag{5.10}$$

Finally, we impose $\overline{u'w'} = 0$ and $\overline{v'w'} = 0$. The Wilcox's hyptothesis allows to take into account the turbulence anisotropy in a boundary layer and has been shown to provide good approximations throughout the log layer and most of the defect layer for zero pressure gradient boundary layer Wilcox et al. [1998].

Generation of the random signal $\widetilde{u}_j(y,z,t)$

The content of this paragraph is inspired by the presentation of the SEM method in Pamiès et al. [2009].
To generate the random signal $\widetilde{u}_j(y,z,t)$, we follow the approach introduced in Pamiès et al. [2009], where the original SEM has been extended to account for the inhomogeneity of scales in the direction normal to the wall for boundary layers computations. Using this approach, the inlet plane is splitted into Þ zones (see figure 5.1) in which the random signal has different scales.

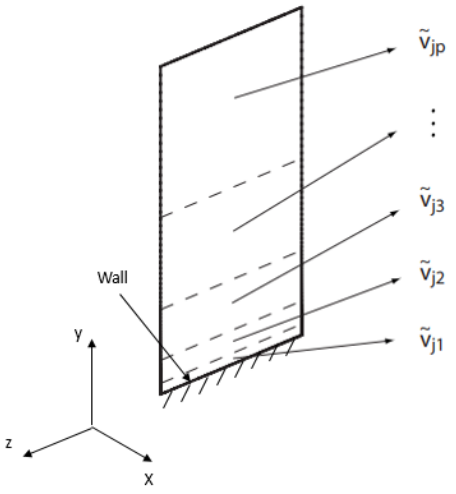

FIGURE 5.1 – Sketch of the sectioning of the inlet plane into several modes from Pamiès et al. [2009].

The random signal $\widetilde{u}_j(y,z,t)$ is then computed as a sum over the Þ zones,

$$\widetilde{u}_j = \sum_{p=1}^{\text{Þ}} \widetilde{v}_{jp}, \tag{5.11}$$

where $\widetilde{v}_{jp}$ are random velocity signals that have compact support on the p^{th} zone and are refered to as modes.
Each mode is the superposition of $\mathrm{N}(p)$ structures. Each structure of the mode have a random time of appearance t_k and a random location of its center (y_k, z_k) in the p^{th} mode's zone, namely in $[y_p^{low}; y_p^{up}][0; \mathrm{L}_z]$ where $y_p^{up} - y_p^{low}$ defines the wall normal extent of the p^{th} zone and L_z is the width of the inlet plane. The number of structures per mode $\mathrm{N}(p)$ is chosen so that the p^{th} zone of the inlet plane is statistically covered by structures:

$$\mathrm{N}(p) = \frac{\mathrm{S}_p}{\mathrm{S}_s}, \tag{5.12}$$

where S_p is the surface of the p^{th} zone ($\mathrm{S}_p = \mathrm{L}_z(y_p^{up} - y_p^{low})$) and S_s is the surface of a structure of the p^{th} mode projected onto the inlet plane ($\mathrm{S}_\mathrm{S} = 4 l_p^y l_p^z$).
Each mode is characterized by the length scales in each direction that are assigned to the structures and that are noted l_p^x, l_p^y and l_p^z. Using the Taylor's frozen turbulence hypothesis, l_p^x is related to a time scale of the structure l_p^t that characterizes the time necessary for a structure to fully pass through the inlet plane:

$$l_p^t = \frac{l_p^x}{c_p}, \tag{5.13}$$

where c_p is the convection velocity of the structres that depends on the mode.
The shape of the structures is characterized by shape functions in each direction g_{jp} depending on the mode. These shape functions depend on time and space coordinates through a product of monodimentional functions $\Xi(\widetilde{t})$, $\Phi(\widetilde{y})$ and $\Psi(\widetilde{z})$ where $\widetilde{t} = \frac{t - t_k - l_p^t}{l_p^t}$, $\widetilde{y} = \frac{y - y_k}{l_p^y}$ and $\widetilde{z} = \frac{z - z_k}{l_p^z}$ are the reduced variables for time, wall-normal direction and transverse direction respectively. The random signal writes finally:

$$\begin{aligned} \widetilde{u}_j = \textstyle\sum_{p=1}^{\mathrm{P}} \widetilde{v}_{jp} &= \textstyle\sum_{p=1}^{\mathrm{P}} \frac{1}{\sqrt{\mathrm{N}(p)}} \sum_{k=1}^{\mathrm{N}(p)} \epsilon_k \Xi_{jp}(\widetilde{t}) \Phi_{jp}(\widetilde{y}) \Psi_{jp}(\widetilde{z}), \\ &= \textstyle\sum_{p=1}^{\mathrm{P}} \frac{1}{\sqrt{\mathrm{N}(p)}} \sum_{k=1}^{\mathrm{N}(p)} \epsilon_k g_{jp}(\widetilde{t}, \widetilde{y}, \widetilde{z}), \end{aligned} \tag{5.14}$$

where ϵ_k is a random sign (i.e. ± 1) assigned to each structure in order to decorrelate the components and to match the zero covariance condition ($\overline{\widetilde{u}_i \widetilde{u}_j}\,|_{i \neq j} = \delta_{ij}$).
Using the formulation 5.14, each structure is convected through the inlet plane. When $(t - t_k - l_p^t)/l_p^t = 1$, the structure k has completely passed through the inlet plane and a new structure is built with a random location (y_k, z_k) and a new random time of appearance chosen in $[t; t + l_p^t]$.
In order to prescribe a random signal with unit variance, the shape functions are normalized as follows:

$$\frac{1}{2^3} \int_{[-1;1]^3} [g_{jp}]^2(\tilde{t}, \tilde{y}, \tilde{z})]^2 d\tilde{t} d\tilde{y} d\tilde{z} = 1, \tag{5.15}$$

with $[-1; 1]$ the support of the shape functions that depend on normalized variables.
The inlet boundary conditions are completely defined when the scales l_p^t, l_p^y and l_p^z are chosen and when the functions $\Xi(\widetilde{t})$, $\Phi(\widetilde{y})$ and $\Psi(\widetilde{z})$ are defined for each mode. These scales and functions are defined in order to mimic the shapes and scales of the turbulent structures in a boundary layer. This approach is also used in Laraufie and Deck [2013] and the parameters and shape functions used in our implementation are extract from Laraufie and Deck [2013]. The inlet plane is divided in 4 zones, the 1^{st} zone being the closest to the wall and the 4^{th} zone being the farthest from the wall. The low and up limits of the 4 zones expressed in wall units are given in table 5.2. Close to the wall (1^{st} mode), the structures injected in the domain are long and thin streamwise structures as

in an real boundary layer. The 2^{nd} mode just above the first one, corresponding to the logarithmic layer, is populated by shorter and thicker structures reproducing the shape of hairpin vortices characteristic of the logarithmic layer. The rest of the boundary layer (3^{rd} and 4^{th} modes), are filled with Gaussian isotropic structures.
The shape functions corresponding to each mode are given in the table 5.1 where:

$$\mathrm{H}(\xi) = \frac{1 - cos(2\pi\xi)}{2\pi\xi\sqrt{0.214}} \tag{5.16}$$

and

$$\mathrm{G}(\xi) = \mathrm{A}(\sigma) e^{-\frac{\xi^2}{2\sigma^2}} \tag{5.17}$$

with $\mathrm{A}(\sigma) = \frac{1}{\sigma\frac{\sqrt{\pi}}{2}}\mathrm{erf}(\frac{1}{\sigma})$ and $\sigma = \frac{1}{3}$.

	g_{1p}	g_{2p}	g_{3p}
p=1,2	$\mathrm{G}(\tilde{t})\mathrm{G}(\tilde{y})\mathrm{H}(\tilde{z})$	$-\mathrm{G}(\tilde{t})\mathrm{G}(\tilde{y})\mathrm{H}(\tilde{z})$	$\mathrm{G}(\tilde{t})\mathrm{H}(\tilde{y})\mathrm{G}(\tilde{z})$
p=3,4	$\epsilon_1\mathrm{G}(\tilde{t})\mathrm{G}(\tilde{y})\mathrm{G}(\tilde{z})$	$\epsilon_2\mathrm{G}(\tilde{t})\mathrm{G}(\tilde{y})\mathrm{G}(\tilde{z})$	$\epsilon_3\mathrm{G}(\tilde{t})\mathrm{G}(\tilde{y})\mathrm{G}(\tilde{z})$

TABLEAU 5.1 – Analytical expression of the shape functions. ϵ_1, ϵ_2 and ϵ_3 are random signs (i.e. ± 1).

The length scales and the convection velocity of turbulent structures associated with each mode, expressed in wall units are given in table 5.2.

	$(y_p^{low})^+$	$(y_p^{up})^+$	$(l_p^y)^+$	$(l_p^x)^+$	$(l_p^z)^+$	c_p^+
p=1	20	40	20	100	30	15
p=2	40	0.188 δ	40	80	40	18
	(y_p^{low})	(y_p^{up})	(l_p^y)	(l_p^x)	(l_p^z)	c_p
p=3	0.188 δ	0.72 δ	0.125 δ	0.125 δ	0.125 δ	0.76 U_∞
p=4	0.4 δ	1.7 δ	0.227 δ	0.227 δ	0.227 δ	0.76 U_∞

TABLEAU 5.2 – Low and up limits, length scales and convection velocity of turbulent structures associated with each mode, expressed in wall units.

5.2.2 Prescription of the temperature and the density fields at the inlet of the domain

The mean temperature profile imposed at the domain inlet is determined from the mean velocity profile using the Crocco's formula [Cousteix [1989]]. Assuming that the Prandtl number $\mathrm{P}r = 1$ and the turbulent number $\mathrm{P}r_t = 1$, this formula links the mean static enthalpy profile with the mean velocity profile as follows:

$$h = h_w + (h_{i\infty} - h_w)\frac{\overline{u}_1}{\mathrm{U}_\infty} - (h_{i\infty} - h_\infty)(\frac{\overline{u}_1}{\mathrm{U}_\infty})^2 \tag{5.18}$$

where h is the static enthalpy, h_i is the total enthalpy, the index "w" denotes the variable estimated at the wall location, and the index ∞ denotes the free stream.
Assuming an adiabatic wall, $h_w = h_{i\infty}$ and the Crocco's formula (5.18) becomes:

$$h = h_{i\infty} + (h_{i\infty} - h_\infty)(\frac{\overline{u}_1}{\mathrm{U}_\infty})^2 \tag{5.19}$$

This hypothesis is convenient. Indeed, avoiding h_w allows to impose the enthalpy profile knowing only the free stream conditions.
As we assume a perfect gaz, equation (5.19) relates directly the mean temperature profile and the mean velocity profile.

The mean density profile is then derived from the mean velocity profile, using the perfect gaz equation of state.
For supersonic boundary layers over adiabatic walls, there is experimental evidence of quasi constant total enthalpy profile if the Mach number is not too high (M<5). It can then be assumed a zero total enthalpy fluctuations in the boundary layer ($h_i' = 0$). This hypothesis leads to the Strong Reynolds Analogy (SRA) [Cousteix [1989]]:

$$\frac{T'}{\overline{T}} \simeq -(\gamma - 1)M^2 u' \overline{u}_1 \tag{5.20}$$

where T' is the temperature fluctuation and u' the longitudinal velocity fluctuation.
Moreover, for compressible turbulent boundary layers until $M \leqslant 5$ the velocity fluctuations are subsonic and experimental evidences show that pressure fluctuations and $\rho' T'$ are second order terms. This leads to:

$$\rho' = -\overline{\rho}\frac{T'}{\overline{T}} \tag{5.21}$$

where ρ' are the density fluctuations.
Relations 5.20 and 5.21 are used for prescribing temperature and density fluctuations at the inlet. This approach has been used by Touber and Sandham [2009] and Aubard et al. [2012].

5.3 Simulation of a turbulent compressible boundary layer over a flat plate

A compressible turbulent boundary layer has been simulated using the SEM introduced in the previous section. The OSMP 7^{th} order scheme is here employed. Following results obtained in chapter 3, 2^{nd}-order discretization is also used for the viscous fluxes. The flow conditions are taken from Mullenix et al. [2013] and summarized in table 5.3

Property	
M_∞	2.33
U_∞ (m/s)	556
P_∞ (Pa)	2351.11
T_∞ (K)	141.71
T_w (K)	269.75
δ (m)	5.310^{-3}
θ (m)	7.6810^{-4}
Re_δ	17520.21
Re_θ	2538.78

TABLEAU 5.3 – Flow conditions.

We employ a structured mesh of size $1033 \times 105 \times 113$ in $(\mathbf{x} \times \mathbf{y} \times \mathbf{z})$ to discretize the domain of simulation that has an extent of $80\delta \times 4\delta \times 3.0\delta$. In the normal to the wall direction, the mesh is tightened close to the wall using a hyperbolic tangent law to ensure a minimum grid spacing at the wall $\Delta y_w^+ = 0.9$ (at $x/\delta = 20$). A uniform mesh is used in the longitudinal and spanwise directions (respectively x and z) with a grid spacing of $\Delta x^+ \simeq 18.3$ and $\Delta z^+ \simeq 6.3$.

5.3.1 Numerical results

A snapshot (Q criterion colored by the longitudinal velocity between $x = 0$ and $x = 40\delta$) of the turbulent boundary layer obtained using this method is shown in figure 5.2. The injection of eddies at the inlet of the domain is visible. As show in figure 5.3, where the longitudinal velocity

contours are plotted in a (x,z) plane at $y^+ \simeq 15$ above the wall, the boundary layer is populated by structures elongated in the streamwise direction close to the wall. Eddy ejections within the boundary layer is also clearly visible in figure 5.2 in the form of hairpin vortices. The qualitative aspect of the structure patterns populating the boundary layer is consistant with a realistic compressible turbulent boundary lyer.

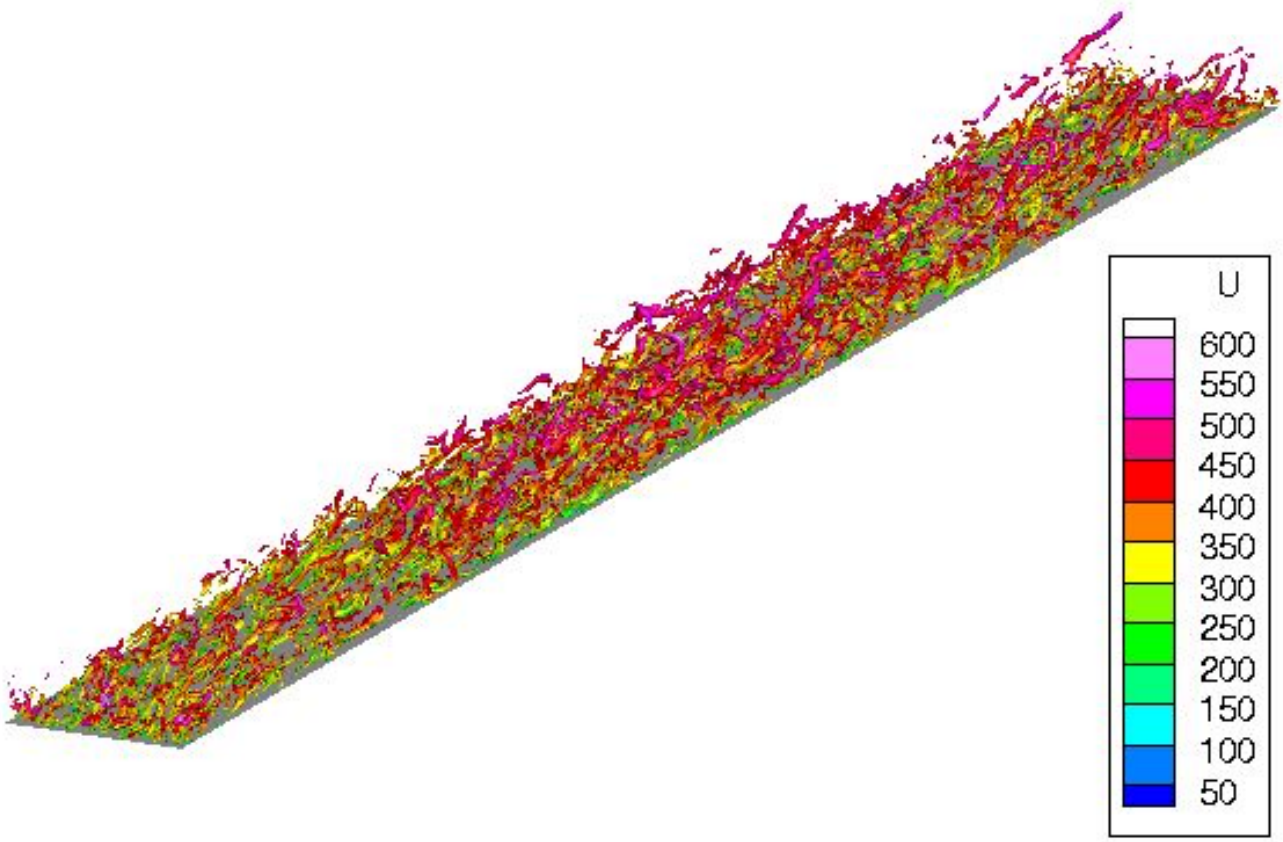

FIGURE 5.2 – Q criterion ($\frac{\delta^2}{U_\infty^2}Q = 1$) colored by the longitudinal velocity between $x = 0$ and $x = 40\delta$.

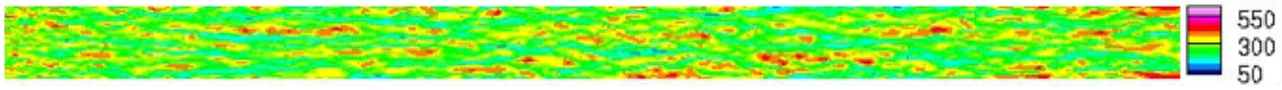

FIGURE 5.3 – Longitudinal velocity isocontours in a (x,z) plane at $y^+ \simeq 15$ above the wall.

The time mean skin friction coefficient, averaged in the spanwise direction is plotted along the flat plate in figure 5.4. The adjustment distance needed to recover the right value of the skin friction coefficient is approximately $\Delta \sim 10\delta - 15\delta$. This adjustment distance appears to be very small compared to the one obtained in Mullenix et al. [2013], in which a steady counterflow actuator with properties based on a dielectric barrier discharge is employed to trip an incoming laminar boundary layer. The simulation of Mullenix et al. [2013] was performed using 2 meshes: a coarse mesh ($\Delta x^+ = 23.5$, $\Delta y_w^+ = 0.4$, $\Delta z^+ = 8.9$ at $x = 65\delta$) and a finer mesh ($\Delta x^+ = 16.4$, $\Delta y_w^+ = 0.4$, $\Delta z^+ = 6.1$ at $x = 65\delta$). Our mesh is comparable to the finest mesh of Mullenix et al. [2013]. The adaptation distance obtained using the implemented SEM compares also well with respect to other turbulent inflow conditions. For instance, the digital filter-based approach used in SWTBLI by Touber and Sandham [2009] needed an adaptation of about 20δ to recover good skin friction coefficient.

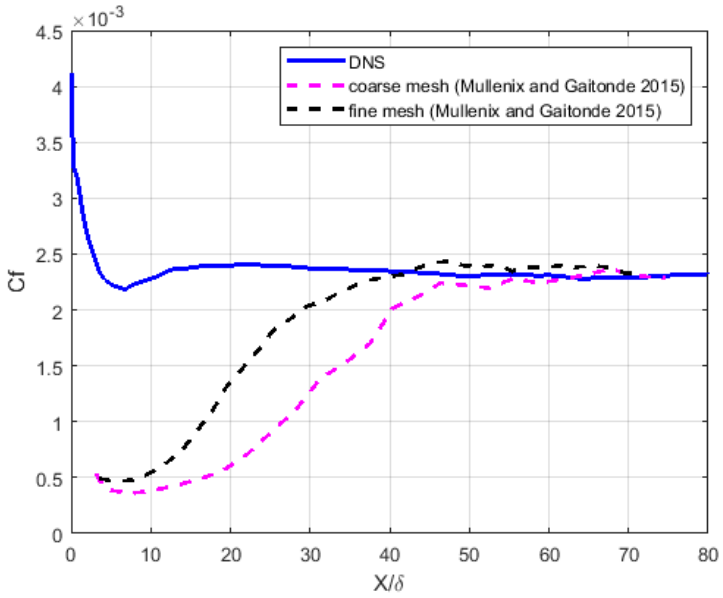

FIGURE 5.4 – Time mean skin friction coefficient (C_f) averaged in the spanwise direction along the flat plate (x/δ).

Figure 5.5 shows the Van Driest velocity profile and the Reynolds stress profiles with respect to y^+ obtained at $x = 20\delta$. This abscissa is chosen in order to highlight the properties of the boundary layer before the incident shock wave impingement in the simulation of the SWTBLI on a mesh with the same resolution presented in chapter 6. The profiles correspond to time mean values averaged in the spanwise direction. The velocity is transformed into an equivalent nondimensional incompressible velocity using the Van Driest transformation (Cousteix [1989]):

$$u^+_{\mathrm{VD}} = \frac{\mathrm{U}_\infty}{u_\tau}\frac{1}{\mathrm{A}}\left[\arcsin\left(\frac{2\mathrm{A}^2\overline{u}_1 - \mathrm{B}}{\sqrt{(4\mathrm{A}^2+\mathrm{B}^2)}}\right) + \arcsin\left(\frac{\mathrm{B}}{\sqrt{(4\mathrm{A}^2+\mathrm{B}^2)}}\right)\right] \tag{5.22}$$

where

$$\begin{aligned} \mathrm{A}^2 &= \tfrac{\gamma-1}{2}\mathrm{M}^2_\infty \tfrac{\mathrm{T}_\infty}{\mathrm{T}_w} \\ \mathrm{B} &= (1+\tfrac{\gamma-1}{2}\mathrm{M}^2_\infty)\tfrac{\mathrm{T}_\infty}{\mathrm{T}_w} - 1 \end{aligned} \tag{5.23}$$

The Reynolds stresses are density-scaled and normalized by the friction velocity as follows:

$$\mathrm{R}_{ij} = \frac{\overline{\rho u'_i u'_j}}{\overline{\rho}_w \overline{u}^2_\tau} \tag{5.24}$$

The Van Driest velocity profile obtained at $x = 20\delta$ corresponds to a turbulent profile with a linear evolution close to the wall, followed by a logarithmic law evolution in the inertial region with the right parameters ($300 \leqslant y^+ \leqslant 2000$) and by a wake region for ($2000 \leqslant y^+$). The Reynolds stress profiles obtained at $x = 20\delta$ are also realistic profiles for a compressible turbulent boundary layer. In particular, the value and the location of the peak of streamwise normal stress fall within the range reported in other studies (Mullenix et al. [2013]: $\mathrm{R}_{11} = 9.24$ at $y^+ = 18.11$, Touber and Sandham [2009]: $\mathrm{R}_{11} = 8.75$ at $y^+ \simeq 18$, Pirozzoli et al. [2004]: $\mathrm{R}_{11} = 8$ at $y^+ \simeq 15$). Moreover, the profile of R_{12} recovers a plateau like evolution in the inertial range that is around -1 which is in accordance with the boundary layer theory.
An adapatation length of about 20δ is then enough to recover realistic values of the skin friction coefficient, a realistic streamwise velocity profile and Reynolds stress profiles.

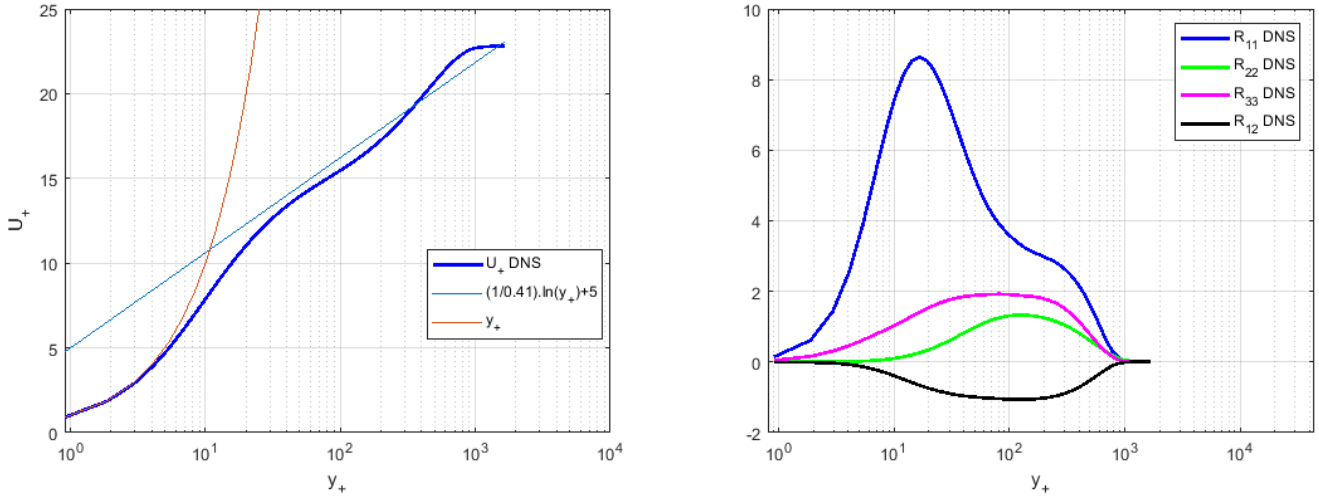

FIGURE 5.5 – Left: Velocity profiles in the Van Driest transformed coordinates for $x = 20.\delta$. Right: Density-scaled Reynolds stresses for $x = 20.\delta$.

A line of probes oriented in the spanwise direction with one probe in each mesh cell has been placed at $x = 10\delta$ and $y_+ = 113$ ($y/\delta \simeq 0.28$). The spanwise autocorrelations of ρ, u, v, w and p fluctuations are plotted in figure 5.6-left. These autocorrelations are computed as follows (see Pirozzoli et al. [2004]):

$$C_{\alpha\alpha}(r_z = k_r \Delta z) = \sum_{k=1}^{N_i - 1} \overline{\alpha'_k \alpha'_{k+k_r}}, \quad k_r = 0, 1..., N_z - 1 \tag{5.25}$$

where N_z is the number of grid points in the **z** direction and α is the variable considered.
v fluctuations have a much wider correlation than u, which is larger than w, which has the narrowest correlation. The density fluctuation correlations are slightly wider than the correlations of v, whereas the pressure is the widest correlation. Figure 5.6-left confirms that the spanwise extent of the domain is large enough such that the fluctuations at the midway point are decorrelated with fluctuations near the boundaries. The Taylor scales can be calculated from the autocorrelation profiles. Regarding the longitudinal velocity (u), the Taylor microscale is $\lambda = 7.10^{-4} m$ and the Taylor macroscale is $\Lambda = 1.05.10^{-3} m$. We have $\lambda/\Delta x \simeq 1.7$ and $\lambda/\Delta z \simeq 4.95$. The grid spacing in the longitudinal and spanwise direction is then significantly smaller than the characteristic scale of the smaller turbulent structures. Moreover $\Lambda/Lz \simeq 6.6.10^{-2}$ (with Lz the spanwise extent of the computational domain) indicating that the larger turbulent structures are significantly small with respect to the spanwise extent of the computational domain.
The one dimensional power spectra of ρ, u, v, w and p in the spanwise direction at $x = 10\delta$ and $y_+ = 113$ are plotted in figure 5.6-left. The energy of these variables versus the spanwise wave number are computed as follows (see Pirozzoli et al. [2004]):

$$E_{\alpha\alpha}(k_z = \frac{n}{(N_z - 1)} \frac{1}{\Delta z}) = 1 + 2 \sum_{k_r=1}^{(N_z-1)/2} C_{\alpha\alpha}(k_r \Delta z) cos(\frac{2\pi n k_r}{N_z - 1}), \quad n = 0, 1..., (N_z - 1)/2 \tag{5.26}$$

These spectra show that no spurious energetic length scale is introduced due to the SEM in the boundary layer. This point is crutial to judge the quality of the method as stated by the 4^{th} criterion introduced by Dhamankar et al. [2015] (see the section 5.1). The spectral content is realistic for a compressible turbulent boundary layer. Moreover, for the velocity components, there is a significant region where the spectra follow a $k^{-5/3}$ profile.

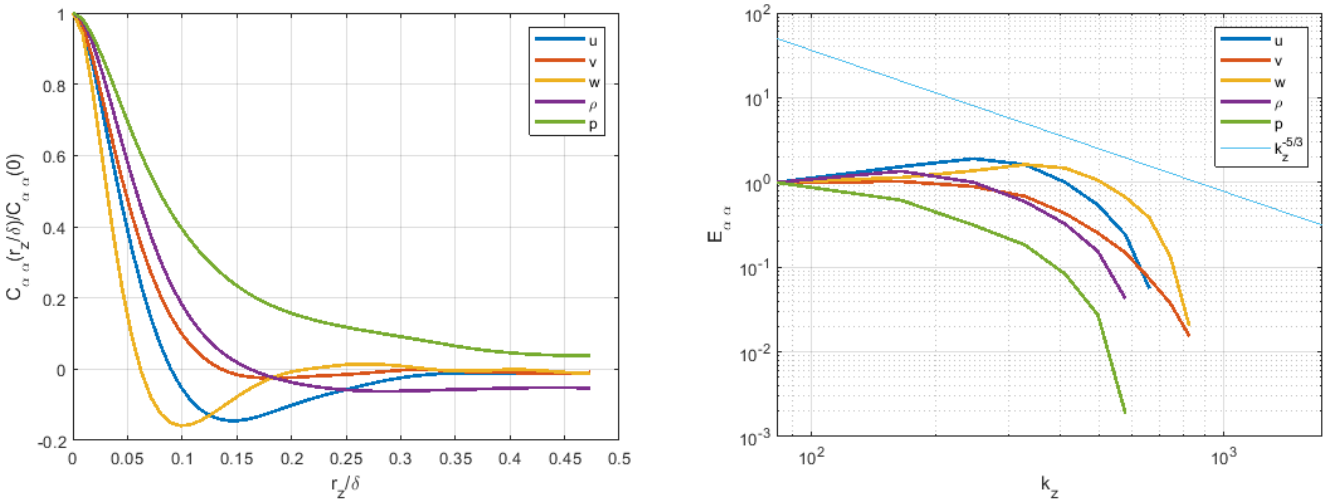

FIGURE 5.6 – Left: Spanwise autocorrelations of the fluctuations at $x = 10\delta$ and $y_+ = 113$ ($y/\delta \simeq 0.28$). Right: Power spectra in the spanwise direction at $x = 10\delta$ and $y_+ = 113$ ($y/\delta \simeq 0.28$).

Figure 5.7 shows a comparison between the results obtained in the current DNS and the results of Mullenix et al. [2013] of the velocity profile and the Reynolds stress tensor profile with respect to y^+. Both the velocity and Reynlods stresses profile are in good agreement with the reference values obtained from Mullenix et al. [2013].

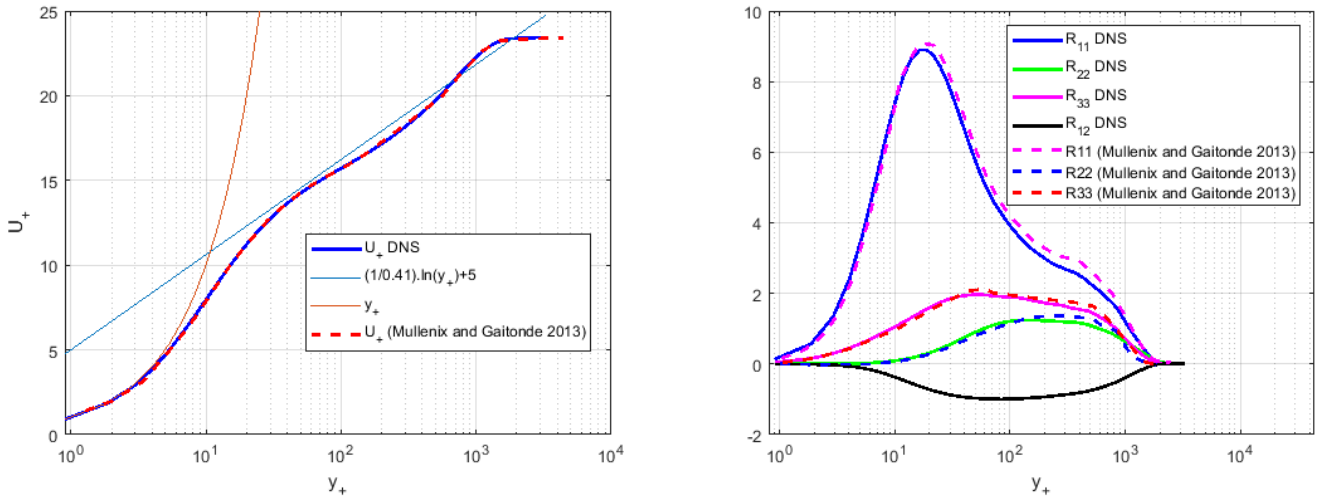

FIGURE 5.7 – Comparison between the SEM and the results from Mullenix et al. [2013] for $Re_\theta \simeq 3500$ and $x/\delta = 62.5$. Left: Velocity profiles in the Van Driest transformed coordinates. Right: Density-scaled Reynolds stresses.

Figure 5.8 shows a comparison between the temperature profile obtained in the current DNS and the reference result of Mullenix et al. [2013]. The profiles are in good agreement showing the ability of the numerical approach (numerical scheme + fine mesh + SEM) to accurately compute thermodynamic fields. We can note that the gradient of T in the normal wall direction is clearly zero at the adiabatic wall.

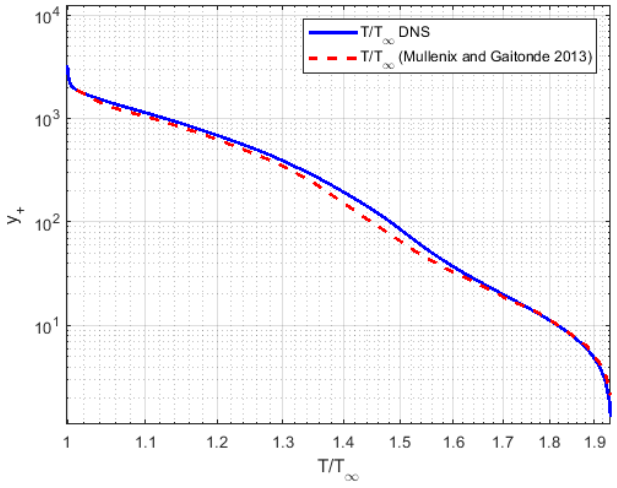

FIGURE 5.8 – Comparison between the SEM and the results from Mullenix et al. [2013] for $Re_\theta \simeq 3500$. Temperature profile.

5.4 Conclusion

The SEM adapted to compressible boundary layer has been implemented in the code CHORUS. It has been used to compute a compressible turbulent boundary layer. The results are in very good agreement with the reference results. An adapatation of about 20δ has been found enough to recover realistic values of the skin friction coefficient, realistic velocity and Reynolds stress profiles. The implemented method will be used in chapter 6 to simulate a SWTBLI.

5.5 References

Jean Cousteix. *Aâerodynamique: Turbulence et Couche Limite*. Cépaduès-editions, 1989. 68, 75, 76, 78

Hermann Schlichting and Klaus Gersten. *Boundary-layer theory*. Springer, 2016. 68

F. Comte, P. Ducros, and M. Lesieur. Large-eddy simulation of transition to turbulence in a boundary layer developing spatially over a flat plate. *Journal of Fluid Mechanics*, 326:1–36, 1996. 68

N. Dhamankar, G. A Blaisdell, and A. Lyrintzis. An overview of turbulent inflow boundary conditions for large eddy simulations (invited). 06 2015. doi: 10.2514/6.2015-3213. 68, 69, 70, 79

G. Tabor and M.H. Baba-Ahmadi. Inlet conditions for large eddy simulation: A review. *Computers & Fluids*, 39:553–567, 04 2010. doi: 10.1016/j.compfluid.2009.10.007. 68

P. Sagaut, S. Deck, and M. Terraco. Multiscale and multiresolution approaches in turbulence. 01 2006. doi: 10.1142/9781860948978. 68

Nathan J Mullenix, Datta V Gaitonde, and Miguel R Visbal. Spatially developing supersonic turbulent boundary layer with a body-force-based method. *AIAA journal*, 51(8):1805–1819, 2013. 5, 68, 76, 77, 78, 80, 81

G. Aubard, X. Gloerfelt, and J.-C. Robinet. Large-Eddy Simulation of Broadband Unsteadiness in a Shock/Boundary-Layer Interaction. *AIAA Journal*, 51:2395–2409, 2013. 68

Thomas Lund, Xiaohua Wu, and Kyle Squires. Generation of turbulent inflow data for spatially-developing boundary layer simulations. *Journal of Computational Physics*, 140:233–258, 03 1998. doi: 10.1006/jcph.1998.5882. 70, 71

Robert H Kraichnan. Diffusion by a random velocity field. *The physics of fluids*, 13(1):22–31, 1970. 70

A Smirnov, S Shi, and I Celik. Random flow generation technique for large eddy simulations and particle-dynamics modeling. *Journal of fluids engineering*, 123(2):359–371, 2001. 70

Markus Klein, Amsini Sadiki, and Johannes Janicka. A digital filter based generation of inflow data for spatially developing direct numerical or large eddy simulations. *Journal of computational Physics*, 186(2):652–665, 2003. 70

I Veloudis, Z Yang, JJ McGuirk, GJ Page, and A Spencer. Novel implementation and assessment of a digital filter based approach for the generation of les inlet conditions. *Flow, Turbulence and Combustion*, 79(1):1–24, 2007. 70

E. Touber and N. D. Sandham. Large-eddy simulation of low-frequency unsteadiness in a turbulent shock-induced separation bubble. *Theoretical and computational fluid dynamics*, 23:79–107, 2009. 70, 76, 77, 78

N. Jarrin, S. Benhamadouche, D. Laurence, and R. Prosser. A synthetic-eddy-method for generating inflow conditions for large-eddy simulation. *International Journal of Heat and Fluid Flow*, 27:585–593, 08 2006. doi: 10.1016/j.ijheatfluidflow.2006.02.006. 70, 71

M. Pamiès , P.-É. Weiss , S Deck , and P Sagaut. Generation of synthetic turbulent inflow data for large eddy simulation of spatially evolving wall-bounded flows. *Phys. Fluids*, 21:1–15, 04 2009. doi: 10.1063/1.3103881. 5, 71, 73

D L. Whitfield. Analytical description of the complete turbulent boundary layer velocity profile. *Final Report, Oct. 1976 - Mar. 1977 ARO, Inc., Arnold Air Force Station, TN.*, 09 1977. doi: 10.2514/6.1978-1158. 72

P. Bradshaw , D H. Ferriss , and N P. Atwell . Calculation of boundary layer using the turbulent energy equation. *Journal of Fluid Mechanics*, 28:593 – 616, 05 1967. doi: 10.1017/S0022112067002319. 73

A.A. Townsend. The structure of turbulent shear flow. *Cambridge Monogr. Mech. Appl. Math.*, 2, 03 1980. 73

David C Wilcox et al. *Turbulence modeling for CFD*, volume 2. DCW industries La Canada, CA, 1998. 73

R. Laraufie and S. Deck. Assessment of reynolds stresses tensor reconstruction methods for synthetic turbulent inflow conditions. application to hybrid rans/les methods. *International Journal of Heat and Fluid Flow*, 42:68 – 78, 08 2013. doi: 10.1016/j.ijheatfluidflow.2013.04.007. 74

G. Aubard, X. Gloerfelt, and J.-C. Robinet. Characterisation of synthetic turbulence methods for large-eddy simulation of supersonic boundary layers. 01 2012. doi: 10.1007/978-3-642-28968-2_17. 76

Sergio Pirozzoli, F Grasso, and TB Gatski. Direct numerical simulation and analysis of a spatially evolving supersonic turbulent boundary layer at m= 2.25. *Physics of fluids*, 16(3):530–545, 2004. 78, 79

Chapter 6

Shock wave turbulent boundary layer interaction

Contents

6.1 Physical parameters, computational domain and mesh 84
6.2 Mean flow organization 85
6.3 Dynamics of the flow 89
6.4 POD analysis 98
6.4.1 POD on the velocity field 99
6.4.2 POD on the pressure field 101
6.4.3 Flow reconstruction using low modes 103
6.5 Conclusions 109
6.6 References 111

The simulation of the SWLBLI, presented in chapter 4, did not reproduce the SWBLI unsteadiness. It highlighted the importance of the turbulent charactere of the incoming boundary layer in triggering this instability. In order to reproduce and analyze the SWBLI unsteadiness, we perform in this chapter the DNS of the interaction between an incident shock wave and an incoming compressible turbulent boundary layer developing on a flat plate. A sketch of the flow is presented in figure 6.1. The SEM presented in chapter 5 is used for initiating a turbulent compressible boundary layer at the inlet of the domain to reduce the numerical cost of the simulation. We first present the physical parameters and the mesh used for the simulation. The mean properties of the flow are then analyzed and compared to reference solutions. The remaining of the chapter is devoted to the analysis of the dynamics of the flow with a special attention paied to the analysis of the low frequency dynamics.

6.1 Physical parameters, computational domain and mesh

The SEM is used at the inlet of the domain for initiating a realistic turbulent boundary layer. The same boundary layer than in chapter 5 is considered here for the simulation of the SWTBLI. The OSMP 7^{th} order scheme is here employed. Following results obtained in chapter 3, 2^{nd}-order discretization is also used for the viscous fluxes. The flow conditions are remainded in table 6.1.

Property	
M_∞	2.33
U_∞ (m/s)	556
P_∞ (Pa)	2351.11
T_∞ (K)	141.71
T_w (K)	269.75
δ (m)	5.310^{-3}
θ (m)	7.6810^{-4}
Re_δ	17520.21
Re_θ	2538.78

TABLEAU 6.1 – Flow conditions.

A structured mesh of size 785×313×113 cells in ($x \times y \times z$) is used to discretize a 3D domain of simulation that has an extent of 0.32 m× 0.0886 m× 0.0159 m in these directions (corresponding to 60.4 δ ×16.7 δ× 3 δ, with δ the boundary layer thickeness at the inlet of the domain). The mesh used is refined near the wall in the y direction normal to the wall. The minimum grid spacing at the wall is $\Delta y_w^+ \simeq 0.9$ in the boundary layer before the interaction (for $x/\delta = 20$). A uniform mesh is used in the longitudinal and spanwise directions (respectively x and z) with a grid spacing of $\Delta x^+ \simeq 18.3$ and $\Delta z^+ \simeq 6.3$. This grid resolution is similar to the grid resolution used in the chapter 5 for the validation of the SEM.
A shock wave of angle 33.2° (corresponding to a flow deviation of 9.25° through the shock wave) is created by imposing the Rankine-Hugoniot relationship at the top boundary of the domain at $x/\delta = 14.07$ (see figure 6.1). The shock wave impinges the boundary layer at $x/\delta \simeq 39.5$. At this abscissa along the flat plate, the boundary layer created using the SEM have been shown to be in a fully turbulent state in chapter 5.

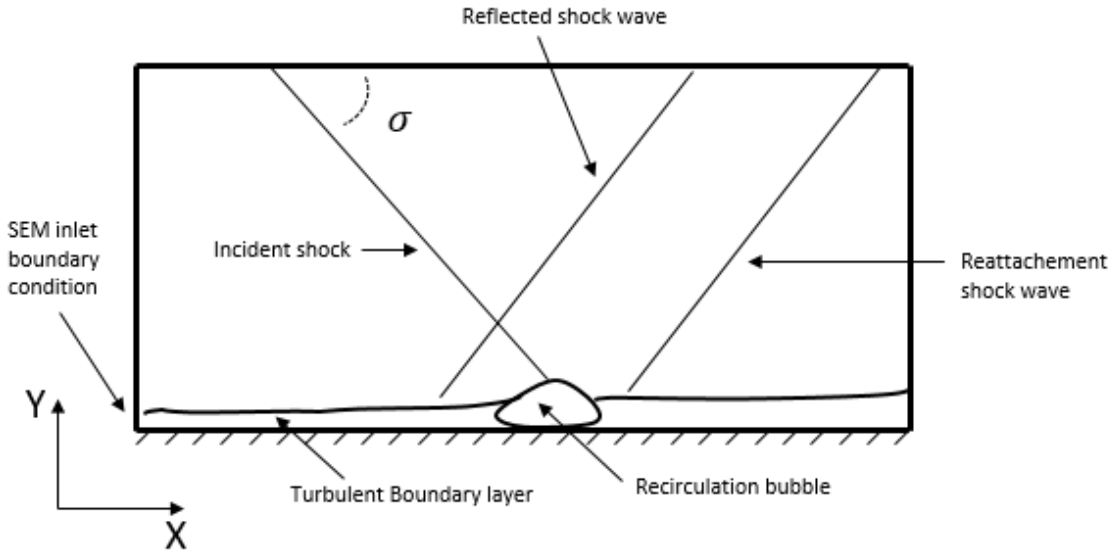

FIGURE 6.1 – Sketch of the flow.

6.2 Mean flow organization

A numerical schlieren visualization (2D (x,y) plane located at $z/\delta = 1.5$) is shown in figure 6.2. The development of the turbulent boundary layer, that is progressively thickened before the interaction zone is visible. A Mach line is also clearly visible, originating at the leading edge of the flat plate. This Mach line is present because of the adaptation of the modeled turbulent profile to the presence of the wall. This visualization also highlights the brutal increase of the boundary layer thickeness through the interaction. The overall shock wave system organization of a SWTBLI described in chapter 1 is recovered. Indeed, due to the incident shock impingement, the boundary layer separates. A recirculation bubble (highlighted in figure 6.3) is created as well as the subsequent reflected shock wave. The reattachment of the boundary layer occurs downstream of the interaction zone. Reattachment compression waves are clearly visible in the numerical Schlieren visualization.

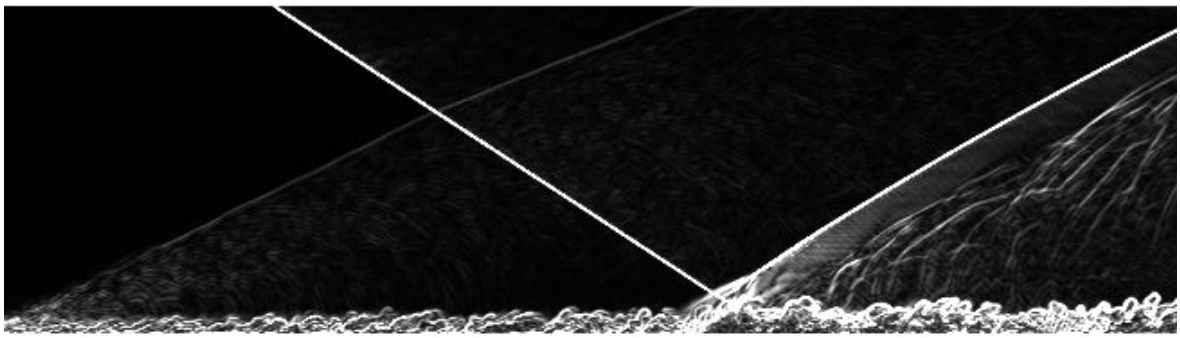

FIGURE 6.2 – Numerical schlieren visualization (2D slice located at the middle of the domain).

Figure 6.3 shows a comparison between the time mean longitudinal and vertical velocities averaged in the spanwise direction in the interaction zone obtained for the current DNS and the simulation of Adler and Gaitonde [2018] of the SWTBLI between the same compressible turbulent boundary layer and a shock wave characterized by a deviation of the flow of 9° (the strength of the shock is slightly lower than in our simulation). The velocities are scaled using U_∞ and the spatial coordinates are scaled using δ. The computations of the time means of the fields are perfor-

med over a simulation time of about 12 cycles of the low frequency unsteadiness corresponding to $\Delta t = 360\frac{L}{U_\infty}$. The time averaging is started after the transient phase corresponding to the creation of the shock wave system and the recirculation bubble. The presence of a mean separation bubble is hilighted by the reverse flow region characterized by negative longitudinal velocity. An overall agreement is found between the two simulations. Moreover, some details obtained by Adler and Gaitonde [2018] using the finer mesh are catched by the current DNS. It is particularly visible in the expansion fan after the shock impingement where the velocity variations computed in the current DNS match the details captured by the fine grid in the simulations of Adler and Gaitonde [2018].

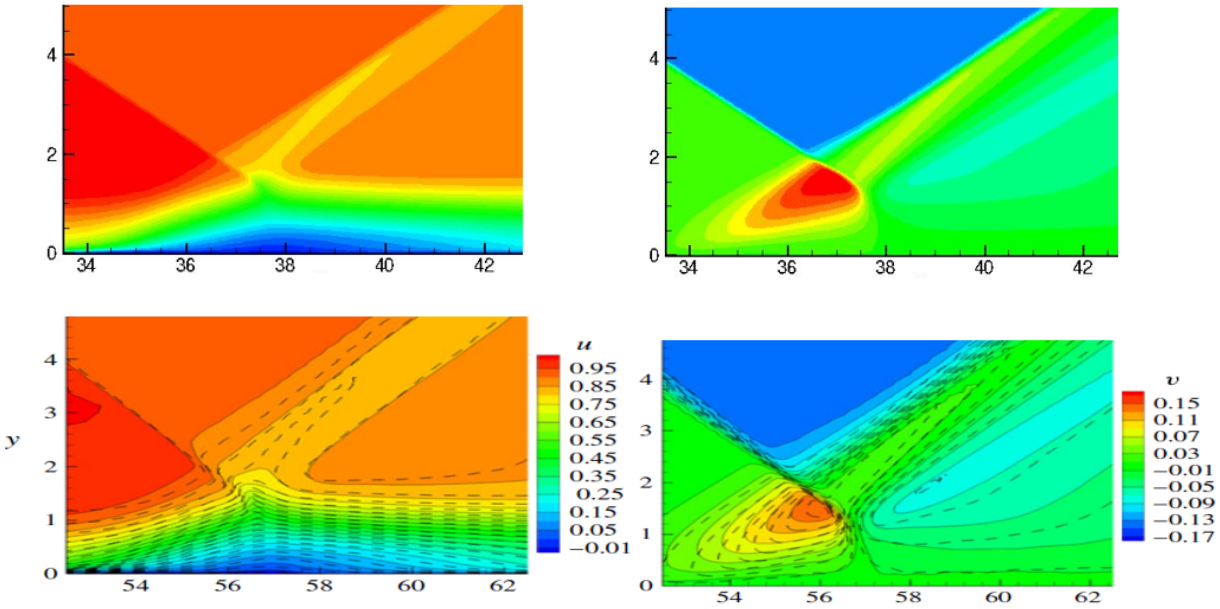

FIGURE 6.3 – Time mean velocity averaged in the spanwise direction in the interaction zone. Up left: longitudinal velocity (current DNS), Up right: vertical velocity (current DNS), Bottom left: longitudinal velocity (from Adler and Gaitonde [2018]), Bottom right: vertical velocity (from Adler and Gaitonde [2018]). For the results from Adler and Gaitonde [2018], the color contours correspond to a coarser mesh ($\Delta x^+ = 23.5$, $\Delta y_w^+ = 0.4$, $\Delta z^+ = 8.9$), whereas the dashed contour lines correspond to a finer mesh solution ($\Delta x^+ = 16.4$, $\Delta y_w^+ = 0.4$, $\Delta z^+ = 6.1$).

The time means of the Reynolds stresses averaged in the spanwise direction are shown in figures 6.4 to 6.7. As these data were not provided by Adler and Gaitonde [2018], the fields are compared to those obtained by the LES of Aubard [2012] for a SWTBLI at M = 2.25, $Re_\theta = 3725$ and a deviation angle of 8°. The shock wave strength (pressure ratio) in the simulation of Aubard [2012] is then slightly lower than in our simulations. The qualitative agreement between the results is good. For both simulations, a strong enhancement of the turbulent intensity occurs at the separation point and denotes the existence of the shear layer surrounding the separation bubble. The maximum turbulent intencities follow the shear layer and decreases progressively as the boundary layer reattaches downstream of the interaction.

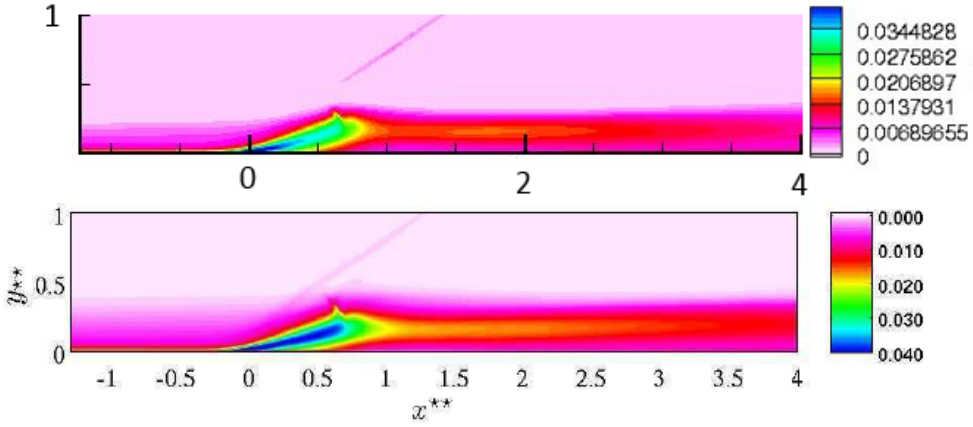

FIGURE 6.4 – Mean value of u^2_{rms}/U^2_∞ averaged in the spanwise direction in the interaction zone. Up: current DNS. Bottom: DNS from Aubard [2012] with $x^{**} = \frac{x-\overline{X}_s}{\overline{X}_r-\overline{X}_s}$ and $y^{**} = \frac{y}{\overline{X}_r-\overline{X}_s}$ ($\overline{X}_s$ is the mean separation point and $\overline{X}_r$ is the mean reattachment point).

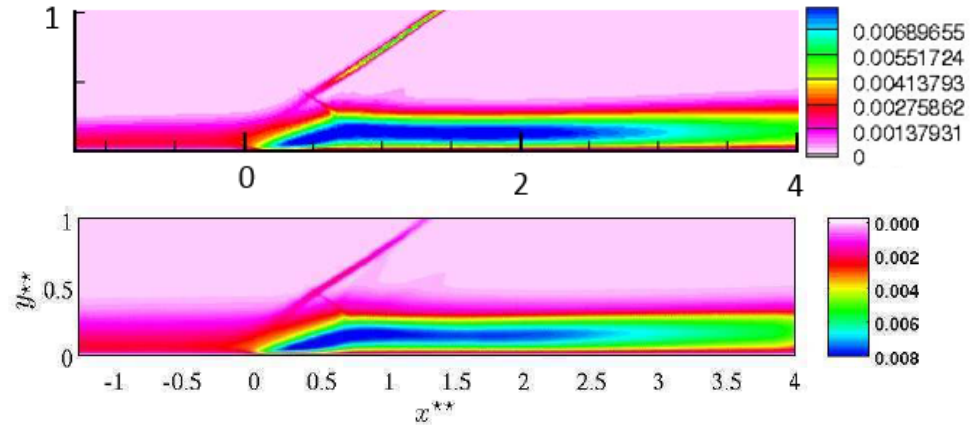

FIGURE 6.5 – Mean value of v^2_{rms}/U^2_∞ averaged in the spanwise direction in the interaction zone. Up: current DNS. Bottom: DNS from Aubard [2012] with $x^{**} = \frac{x-\overline{X}_s}{\overline{X}_r-\overline{X}_s}$ and $y^{**} = \frac{y}{\overline{X}_r-\overline{X}_s}$ ($\overline{X}_s$ is the mean separation point and $\overline{X}_r$ is the mean reattachment point).

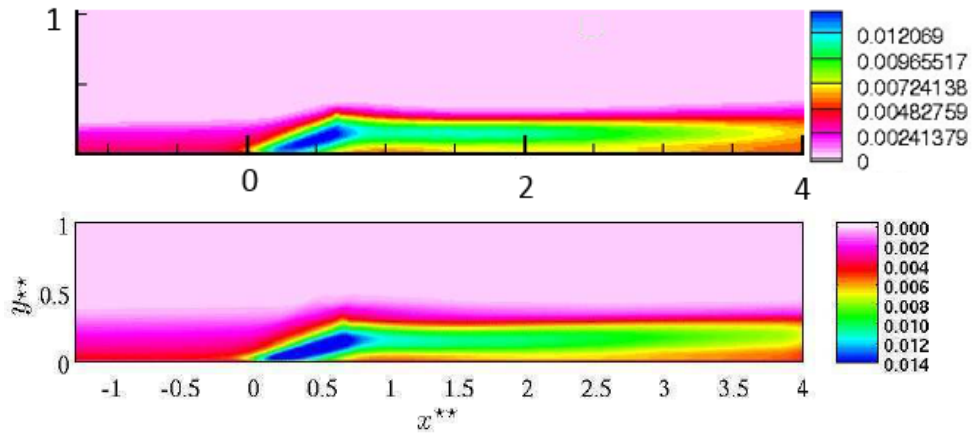

FIGURE 6.6 – Mean value of w^2_{rms}/U^2_∞ averaged in the spanwise direction in the interaction zone. Up: current DNS. Bottom: DNS from Aubard [2012] with $x^{**} = \frac{x-\overline{X}_s}{\overline{X}_r-\overline{X}_s}$ and $y^{**} = \frac{y}{\overline{X}_r-\overline{X}_s}$ ($\overline{X}_s$ is the mean separation point and $\overline{X}_r$ is the mean reattachment point).

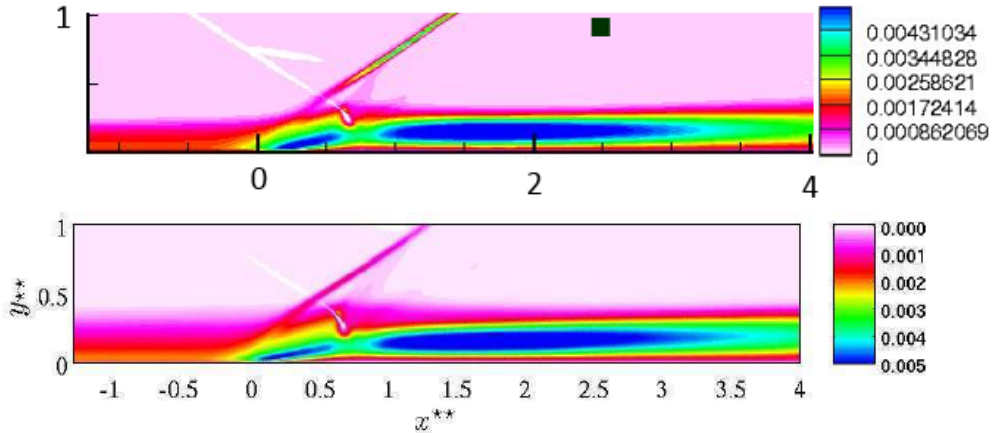

FIGURE 6.7 – Mean value of uv_{rms}/U_∞^2 averaged in the spanwise direction in the interaction zone. Up: current DNS. Bottom: DNS from Aubard [2012] with $x^{**} = \frac{x-\overline{X}_s}{\overline{X}_r-\overline{X}_s}$ and $y^{**} = \frac{y}{\overline{X}_r-\overline{X}_s}$ ($\overline{X}_s$ is the mean separation point and $\overline{X}_r$ is the mean reattachment point).

The time mean value of the skin friction coefficient (C_f) averaged in the spanwise direction is shown in figure 6.8. The mean abscissa of the separation point can be defined as the abscissa for which this curve becomes negative. We obtain $\overline{X}_s = 34.21\delta$. The mean abscissa of the reattachment point can be defined as the abscissa for which this curve becomes positive again. We obtain $\overline{X}_r = 39.13\delta$. The mean separation length can be defined as the difference $\overline{X}_r - \overline{X}_s$. We obtain $\overline{L} = 4.92\delta$. This value is to be compared to the mean separation length of 4δ obtained by Adler and Gaitonde [2018]. The lower value of the mean separation length obtained by Adler and Gaitonde [2018] is consistant with the lower strength of the shock in their simulation than in our present configuration.

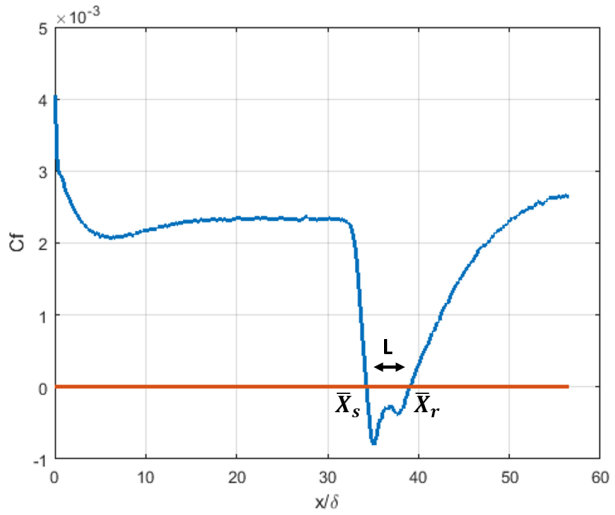

FIGURE 6.8 – Time mean C_f averaged in the spanwise direction with respect to x/δ. $\overline{L}$ denotes the mean separation length, $\overline{X}_s$ denotes the mean separation point and $\overline{X}_r$ denotes the mean reattachment point.

The time mean values of the wall pressure and the skin friction coefficient averaged in the spanwise direction are shown in figures 6.9 and 6.10. The values are compared with the results from Adler and Gaitonde [2018]. The strength of the shock wave being slightly smaller in the SWTBLI simulated by Adler and Gaitonde [2018] than in the current DNS, some discrepancies are observed. The pressure rise is sharper in the current simulation than in Adler and Gaitonde [2018], which is consistent with the higher pressure ratio of the SWTBLI. The skin friction coefficient upstream of the interaction appears to be lower in the simulation of Adler and Gaitonde [2018] than

in the current DNS. This discrepancy between the values of the skin friction coefficient before the interaction is in contradiction with the results presented in chapter 5 for the same boundary layer in which perfect agreement was obtained for the skin friction coefficient. Results from Adler and Gaitonde [2018] are therefore not consistant with the results from Mullenix et al. [2013] and must therefore be interpreted with caution. Within the separation, discrepancies are also observed between the skin friction disctributions obtained. The skin friction distribution within the separation bubble reported in Adler and Gaitonde [2018] in much intense (with lower skin friction values) than the one obtained in our DNS. Moreover, as for the SWLBLI presented in chapter 4, two local minima are observed in the skin friction distribution obtained in our DNS. The local maximum between these minima has nevertheless a lower value than in the SWLBLI simulation. This behavior, not observed in the results reported by Adler and Gaitonde [2018] is observed in other studies such as Pirozzoli and Grasso [2006]. The discrepancies observed between the skin friction coefficients can be attributed to the difference in the grid resolution between the two simulations. Indeed, the mesh used in Adler and Gaitonde [2018] ($\Delta x^+ = 23.5$, $\Delta y_w^+ = 0.4$, $\Delta z^+ = 8.9$) is coarser than our mesh in the longitudinal and transversal directions. In Aubard [2012], a study of the skin friction variability between different studies concluded that the skin friction distribution in the separated zone is particularly sensitive to the grid refinement in the longitudinal direction.

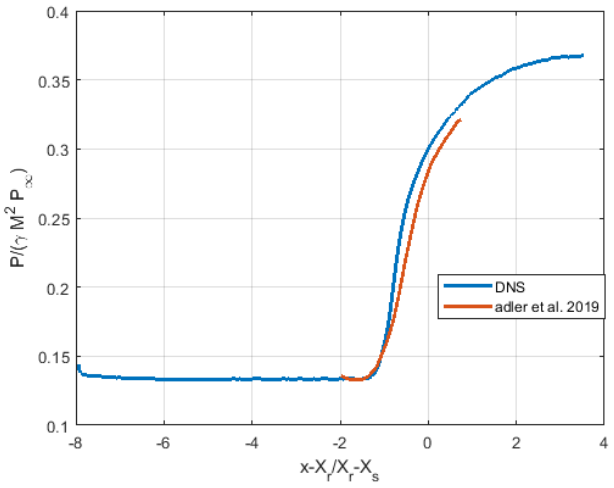

FIGURE 6.9 – Time mean pressure averaged in the spanwise direction with respect to $(x-\overline{x}_r)/(\overline{x}_r-\overline{x}_s)$.

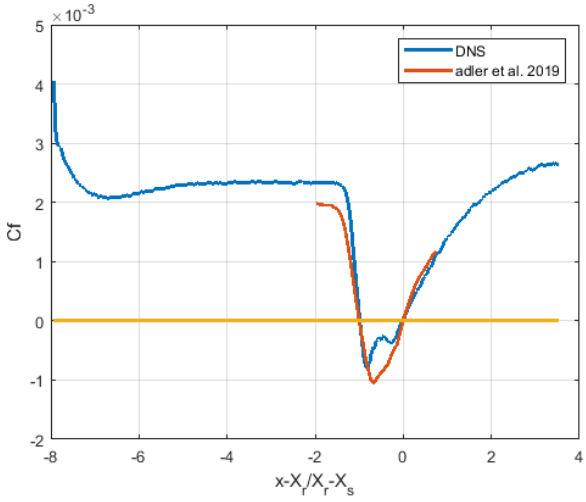

FIGURE 6.10 – Time mean C_f averaged in the spanwise direction with respect to $(x-\overline{x}_r)/(\overline{x}_r-\overline{x}_s)$.

6.3 Dynamics of the flow

We now focus on the dynamics of the interaction zone.
We first recall some well known dynamical properties of the SWTBLI already presented in chapter 1.

— the incoming boundary layer is turbulent with the most energetic fluctuations at high frequencies characterized by a Strouhal number $S_\delta = \frac{f\delta}{U_\infty} \sim 1$ (where f, is the characteristic frequency of the fluctuations).

— The shear layer is submitted to a convective instability (Kelvin-Helmholtz waves). The non linear evolution of the Kelvin-Helmholtz waves leads to a vortex shedding at a Strouhal number around $S_L = \frac{fL}{U_\infty} \simeq 0.6-0.8$ based on the length (L) of the recirculation bubble .

— The shear layer is also submitted to an absolute instability called "flapping" of the shear layer that has the characteristic frequency $S_L = \frac{fL}{U_\infty} \simeq 0.12-0.15$. This flapping consists in successive enlargment and shrinkage of the recirculation bubble. The shrinkage is associated to a vortex shedding downstream of the recirculation bubble.

— For supersonic flows, a low frequency flapping mode of the shear layer have also been observed in addition to the medium frequency flapping at a Strouhal number of $S_L = \frac{fL}{U_\infty} \simeq 0.03 - 0.04$ (Dupont et al. [2007] Piponniau et al. [2009]). This low frequency flapping mode is also called the "breathing" of the separation bubble.

— A low frequency oscillation of the whole SWBLI system (the recirculation bubble in phase with the system of shock waves) is also observed in simulations and experiments (Délery and Dussauge [2009]). This instability, called the "unsteadiness" of the SWBLI, consists in an oscillation of the recirculation bubble coupled to the shock wave system. This low frequency phenomenon has the same characteristic Strouhal number as the breathing of the separation bubble, namely $S_L = \frac{fL}{U_\infty} \simeq 0.03 - 0.04$.

We first focus the analyses on the high frequency convective of the shear layer. In order to highlight the mechanism of vortex shedding at play in the shear layer bounding the recirculation bubble, a sequence of 2D slices of the flow is shown in figure 6.11 where $\mid \nabla P \mid$ is plotted, highlighting the position of the shock waves. Black patches are surimposed, corresponding to vortex structures identified according to the discriminant criterion introduced in Chong et al. [1998] and already used by Pirozzoli and Grasso [2006] in the context of SWTBLI simulations. The discriminant is defined as follows:

$$\Delta = \frac{27}{4} I_3^2 + (I_1^3 - \frac{9}{2} I_1 I_2) I_3 + (I_2^3 - \frac{1}{4} I_1^2 I_2^2) \tag{6.1}$$

where I_1, I_2 and I_3 are respectively the first, second and third invariant of $\nabla \mathbf{U}$ defined as follows:

$$\begin{aligned} I_1 &= \mathrm{tr}(\nabla \mathbf{U}) \\ I_2 &= \mathrm{tr}(\mathrm{com}(\nabla \mathbf{U})) \\ I_3 &= \det(\nabla \mathbf{U}) \end{aligned} \tag{6.2}$$

with tr denoting the trace, com denoting the comatrix and det denoting the determinant. Vortices are identified as regions in which the local topology of the streamlines is focal as defined in Chong et al. [1998]. The discriminant is positive in these regions. These regions where the discriminant is positive. In figure 6.11, the black patches identifying the vortices are regions where:

$$\frac{\Delta}{(U_\infty/\theta)^6} > 10^{-3} \tag{6.3}$$

This sequence shows the formation of vortices near the separation point that are convected in the shear layer and shed in the downstream boundary layer. Moreover, as alreary pointed out by Pirozzoli and Grasso [2006], the passage of the vortices at the foot of the incident shock wave results in an oscillatory motion of the incident shock waves foot. This phenomenon is highlighted in figure 6.11 where the location of one specific vortex is shown by a black circle. As this vortex approaches the foot of the incident shock, the incident shock wave moves in the downstream direction. The instantaneous motion of the foot of the incident shock wave is shown in figure 6.11 by the arrows. When the vortex reaches the incident shock wave, the intensity of the vortex decreases and the motion of the incident shock wave changes its direction.

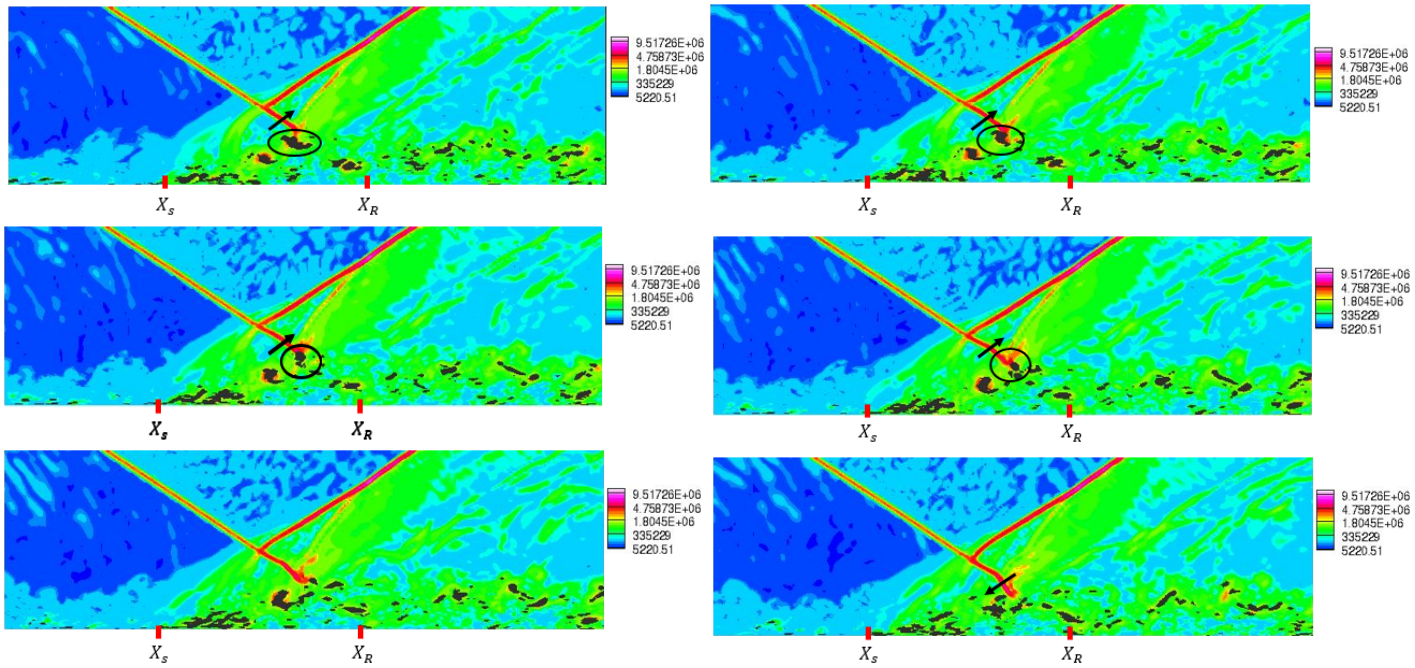

FIGURE 6.11 – 2D slices visualization of | ∇P | at time intervals of 1.92.L/U_∞ (from left to right and top to bottom). The position of the time mean separation and reattachment points positions averaged in the spanwise direction are respectively denoted by $\overline{X}_s$ and $\overline{X}_r$.

Several lines of probes have been placed in the shear layer bounding the recirculation bubble and in the downstream boundary layer. These lines are oriented in the spanwise direction with one probe in each mesh cell. For the sake of simplicity, in the following these lines of probes are abusibely called "probes". The signal of any quantity at these probes corresponds to the averaged value of the signal over all probes placed in the spanwise direction. The locations of these lines of probe in the plane $(\mathbf{x},\mathbf{y})$ are shown in figure 6.12. Probe 1 ($x/\delta = 34.3$, $y^+ = 0$) is located near the mean separation point. Probe 2 ($x/\delta = 36.2$, $y^+ = 150$ ($y/\delta \simeq 0.37$)) is located in the shear layer in the early part of the interaction. Probe 3 ($x/\delta = 37.5$, $y^+ = 150$ ($y/\delta \simeq 0.37$)) is quasi equidistant from $\overline{X}_s$ and $\overline{X}_r$. Probe 4 ($x/\delta = 41$, $y^+ = 150$ ($y/\delta \simeq 0.37$) is located just after the mean reattachment point. Probes 5 ($x/\delta = 46$, $y^+ = 150$ ($y/\delta \simeq 0.37$)) and 6 ($x/\delta = 56.6$, $y^+ = 150$ ($y/\delta \simeq 0.37$)) are in the downstream boundary layer. For each probe location in the plane $(\mathbf{x},\mathbf{y})$, a probe have been placed in each mesh cell in the spanwise direction.

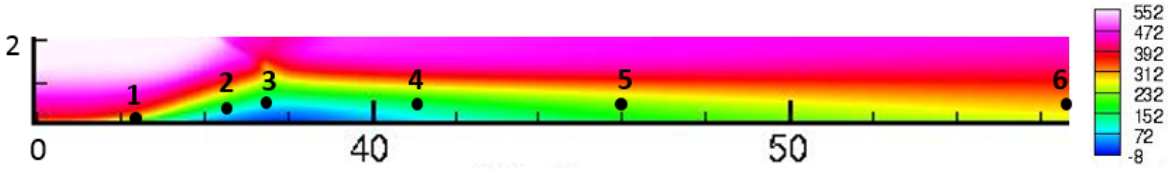

FIGURE 6.12 – Time mean longitudinal velocity field averaged in the spanwise direction. Locations of the probes. Probe 1: $x/\delta = 34.3$, $y^+ = 0$, Probe 2: $x/\delta = 36.2$, $y^+ = 150$ ($y/\delta \simeq 0.37$), Probe 3: $x/\delta = 37.5$, $y^+ = 150$ ($y/\delta \simeq 0.37$), Probe 4: $x/\delta = 41$, $y^+ = 150$ ($y/\delta \simeq 0.37$), Probe 5: $x/\delta = 46$, $y^+ = 150$ ($y/\delta \simeq 0.37$), Probe 6: $x/\delta = 56.6$, $y^+ = 150$ ($y/\delta \simeq 0.37$).

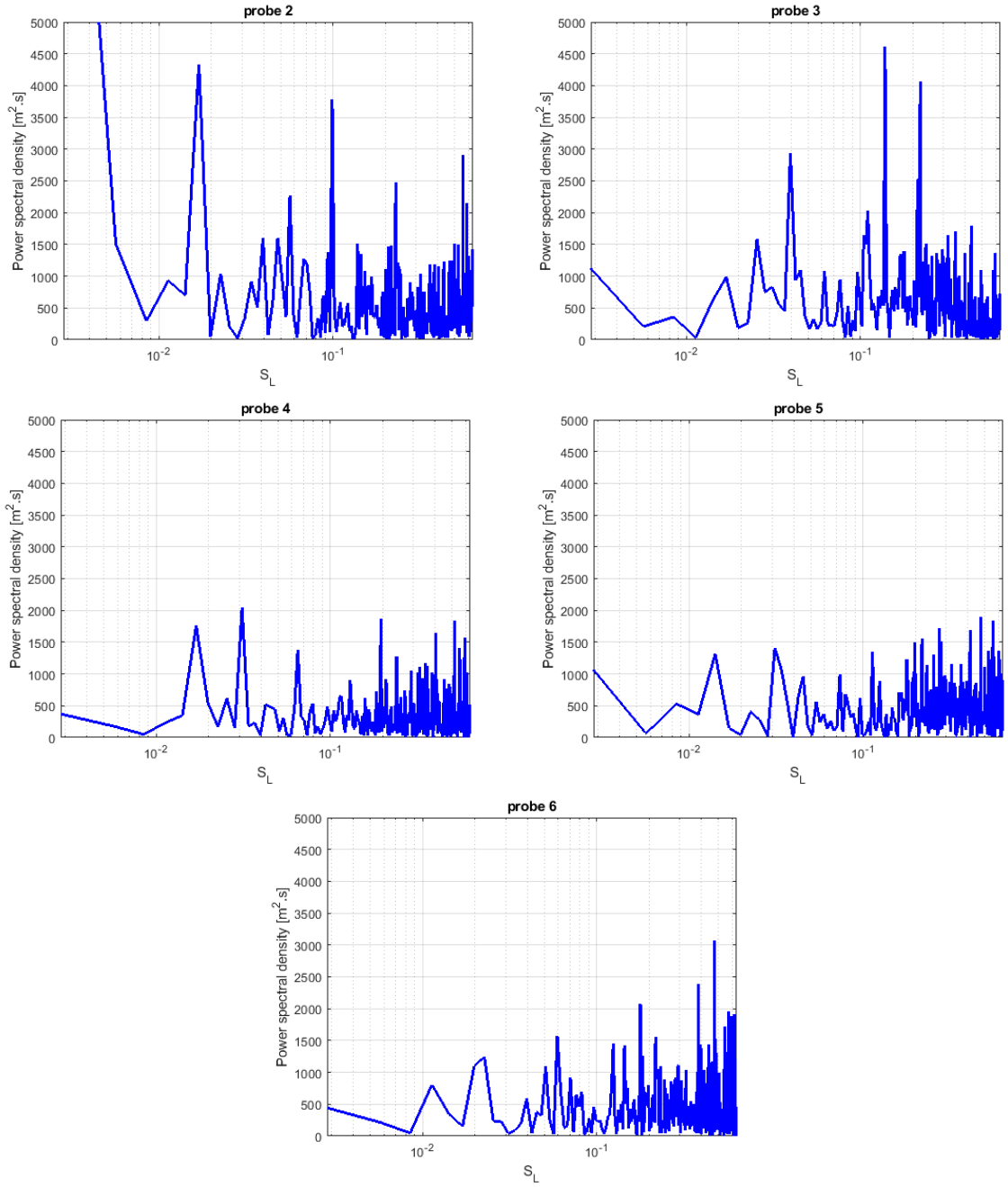

FIGURE 6.13 – Power spectral density of the longitudinal velocity signal for several probes located in the shear layer and the downstream boundary layer (see figure 6.12) with respect to the Strouhal number based on the separation length: Up left: probe 2. Up right: probe 3. Middle left: probe 4. Middle right: probe 5. Bottom: probe 6.

The power spectral density of the longitudinal velocity signals for the probes 2 to 6 are shown in figure 6.13. The spectra of probes 2 and 3 show the broadband dynamics of the flow at low and medium frequency scales with peak values characteristic of the medium frequency ($S_L \simeq 0.12 - 0.15$) and low frequency ($S_L \simeq 0.03 - 0.04$) flapping modes of the shear layer. Probe 2, located in the early part of the separation zone also has an intense peak value at a lower frequency $S_L \simeq 0.017$. The low frequency scales are still present in the downstream boundary layer (probes 4, 5 and 6) but with a decaying amplitude.

Histories of the separation and reattachment point abscissa averaged in the spanwise direction (respectively x_s and x_r) are plotted in figure 6.14. x_s corresponds to the most upstream abscissa at which the skin friction coefficient becomes negative. x_r corresponds to the most downtream abscissa at which the skin friction coefficient becomes positive again. Alternatively to the definitions

of the mean abscissa of the separation and reattachment point previously given in the commentary of figure 6.8, these quantities can be defined respectively as the time mean of x_s and x_r. We obtain $\overline{x}_s \simeq 34.25\delta$ and $\overline{x}_r \simeq 40.9\delta$. The amplitude of the reattachment point motion is significantly larger than the amplitude of the separation point motion. This is in accordance with results obtained by other authors (Pirozzoli and Grasso [2006], Aubard [2012]). The power spectral densities of these two signals have been computed and are shown in figure 6.15. The reattachment point is dominated by frequencies characteristic of the medium frequency ($S_L \simeq 0.15$) and low frequency ($S_L \simeq 0.03-0.05$) flapping of the shear layer, the medium frequency being more energetic. The motion of the separation point is dominated by the low frequency activity of the recirculation bubble and is characterized by the presence of very low frequency activity ($S_L \simeq 0.015$) already observed for the longitudinal velocity signal of probe 2 located in the early part of the recirculation bubble.

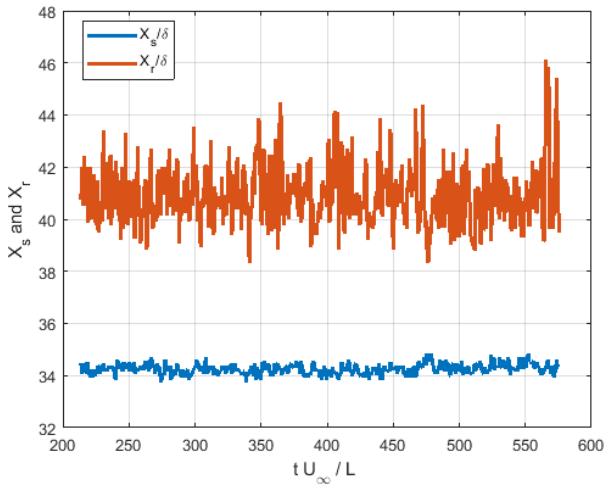

FIGURE 6.14 – Time history of the spanwise averaged locations of the separation point $x_s(t)$ and the reattachment point $x_r(t)$

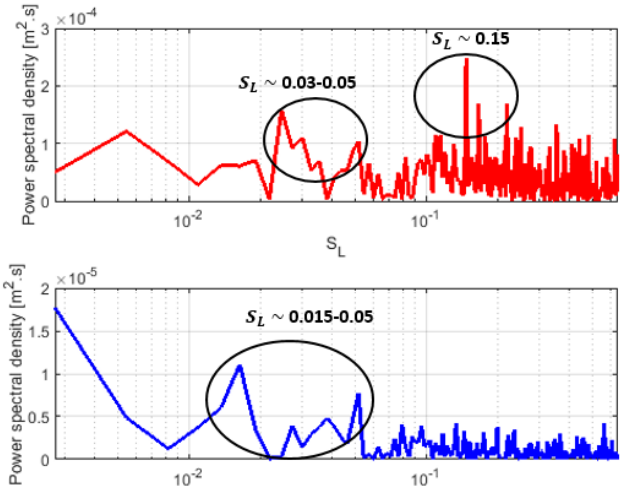

FIGURE 6.15 – Power spectral density of the time history of the spanwise averaged location of the separation point $x_s(t)$ (red) and the time history of the spanwise averaged location of the reattachment point $x_r(t)$ (blue).

The cross power spectral density between the histories of the spanwise averaged separation and reattachment point is shown in figure 6.16. It shows that these signals share energy at low frequency $S_L \simeq 0.015-0.05$ in the characteristic range of the low frequency flapping of the separation bubble.

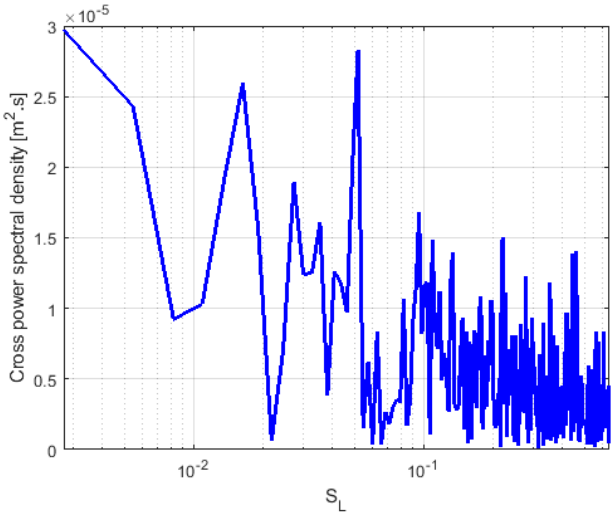

FIGURE 6.16 – Cross power spectral density between the histories of the spanwise averaged location of separation point $x_s(t)$ and reattachment point $x_r(t)$.

The covariance of $x_s(t)$ and $x_r(t)$ is shown in figure 6.17 highlighting the phase opposition between the motions of the separation point and the reattachment point. It shows that the separation zone is submitted to successive enlargments and shrinkages. The enlargments correspond to simultaneous upstream motion of the separation point and downstream motion of the reattachment point whereas the shrinkages correspond to simultaneous downstream motions of the separation point and upstream motion of the reattachment point. The covariance between the two signals have been computed as follows:

$$C_{x_s x_r}(\tau) = \frac{E([x_s(t) - \overline{x}_s][x_r(t+\tau) - \overline{x}_r])}{\sqrt{E([x_s - \overline{x}_s]^2)E([x_r - \overline{x}_r]^2)}} \tag{6.4}$$

where E(.) is the expected value of a random variable and τ the time lag.

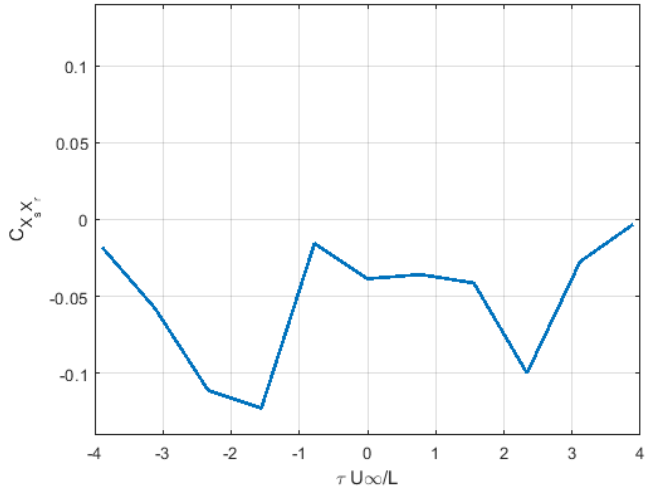

FIGURE 6.17 – Distribution of the covariance coefficient between the spanwise averaged separation and reattachment point positions as a function of the non dimensionalized time lag $\tau U_\infty / L$

The probability density function of $Cf = 0$ averaged in the spanwise direction (hereafter noted PDF($Cf = 0$)) in the interaction region is shown in figure 6.18. The mean separation abscissa ($\overline{x}_s/\delta = 34.25$) and the mean reattachment abscissa ($\overline{x}_r/\delta = 40.9$) are reported by vertical lines. The increase of PDF($Cf = 0$) before $\overline{x}_s$ is sharper than its decrease after $\overline{x}_r$. It is coherent with the

observation made in figure 6.14 that the amplitude of the motion of the reattachment point is significantly larger than the amplitude of the motion of the separation point.
Moreover, the progressive increase (respectively decrease) of PDF(Cf = 0) before $\overline{x}_s$ (respectively after $\overline{x}_r$) highlights the irregular amplitude of the separation (respectively reattachment) point oscillations that are submitted to temporal modulations. The modulation of the reattachment point oscillations are larger than the separation points oscillations.
The history of the skin friction averaged in the spanwise direction at $x = \overline{x}_s$ (respectively $x = \overline{x}_r$) is plotted in figure 6.19-top-left (respectively 6.19-top-right). The time average interval dt between two consecutive sign changes (Cf becoming negative) at $x = \overline{x}_s$ is $dt\mathrm{U}_\infty/\overline{\mathrm{L}} \simeq 4.1$, that corresponds to a frequency of $\mathrm{S}_\mathrm{L} \simeq 0.24$. At $x = \overline{x}_r$, we have $dt\mathrm{U}_\infty/\overline{\mathrm{L}} \simeq 9.1$ that corresponds to a frequency of $\mathrm{S}_\mathrm{L} \simeq 0.11$. Therefore, the sign change of the spanwise averaged skin friction coefficient at $x = \overline{x}_s$ and $x = \overline{x}_r$ occurs at frequencies more or less in the range of the characteristic frequency of the medium frequency flapping of the recirculation bubble. The probability of a change in the sign of Cf upstream of $x = \overline{x}_s$ is lower than at $x = \overline{x}_s$. The frequency of such a sign change is then lower. For example, the history of the skin friction averaged in the spanwise direction at $x/\delta = 34$ is plotted in figure 6.19-bottom-left. At this abscissa, the frequency of the change of the sign of Cf is $\mathrm{S}_\mathrm{L} \simeq 0.05$. Similarly, the probability of a change in the sign of Cf downstream of $x = \overline{x}_r$ is lower than at $x = \overline{x}_r$. The history of the skin friction averaged in the spanwise direction at $x/\delta = 42.75$ is plotted in figure 6.19-bottom-right. At this abscissa (downstream of $x = \overline{x}_r$), the frequency of the change of the sign of Cf is $\mathrm{S}_\mathrm{L} \simeq 0.03$.
The changes of the sign of the spanwise average skin friction coefficient upstream (respectively downstream) of the mean separation point (respectively reattachment point) therefore occurs at lower frequencies than near the mean separation point (respectively mean reattachment point). At the two selected abscissa, this low frequency falls in the characteristic range of the low frequency flapping of the recirculation bubble. These low frequency change of sign of the skin friction upstream (respectively downstream) of the mean separation (respectively reattachment) point corresponds to large displacements of the separation (respectively reattachment) point occuring at low frequency.

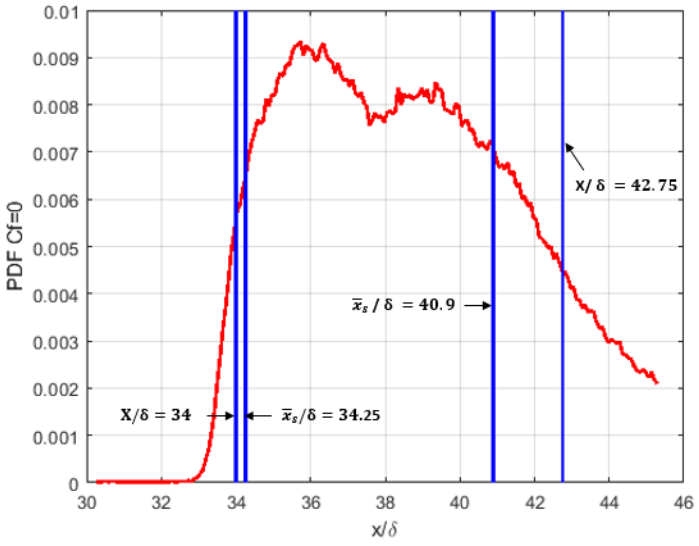

FIGURE 6.18 – Probability density function of Cf = 0 averaged in the spanwise direction

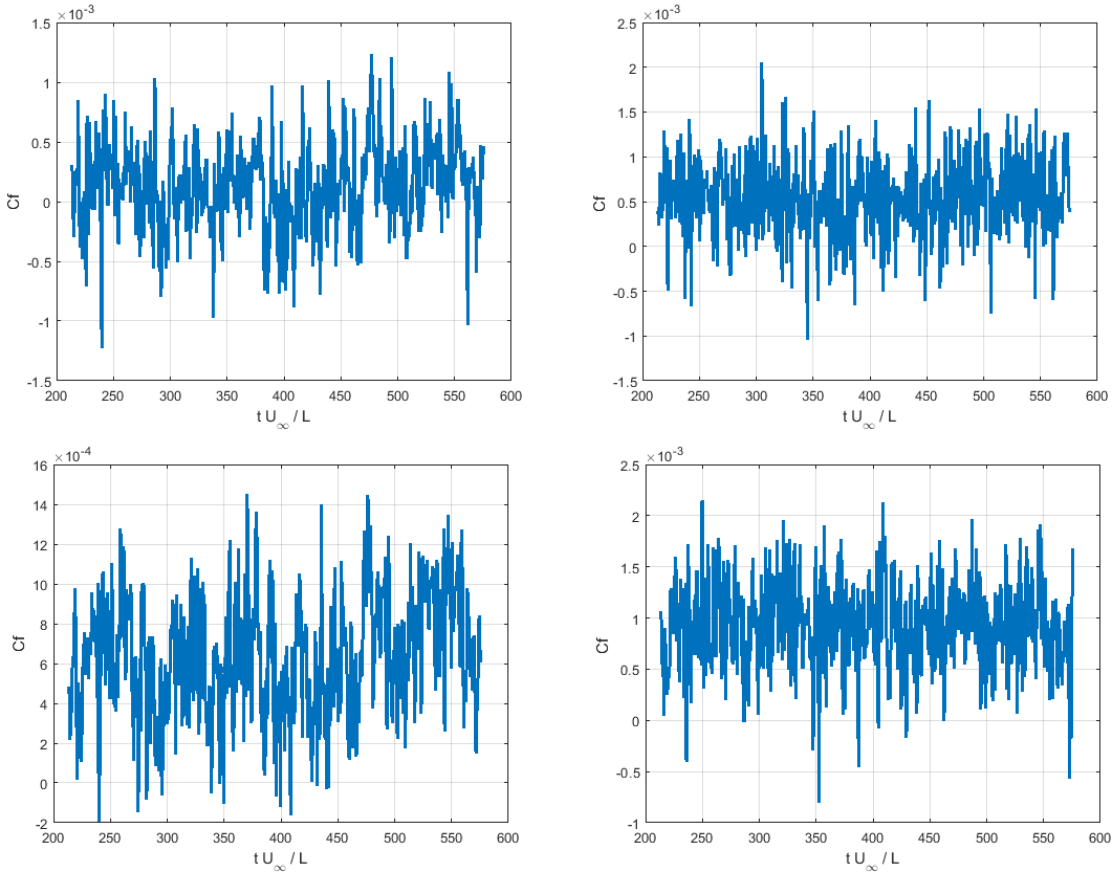

FIGURE 6.19 – History of the skin friction averaged in the spanwise direction at 4 abscissa in the interaction region. The 4 abscissa are highlighted by vertical lines in figure 6.18. Up left: $x/\delta = 34.25$ (mean separation point). Up right: $x/\delta = 40.9$ (mean reattachment point). Bottom left: $x/\delta = 34.0$. Bottom right: $x/\delta = 42.75$.

The extent of the separation bubble L (computed as $L = x_r - x_s$) versus time is shown in figure 6.20. The separation zone is submitted to successive enlargments and shrinkages. The standard deviation of L is 0.25L. The characteristic frequencies of this breathing motion of the separation bubble are shown in figure 6.21 where the power spectral density of $L(t)$ is plotted. It is very similar to the spectra of $x_r(t)$ as the amplitude of the reattachment point motion is significantly larger than the amplitude of the separation point motion.

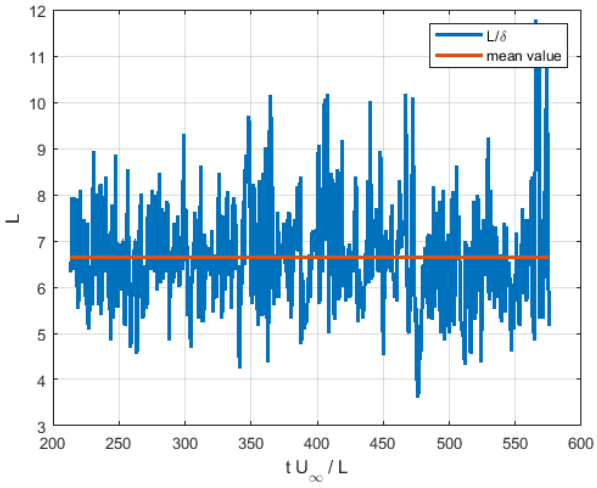

FIGURE 6.20 – Time history of the length of the separation bubble $L(t) = x_r(t) - x_s(t)$

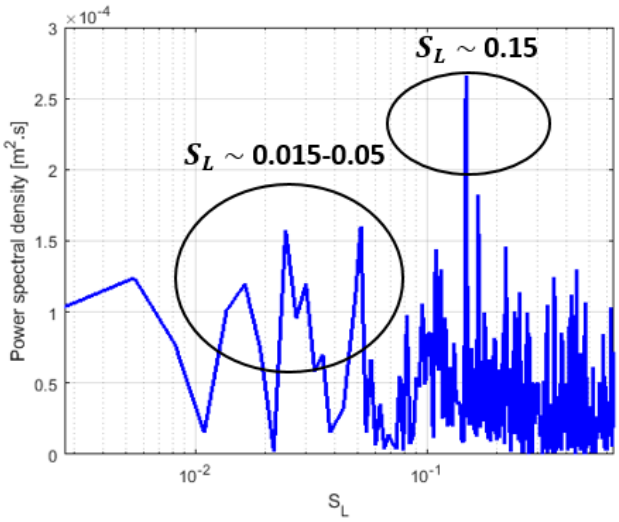

FIGURE 6.21 – Power spectral density of the time history of the length of the separation bubble $L(t) = x_r(t) - x_s(t)$.

Power spectral density of the wall pressure signal at the reflected shock foot (probe 1) is shown in figure 6.22. This spectrum is dominated by low frequencies, characterizing the dynamics of the eraly part of the separation, in the same range than the separation point. This spectrum of the pressure signal at the shock foot is characteristic of the SWTBLI unsteadiness (Touber and Sandham [2009]) and is due to the oscillations of the reflected shock wave.

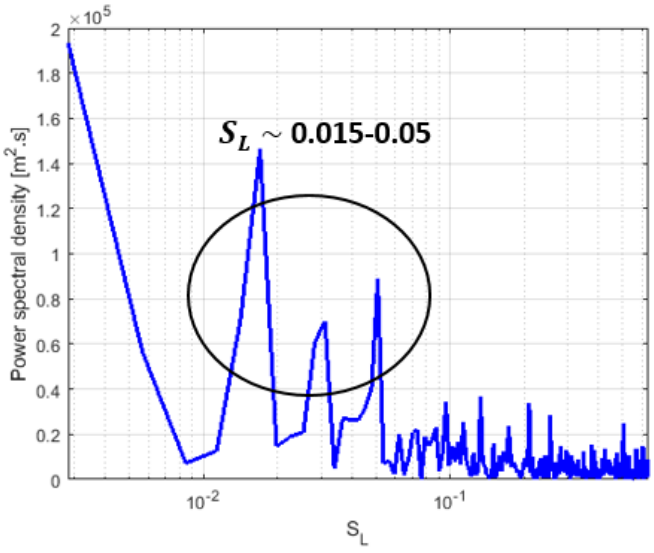

FIGURE 6.22 – Power spectral density of the wall pressure signal at the reflected shock foot (probe 1) with respect to the Strouhal number based on the separation length.

Figure 6.23 shows the history of the separation point location along the flat plate and the history of the position of the reflected shock waves foot X_{shock}. As in Aubard [2012], the position of the shock wave is identified at each time of acquisition as the abscissa for which the wall pressure becomes 30% bigger than P_∞. The standard deviation of X_{shock} is 0.16δ. The covariance of $X_s(t)$ and $X_{shock}(t)$ is shown in figure 6.24 highlighting the high correlation between the motions of the separation point and the reflected shock wave.

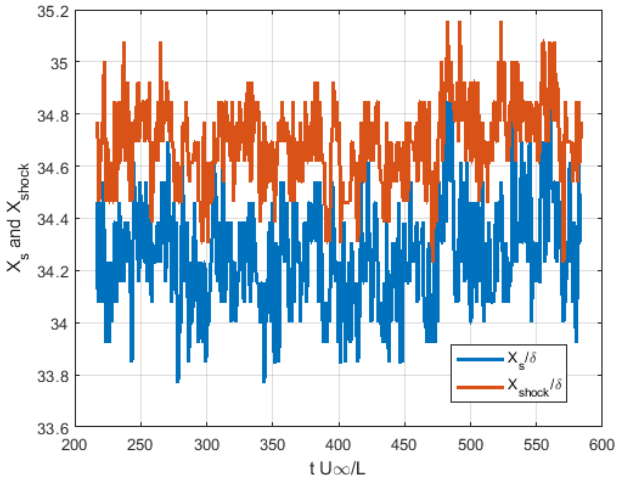

FIGURE 6.23 – Time history of the spanwise averaged location of the separation point $x_s(t)$ and the reflected shock foot $X_{shock}(t)$.

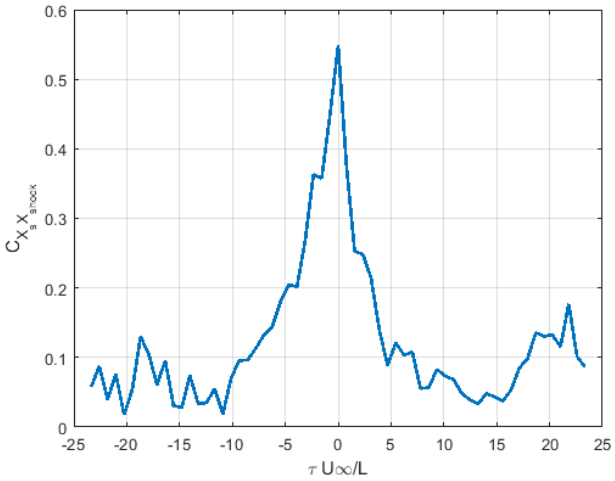

FIGURE 6.24 – Covariance between $x_s(t)$ and $X_{shock}(t)$.

The dynamics of the simulated SWTBLI exhibits most of the characteristic features already identified in the litterature. In particular, the shear layer surrounding the separation bubble is submitted to low frequency and medium frequency flapping associated to a vortex shedding in the downstream boundary layer. The dynamics of the early part of the interaction exhibits lower characteristic frequencies than the remaining of the interaction zone. The SWTBLI unsteadiness have also been reproduced. Indeed, the separation point and the reattachment point are submitted to low frequency oscillations and the reflected shock oscillates with the separation point.

6.4 POD analysis

POD is a method of data analysis that allows to obtain low dimensional approximate descriptions of high-dimensional processes. It is widely used data processing and has first been used by Lumley [1967] to identify coherent structures in turbulent flows. An introduction to POD and its use for the study of turbulent flows can be found in Holmes et al. [2012].
Any scalar (respectively vectorial) physical quantity $q(x,y,z,t)$ can be decomposed in scalar (respectively vectorial) spatial modes $\Phi^m(x,y,z)$ sorted by decaying energy ($\int_x\int_y\int_z(\Phi^m)^2dxdydz > \int_x\int_y\int_z(\Phi^{m+1})^2dxdydz \quad \forall \quad m \geqslant 1$):

$$q(x,y,z,t) = \sum_{m\geqslant 1} \alpha^m(t)\Phi^m(x,y,z), \tag{6.5}$$

where α^m is the temporal coefficient representing the amplitude of the m^{th} mode.
In our study, this decomposition is obtained using the snapshot POD technique Sirovich [1987] in which the temporal coefficients are obtained by solving the following eigenvalue problem:

$$\sum_{t'} C_{tt'}\alpha^m(t') = \lambda^m\alpha^m(t), \tag{6.6}$$

where the temporal correlation tensor writes

$$C_{tt'} = \int_x\int_y\int_z q(x,y,z,t).q(x,y,z,t')dxdydz. \tag{6.7}$$

where "." denotes a scalar product. The Euclidian scalar product is used in our study.
The eigen values λ^m represents the energy of the m^{th} mode.

The spatial modes Φ^m are computed by projecting the realizations ($q(x,y,z,t)$) onto the temporal coefficients as follows:

$$\Phi^m(x,y,z) = \sum_t q(x,y,z,t)\alpha^m(t) \tag{6.8}$$

The size of the eigen value problem to be solved (equation 6.6) is N_t (the number of snapshot considered). It has to be compared to the size of the eigen value problem to be solved in the classical POD technique introduced by Lumley [1967]. For the classical POD technique the problem size is $M.n_c$ where M is the number of mesh cells and n_c is the number of vector coordinates of the physical quantity q. When $N_t << M$, as in the present work, the size of the eigen value problem is then much lower for the snapshot POD technique than for the classical POD. It allows to save computing time and memory required to performe the POD.

In order to get more insight in the low frequency dynamics of the SWTBLI, a snapshot POD has been applied to the pressure and velocity fields in a subdomain bounding the interaction zone ($30.18 \leqslant x/\delta \leqslant 45.28$ and $0 \leqslant y/\delta \leqslant 4.45$). The method of snapshots was used with 361 fields with a time separation of $0.192\frac{L}{U_\infty}$. The time interval between the first and the last snapshot corresponds to about 2.5 low frequency SWTBLI unsteadiness periods and about 7 periods of the medium frequency flapping of the recirculation bubble. The DSYEVR function of the Lapack library, that computes both the eigenvalues and corresponding eigenvectors has been used to solve the eigen value problem (equation 6.6).

6.4.1 POD on the velocity field

The snapshot POD has been applied to the vectorial velocity field $\mathbf{u} = (u,v,w)^T$. The POD is applied on the whole part of the velocity; in other words, the analysis is not conducted on the velocity fluctuations after the time mean is substracted, as often employed. Then, the first POD mode is supposed to be representative of the time average of the field. In the following, the fluctuating modes refer to the modes higher than 1. The distribution of the eigenvalues obtained for the POD on the velocity field are shown in figure 6.25. The first mode, corresponding to the mean flow has an energy ($\lambda^1 = 2278$) much larger than the total fuctuating energy ($\sum_{m\geqslant 2}\lambda^m$). λ^1 is then not shown in figure 6.25.

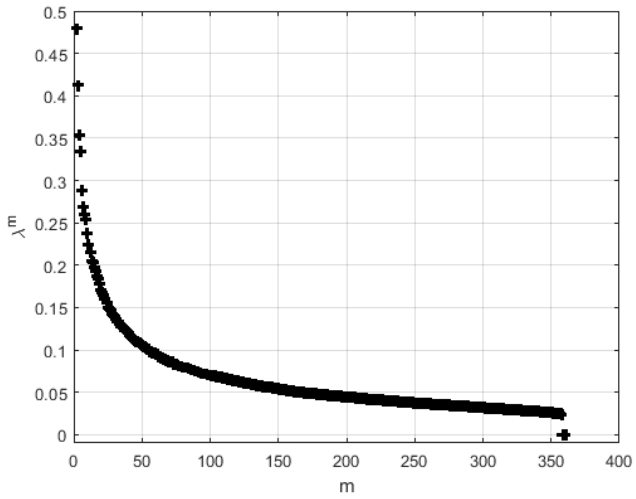

FIGURE 6.25 – POD spectrum on the velocity field. The first mode is not shown because it is too large, representing the time-average of the field.

In order to evaluate the dynamics associated to each fluctuating mode, their temporal amplitudes (α^m) have been computed and their Fourier transform are presented in figure 6.26. It shows that the POD decomposition consists roughly in modes associated to frequencies that roughly

grow linearly with the number of mode. The low frequency packets are mainly represented by the low order POD modes and on the opposite, the high order POD modes concern high frequencies. Consequently, the first fluctuating modes dominate the low frequency activity of the SWTBLI.

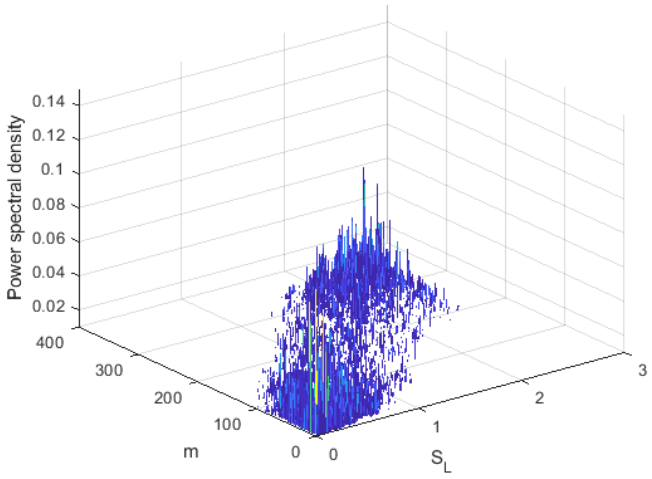

FIGURE 6.26 – Power spectral density of the temporal amplitudes α^m for the POD on the velocity field; only values bigger than 0.01 are plotted.

It can be visualized in figure 6.27-left where the average value of the power spectral density of α^m over two distinct sets of modes is plotted: for the first 29 fluctuating modes ($2 \leqslant m \leqslant 30$) (blue) and for the remaining modes ($m > 30$) (red). We see that the dynamical activity of the first 29 first fluctuating modes is dominated by low frequencies, especially in the range of frequency characteristic of the SWTBLI unsteadiness ($S_L \simeq 0.03 - 0.04$). In contrast, the dynamical activity of the other modes is located at higher frequencies. The spectral density of the POD energy contained in a set of modes Υ is defined as follows:

$$\varpi(\Upsilon) = \sum_{m \in \Upsilon} \lambda^m \, | \, \hat{\alpha}^m(f) \, |^2 \tag{6.9}$$

where $\hat{\alpha}^m(f)$ is the Fourier transform of α^m.
The spectral density of the POD energy is plotted in figure 6.27-right for the first 29 fluctuating modes ($2 \leqslant m \leqslant 30$) (blue) and for the remaining modes ($m > 30$) (red). It shows that the first 29 fluctuating modes contain most of the POD energy at low frequency. Nevertheless, we see that the medium frequency dynamics ($S_L \simeq 0.1$) is more energetic than the low frequency dynamics characteristic of the SWTBLI unsteadiness ($S_L \simeq 0.03 - 0.04$).

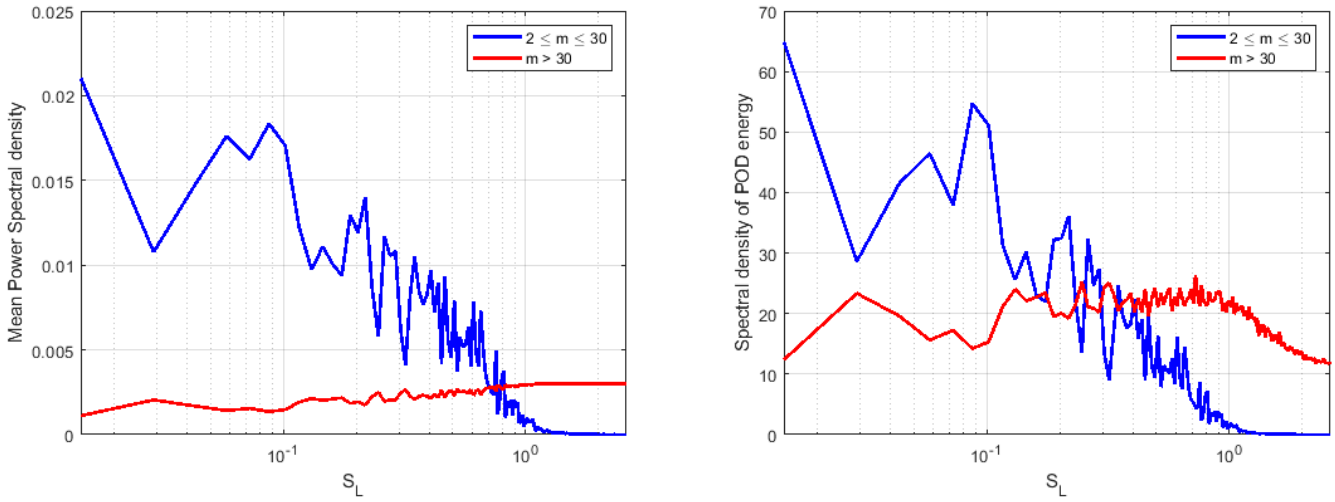

FIGURE 6.27 – Left: average of the power spectral density of α^m over two distinct sets of modes for the POD on the velocity field. Right: spectral density of POD energy for two distinct sets of modes for the POD on the velocity field.

6.4.2 POD on the pressure field

The snapshot POD has been applied to the pressure field. The POD spectrum on the pressure fluctuating field is shown in figure 6.28. The decay of the POD energy is much sharper for the pressure than for the velocity. It shows the much higher complexity of the velocity field (3 component vector) with respect to the pressure field (scalar).

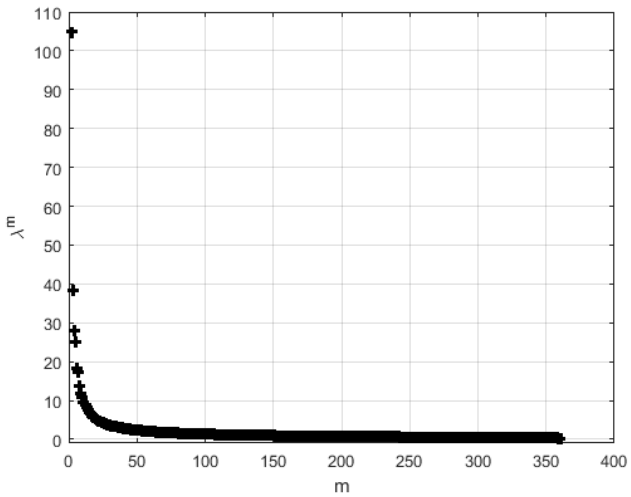

FIGURE 6.28 – POD spectrum on the pressure field. The first mode is not shown because it is too large ($\lambda^1 = 236432$).

The POD on the pressure consists in modes whose dynamical activity is located at frequencies increasing with the number of the mode. It is visible in figure 6.29 where the Fourier transform of the temporal amplitudes α^m have been plotted for each mode.

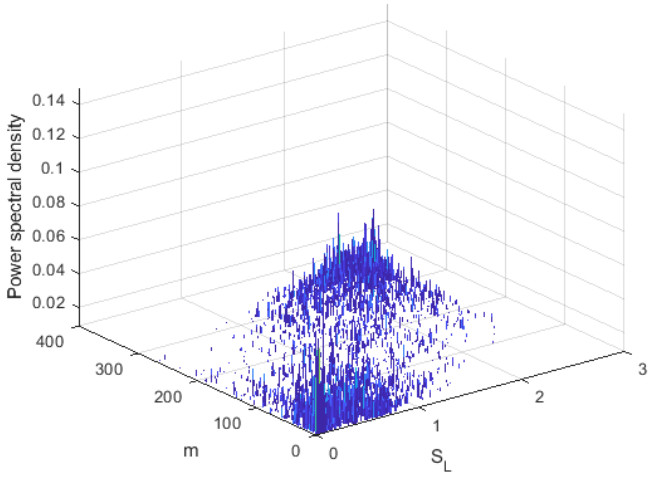

FIGURE 6.29 – Power spectral density of the temporal amplitudes α^m for the POD on the pressure field; only values bigger than 0.01 are plotted.

The power spectral density of α^m averaged on the 29 first fluctuating modes ($2 \leqslant m \leqslant 30$) (blue) and the remaining modes ($m > 30$) (red) are plotted in figure 6.30-left for the POD on the pressure field. As for the POD of the velocity field, the dynamical activity of the first 29 fluctuating modes is dominated by low frequency activity in contrast with higher order modes. The spectral density of the POD energy (defined in equation 6.9) is plotted in figure 6.30-right for the first 29 fluctuating modes (blue) and for the remaining modes ($m \geqslant 30$) (red). Most of the POD energy at low frequency is contained in the 29 first fluctuating modes. Nevertheless, as for the reconstruction of the velocity field, we see that the medium frequency dynamics ($S_L \simeq 0.1$) is more energetic than the low frequency dynamics characteristic of the SWTBLI unsteadiness ($S_L \simeq 0.03-0.04$). The difference between the POD energy contained in the 29 first fluctuating modes and in the remainder of modes is much larger than for the POD on the velocity field. It is due to the sharper decay of the energy contained in each mode in the POD on the pressure field with respect to the POD on the velocity field.

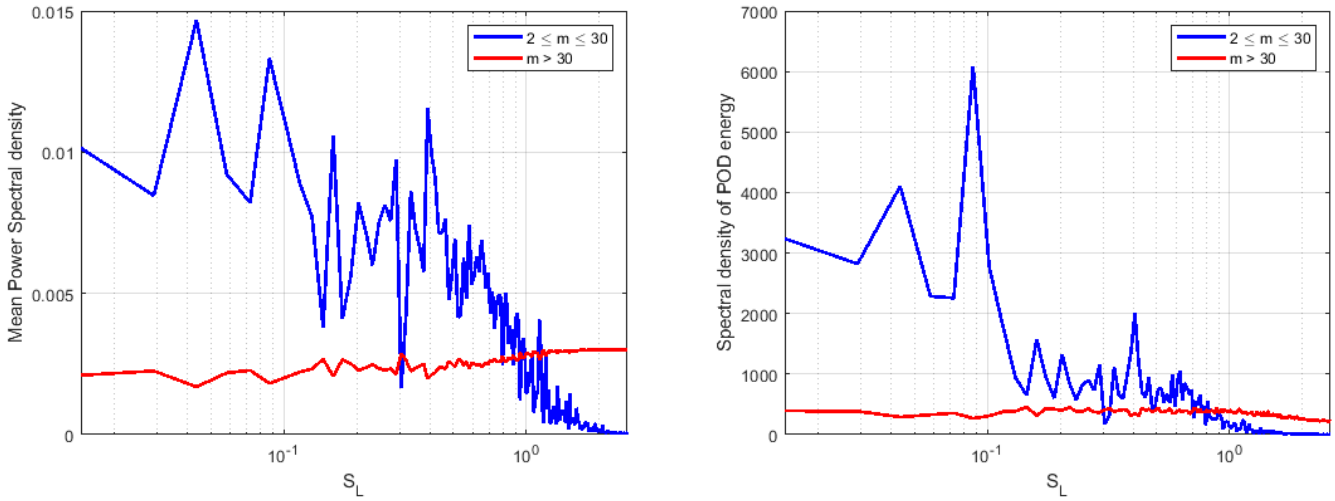

FIGURE 6.30 – Left: average of the power spectral density of α^m over two distinct sets of modes for the POD on the pressure field . Right: spectral density of POD energy for two distinct sets of modes for the POD on the pressure field.

6.4.3 Flow reconstruction using low modes

As shown above, both on the velocity field and on the pressure field, the low frequency activity of the flow is mostly contained in the first 29 fluctuating modes, both for the velocity field and the pressure field. In order to get more insight in the low frequency dynamics of the flow, especially in the range of frequency of the SWTBLI unsteadiness, we reconstructed the time evolution of the velocity and of the pressure fields using only the first 30 POD modes as follows:

$$q_r(x,y,z,t) = \sum_{m=1}^{30} \alpha^m(t)\Phi^m(x,y,z) \tag{6.10}$$

where q_r is the reconstructed field (velocity or pressure field).

The reconstruction obtained have then been averaged in the homogeneous spanwise direction. A representative snapshot visualization of the 2D reconstructed fields is shown in figure 6.31. The magnitude of the vorticity ω_z (in the spanwise direction) of the reconstructed velocity field shows the creation of vortices in the vicinity of the separation point that are convected through the shear layer bounding the recirculation bubble. The shedding of these structures in the downstream boundary layer is also clearly visible. It can also be indentified in the pressure field where a large region of low pressure is released from the separation zone. The creation of vortex structures and their shedding downstream of the boundary layer have already been identified in snaphsot visualisation of the actual flow (see section 6.3). The prevalence of this phenomenon in the low modes reconstruction of the flow highlights its importance in the low frequency dynamics of the SWTBLI.

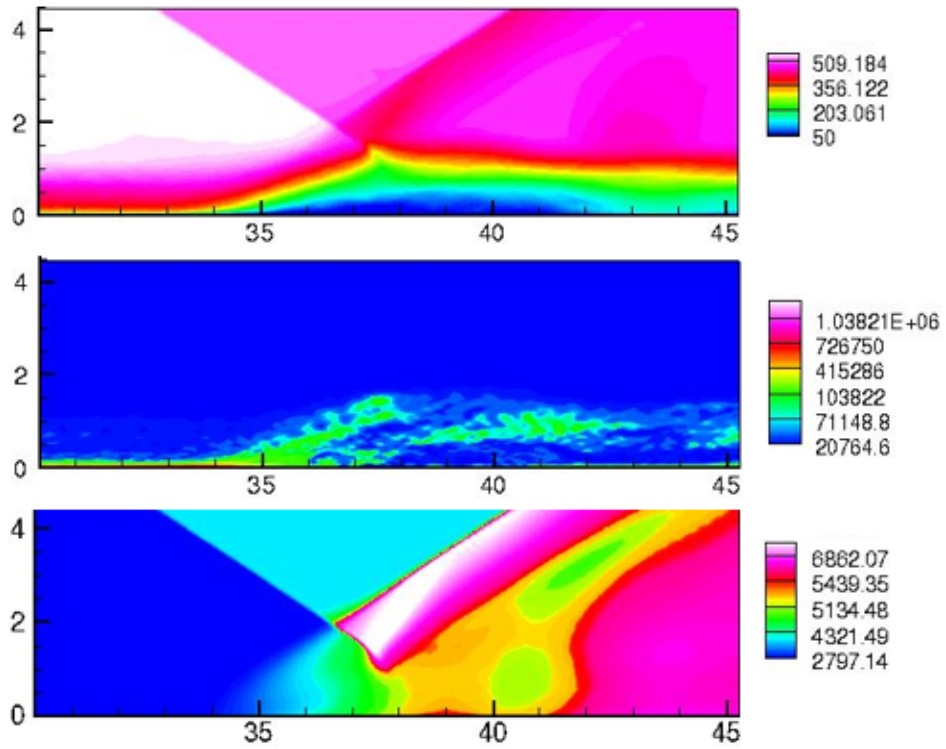

FIGURE 6.31 – Reconstructed fields using the first 30 POD modes. Top: longitudinal reconstructed velocity. Middle: magnitude of the spanwise vorticity reconstructed with the velocity field. Bottom: reconstructed pressure.

In order to get more insight in the dynamics of the reconstructed flow, the power spectral densities of the reconstructed longitudinal velocity at probes 2, 3 and 4 are shown in figure 6.32. In the early part of the separation bubble (probe 2), the dynamical activity is dominated by low frequencies $S_L \simeq 0.015 - 0.04$ characteristic of the breathing of the recirculation bubble. An other peak

is observed at higher frequency ($S_L \simeq 0.06 - 0.1$) that may be interpreted as the signature of the flapping of the shear layer at medium frequency in the low mode reconstruction. At probe 3, located more downstream in the separation bubble, the low frequency activity is less intense contrary to the medium frequency activity ($S_L \simeq 0.1$) that is greatly increased. At probe 4, located in the downstream boundary layer just after the reattachment of the boundary layer, the low and medium frequency activity is still present in the flow but with a lower amplitude. This analysis of the reconstructed longitudinal velocity signal at probes 2, 3 and 4 is globally in accordance with the analysis of the actual longitudinal velocity signal at same locations (figure 6.13). It shows that the main features of the low frequency activity of the flow are conserved in the low modes reconstruction of the flow.

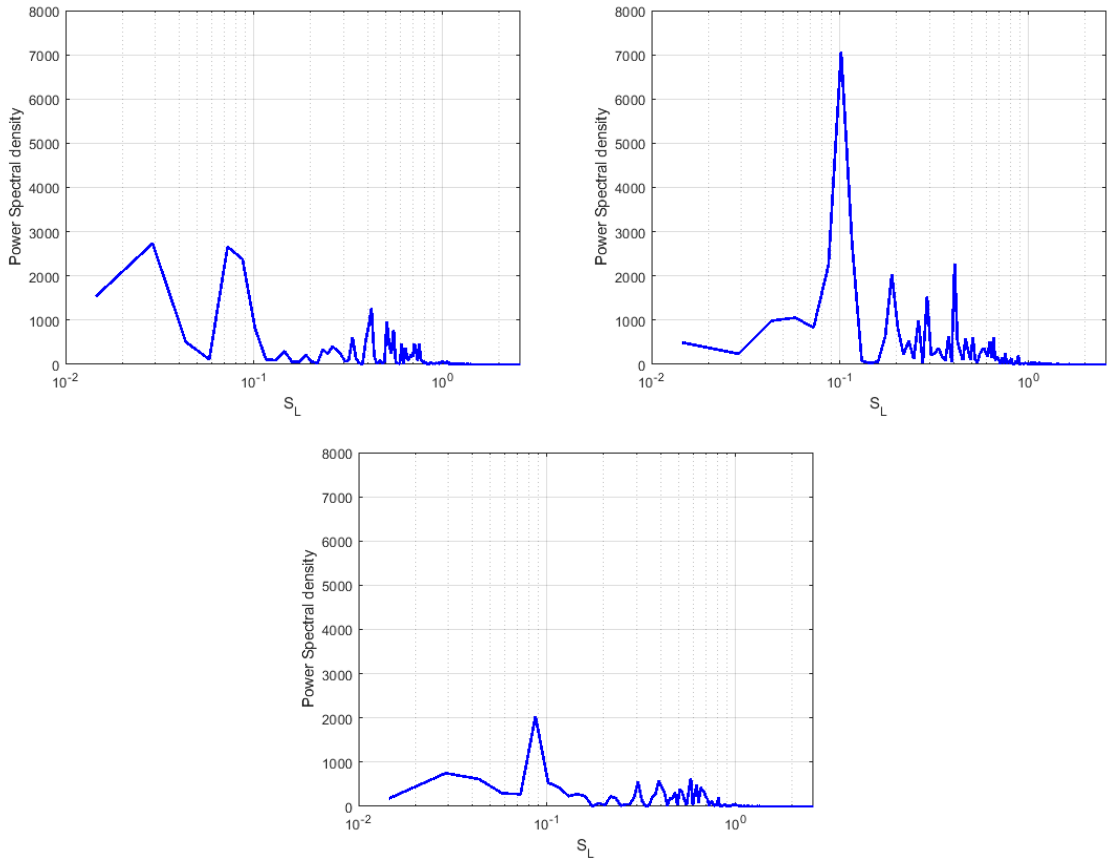

FIGURE 6.32 – Power spectral density of the longitudinal velocity signal for several probes (see figure 6.12) with respect to the Strouhal number based on the separation length: Up left: probe 2. Up right: probe 3. Bottom: probe 4.

The pressure signal in the viscinity of the reflected shock foot (same coordinates than probe 1, see figure 6.12) is plotted in figure 6.33-left. The clearly visible low frequencies oscillations of this signal are due to the motion of the reflected shock wave foot. The power spectral density of the pressure signal at the shock foot is shown in figure 6.33-right. The spectrum is dominated by low frequencies characterizing the SWTBLI unsteadiness in the same range than the spectrum of the wall pressure near the reflected shock foot in the actual flow shown in figure 6.22.

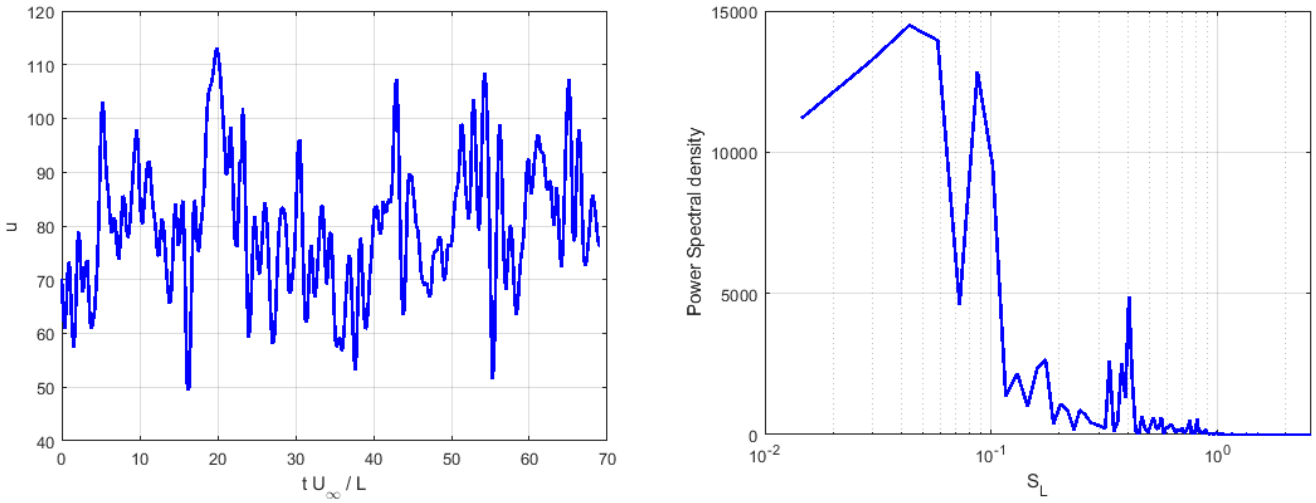

FIGURE 6.33 – Left: pressure signal at the reflected shock foot (same coordinates than probe 1, see figure 6.12). Right: power spectral density of the wall pressure signal at the reflected shock foot with respect to the Strouhal number based on the separation length.

The time evolution of the reconstructed velocity and pressure fields averaged in the spanwise direction allows the analysis of the low frequency dynamics of the separated zone. Indeed, only the modes responsible for the low frequency dynamics of the flow are used for the reconstruction. When looking at animations of the reconstructed flow (not shown here), one can see that the dynamic of the flow is dominated by the medium frequency flapping of the recirculation bubble. As an illustration of this dominant dynamic feature of the reconstructed flow frequency packets, a sequence of visualizations of the reconstructed longitudinal velocity averaged in the spanwise direction at time interval of $1.92L/U_\infty$ is shown in figure 6.34-left The sequence shown in figure 6.34 spreads over a period of $7.68L/U_\infty$ that corresponds to a Strouhal number based on the length of the separation zone $S_L \simeq 0.13$ characteristic of the medium frequency flapping of the separation bubble. A sequence of visualizations of the reconstructed pressure field averaged in the spanwise direction at the same times is shown in figure 6.34-right. These sequences correspond to a cycle of enlargment and shrinkage of the separation bubble. The phase of enlargment corresponds to a motion of the reflected shock wave in the upstream direction (in phase with the motion of the separation point as shown in figure 6.24). It is shown by the arrow indicating the instantaneous direction of the reflected shock wave. The shrinkage phase is accompanied with a shedding of a large amount of fluid from the recirculation zone shown by a circle. This shedding is particularly easily identifiable in the last visualisation of the pressure field sequence where a region of low pressure is shed from the recirculation bubble in the downstream boundary layer.

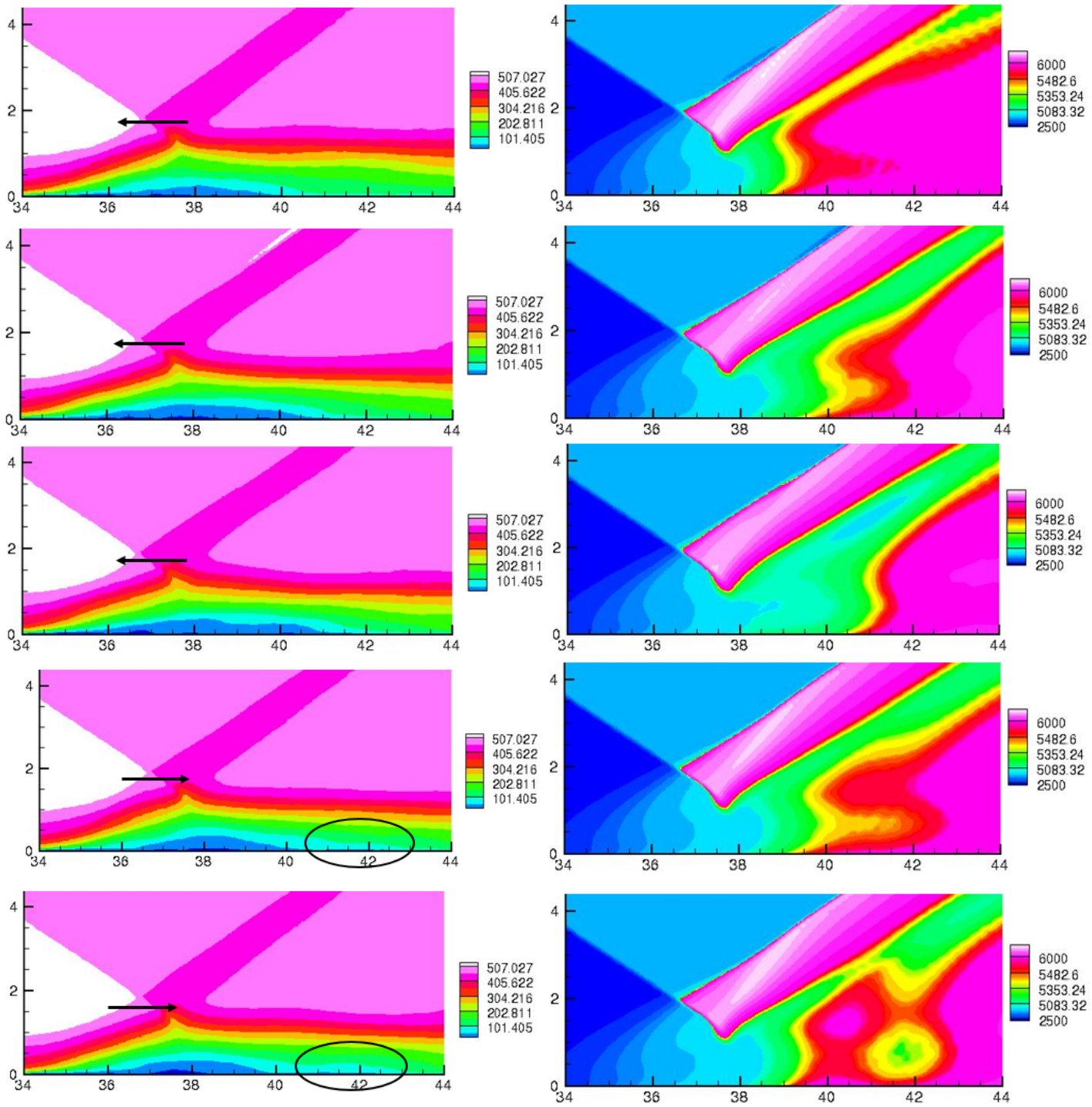

FIGURE 6.34 – Left: sequence of visualizations of the reconstructed longitudinal velocity averaged in the spanwise direction at time intervals of $1.92L/U_\infty$. Right: sequence of visualizations of the reconstructed pressure field averaged in the spanwise direction at the same times.

A probe has been placed in the flow at the location ($x/\delta = 41$, $y/\delta = 0.1$ corresponding to $y^+ \simeq 30$), in the region of large shedding of fluid from the recirculation bubble (see figure 6.34). The power spectral density of the reconstructed longitudinal velocity signal is plotted in figure 6.35. The spectrum contains two main peaks. One peak at medium frequency ($S_L \simeq 0.09$) corresponds to the medium frequency flapping of the shear layer. A second peak at low frequency $S_L \simeq 0.03$ falls in the range of low frequency flapping of the separation zone. The shedding is therefore associated to medium and low frequencies of the recirculation bubbles dynamics.

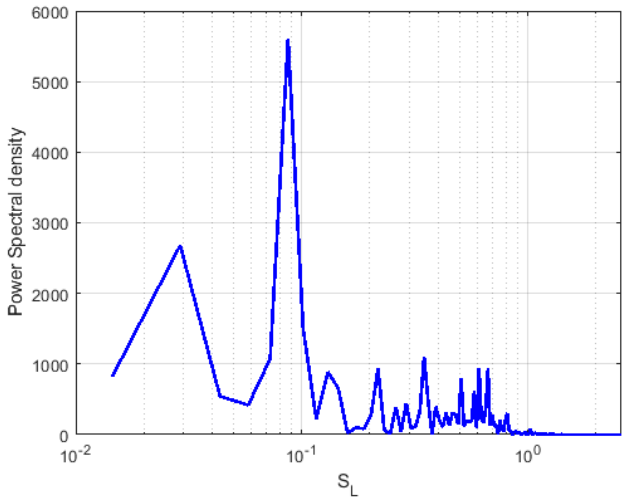

FIGURE 6.35 – Power spectral density of the longitudinal velocity signal for a probe located at ($x/\delta = 41$, $y/\delta = 0.1$ corresponding to $y^+ \simeq 30$) in the zone of large shedding of fluid from the recirculation bubble (see figure 6.34).

A sequence of visualizations of the reconstructed longitudinal velocity averaged in the spanwise direction at time intervals of $11L/U_\infty$ (corresponding to a frequency of sampling of $S_L \simeq 0.09$) is shown in figure 6.36. These visualization correspond to the maximum extent of the recirculation bubble for five successive medium frequency flapping cycles. These visualizations highlight the irregularity of the flapping patterns at the medium frequency. Indeed visible discrepancies are visible between the size of the recirculation bubble (maximum size of the cycle) for these consecutive flapping cycles. This irregularity of the medium frequency flapping can be related to the irregularities highlighted in the amplitudes of the separation and reattachment point oscillations, already mentionned in figures 6.18 and 6.19, that were found to introduce low frequencies in the characteristic range of the breathing of the separation bubble ($S_L \simeq 0.03$).

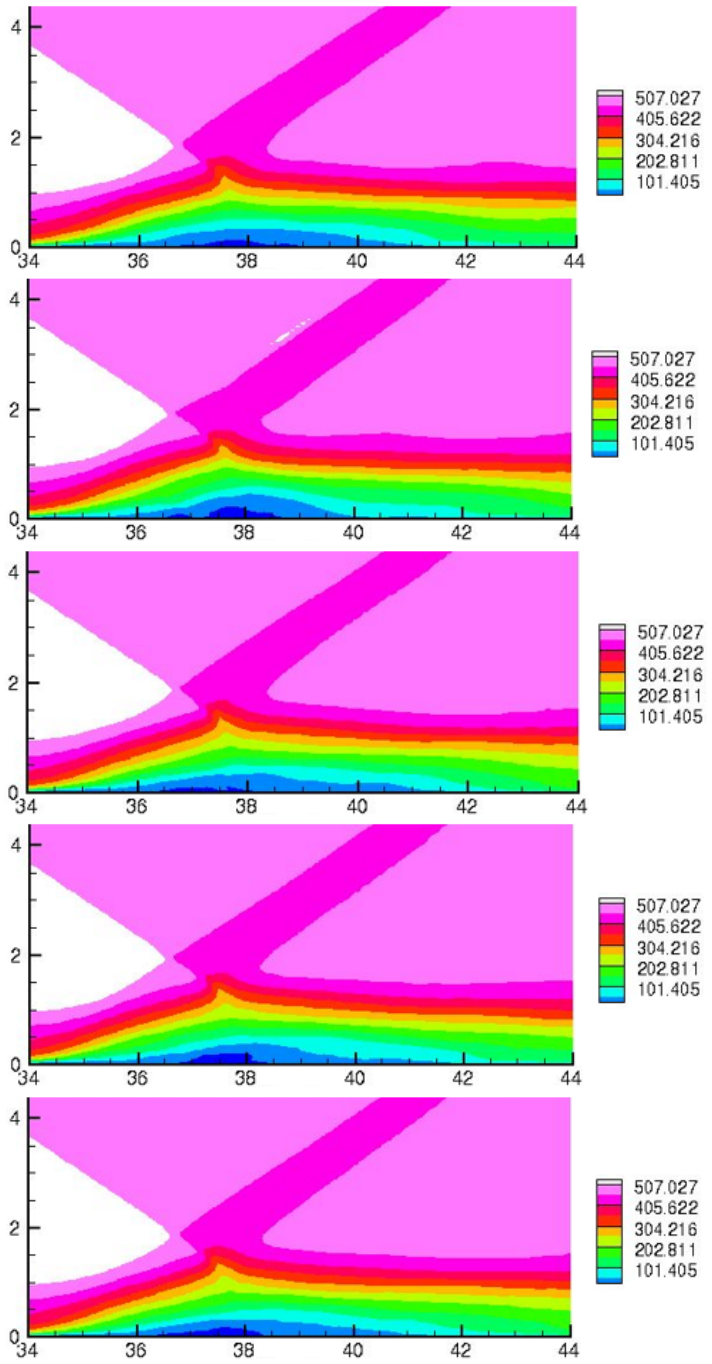

FIGURE 6.36 – Visualization of the reconstructed longitudinal velocity field at different times.

Isocontours of the longitudinal component of the 7^{th} and 8^{th} spatial modes of the POD of the velocity field are shown in figure 6.37. The power spectral density α^7 (respectively α^8) is plotted in figure 6.38-left (respectively figure 6.38-right). On the one hand, the power spectral density of the 7^{th} mode shows that this mode is involved in the low frequency dynamics of the interaction as its spectrum is dominated by a peak value at $S_L \simeq 0.04$. On the other hand, the power spectral density of the 8^{th} mode shows that this mode is mainly involved in the medium frequency dynamics of the interaction as its spectrum is dominated by peaks located at medium frequencies $S_L \simeq 0.1 - 0.2$. The qualitative aspects of the modes are very similar. For both modes, the separation bubble is populated by elongated streamwise structures. Other elongated streamwise structures populate the region located downstream of the separation bubble. These two modes describe the same dynamical phenomenon, namely the flapping of the recirculation zone associated to the shedding of large elongated structures from the separated zone. Nevertheless, structures of the 7^{th} mode ap-

pear to be more elongated than structures of the 8^{th} mode. They can thus be associated to larger amounts of fluid being shed from a larger separated zone.

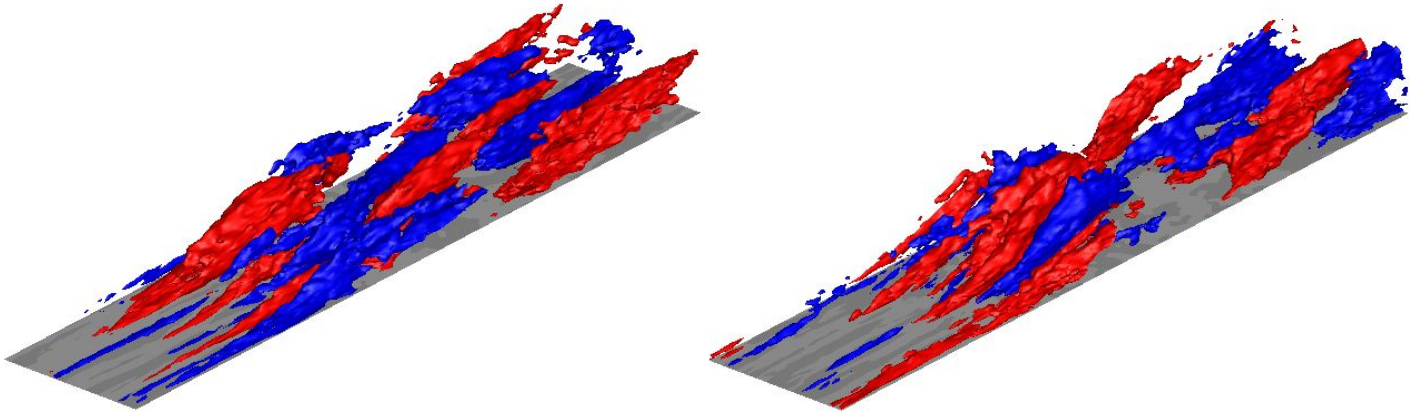

FIGURE 6.37 – Left: Isocontours of the longitudinal component of the 7^{th} spatial modes of the POD of the velocity field. Right: Isocontours of the longitudinal component of the 8^{th} spatial modes of the POD of the velocity field.

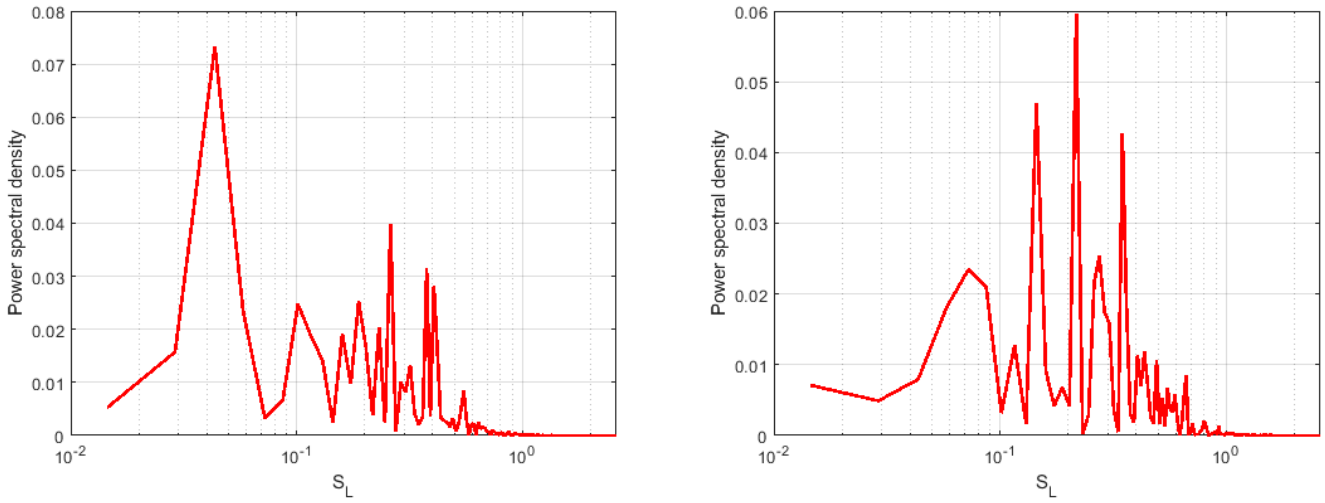

FIGURE 6.38 – Left: power spectral density of α^7. Right: power spectral density of α^8.

These results tend to confirm that the low frequency flapping of the recirculation bubble corresponds to a modulation in time of the medium frequency flapping and is associated to modulations of the cycles of successive enlargments and shrinkages. The motion of the reflected shock wave being in phase with the oscillations of the separation point, the SWTBLI unsteadiness seems to be a consequence of this low frequency modulation of the flapping of the separation bubble. This interpretation was already stated in Aubard [2012]. Nevertheless, our analyses did not allow us to evidence the origine of this temporal modulation of the flapping mode.

6.5 Conclusions

In this chapter, the SEM has been used at the inlet of a 3D domain in order to perform the DNS of a SWTBLI. The mean properties of the flow have been analyzed and compared to reference solutions. The dynamics of the flow have been studied by different means. First, the analysis of a sequence of 2D slice visualisations of the flow have been performed. It highlighted the existence of vortex structures in the shear layer, originating from the separation point, that are

shed in the downstream boundary layer. As noticed by Pirozzoli and Grasso [2006], the interaction between these vortices and the incident shock wave is responsible for an intense flapping of the incident shock wave. The characteristic frequencies of this vortex shedding have been evidenced using probes located in the shear layer.
The low frequency dynamics of the SWTBLI have then been studied in order to contribute to the understanding of the SWTBLI unsteadiness. A particular attention was paid to the low frequency dynamics of the recirculation bubble. Several conclusions result from this analysis:

— The oscillations of the separation and reattachment points are in phase opposition showing that the separation zone is submitted to successive enlargments and shrinkages.

— The frequencies characterizing the motions of the separation and reattachment points are found to be in the characteristic ranges of the low and medium frequency flapping of the separation bubble.

— The amplitudes of the separation and reattachment point motions are submitted to a temporal modulation leading to events associated to large upstream (respectively downstream) displacements of the separation (respectively reattachment) point. These events occur at low frequency ranges $S_L \simeq 0.03$.

— The reflected shock wave oscillates in phase with the separation point.

The POD of the velocity and pressure fields have been calculated in a close region embedding the interaction zone and have then been presented. For both fields, the PODs constist in the superposition of modes associated with frequencies which increase linearly with the order of the modes. The reconstuction of the fields using only low order modes therefore allows to reproduce the low frequency dynamics of the SWTBLI. A medium frequency flapping of the separation bubble, at a characteristic frequency $S_L \simeq 0.1$, has been identified as the dominant dynamical phenomenon of such a flow reconstruction. It corresponds to successive enlargments and shrinkages of the separated bubble, the shrinkage phase of the cycle being associated to a large shedding of fluid from the separated zone in the downstream flow. This medium frenquency flapping have been shown to be irregular in time, the maximum size of the recirculation bubble being submitted to modulations between successive cycles. This behavior of the separation bubble is responsible for the low frequency temporal modulation of the amplitude of the separation and reattachment points. Finally, the analysis of the longitudinal component of the spatial mode of two different POD modes have been performed. The first mode is associated to the low frequency dynamics of the flow whereas the second is associated to the medium frequency dynamics of the flow. The two modes are associated to the flapping of the recirculation zone associated to the shedding of large elongated structures from the separated zone. Nevertheless the low frequency mode is associated to the shedding of larger (and more elongated) structures than the medium frequency mode confirming that the low frequency and the medium frequency dynamics are associated to the same dynamical phenomenon, namely medium frequency flapping, which is irregular in time.
The low frequency flapping and consequently the low frequency oscillations of the reattachment shock wave are then found to be associated to a low frequency modulation of the medium frequency flapping of the recirculation bubble. This result tends to relate the SWTBLI unsteadiness to the dynamics of the separation bubble and not to the fluctuations of the incoming boundary layer. Nevertheless, our results are not in accordance with the model introduced by Piponniau et al. [2009] in which the SWTBLI unsteadiness is associated with cycles of rapid enlargment and slow shrinkage of the separation bubble at a frequency $S_L \simeq 0.03$, the shrinkage being due to the mass entrainment trough the shear layer. Indeed, our results tend to show that this cycles occurs at medium frequency ($S_L \simeq 0.1$) and not at low frequency. Unfortunately, the origin of the temporal modulation of these cycles is not evidenced by our results.

6.6 References

M. C. Adler and D. V. Gaitonde. Dynamic linear response of a shock/turbulent-boundary-layer interaction using constrained perturbations. *Journal of Fluid Mechanics*, 840:291–341, 2018. 6, 85, 86, 88, 89

Guillaume Aubard. *Large Eddy Simulation of the low-frequency unsteadiness of a shock-wave turbulent boundary layer interaction on a flat plate*. Theses, Arts et Métiers ParisTech, June 2012. URL https://pastel.archives-ouvertes.fr/pastel-00728991. 6, 86, 87, 88, 89, 93, 97, 109

Nathan J Mullenix, Datta V Gaitonde, and Miguel R Visbal. Spatially developing supersonic turbulent boundary layer with a body-force-based method. *AIAA journal*, 51(8):1805–1819, 2013. 89

S. Pirozzoli and F. Grasso. Direct numerical simulation of impinging shock wave/turbulent boundary layer interaction at m=2.25. *Physics of Fluids*, 18(6):065113, 2006. doi: 10.1063/1.2216989. 89, 90, 93, 110

Pierre Dupont, Sébastien Piponniau, Andreï Sidorenko, and Jean François Debiève. Investigation of an oblique shock reflection with separation by piv measurements. In *45th AIAA Aerospace Sciences Meeting and Exhibit*, page 119, 2007. 90

S. Piponniau, J. P. Dussauge, J. F. Debiève, and P. Dupont. A simple model for low-frequency unsteadiness in shock-induced separation. *Journal of Fluid Mechanics*, 629:87–108, 2009. 90, 110

Jean Délery and Jean-Paul Dussauge. Some physical aspects of shock wave/boundary layer interactions. *Shock waves*, 19(6):453, 2009. 90

Min S Chong, Julio Soria, AE Perry, J Chacin, BJ Cantwell, and Y Na. Turbulence structures of wall-bounded shear flows found using dns data. *Journal of Fluid Mechanics*, 357:225–247, 1998. 90

E. Touber and N. D. Sandham. Large-eddy simulation of low-frequency unsteadiness in a turbulent shock-induced separation bubble. *Theoretical and computational fluid dynamics*, 23:79–107, 2009. 97

JL Lumley. Atmospheric turbulence and wave propagation. the structure of inhomogeneous turbulence. *AM Yaglom et VI Tatarski*, page 166–178, 1967. 98, 99

Philip Holmes, John L Lumley, Gahl Berkooz, and Clarence W Rowley. *Turbulence, coherent structures, dynamical systems and symmetry*. Cambridge university press, 2012. 98

L. Sirovich. Turbulence and the dynamics of coherent structures. i. coherent structures. *Quarterly of applied mathematics*, 45(3):561–571, 1987. 98

Conclusions and perspectives

Concluding remarks

The aim of the present work was the unsteady numerical simulation of SWBLIs in order to contribute to a better understanding of the SWBLI unsteadiness and the physical mechanism causing these low frequency oscillations of the interaction zone. To perform this study, an original numerical approach implemented in the in house CHORUS code has been used. This one step FV approach relies on the discretization of the convective fluxes of the Navier Stokes equations using the OSMP scheme developed up to the 7^{th} order both in space and time, the viscous fluxes being discretized using a standard FD scheme.

A first part of the work has been devoted to the validation of the numerical tool for the simulation of high Reynolds number turbulent and shocked flows such as SWBLIs. We evaluated separately the ability of the numerical schemes to compute turbulent flows with accuracy and to capture shock waves with robustness. To this end, two well documented test-cases have been simulated: the 3D Taylor-Green vortex and the steady laminar shock-wave boundary layer interaction.
Results demonstrate the correct accuracy of the OSMP scheme to predict turbulent features and the great efficiency of the MP procedure to capture discontinuities without spoiling the solution and with an almost negligible additional cost. It has been shown that the use of the highest order tested of the OSMP scheme is relevant in term of simulation time and accuracy compromise. Moreover, an order of accuracy higher than 2^{nd}-order for approximating the diffusive fluxes seems to have a negligible influence on the solution for such relatively high Reynolds numbers.

The numerical approach being validated, a second part of the work has been devoted to the simulation and physical analysis of the SWBLI.

We first chose to perform a SWBLI simulation supressing one of the two suspected mechanisms leading to the SWBLI unsteadiness. By simulating the interaction between a laminar boundary layer and an incident shock wave, we suppressed the suspected influence of the large turbulent structures of the boundary layer on the SWBLI unsteadiness, the only remaining suspected cause of unsteadiness in this configuration being the dynamics of the separation bubble. Results have shown that the separation point of the recirculation bubble and the foot of the reflected shock wave have a fixed location along the flat plate with respect to time. This result shows that, in this configuration, the SWBLI unsteadiness has not been observed.
The analysis of the dynamics of the recirculation bubble has been performed. Two regions have been identified in the recirculation bubble: the first part of the separation, upstream of the incident shock wave impingement and the second part downstream of the incident shock wave. Characteristic frequencies of the instabilities of the recirculation bubble have been observed. The first part of the separation has been found mainly submitted to the frequencies characterizing the low frequency breathing of the recirculation bubble and the medium frequency flapping of the shear layer. The second part, submitted to fluctuations of higher intensity, is also submitted to the low frequency breathing of the recirculation bubble and the medium frequency flapping of the shear layer in addition to higher frequencies characterizing the vortex shedding from the shear layer. In particular, the reattachment location is sensitive to the instabilities of the recirculation bubble,

namely the breathing, the flapping and the Kelvin-Helmholtz frequencies.
Therefore, in this configuration, in which no SWBLI unsteadiness has been observed (in particular no motion of the reflected shock wave has been observed), low frequencies in the range of the characteristic frequency of the SWBLI unsteadiness has been found to characterize, among others, the dynamics of the whole recirculation bubble, both in its first and second part. This suggests that the low frequency breathing of the recirculation bubble is an intrinsic dynamical feature of the separated zone, not coupled with the dynamics of the reflected shock wave.

In order to reproduce and analyse the SWBLI unsteadiness, the simulation of the interaction between a incident shock wave and a turbulent boundary layer has then been undertaken.
In this context, the accurate simulation of a turbulent compressible incoming boundary layer is of great importance. A SEM that we adapted to compressible flows, has been developed to achieve this objective without prohibitive additional computational costs. The simulation of a flat plate compressible turbulent boundary layer has shown that this turbulent inflow condition is efficient to reduce the adaptation distance needed to obtain a fully turbulent state with respect to more classical methods.
The implemented SEM has been used at the inler boundary of the simulation domain for performing a DNS of a SWTBLI. For this simulation, the SWTBLI unsteadiness has been observed. In particular, the separation and reattachment points have been found to oscillate. The frequencies characterizing motion of the reattachement point are characteristic of the low and medium frequency flapping of the separation zone. The frequencies characterizing motion of the separation point are characteristic of the low frequency flapping of the separation zone. The motions of the separation and reattachment points have been found mainly in phase opposition indicating a dynamics of the recirculation bubble corresponding to successive enlargement and shrinkages. Moreover, the foot of the reflected shock wave has been found to oscillate in phase with the separation point.
A snapshot-POD analysis of velocity and pressure fields in the interaction zone has been performed. The time evolution of the reconstructed velocity and pressure fields using only low order modes, containing most of the POD energy involved in the low frequency dynamics of the flow, has been shown dominated by a medium frequency flapping of the recirculation bubble at a characteristic frequency $S_L \simeq 0.1$ corresponding to successive enlargment and shrinkages of the separated bubble, the shrinkage phase of the cycle being associated to a large shedding of fluid from the separated zone in the downstream flow. This medium frenquency flapping have been shown to be irregular in time, the maximum size of the recirculation bubble being submitted to discrepancies between successive cycles. This behaviour of the separation bubble is responsible for the low frequency temporal modulation of the amplitude of the separation and reattachement points and thus for the low frequency breathing of the separation bubble. Nevertheless, the origin of the temporal modulation of the medium frequency flapping cycles is not evidenced by our results.
This results tend to suggest that the SWTBLI unsteadiness is related to this low frequency dynamics of the recirculation bubble; the oscillations of the reflected shocks foot being in phase with the motion of the separation point.
This low frequency activity of the recirculation bubble seems to be also at play in the SWLBLI. Nevertheless, in this case, the recirculation bubble is much larger than in a SWTBLI. Moreover, in the case of a laminar boundary layer the separation bubble is not submitted to the incoming turbulent fluctuations. The vortical dynamics in the separation zone is consequently much less intense than in the case of a turbulent boundary layer. The relative amount of fluid being shed (with respect to the size of the separated zone) from the separation bubble in each flapping cycle is then lower in a SWLBLI than in a SWTBLI. This is confirmed by comparing the standard deviation of the L(t) in a SWLBLI (0.0093L) with the standard deviation of the L(t) in a SWLBLI (0.25L). Consequently, in the laminar case, the low frequency activity felt in the first part of the separation is not intense enough to porvoke the oscillations of the separation point and the subsequent oscillations of the reflected shock foot.

Perspectives

Further analysis of the SWBLI must be undertaken in order to understand the origin of the temporal modulation of the medium frequency flapping cycles responsible for the low frequency breathing of the recirculation bubble and leading to the onset of the SWTBLI unsteadiness. This work could highlight the physical origin of the SWTBLI unsteadiness. In this context, the use of the DMD technique could be promising, as it allows to decompose the flow in modes associated to identified frequency ranges. The analysis of the modes associated to the low frequency breathing of the separation bubble could be fruitful. More generally, this work might be achieved by using data processing tools which nowaday become more and more popular in fluid dynamics analyses. It would be also interesting to undertake the simulation of other configurations, for instance the SWBLI over a compression ramp, to see if the same dynamical behavior is present and could be reproduced using the numerical approach used in this work.
An other direction could be to study how the oscillations of the recirculation bubble could be controlled in order to avoid its low frequency activity and consequently avoid the low frequency unsteadiness and the subsequent reflected shock wave oscillations. This work would benefit from the physical knowledge obtained from the physical analysis evoked above.

Glossary

CFD Computational Fluid Dynamics. 5

DBD Dielectric Barrier Discharge. 68
DG Discontinuous Galerkin. 26
DMD Dynamic Mode Decomposition. 18, 115
DNS Direct Numerical Simulation. 4–6, 18, 24, 26, 56, 64, 68, 69, 80, 84–89, 109, 114

ENO Essentially Non-Oscillatory. 28

FD Finite Difference. 26, 29, 35, 36, 113
FE Finite Element. 26
FV Finite Volume. 5, 26, 27, 113

LES Large Eddy Simulation. 26, 68, 86

MP Monotonicity Preserving. 4, 28, 36, 41, 45, 49, 50, 52, 113
MPI Message Passing Interface. 5

OS One Step. 3, 4, 27, 41–45, 49
OSMP One Step Monotonicity-Preserving. 4, 5, 42, 44, 45, 48–52, 113

POD Proper Orthogonal Decomposition. 6, 7, 83, 98–103, 108–110, 114

RANS Reynolds-averaged Navier–Stokes equations. 4
RFG Random Flow Generation. 70

SD Spectral Difference. 26
SEM Synthetic Eddy Method. 5, 34, 68, 70, 71, 73, 76, 77, 79–81, 84, 109, 114
SRA Strong Reynolds Analogy. 76
SV Spectral Volume. 26
SWBLI Shock Wave Boundary Layer Interaction. 1–5, 10, 12–19, 23, 24, 26, 29, 34–36, 47, 56, 63, 64, 70, 84, 90, 113–115
SWLBLI Shock Wave Laminar Boundary Layer Interaction. 5, 12, 18, 25, 34, 47, 56, 57, 64, 84, 89, 114
SWTBLI Shock Wave Turbulent Boundary Layer Interaction. 5, 6, 12, 15, 18, 19, 34, 59, 68–71, 77, 78, 81, 84–86, 88–90, 97–100, 102–104, 109, 110, 114, 115

TV Total Variation. 27
TVD Total Variation Diminishing. 26–30, 44

WENO Weighted Essentially Non-Oscillatory. 28, 29

université PARIS-SACLAY
ÉCOLE DOCTORALE
Sciences mécaniques et énergétiques, matériaux et géosciences (SMEMAG)

Titre : Simulations numériques de l'interaction onde de choc couche limite

Mots clés : Mécanique des fluides, Ecoulements compressibles, Simulations Numériques Directes, turbulence, Calcul Haute Performance.

Résumé :
Les situations dans lesquelles une onde de choc interagit avec une couche limite sont nombreuses dans les industries aéronautiques et spatiales. Sous certaines conditions (nombre de Mach élevé, grand angle de choc...), ces interactions entrainent un décollement de la couche limite. Des études antérieures ont montré que la zone de recirculation et le choc réfléchi sont tous deux soumis à un mouvement d'oscillation longitudinale à basse fréquence connu sous le nom d'instabilité de l'interaction onde de choc / couche limite (IOCCL). Ce phénomène soumet les structures à des chargement oscillants à basse fréquence qui peuvent endommager les structures.
L'objectif du travail de thèse est de réaliser des simulations instationnaires de l'IOCCL afin de contribuer à une meilleure compréhension de l'instabilité de l'IOCCL et des mécanismes physiques sous-jacents.
Pour effectuer cette étude, une approche numérique originale est utilisée. Un schéma « One step » volume fini qui couple l'espace et le temps, reposant sur une discrétisation des flux convectifs par le schéma OSMP, est développé jusqu'à l'ordre 7 en temps et en espace. Les flux visqueux sont discrétisés en utilisant un schéma aux différences finies centré standard. Une contrainte de préservation de la monotonie (MP) est utilisée pour la capture de choc. La validation de cette approche démontre sa capacité à calculer les écoulements turbulents et la grande efficacité de la procédure MP pour capturer les ondes de choc sans dégrader la solution pour un surcoût négligeable. Il est également montré que l'ordre le plus élevé du schéma OSMP testé représente le meilleur compromis précision / temps de calcul. De plus un ordre de discrétisation des flux visqueux supérieur à 2 semble avoir une influence négligeable sur la solution pour les nombres de Reynolds relativement élevés considérés.
En simulant un cas d'IOCCL 3D avec une couche limite incidente laminaire, l'influence des structures turbulentes de la couche limite sur l'instabilité de l'IOCCL est supprimée. Dans ce cas, l'unique cause d'IOCCL suspectée est liée à la dynamique de la zone de recirculation. Les résultats montrent que seul le choc de rattachement oscille aux fréquences caractéristiques de la respiration basse fréquence du bulbe de recirculation. Le point de séparation ainsi que le choc réfléchi ont une position fixe. Cela montre que dans cette configuration, l'instabilité de l'IOCCL n'a pas été reproduite.
Afin de reproduire l'instabilité de l'IOCCL, la simulation de l'interaction entre une onde de choc et une couche limite turbulente est réalisée. Une méthode de turbulence synthétique (Synthetic Eddy Method - SEM) est développée et utilisée à l'entrée du domaine de calcul pour initier une couche limite turbulente à moindre coût. L'analyse des résultats est effectuée en utilisant notamment la méthode snapshot-POD (Proper Orthogonal Decomposition). Pour cette simulation, l'instabilité de l'IOCCL a été reproduite. Les résultats suggèrent que la dynamique du bulbe de recirculation est dominée par une respiration à moyenne fréquence. Ces cycles successifs de remplissage / vidange de la zone séparée sont irréguliers dans le temps avec une taille maximale du bulbe de recirculation variant d'un cycle à l'autre. Ce comportement du bulbe de recirculation traduit une modulation basse fréquence des amplitudes des oscillations des points de séparation et de recollement et donc une respiration basse fréquence de la zone séparée. Ces résultats suggèrent que l'instabilité de l'IOCCL est liée à cette dynamique basse fréquence du bulbe de recirculation, les oscillations du pied du choc réfléchi étant en phase avec le point de séparation.

Title : Numerical simulation of shock wave boundary layer interactions

Keywords : Fluid Dynamics, Compressible flows, Direct Numerical Simulations, turbulence, HPC.

Abstract : Situations where an incident shock wave impinges upon a boundary layer are common in the aeronautical and spatial industries. Under certain circumstances (High Mach number, large shock angle...), the interaction between an incident shock wave and a boundary layer may create an unsteady separation bubble. This bubble, as well as the subsequent reflected shock wave, are known to oscillate in a low-frequency streamwise motion. This phenomenon, called the unsteadiness of the shock wave boundary layer interaction (SWBLI), subjects structures to oscillating loads that can lead to damages for the solid structure integrity.

The aim of the present work is the unsteady numerical simulation of (SWBLI) in order to contribute to a better understanding of the SWBLI unsteadiness and the physical mechanism causing these low frequency oscillations of the interaction zone.

To perform this study, an original numerical approach is used. The one step Finite Volume approach relies on the discretization of the convective fluxes of the Navier Stokes equations using the OSMP scheme developed up to the 7-th order both in space and time, the viscous fluxes being discretized using a standard centered Finite-Difference scheme. A Monotonicity-Preserving (MP) constraint is employed as a shock capturing procedure. The validation of this approach demonstrates the correct accuracy of the OSMP scheme to predict turbulent features and the great efficiency of the MP procedure to capture discontinuities without spoiling the solution and with an almost negligible additional cost. It is also shown that the use of the highest order tested of the OSMP scheme is relevant in term of simulation time and accuracy compromise. Moreover, an order of accuracy higher than 2-nd order for approximating the diffusive fluxes seems to have a negligible influence on the solution for such relatively high Reynolds numbers.

By simulating the 3D unsteady interaction between a laminar boundary layer and an incident shock wave, we suppress the suspected influence of the large turbulent structures of the boundary layer on the SWBLI unsteadiness, the only remaining suspected cause of unsteadiness being the dynamics of the separation bubble. Results show that only the reattachment point oscillates at low frequencies characteristic of the breathing of the separation bubble. The separation point of the recirculation bubble and the foot of the reflected shock wave have a fixed location along the flat plate with respect to time. It shows that, in this configuration, the SWBLI unsteadiness is not observed.

In order to reproduce and analyse the SWBLI unsteadiness, the simulation of a shock wave turbulent boundary layer interaction (SWTBLI) is performed. A Synthetic Eddy Method (SEM), adapted to compressible flows, has been developed and used at the inlet of the simulation domain for initiating the turbulent boundary layer without prohibitive additional computational costs. Analyses of the results are performed using, among others, the snapshot Proper Orthogonal Decomposition (POD) technique. For this simulation, the SWBLI unsteadiness has been observed. Results suggest that the dominant flapping mode of the recirculation bubble occurs at medium frequency. These cycles of successive enlargement and shrinkage of the separated zone are shown to be irregular in time, the maximum size of the recirculation bubble being submitted to discrepancies between successive cycles. This behaviour of the separation bubble is responsible for a low frequency temporal modulation of the amplitude of the separation and reattachment point motions and thus for the low frequency breathing of the separation bubble. These results tend to suggest that the SWBLI unsteadiness is related to this low frequency dynamics of the recirculation bubble; the oscillations of the reflected shocks foot being in phase with the motion of the separation point.

Université Paris-Saclay
Espace Technologique / Immeuble Discovery
Route de l'Orme aux Merisiers RD 128 / 91190 Saint-Aubin, France